A STUDY OF MASSIVE MUON PAIR PRODUCTION AT HIGH X_F

BY

JAMES P. ALEXANDER

MARCH, 1985

FERMILAB
LIBRARY

THE UNIVERSITY OF CHICAGO

A STUDY OF MASSIVE MUON PAIR PRODUCTION AT HIGH X_F

A DISSERTATION SUBMITTED TO
THE FACULTY OF THE DIVISION OF PHYSICAL SCIENCES
IN CANDIDACY FOR THE DEGREE OF
DOCTOR OF PHILOSOPHY

DEPARTMENT OF PHYSICS

BY

JAMES P. ALEXANDER

CHICAGO, ILLINOIS

MARCH 1985

FAB1778

ACKNOWLEDGEMENTS

Many people contributed their time, energy, and talent to this experiment. I owe a large measure of thanks to my Princeton collaborators, Stew Smith, Frank Shoemaker, Kirk McDonald, Bill Louis, John Greenhalgh, Sandro Palestini, and Cristina Biino, as well as my collaborator from Iowa State University, and former advisor, Eli Rosenberg. In Chicago a key role was played by the Engineering Services Group, with many invaluable contributions coming from Dick Armstrong, Rudi Gabriel, Rich Northrup, Archie Ryan, and Larry Fiscelli. Special thanks are due in particular to Harold Sanders and the Electronics Development Group for their many electronic wonders, most especially the proportional chamber readout system.

Finally I wish to thank my colleagues at the University of Chicago for their help, stimulation, patience, and support. Wyatt Merritt, John Conway, Joel Heinrich, and Chris Adolphsen have contributed tremendously to this experiment and its successful outcome. Most of all, I thank my advisor, Jim Pilcher, and colleague Kelby Anderson for the finest training anyone could have asked for.

Table of Contents

ACKNOWLEDGEMENTS ii

LIST OF TABLES vi

LIST OF ILLUSTRATIONS vii

ABSTRACT xi

Chapter

I. LEPTON PAIR PRODUCTION AND THE STRUCTURE OF HADRONS 1

1.1 Introduction
1.2 Kinematics of Lepton Pair Production
1.3 The General Form of the Lepton Pair Production Cross Section
1.4 Parton Model Description of Lepton Pair Production
1.5 Structure Functions: Predictions
1.6 QCD and Massive Lepton Pair Production
1.7 QCD and Structure Functions
1.8 This Experiment

II. THE APPARATUS 19

2.1 Overview of the Experiment
2.2 The Beam
2.3 The Target

2.4 The Absorber
2.5 The Magnets
2.6 Proportional Chambers
2.7 Drift Chambers
2.8 Hodoscopes
2.9 The Trigger
2.10 Data Acquisition

III. THE ANALYSIS 36

3.1 Event Reconstruction
3.2 Event Selection
3.3 The Monte Carlo
3.4 Detector Acceptance
3.5 Hodoscope Efficiencies
3.6 Chamber Efficiencies
3.7 Reconstruction Efficiencies
3.8 Beam Momentum
3.9 Resolution and Smearing of Kinematic Variables
3.10 Background Subtraction
3.11 Normalization

IV. THE PION STRUCTURE FUNCTION 58

4.1 Structure Functions and the Lepton Pair Cross Section
4.1 Parametrizations (and Nomenclature)
4.1 Pion Structure Function: Results of Other Experiments
4.1 Nucleon Structure Functions: Results of Other Experiments
4.1 Methods of Analysis: General Remarks
4.1 The Pion Structure Function: Results
4.1 Systematic Considerations
4.1 Concluding Remarks on Structure Functions

V. THE LEPTON PAIR ANGULAR DISTRIBUTION 76

5.1 The Cross Section in θ^* and ϕ^*

5.2 Measurements of α vs. x: Results of Other Experiments

5.3 Results on $\cos\theta^*$ Distributions

5.4 Conclusions

VI. CONCLUSION 84

REFERENCES 86

LIST OF TABLES

1. Characteristics of the Absorber 23
2. MWPC Sizes, Positions, and Wire Tilts 25
3. Drift Chamber Sizes, Positions, and Wire Tilts 30
4. Hodoscope Positions and Counter Sizes 31
5. Beam Hole Position 32
6. Event Selection Cuts 45
7. Recent Fits to the Pion Structure Function 62
8. Fits to Pion Structure Function 67
9. Fits to Pion Structure Function after Iteration 70
10. Values of Pion and Nucleon Structure Functions 71
11. Comparison of Pion Structure Function in Two Mass Regions 72
12. Systematic Errors in the Pion Structure Function 73
13. Summary of Measurements of α 78
14. Global Fits to $1+\alpha\cos^2\theta$ 79
15. Fits to $1+\alpha\cos^2\theta$ in Bins of x_1 80
16. Fits to $1+\alpha\cos^2\theta$ in Bins of P_T 82

LIST OF ILLUSTRATIONS

1. Parton model picture of deep inelastic scattering. 93
2. Parton model picture of lepton pair production. 95
3. Definition of reference axes in γ^* rest frame. 97
4. General illustration of lepton pair production process. 99
5. Illustration of the process used by Farrar and Jackson. 101
6. Illustration of the lowest order QCD corrections. production. 103
7. Diagrams used in the higher twist model. 105
8. Plan and elevation views of the E615 experimental apparatus. 107
9. Plan view of the selection magnet. 109
10. Elevation view of the selection magnet. 111
11. Vertical field strength in the selection magnet. 113
12. Vertical field strength in the analysis magnet. 115
13. Plan view of spectrometer region. 117
14. MWPC cathode and anode layouts. 119
15. Organization of MWPC readout electronics. 121
16. Perspective drawing of hodoscope trigger planes. 123
17. Diagram of C hodoscope bank. 125
18. Diagram of D hodoscope bank. 127
19. Diagram of E and F hodoscope banks. 129

20. Plot of θ_z vs. p at the target before halo cut. 131

21. Comparison of momentum spectra before halo cut. 133

22. Illustration of the halo cut. 135

23. Plot of θ_z vs. p after the halo cut. 137

24. Comparison of momentum spectra after halo cut. 139

25. Comparison between Monte Carlo and data. 141

26. Comparison between Monte Carlo and data. 143

27. Comparison between Monte Carlo and data. 145

28. Comparison between Monte Carlo and data in $\cos\theta^*$. 147

29. Acceptance in Mass and P_T. 149

30. Acceptance in x_F and x_1. 151

31. Acceptance in ϕ^* and Φ_{LAB}. 153

32. Acceptance in $\cos\theta^*$ in four helicity frames. 155

33. Acceptance in $\cos\theta^*$ in four bins of x_1. 157

34. Illumination plot at the D-bank. 159

35. Efficiencies of hodoscopes DY15 and DY39. 161

36. Comparison of Monte Carlo and data at DX bank. 163

37. Comparison of Monte Carlo and data at DY bank. 165

38. Acceptance in $\cos\theta^*$ before and after efficiency correction. 167

39. Acceptance in $\cos\theta^*$ before and after efficiency correction. 169

40. Efficiency of MWPC plane #1. 171

41. Efficiency of Drift Chamber plane #6. 173

42. Reconstruction efficiency as a function of kinematic variables. 175

43. Reconstruction efficiency vs. $\cos\theta^*$ in four bins of x_1. 177

44. Comparison of data and Monte Carlo for momentum spectrum of beam muons..... 179

45. Beam momentum spectrum predicted by HALO. 181

46. Resolution and smearing of x_1. 183

47. Resolution and smearing of $\cos\theta^*$. 185

48. $\mathrm{Cos}\theta^*$ distributions for real events and background. 187

49. Distributions of the 13.1 background events. 189

50. Comparison of $G(x_2)$ determined by CDHS and CCFRR. 191

51. Scatter plot of all events in x_1–x_2. 193

52. $G(x_2)$ after iterated projections. 205

53. $G(x_2)$ after iterated projections. 197

54. Measurements of $G(x_2)$ by three muon-pair experiments. 199

55. $F^\pi(x_1)$ after iterated projections (fit #1). 191

56. $F^\pi(x_1)$ after iterated projections (fit #4). 203

57. Plot of $<p_T^2>$ as a function of x_1. 205

58. Existing measurements of α at various x_1 values. 207

59. $\mathrm{Cos}\theta^*$ distributions in four helicity frames. 209

60. $\mathrm{Cos}\theta^*$ distributions in four regions of x_1 (Collins-Soper). 211

61. $\mathrm{Cos}\theta^*$ distributions in four regions of x_1 (T-channel). 213

62. Plot of α vs. x_1 (Collins-Soper). 215

63. Plot of α vs. x_1 (T-channel). 217

64. $\mathrm{Cos}\theta^*$ distributions in three regions of P_T/M (Collins-Soper). 219

65. Cosθ^* distributions in three regions of P_T/M (T-channel). 221

66. Plots of α vs. P_T/M. 223

ABSTRACT

A study of muon pair production in the reaction $\pi^- N \rightarrow \mu^+\mu^- X$ has been completed and results are reported. Experimental apparatus maximizes acceptance at high x_F and maintains good acceptance out to $\cos\theta^* = \pm 1$. Interest in these kinematic regions stems from QCD models which incorporate higher twist and predict significant departures from the classical Drell-Yan model at high x_F. Distributions in $\cos\theta^*$ are expected to show the effect most clearly. Results presented here include measurement of pion and nucleon structure functions, mean square transverse momentum of the muon pair, global $\cos\theta^*$ distributions, and $\cos\theta^*$ distributions in bins of x and P_T/M. Consistency with the QCD model is observed. At $x \leq 0.1$ and $Q^2 \sim 25$ GeV^2 the nucleon structure function exhibits a deviation from the expectation based on deep inelastic neutrino scattering measurements, but agrees well with measurements made in other muon pair experiments.

CHAPTER I

LEPTON PAIR PRODUCTION AND THE STRUCTURE OF HADRONS

1.1 Introduction

The structure of matter has been studied by physicists for many decades on ever finer scales of distance. Atoms have been seen to consist of nuclei and electrons, and nuclei to consist of protons and neutrons. The observation of new particles has led to the realization that protons and neutrons are part of a larger class of objects, called ***hadrons***, and electrons are part of larger class known as ***leptons***. In our current understanding of the world, matter consists of hadrons and leptons. Within the resolving power ($\sim 10^{-16}$ cm) of present day "microscopes," the leptons appear to be completely structureless, and are considered fundamental. The hadrons, by contrast, are known to be composite particles, with constituents which we call quarks. These quarks, in turn, appear to be indivisible and fundamental like the leptons. Indeed, leptons and quarks seem to be related in a deep way. The principle difference (the only difference?) is that quarks possess a property we call "color" and respond to the strong interaction, whereas leptons lack color and do not respond to the strong interactions.

This ability to interact strongly, of course, lies behind the formation and existence of hadrons in the first place. Although composites of leptons may be formed (eg. positronium or muonium), it appears that with quarks, composite particles (hadrons) ***must*** be formed, because the color charge which allows them to interact strongly in the first place seems also to compel them to bind together in "colorless" units. Color lies at the heart of the most successful understanding to date of the strong interactions, the theory of Quantum Chromodynamics, or QCD.[1] QCD, however, has not yielded ready solutions to the problem of binding. A characteristic feature of QCD is that the coupling constant grows as the

distance between the interacting particles grows. At the distance scale typical of most hadrons ($\sim 10^{-13}$ cm) the coupling constant is too large to permit perturbative calculations. The problem of predicting hadronic structure *ab initio* thus remains unsolved.

In practice, however, the full complexity of QCD is not needed to understand the general features of hadronic structure. The same phenomenon of the "running coupling constant" that makes perturbative calculations hopeless at large distances gives rise to "asymptotic freedom" at short distances: a situation in which the coupling constant is small and interactions are weak. Applied to the hadron this means the constituent quarks will appear to be free if the hadron is probed on a small enough scale. The quark-parton model embraces this concept. It assumes the hadron is an incoherent collection of noninteracting quarks and gluons. The structure we seek to understand in this picture is then embodied in the momentum distributions of these *partons*. In the absence of transverse momentum, the quark momenta may be characterized by x, the fraction of the momentum of the parent hadron. The distributions in x, $q(x)$, then summarize our knowledge of the hadron's structure. The model does not suggest, however, what the $q(x)$ might be; indeed, there is no first-principles prediction for $q(x)$. Given this situation, our recourse has been to use phenomenological arguments to suggest possible forms of $q(x)$.

On the experimental side, much of what we know about hadronic structure comes from deep inelastic scattering experiments. In these experiments a lepton is used to probe the interior of the hadron. In the parton model interpretation the lepton interacts with a constituent quark as illustrated in figure 1. The final observed state is a single lepton and is thus characterized by 3 parameters, which one may think of as the 3 components of the lepton momentum. Two of the parameters are of physical interest* and are commonly chosen to be represented by Q^2 and x, where $Q^2=-q^2$ and $x=Q^2/2M\nu$, $\nu=q\cdot P/M$. The quantity x can be shown to be equal to the same x used to denote the momentum fraction alluded to above, and thus these experiments offer a window on the hadronic structure functions $q(x)$. Indeed, one is able to extract the momentum distributions for the valence quarks of the nucleon, as well as the sea quarks and the gluons.

*The third is the azimuthal angle about the beam axis.

Massive lepton pair production has proven to be another means of exploring and probing the activities of quarks in hadrons.[2] Lepton pairs displaying a continuum of masses were first observed[3] in 1969 and subsequently explained by a simple parton model of Drell and Yan.[4] Here the central idea is that the lepton pair results from the annihilation of quarks and antiquarks drawn from the colliding hadrons. The interaction proceeds through an intermediate virtual photon, as illustrated in figure 2. The similarity to deep inelastic scattering (figure 1) cannot be missed, of course, and it is no surprise that in many ways the description of the two processes and the capabilities of the two experiments overlap. In lepton pair production, however, one measures a 2-lepton final state and thus has 6 variables to work with. The additional variables are a mixed blessing. While they give one more "handles" on the problem, the problem itself becomes more complex: with two hadrons in the initial state, for instance, there are now two sets of structure functions to be extracted. In addition, the analysis becomes complicated by the many ways the data must be divided up; more data is needed to handle the additional binning. Still, there are many advantages to be reaped. Lepton pair experiments explore a kinematic region different from that explored by deep inelastic scattering, and allow one to study a variety hadrons since the beam itself is hadronic and need not be stable; moreover, as will be seen later, lepton pair experiments offer clean tests of QCD that are not available in deep inelastic scattering.

In the remainder of this chapter, lepton pair production will be explored in some detail: §1.2 and §1.3 will cover kinematics and the standard formalism, to establish a common language in which to discuss models and predictions; §1.4 will cover the parton model and its predictions; §1.5 will discuss phenomenological models used to predict structure functions; §1.6 will discuss the modifications QCD makes to the classical Drell-Yan picture, focussing on the leading-twist diagrams; §1.7 will review a higher-twist model and its predictions for the pion structure function and the lepton pair cross section; and §1.8 will adumbrate the history and goals of the experiment this dissertation is reporting on.

1.2 Kinematics of Lepton Pair Production

Two frames of reference are used in the standard kinematical description of lepton pair production, the center of mass of the π–N system, in which the virtual photon (γ^*) is produced, and the rest frame of the γ^* itself, in which the decay to l^+l^- is most readily treated. The mass (M), transverse momentum (P_T), azimuthal angle (Φ_{LAB}), and Feynman-x, (x_F), of the virtual photon completely characterize its 4-momentum. A few words about x_F are in order. The maximum momentum the γ^* can take is dictated by simple kinematics; assuming the recoil system is a proton (the lightest recoil system consistent with baryon conservation) one has

$$P^*_{\max} = \frac{\sqrt{s}}{2}\left[\left(1-\frac{(M_p+M)^2}{s}\right)\left(1-\frac{(M_p-M)^2}{s}\right)\right]^{\frac{1}{2}}. \qquad 1.1$$

The maximum value the *longitudinal* component of P^* is then reduced by the P_T of the virtual photon:

$$P^*_{L_{\max}} = \left(P^{*2}_{\max} - P_T^2\right)^{\frac{1}{2}}.$$

One then defines x_F using this kinematically correct version of $P^*_{L_{\max}}$:

$$x_F = \frac{P^*_L}{P^*_{L_{\max}}}.$$

At high x_F this care is needed in the definitions. At low P_T, x_F is well approximated by $x_F = 2P^*_L/\sqrt{s}(1-\tau)$, where $\tau = M^2/s$.

If the quark from the pion has momentum fraction x_1 and the quark from the nucleon has momentum fraction x_2, then one readily computes

$$M^2 = x_1 x_2 s,$$

and

$$x_F = \frac{x_1 - x_2}{1-\tau},$$

which may be inverted to give x_1 and x_2 in terms of the (measured) quantities M and x_F:

$$x_{\substack{1\\2}} = \frac{1}{2}\left[x_F(1-\tau) \pm \left(x_F^2(1-\tau)^2 + 4\frac{M^2}{s}\right)^{\frac{1}{2}}\right]$$

The discussion so far has covered only the variables describing the γ^*. These parameters characterize all the hadronic aspects of the interaction. The two remaining variables characterize the momenta of the two leptons in their center of mass, the rest frame of the γ^*. Since their energies and momenta are determined by the kinematics of two-body decay, only the direction of the decay axis remains to be specified. In the γ^* rest frame this axis may be characterized by a polar angle θ^* and azimuthal angle ϕ^*, referred to a suitable set of axes. Ideally the original quark-antiquark annihilation axis should be used to form the $\hat{z}$ axis, but because the quarks have some intrinsic transverse momentum in the parent hadrons, this axis is never known; one makes do with some best-guess. As as result of this inherent uncertainty of the annihilation axis, various sets of axes are in common use. Each set defines a ***helicity frame*** which may be described as follows. Let $\hat{\pi}$, $\hat{p}$, and $\hat{\mu}^+$ be unit vectors indicating the direction of the pion, nucleon, and μ^+ in the rest frame of the γ^*. Because the γ^* has in general some nonzero P_T, these vectors will normally not be collinear, and thus a reaction plane $(\hat{\pi},\hat{p})$ is defined. Let $\hat{r}$ be the direction of the (unobserved) recoil system, also in the γ^* rest frame. The four standard helicity frames choose their $\hat{z}$-axes by the following convention:

Helicity Frame	$\hat{z}$
Collins-Soper	$(\hat{\pi}-\hat{p})/\lvert\hat{\pi}-\hat{p}\rvert$
S-Channel	$\hat{r}$
T-Channel	$\hat{\pi}$
U-Channel	$-\hat{p}$

Note that the Collins-Soper axis is midway between the beam and target axes. The angle between Collins-Soper and either of these axes is $\sim P_T/M$, or about 12° in the kinematic range of this experiment.

The $\hat{x}$-axis lies in the $(\hat{\pi},\hat{p})$ plane, orthogonal to $\hat{z}$ and pointing away from $\hat{\pi}+\hat{p}$; $\hat{y}$ is defined to complete a right-handed orthonormal system.

With these definitions, $\cos\theta^*=\hat{\mu}^+\cdot\hat{z}$ and $\sin\theta^*\cos\phi^*=\hat{\mu}^+\cdot\hat{x}$. Figure 3 shows a diagram of the vectors in the γ^* rest frame, with the axes indicated.

1.3 The General Form of the Lepton Pair Production Cross Section

Although the parton model makes a prediction for the cross section (which I will discuss shortly), and some QCD-based models make other predictions (which I will discuss later), a general model- independent approach may be taken[5] to spell out the form all models must follow. This not only clarifies the physics issues which may be addressed by a lepton pair experiment, but also supplies a common language in which to express both experimental results and predictions of the many available models.

In this approach parton model concepts are not presumed, and one begins from the most general statement of the problem, as illustrated in figure 4. Much as is done in deriving the deep inelastic scattering cross section, we may apply invariance principles to write the cross section in terms of structure functions which characterize the unknown goings-on in the hadronic "blob" of figure 4. In terms of helicity structure functions, one finds the cross section takes the form

$$\frac{d\sigma}{d^4q\,d\Omega^*} = \frac{1}{32\pi^4}\left(\frac{\alpha}{Ms}\right)^2\Big[W_T(1+\cos^2\theta^*) + W_L\sin^2\theta^* + W_\Delta\sin 2\theta^*\cos\phi^* + W_{\Delta\Delta}\sin^2\theta^*\cos 2\phi^*\Big] \qquad 1.3$$

In this equation all dependence on the leptonic angles θ^* and ϕ^* is explicit; the structure functions W_T, W_L, W_Δ, and $W_{\Delta\Delta}$ depend only on hadronic variables s, M, x_F, and P_T. This equation completely separates the hadronic variables from the leptonic ones.

A number of relationships can be shown to hold among the helicity structure functions, the most physically interesting of which is[6]

$$W_L = 2\,W_{\Delta\Delta}. \qquad 1.4$$

This is directly related to the spin-1/2 nature of the quarks, and is not affected by first order QCD corrections (in contrast to the Callan-Gross relation, which is the deep inelastic analog of equation 1.4). This relationship is also independent of the choice of helicity frame. A similar relationship relates to the spin of the gluon[7], but is not readily expressible in terms of helicity structure functions.[8]

The structure functions W_T and W_L correspond to transverse ($J_z=\pm 1$) and longitudinal ($J_z=0$) polarizations of the virtual photon, while the W_Δ and $W_{\Delta\Delta}$ are related to off-diagonal states. The J_z component is highlighted when one

considers the angular distribution in $\cos\theta^*$ alone. Integrating over ϕ^*, equation 1.3 becomes

$$\frac{d\sigma}{d^4q\,d(\cos\theta^*)} \sim W_T(1+\cos^2\theta^*) + W_L\sin^2\theta^*.$$

This may be expressed as

$$\frac{d\sigma}{d^4q\,d(\cos\theta^*)} \sim 1+\alpha\cos^2\theta^*$$

where $\alpha=(W_T-W_L)/(W_T+W_L)$. If the produced γ^* is purely transverse, $W_L=0$, and hence $\alpha = 1$; while if it is purely longitudinal, $W_T=0$ and hence $\alpha = -1$. Thus a study of the $\cos\theta^*$ distribution of the lepton pairs provides a direct handle on the polarization of the virtual photon, which in turn is related to the relative magnitudes of the structure functions W_T and W_L.

Integrating now over $\cos\theta^*$ one finds the cross section has become

$$\frac{d\sigma}{d^4q} \sim W_T+\frac{1}{2}W_L.$$

In this form, all leptonic information has been eliminated entirely, and one is dealing directly with the hadronic structure functions.

In the following sections, various ways of predicting these structure functions will be discussed.

1.4 Parton Model Description of Lepton Pair Production

The simplest approach to describing lepton pair production is the parton model.[9] As with deep inelastic scattering, the model is not only highly illuminating, but also, despite its simplicity, able to account for the bulk of the observed features of the process.

The crux of the model lies in the impulse approximation, in which it is argued that the hadronic processes responsible for the creation of the parton momentum states operate on a time scale very long compared to that required for the hard annihilation process. The partons are therefore regarded as quasi-free particles, temporarily unhindered by the binding that keeps them in the hadron, but carrying its signature in their momentum distributions. Predictions of cross sections in this model then arise from convoluting elementary cross sections with

the parton momentum distributions. Thus, for instance, the basic annihilation cross section for two charged fermions of charge Q,

$$\sigma = \frac{4\pi\alpha^2}{3M^2} Q^2, \qquad 1.5$$

may be used to compute the lepton pair cross section in the following way. Let the parton distributions for partons of flavor i be given by $q_i^\pi(x_1,\mathbf{k}_{T_1})$ and $q_i^N(x_2,\mathbf{k}_{T_2})$ for the pion and nucleon respectively. (In these expressions $\mathbf{k}_T$ refers to the transverse momentum of the parton.) The probability for finding a parton and an anti-parton in these momentum states is then

$$P = \left[\bar{q}_i^\pi(x_1,\mathbf{k}_{T_1})q_i^N(x_2,\mathbf{k}_{T_2}) + q_i^\pi(x_1,\mathbf{k}_{T_1})\bar{q}_i^N(x_2,\mathbf{k}_{T_2})\right] dx_1\, dx_2\, d\mathbf{k}_{T_1} d\mathbf{k}_{T_2}. \qquad 1.6$$

Since $M^2 = x_1 x_2 s$, one may convolute equation 1.5 with equation 1.6 to obtain the total cross section for the production of lepton pairs:

$$\sigma = \int\int\int\int \frac{4\pi\alpha^2}{3s}\frac{1}{x_1 x_2}\frac{1}{3}\sum_i Q_i^2\Big[\bar{q}_i^\pi(x_1,\mathbf{k}_{T_1})q_i^N(x_2,\mathbf{k}_{T_2})$$
$$+ q_i^\pi(x_1,\mathbf{k}_{T_1})\bar{q}_i^N(x_2,\mathbf{k}_{T_2})\Big] dx_1\, dx_2\, d\mathbf{k}_{T_1} d\mathbf{k}_{T_2}. \qquad 1.7$$

The factor 1/3 is included for matching the colors of the annihilating partons. This expression is most often encountered in its differential form:

$$\frac{d^2\sigma}{dx_1\, dx_2} = \frac{4\pi\alpha^2}{3M^2}\frac{1}{3}\sum_i Q_i^2\Big[\bar{q}_i^\pi(x_1)q_i^N(x_2) + q_i^\pi(x_1)\bar{q}_i^N(x_2)\Big]. \qquad 1.8$$

Here $q_i^\pi(x_1)$, etc., represent the parton distributions integrated over transverse momentum. This equation will see use in chapter 4 when these distributions are extracted from the data. Equation 1.8 may also be expressed in terms of M and x_F to reveal the *scaling* prediction intrinsic to the parton model:

$$M^3\frac{d^2\sigma}{dM dx_F} = \frac{8\pi\alpha^2}{9}\frac{x_1 x_2}{x_1+x_2}\sum_i Q_i^2\Big[\bar{q}_i^\pi(x_1)q_i^N(x_2) + q_i^\pi(x_1)\bar{q}_i^N(x_2)\Big]. \qquad 1.9$$

Since x_1 and x_2 may be expressed in terms of the scaling variables x_F and τ, one finds the cross section is scale-invariant:

$$M^3\frac{d^2\sigma}{dM dx_F} = f(x_F,\tau) \qquad 1.10$$

The angular distribution of the lepton pair may also be derived in the parton model by considering the fundamental angular distribution expected in the annihilation of two free fermions into two other (different) fermions. In this case the angular part decouples from the other variables and there is no need for convolution; one may look directly at the angular distribution predicted by QED. The obvious analog is $e^+e^- \rightarrow \mu^+\mu^-$. One easily computes

$$d\sigma \sim (k\cdot p)(k'\cdot p') + (k\cdot p')(k'\cdot p) + k^2 p\cdot p' + p^2 k\cdot k' + 2k^2p^2 \qquad 1.11$$

where the incoming fermions have four-momenta p and p', and the outgoing fermions have four-momenta k and k'. The final three terms are proportional to the squares of the invariant masses of the participating fermions, and are negligible in the limit of high center of mass energy; the first two terms have angular dependences of $(1 - \cos\theta)^2$ and $(1 + \cos\theta)^2$, respectively. This yields therefore

$$\frac{d\sigma}{d\Omega} \sim 1+\cos^2\theta. \qquad 1.12$$

Comparing this with equation 1.3 shows the parton model prediction

$$W_L = W_\Delta = W_{\Delta\Delta} = 0. \qquad 1.13$$

Two kinematic issues have been smoothed over to reach this statement, however. The most obvious is that three terms dropped from equation 1.11 contribute to a piece that has no angular dependence and thus to the constant term in equation 1.12. This reduces the relative contribution of $\cos^2\theta$, and hence is equivalent to introducing a $\sin^2\theta$ term. This means $W_L \neq 0$, and one finds that

$$W_L \sim \frac{p^2 + k^2}{M^2}.$$

In lepton pair experiments this term is usually small, because the quark masses are small relative to the virtual photon mass, but one sees in a general way that if the quark masses *were* large -- if, for instance, the quarks were far off-shell -- then a $\sin^2\theta$ term in the angular distribution could be expected to appear.

The second issue concerns intrinsic transverse momentum, k_T. In reaching equation 1.12, the angle θ between the incoming and outgoing fermions was used. This assumes one knows the direction of the incoming fermions -- but in lepton pair experiments, as noted earlier, one does not know this angle precisely, since unmeasured transverse momenta of the initial state partons smear it. The

angular distribution may be recomputed using a set of reference axes that are not so conveniently aligned with the incoming fermions. In this case the non-transverse structure functions no longer vanish. One finds

$$W_L \sim \frac{k_T^2}{M^2}, \quad W_\Delta \sim \frac{k_T}{M}, \quad \text{and} \quad W_{\Delta\Delta} \sim \frac{k_T^2}{M^2}.$$

These arguments are intended primarily to be illustrative. The point is to observe the general way in which constituent masses and transverse momenta enter the problem and affect the nontransverse structure functions (and hence the angular distributions). The factor $1/M^2$ is seen to be a characteristic feature of the effect.

Proper calculations of the effect of intrinsic transverse momentum may be done within the parton model, of course, and have been.[10] The result is that one expects

$$\frac{d\sigma}{d\cos\theta} \sim 1 + \alpha\cos^2\theta$$

where

$$\alpha = \frac{1-\frac{3}{2}\frac{<k_T^2>}{M^2}}{1+\frac{1}{2}\frac{<k_T^2>}{M^2}} \qquad 1.14$$

In this equation, $<k_T^2>$ is the mean intrinsic transverse momentum of the partons. Experimentally one finds[11] α close to 1.

The parton model sets the stage for more complex models. Since there are no dynamics in the parton model, the prediction that the cross section will scale (equation 1.10) or that the nontransverse structure functions will vanish (equation 1.13) reflects the minimal situation. Indeed, these "predictions" are really just restatements of the initial assumptions of the impulse approximation and the lack of mass and transverse momentum in the quarks. One expects that a model with significant dynamics will violate these expectations, and, conversely, an experimental observation of a violation will be *prima facie* evidence for the presence of interesting dynamics in the hadron.

1.5 Structure Functions: Predictions

While the quark distributions in equation 1.8 should in principle be predicted by a theory of strong interactions, QCD has not yet yielded full solutions. Predictions for the quark distributions are therefore based largely on phenomenological arguments.

Early work in this area lead to the Drell-Yan-West relation[12], which argued that if inclusive reactions merged smoothly with exclusive, then the behaviour of the structure functions could be related to the behaviour of the elastic form factor. This led to the predictions, for $x \to 1$, that the nucleon and pion structure functions should look like

$$xq^N(x) \sim (1-x)^3 \qquad \text{and} \qquad xq^\pi(x) \sim (1-x)^1.$$

The nucleon prediction was in good agreement with existing data. Later work based on phase space arguments[13] led to "counting rules" which were applied to the pion and nucleon structure functions and yielded predictions identical to those given above. Modified versions of the counting rules took the spin of the constituents into account,[14] and predicted $(1-x)^2$ for the pion.

Predictions for the other end of the spectrum, $x \to 0$, have been based on Regge theory arguments.[15] The result suggests that the pion valence and sea distributions should go like

$$xV(x) \sim \sqrt{x} \qquad \text{and} \qquad xS(x) \sim 1,$$

leading to a complete picture of the pion valence distribution:

$$xq^\pi(x) \sim x^\alpha(1-x)^\beta,$$

where $\alpha = 1/2$ and β may be 1 or 2.

None of these predictions, however, addresses directly the problem of the underlying dynamics of the quark-gluon interactions. Clearly any fundamental grasp of the structure functions must begin with, or at least be based on, an understanding of such interactions. Farrar and Jackson pointed out[16] that the $x \to 1$ limit may in fact be precisely the kinematic region in which perturbative calculations of the the quark distributions could be done reliably. The basis of their argument is that the high-x component of the hadron wave function can be generated by gluon exchange between the constituent quarks, as illustrated in figure 5. In this case, however, one sees by simple kinematics that the interacting

quark becomes far off shell as $x \to 1$:

$$p^2 \sim \frac{m^2}{1-x}.$$

Here m^2 represents the characteristic mass or transverse momentum of the quarks. The large invariant mass of the propagators would then give rise to small couplings and permit one to use first order perturbation theory. The result of their calculation is a prediction for both a transverse and a longitudinal structure function for the pion. That is, as $x \to 1$,

$$W_T^\pi \sim (1-x)^2 \qquad \text{and} \qquad W_L^\pi \sim \frac{\mu^2}{Q^2} \tag{1.15}$$

where the μ^2 is an undetermined parameter and $-Q^2$ is the 4-momentum transfer (in the case of a lepton pair experiment, one would have $Q^2 = M^2$). The source of the longitudinal structure function can be understood by considering the amplitude for coupling a spin 1 object (gluon or photon) to a spin 1/2 quark.[17] As the internal lines become far off-shell ($x \to 1$), the favored situation is for the gluon of figure 5 to be transversely polarized, and the photon to be longitudinally polarized. This in turn is related to the fact that the spins of the two pion quarks are constrained by the spin of the pion; the exchange of the transverse gluon flips the spins of the quarks, but preserves the over all spin of the pion.

The appearance of the longitudinal piece was a novel feature of the model. The fact that a model with internal dynamics would introduce a nontransverse structure function, proportional to $1/M^2$, however, is in line with the heuristic arguments presented in the last section. The very different x_1-dependences of the transverse and longitudinal components is a distinctive feature of the model, and one that is not available to a parton-model treatment where the x_1-dependences are simply factorized away by the impulse approximation. A more sophisticated version of this model will be treated in §1.7.

1.6 QCD and Massive Lepton Pair Production

The parton model picture of lepton pair production is remarkably simple, managing not only to finesse the issue of the binding of the partons, but also to ignore any other strong interactions they might undergo, and yet still come away

with highly accurate predictions. One suspects, however, that the purely electromagnetic process must be modified at some level by the strong interactions. Indeed, many diagrams besides the straightforward annihilation diagram of figure 2 are expected to contribute; figure 6 shows some of the lowest order possibilities. In the case of πN interactions, where one has valence antiquarks available, the annihilation channels (figures 6a and 6b) are expected to dominate over the Compton channels (figures 6c and 6d); and as noted in the last section, the description of lepton pair production at high-x probably involves diagrams with a gluon exchanged between the two constituent quarks of the pion.

Many predictions arise from the study of these additional diagrams. Of interest to the results presented in this thesis are the questions of absolute normalization (the so-called 'K-factor'), of angular distributions, and of quark distributions.

As discussed in §1.4, the impulse approximation and the annihilation diagram (figure 2) lead directly to the expectation, equation 1.10, that the cross section $M^3 d^2\sigma/dMdx_F$ will be scale invariant. Introduction of additional diagrams changes this picture. Expanding in powers of the strong coupling constant (which in this kinematic range is $\alpha_s \sim .2$–$.3$) the cross section may be expressed

$$\frac{d^2\sigma}{dMdx_F} \sim \sigma_0(\tau,x_F,M) + \alpha_s(M^2)\sigma_1(\tau,x_F,M) + \alpha_s^2(M^2)\sigma_2(\tau,x_F,M) + \cdots$$

Each term is further expanded

$$\sigma_i(\tau,x_F,M) \sim a_i(\tau,x_F)\ln^i(M^2) + b_i(\tau,x_F)\ln^{i-1}(M^2) + \cdots .$$

The leading log approximation consists of retaining only the first term of the second series. It has been shown[18] that in this approximation, equation 1.9 remains valid, but the scale-invariant quark distributions are replaced by scale dependent ones, $q(x) \rightarrow q(x,M^2)$. These correspond to the familiar logarithmic scaling violations one measured in deep inelastic scattering, and are not expected to be large in the kinematic region probed here. Of more significance are the power-law scaling violations implied by equation 1.15; these will be discussed in the next section.

Beyond the leading log --next to leading log-- one finds a large correction. Experimentally it is observed that

$$\frac{d^2\sigma}{dMdx_F} \approx K\left(\frac{d^2\sigma}{dMdx_F}\right)_{\text{LeadingLog}}$$

with $K \approx 2$. Theoretical attempts[19] to calculate $K(\tau, x_F)$ have suggested

$$K \sim 1 + \frac{\alpha_s}{2\pi}\frac{4}{3}\pi^2 \sim 1.6$$

with a marked dependence on τ. It should be noted, however, that the prediction is only to first order in α_s and does not include all the next-to-leading log terms. Moreover, the dependence of K on x_F, particularly near $x_F \rightarrow 1$ is not known. This has implications for measuring the pion structure function.

While the effects described above can be attributed to the radiation of soft gluons, interesting effects also arise from hard gluon emission. The P_T spectrum of lepton pairs has been the object of many QCD calculations[20] as it is believed to arise from diagrams involving hard gluon emissions, such as illustrated in figure 6. Of particular relevance to this thesis are predictions concerning the effect of P_T on the lepton pair angular distribution.[21]

At high P_T specific processes are invoked to explain the production of large transverse momentum. Collins[22] argues that in $\pi^- N$ interactions, where a valence antiquark is available, the quark-antiquark annihilation diagram will dominate, and high P_T will be generated by the process illustrated in figures 6a and 6b. This leads to a prediction, for high P_T,

$$\frac{d\sigma}{d(\cos\theta^*)} \sim 1 + \alpha\cos^2\theta^*$$

where

$$\alpha = \frac{1 - \frac{1}{2}\frac{P_T^2}{M^2}}{1 + \frac{3}{2}\frac{P_T^2}{M^2}}. \qquad 1.16$$

At low P_T, this merges with the prediction given in equation 1.14 for the effect of intrinsic k_T.

1.7 QCD and Structure Functions

The QCD corrections discussed in the previous section involve attaching gluon lines to quark lines in various ways, but do not address the binding issue

raised earlier. In QCD, binding problems, and coherent or multiparticle processes such as that incorporated in the Farrar-Jackson model, fall under the rubric of "higher-twist effects." The model of Farrar and Jackson suggests that such effects might be interesting, and has been translated into a QCD higher-twist model by Berger and Brodsky.[23]. The higher-twist model makes explicit predictions for the structure functions W_T, W_L, and W_Δ, and thus also for the angular distributions.

Berger and Brodsky compute the cross section associated with the diagrams of figure 7, with the result that

$$\frac{d\sigma}{dx_1 d\Omega^*} \sim (1-x_1)^2(1+\cos^2\theta^*) + \frac{4}{9}\frac{<k_T^2>}{M^2}\sin^2\theta^* + \frac{2}{3}\left(\frac{<k_T^2>}{M^2}\right)^{\frac{1}{2}}(1-x_1)\sin 2\theta^*\cos\phi^*. \qquad 1.17$$

Here $<k_T^2>$ refers to the mean square transverse momentum of the annihilating quarks, and the angles θ^* and ϕ^* are referred to the T-channel axes. From this equation the helicity structure functions discussed earlier may be read off directly:

$$W_T = (1-x_1)^2$$
$$W_L = \frac{4}{9}\frac{<k_T^2>}{M^2} \qquad 1.18$$
$$W_\Delta = \frac{2}{3}\left(\frac{<k_T^2>}{M^2}\right)(1-x_1).$$

The model makes no special prediction for $W_{\Delta\Delta}$.

Integrating over ϕ^* yields

$$\frac{d\sigma}{dx_1 d\cos\theta^*} \sim (1-x_1)^2(1+\cos^2\theta^*) + \frac{4}{9}\frac{<k_T^2>}{M^2}\sin^2\theta^*.$$

From this one immediately sees an angular distribution of the form $1+\alpha(x_1,M)\cos^2\theta^*$ where

$$\alpha(x_1,M) = \frac{(1-x_1)^2 - \frac{4}{9}\frac{<k_T^2>}{M^2}}{(1-x_1)^2 + \frac{4}{9}\frac{<k_T^2>}{M^2}}. \qquad 1.19$$

At the low end of the range, $x_1 \rightarrow 0$, this is a quantity near 1, while at the high end of the range, $x_1 \rightarrow 1$, it approaches -1. This change of the angular distribution with increasing x gives the higher-twist effect a striking signature.

Integrating now over $\cos\theta^*$, one finds

$$q^\pi(x_1) \sim (1-x_1)^2 + \frac{2}{9}\frac{<k_T^2>}{M^2} \qquad 1.20$$

thus giving an explicit form for the Farrar and Jackson result, equation 1.15. In this model all P_T of the final lepton pair comes from the intrinsic transverse momentum of the annihilating quarks, and $<k_T^2>$ is approximately the mean square of the pion quark's transverse momentum. Approximations made in reaching equation 1.17 restrict the applicability to $P_T/M << 1$ and $x_1 < .95$; the assumption built into the 1-gluon exchange limits it to "high-x_1", a region suggested by the authors to be $x_1 \geq .5$. Under the terms of the model, all P_T is due to intrinsic transverse momentum, as noted above, and one has different P_T^2 dependence in the transverse and longitudinal contributions:

$$\frac{d\sigma_T}{dx_1 dP_T^2} \sim \frac{(1-x_1)^2}{P_T^4} \qquad \text{and} \qquad \frac{d\sigma_L}{dx_1 dP_T^2} \sim \frac{1}{M^2 P_T^2}.$$

Subsequent work by these authors led to a modification of the longitudinal term[24], introducing a factor x_1^2. This yields

$$W_L \sim x_1^2 \frac{\lambda^2}{M^2}$$

$$W_\Delta \sim \left(\frac{\lambda^2}{M^2}\right)^{\frac{1}{2}} x_1(1-x_1),$$

where λ^2 is related to the pion form factor, and expected to be of the order $\lambda^2 \sim 0.1$ GeV^2. In this case,

$$\frac{d\sigma_L}{dx_1 dP_T^2} \sim \frac{x_1^2}{M^2 P_T^2}.$$

The model assumes a weak binding approximation in which the quarks each carry 1/2 the momentum of the pion before the interaction; reference 25 seeks to lift this restriction. The requirement $P_T/M << 1$ is discarded in reference 26.

The angular distributions predicted by the higher twist model are striking, but it has been pointed out[27] that there may be higher twist terms (of order $1/M^2$) that go like $1+\cos^2\theta^*$, and leading twist terms that go like $\sin^2\theta^*$. It is also known, as pointed out in the previous sections, that leading twist diagrams will give rise to a dependence of α on P_T, but this is not also correlated with x_1. In addition, kinematics alone contribute a $\sin^2\theta^*$ component, but this will still have the x_1-dependence of the $1+\cos^2\theta^*$ piece.

The model has also been applied[28] to high-P_T inclusive pion production, to $lN \rightarrow l'\pi X$, and to $e^+e^- \rightarrow \pi X$, and there is some suggestion of a positive result in the lepton scattering case.[29]

The possibility that higher twist effects might play a role in deep inelastic scattering has arisen in the literature,[30] but leading twist and higher twist effects are not clearly separated in such experiments.[31] In the case of lepton pair production, leading twist and higher twist are separated by the marked effect of the higher twist mechanism on the angular distributions, and its predominance at high-x_1 over other mechanisms.

1.8 This Experiment

The current effort grew out of a previous experiment, Fermilab E444, in which a broad range of issues in lepton pair production were studied using a large acceptance spectrometer.[32] Investigation of the lepton pair angular distribution revealed a distinct change in the character of the distribution at high x, consistent with the predictions of the (simultaneously published) Berger-Brodsky model, but not statistically overwhelming. The present experiment, Fermilab E615, was designed to focus specifically on mu-pair production at high x, to study both the pion structure function and the angular distribution in that region, as well as to search for any other unusual phenomena that might occur at this extreme edge of phase space.

The apparatus was assembled by the spring of 1982, at which point approximately 2 months of beam time became available for testing and debugging the equipment. During the course of this shakedown cruise, a few weeks of actual data-taking were logged, and resulted in a data sample of about 1300 high-mass pairs -- roughly 1/2 of the sample used in the E444 analysis. Analysis of this sample has led to the present dissertation.

Data taking in E615 was resumed in the fall of 1983 and continued until the summer of 1984. During this period a sample of approximately 60,000 high-mass pairs was obtained, on which analysis is now underway. In addition, a special run at lower beam energy yielded about 4000 events, which have been analysed.[33] The 1982 data also yielded a sample of about 75,000 J/ψ's which have been analyzed in a separate dissertation.[34] This analysis focusses on the extraction of the pion and nucleon structure functions and the presentation of mu-pair angular distributions in $\cos\theta^*$.

The material which follows has been organized into 5 chapters. Chapter II deals with hardware; chapter III, with analysis; chapter IV with structure functions; chapter V with angular distributions; chapter VI surveys the result and offers some conclusions.

CHAPTER II

THE APPARATUS

2.1 Overview of the Experiment

The fundamental problem faced by this experiment is the intrinsically small cross section for mu-pair production. When compared to the ~20 mb total inelastic cross section for pions on protons, the ~100 pb cross section for producing mu-pairs with masses $\geq$4 GeV is seen to be very small indeed. The bulk of the mu-pair cross section is known to be explained by the Drell-Yan annihilation model, which, being electromagnetic, is already down by α^2 relative to the hadronic cross sections. In addition, the photon propagator means the cross section falls rapidly with the mu-pair mass,

$$\frac{d\sigma}{dM^2} \sim \frac{1}{M^4},$$

and the x-dependence of the structure functions contributes yet more fall-off.

Since the object of the experiment was to measure detailed properties of the mu-pairs, such as structure functions and angular distributions, large numbers of events were required. From the start it was therefore clear that an intense beam and large acceptance spectrometer would be necessary. The desire to focus on specific kinematic regions -- high x_F and high $|\cos\theta^*|$ -- further demanded good acceptance in these regions.

The kinematics of the mu-pairs dictate much of the design. The mass of the pairs is given to good approximation by

$$M^2 = p^+ p^- \theta_{+-}^2 \qquad 2.1$$

where θ_{+-} is the angle between the μ^+ and μ^- at the production point. (All

quantities are in the lab frame.) Thus high-mass pairs are *wide* events and demand a large aperture spectrometer. This demand is mitigated somewhat, however, at high x_F, because

$$x_F \approx \frac{p_z^+ + p_z^-}{p_\pi} \qquad 2.2$$

and thus high-x_F events, with their large values of $p_z^\pm$, are focussed very forward. (In effect, the mass of a high mass, high-x_F event comes more from the 'p' than from the 'θ' in equation 2.1.) The forward, compressed topology of high-x_F events requires a spectrometer which is sensitive through the central region of the aperture; toroidal designs are ruled out. Finally $\cos\theta^*$ is characterized roughly by

$$\cos\theta^* \sim \frac{p_z^+ - p_z^-}{p_z^+ + p_z^-} \qquad 2.3$$

so that an event with large $|\cos\theta^*|$ has a soft track and a stiff track. Thus the "dynamic range" of the acceptance must be substantial. This feature of high-$\cos\theta^*$ events is due to the fact that in the mu-pair center of mass a high-$\cos\theta^*$ event is aligned close to the $\hat{z}$-axis, so one muon goes forward and the other backward. In the lab these are the stiff and soft tracks. The soft track tends to have a large angle, so again the need for a large aperture arises.

In addition to the signal, one must consider the character of the backgrounds. First there is the problem of the beam itself and the spray of secondary hadrons it produces. Second, there is the fact that even for mu-pair production, the cross section is dominated by the low-x region which is not of great interest here. Third, there are many resonant sources of mu-pairs, mostly at low mass.[35] At high mass there is the J/ψ with its $\sim$7% branching ratio to $\mu^+\mu^-$. Finally there is the problem of accidentals: the random pairings of single muons that fake mu-pair events. The two dominant sources of single muons are the decay of beam pions and the decay of secondary pions and kaons produced in the target.

The apparatus is shown in figure 8. It consists of a conventional spectrometer -- an analysis magnet flanked by tracking chambers -- and several more specialized additions. The large magnet standing between the target and the spectrometer is filled with beryllium and carbon absorber and has a three-fold function: to prevent the beam and secondary hadrons from entering the spectrometer, to sweep the low-momentum tracks out of the acceptance, and to focus the high

mass events into the spectrometer. The magnetic field is tuned to optimize the acceptance in the regions of mass and x_F of interest, and the absorber is chosen to have low Z to minimize multiple scattering and therefore preserve good mass resolution so resonant states can be rejected. The flight path between the target and absorber was kept short to minimize the production of single muons by decaying secondaries. Fast electronics and tight timing narrowed the available window for accidental coincidences. Upstream of the target hodoscope banks provided a veto against the muon *halo* accompanying the beam, and in the spectrometer region, six more banks of hodoscopes provided a trigger for events with two tracks. Iron walls at the far downstream end supply muon identification.

Each of the elements of the apparatus will now be discussed in more detail. The coordinate system used throughout has $\hat{z}$ pointing in the beam direction, with z=0 at a point 7.6cm in from the upstream face of the target (the reason for this will be noted later). The beam direction is referred to as "North". The $\hat{x}$ axis lies in the horizontal plane and points west, while the $\hat{y}$ axis is vertical and points up.

2.2 The Beam

The experiment was conducted in the Fermilab Proton-West Area, served by a high-intensity pion beam. Protons extracted from the main ring at 400 GeV struck a 1-absorption length beryllium target, producing secondaries which were sign-selected by a dipole magnet and focussed by a quadrupole triplet onto a momentum slit located 240 feet from the primary target. The beam emerging from this slit had a momentum bite of $\pm 4\%$. The beam was transported to a final focus at the experimental target, located 812 feet downstream from the primary target. Details concerning the beamline are well documented elsewhere.[36] The momentum spectrum of pions at the experimental target is shown in figure 45; this distribution is the result of a Monte Carlo calculation using the program HALO.[37] The rms beam size at the target was about 1.0cm; HALO predicts 0.8cm.

Approximately 0.5×10^{-4} pions were delivered to the experimental target for each proton striking the primary target. With a typical primary intensity of 2×10^{12} protons per spill, the pion intensity was therefore about 1×10^{8} per spill.

Each spill was approximately 1 second long, occuring every 10-15 seconds, with the beam structured in time within the spill to occur in 2ns buckets every 18.3ns. A signal at this frequency and in phase with the bucket structure (the RF signal) was delivered to the experimental area for use in timing and triggering.

The composition of the beam is not measured in this experiment, but measurements made on a similar beam elsewhere[38] indicate it to be about 97.7% π^-, 1.8% K^-, and 0.5% $\bar{p}$. The decay of pions and kaons gives rise to a muon component which, by a simple calculation, is seen to be about 1.7% of the pion flux. Part of the muon flux is transported by the beam and part of it leaves the beam to form a muon halo about the beam. This latter component is deflected by a system of magnetized toroids known as *spoilers*. Veto hodoscopes upstream of the detector veto potential triggers involving halo muons. Muons in the beam were measured by placing a counter behind the final iron wall at the location where the beam passed through. This measurement indicated that the μ/π ratio in the beam was 0.8%, in excellent agreement with the HALO prediction of 0.76%. Measurements of the muon halo were less certain; rates in the A and B veto banks suggested the muon halo was about 1% of the pion flux, but the veto rate was known to be contaminated by backscatter from the target, and probably also by soft debris from upstream.

Beam monitoring was provided by various devices. A secondary emission monitor (SEM) located at the primary target measured the primary proton flux; segmented wire ionization chambers measured beam profiles at various points along the beam line; and ionization chambers measured secondary flux at the experimental target. The ratio of the the ionization chamber measurement to the SEM measurement was monitored regularly to check the stability of the beam tune.

2.3 The Target

The target consisted of a $2\times2\times8.5$ inch long block of tungsten alloy whose composition was 90% tungsten, 6% nickel, and 4% copper. The target was 1.7 absorption lengths long, resulting in over 80% of the beam interacting. It was 62 radiation lengths long, and thus was a major contributor to multiple scattering. The downstream end of the target was .93m from the upstream face of the

magnet, and .33m from the upstream edge of the first absorber.

2.4 The Absorber (Beam Dump)

Following the target, the noninteracting beam and the debris from hadronic interactions in the target are stopped in the beam dump that fills the selection magnet. Table 1 below summarizes the essential properties of the dump.

TABLE 1

CHARACTERISTICS OF THE ABSORBER

Material	Length (meters)	Density (g/cm^3)	Absorption Lengths	Radiation Lengths
BeO	0.61	3.0	1.57	4.45
Be/SiO_2	3.20	1.86	5.54	9.24
C	4.12	1.77	6.35	17.1
BeO	0.61	3.0	1.57	4.45

The beryllium oxide was in the form of bricks, stacked at each end of the magnet. The material referred to in the table as Be/SiO_2 was actually small blocks of pure beryllium contained in stainless steel boxes into which sand had been poured to fill the cracks. Beryllium and carbon were chosen for the main constituents of the dump because their low Z to A ratio minimizes the amount of multiple scattering for a given amount of hadronic absorption. Densities were obtained by direct measurement, and absorption lengths from other data.[39]

2.5 The Magnets

As shown in figure 8, and discussed above, this experiment employed two magnets: a large, absorber-filled magnet between the target and spectrometer,

and a smaller momentum-analysis magnet in the spectrometer itself.

The upstream magnet, known as the selection magnet, for its role in selection events of high mass and high x_F, was 24 feet long and had a P_T-kick of 2.7 GeV/c. Figures 9 and 10 show plan and elevation views of the magnet, indicating the piece-wise tapered design. The upstream aperture of the selection magnet was 5.5 inches high by 24 inches wide, and the downstream aperture was 25.5 inches high by 54 inches wide. The tapered pole faces contributed somewhat to nonvertical components of the field and therefore to a small amount of vertical focussing, but this could be shown to be less than 1mr for very soft ($<$ 10 GeV/c) tracks. Both the copper for the coils and the steel for the yokes were obtained from the Zero Gradient synchrotron. The magnet had a total mass of 400 tons, and was mounted on rollers which sat in steel tracks atop an 18 inch concrete pad. A motor drive allows the magnet to be moved back and forth, thus permitting one to change the spectrometer geometry and optimize acceptance at different beam energies. This feature was not, however, used in this run of the experiment.

The momentum analysis magnet had a P_T-kick of 0.796 GeV/c of the same sign as the selection magnet, and an aperture 36 inches high by 72 inches wide. When combined with the tracking chambers, the final momentum resolution was

$$\frac{\sigma_p}{p} = 0.00016p.$$

Field measurements were made on both magnets, and field maps were prepared and fitted to functional forms involving harmonic polynomials expressed in x, y, and z. These field maps were used in the Monte Carlo and in track fits. Figures 11 and 12 give the field strength of the vertical components of the magnetic fields of the two magnets, as a function of z.

2.6 Proportional Chambers

The multiwire proportional chambers upstream of the analysis magnet were designed and built for this experiment. They consisted of 9 planes of sense wires, grouped in 3 *modules* of 3 planes each. Each module was a rigid stainless steel (aluminum, in the case of the first module) frame with planes of sense wires and cathodes mounted rigidly on one side. The 3 modules were hung from a gantry

that allowed continuous motion of each module in z, and easy adjustment in x and y. The tilt of the module could also be adjusted. All modules were surveyed during the running period to establish z-positions and precise orientations of the wire planes. A plan view of the spectrometer is shown in figure 13, with a typical (clean) event superimposed. (All distances are to scale except the MWPC gaps which are exaggerated to show the hits.) Table 2 summarizes much of the basic data about the MWPC's.

TABLE 2

MWPC SIZES, POSITIONS, AND WIRE TILTS

Module	Plane	Width	Height	# wires	z	θ	$<\epsilon>$
	V			672	9.579	+15.09	0.94
I	U	1.47	0.76	672	9.604	-15.24	0.96
	X			696	9.629	0.08	0.97
	V			792	11.060	+15.50	0.92
II	U	1.74	0.81	792	11.085	-15.44	0.88
	X			824	11.111	0.16	0.97
	V			928	12.525	+15.31	0.94
III	U	2.04	1.02	928	12.550	-15.64	0.90
	X			960	12.576	0.01	0.95

Note θ is the angle of the wires from vertical in degrees,
z is the distance from the target in meters, and
$<\epsilon>$ is the mean plane efficiency.

2.6.1 Chamber Hardware

Each module had x, u, and v planes of wires, the u and v-planes being tilted about 15° from the vertical. The wire spacing was 1/12 inch and the anode-cathode gap, 1/4 inch. The wires were 0.0008 inch gold-plated tungsten,

approximately 1m long, strung with 60 ± 5 grams of tension. In each plane a support wire ran roughly perpendicular to the wires, and the wires were glued to it with a small drop of Glyptol; care was taken to ensure that the support wire did not pull the sense wires out of their plane. Support wires in neighboring planes were tilted at different angles in order not to deaden a whole swath of detector. The position of every 50th wire in each plane was surveyed and the final wire spacing and tilt of the wires was determined by fits to these data.

The high voltage cathode planes were made of aluminized Mylar (polyester film). This material was a sandwich of 0.00035 inch aluminum laminated to each side of 0.002 inch Mylar. By chemically etching the aluminum laminate, the cathode was segmented into electrically isolated regions as shown in figure 14. Each region could be powered separately, though in practice all regions were operated at the same voltage. The rectangular "bulls-eye" pattern could be powered down to reduce the detection efficiency in the beam region if necessary, but this feature did not have to be used.

To condition a newly constructed chamber and bring it to normal operation, it proved useful to oscillate the high voltage applied to the cathodes, from positive to negative, with the amplitude of the oscillation slowly increasing over approximately a 24 hour period, while N_2 was circulated through the chamber. A computer driven system was used to automate the voltage oscillation. The period, amplitude, and shape of the oscillation were under program control. The current delivered by the high voltage supplies was fed back to the program both to protect the chambers and to adjust the amplitude of the voltage swing; when the current exceeded some preset maximum value (usually 30-40 μA) or if the voltage supply tripped, the voltage amplitude was reset to its starting value and the slow ramping process repeated.

The chambers were operated with a gas mixture of 80% Argon, 19.6% CO_2, and 0.4% freon. The high voltage was set at 3.7kV, approximately 100 volts above the onset of the efficiency plateau. Between beam spills the voltage was held at 500V to prevent the build up of dark current, and automatically ramped up to 3.7kV 1 second before the spill. A few of the planes had missing wires and instances where pre-amps had been swapped, leading to localized inefficiencies. These problems lowered the *mean* efficiencies of the planes, shown in table 2. A more detailed account of chamber efficiencies will be given in §3.6.

2.6.2 Chamber Electronics

A signal produced in the chambers was amplified in a pre-amp, sent down a long delay cable, amplified again, discriminated, and gated by a trigger pulse. The resulting bit was stored and subseqently read and encoded with its original wire and chamber address, and eventually passed to the on-line computer. A schematic overview of the electronics for this process is shown in figure 15, illustrating the tree structure that allowed ~7300 wires to be read in and condensed to a few words for storage on data tapes. The paragraphs which follow flesh out some of the details of this scheme.

The pre-amps were mounted directly on the chambers, while the remainder of the system was located in the main counting room. Input to the preamps was impedance-matched to the sense wires (~30Ω) and a Motorola NE592 amplifier fed a differential output directly onto twisted pair delay cable. A wire-OR of the 8 wires associated with each pre-amp was available but never exploited in this experiment. Each delay cable comprised 16 sets of shielded, twisted pairs (shielding grounded at each end). Cables were ~280 feet long, with a delay of ~450 ns and a .5% channel to channel variation in the delay. Because of the shielding, there was no detectable cross talk. Signals attenuated about a factor of 2 over the length of the cable, and broadened to a width of about 50 ns from a starting width of 20 ns.

At the far end of the delay cable was a receiver board where signals were shaped by an RC network to reduce the width and eliminate the tail, and then amplified, again with an NE592. The typical signal at this point was about 50ns wide and nearly square (due to saturation), with a residual tail about 100-200 ns long. The signal was kept as narrow as possible to avoid pile-up in high rate conditions, and the RC network was tuned carefully to minimize the tail. This signal was then discriminated and latched if a gate signal was present. All hits present in the MWPC system at the time of the trigger gate were stored in these latches, and could subsequently be read out. The trigger gate was set to 60 ns width. Each receiver board was fed from 16 sense wires, and has 16 such latches. In addition to these 16 individual hits, each receiver board supplied the OR of the 16 channels.

Readout was initiated by a pulse to the master device, the secondary scanner. The secondary scanner addressed each of the primary scanners in

sequence, issuing instructions to them to begin their scanning procedures. To understand the scanning procedure it is necessary to elaborate briefly on the organization of the system, illustrated schematically in figure 15.

The receiver boards reside in 33 crates, 9 crates for module 1, and 12 each for modules 2 and 3; each crate has slots for 16 receiver boards, though not all crates are full. Each primary scanner is associated with a particular MWPC module and can address only those crates belonging to that module. All communication between a primary scanner and the receiver boards of a particular crate takes place through the intermediary of a *buffer board* which lives in the crate. The buffer board does little more than identify the crate number so it may be addressed uniquely, and pass signals and instructions back and forth between the external bus linking it to the primary scanner and the back plane linking it to the receiver boards.

The primary scanners extract hits from the latches of the receiver boards for later transmission to the online computer. This extraction takes place in a series of 3 nested loops. Upon receiving the signal to scan its crates, the primary scanner begins addressing the crates in sequence (this is the outermost loop). At each crate it reads the OR's of the 16 receiver boards, and then tests the state of each OR to see which of the receiver boards, if any, has hits (middle loop). If any board has a valid OR, the 16 individual latches of that board are read in and priority encoded. Each of the valid latches is then reviewed (innermost loop) and the hit is encoded in 12 bits: 4 for the wire number, 4 for the receiver board number, and 4 for the crate number. This word is stored in the memory module, and the execution of the loops continues until all crates, boards, and latches have been reviewed.

When all three primary scanners have completed this process, the secondary scanner reads each of the 3 memories to extract the hits and transfers them to the CAMAC interface and then to the online computer. As it does so it adds 2 more bits to the hit word to identify the module number, and left justifies the resulting 14 bit word in a 16 bit word, which eventually appears on the primary data tape.

2.7 Drift Chambers

The tracking chambers in the downstream portion of the spectrometer were drift chambers, supplied to the experiment by Princeton University. Half of these chambers had been built and used in a previous experiment (Fermilab E-203), and the remaining chambers were built on the same design principal, with the same electronics and essentially the same mechanical specifications. Details of the old chambers have been documented elsewhere[40] and will not be repeated in detail here. To summarize, however, the chambers have 3/8 inch drift space, $\sim$250μm resolution, and in this experiment were arranged to have 8 planes of vertical wires, 2 planes of wires at +18° and 2 planes of wires at -18° from the vertical. Signals were amplified at the chamber and time-digitized in bins of 8 ns. Each time digitizer took inputs from 8 sense wires, chosen to be not 8 consecutive wires but rather every 7th wire in the (56-wire) chamber. This was done so the burden of handling high-rate regions of the chambers would be spread over many digitizer boards. Since a number of the digitizers experienced problems in the course of the run, this also had the unexpected advantage of spreading inefficiencies more uniformly across the chamber. Details of positions, wire orientations, efficiencies, and other information are given in table 3.

Figure 13 shows how the chambers were arranged in the detector. The placement of the chambers in z, being concentrated at the upstream and downstream portions of the drift chamber region, optimizes track *fitting*, and therefore momentum resolution, but makes track *finding* somewhat more difficult. The closely spaced pairs of chambers were in practice too far apart to be of much use in resolving left-right ambiguities, although they were offset 1/2 cell relative to one another for that purpose. Mean efficiencies tended to be lower than mean efficiencies in the MWPCs, and were in large part due to difficulties in the electronics. The 7-cell periodicity seen in figure 41 is clear indication of this. In the next chapter these measurements will be covered in more detail.

TABLE 3

DRIFT CHAMBER SIZES, POSITIONS, AND WIRE TILTS

Plane	Width	Height	# wires	z	θ	$<\epsilon>$
1	2.44	1.22	126	15.80	0.00	.96
2	2.44	1.22	126	15.98	0.00	.83
3	2.44	1.22	140	16.08	-18.00	.85
4	2.44	1.22	140	16.26	+18.00	.90
5	2.44	1.22	126	16.36	0.00	.96
6	2.44	1.22	126	16.54	0.01	.95
7 East	1.07	1.83	56	18.48	0.00	.81
Center	1.07	1.83	56	18.60	0.00	.95
West	1.07	1.83	56	18.49	0.00	.94
8 East	1.07	1.83	56	18.55	0.00	.78
Center	1.07	1.83	56	18.66	0.00	.94
West	1.07	1.83	56	18.54	0.00	.92
9 East	1.07	1.83	56	19.02	-17.99	.86
Center	1.07	1.83	56	18.96	-17.99	.90
West	1.07	1.83	56	19.01	-17.99	.86
10 East	1.07	1.83	56	19.42	+18.01	.77
Center	1.07	1.83	56	19.35	+18.01	.85
West	1.07	1.83	56	19.40	+18.01	.98
11 East	1.07	1.83	56	19.71	0.01	.91
Center	1.07	1.83	56	19.83	0.01	.96
West	1.07	1.83	56	19.72	0.00	.92
12 East	1.07	1.83	56	19.78	0.00	.91
Center	1.07	1.83	56	19.89	0.00	.96
West	1.07	1.83	56	19.77	0.01	.97

Note θ is the angle of the wires from vertical, z is the distance from the target, and $<\epsilon>$ is the mean plane efficiency. All dimensions are in meters and angles in degrees.

2.8 Hodoscopes

Ten planes of hodoscopes were used in this experiment, six to form a positive trigger, and four to form a veto.

The six trigger planes are illustrated in figures 13 and 16; figure 16 also indicates some general features of the trigger criteria. (The trigger will be discussed in more detail in the next section.) The C-bank was located immediately downstream from the selection magnet, and the D-bank immediately downstream from the analysis magnet. The E and F banks were behind steel walls at the far downstream end of the apparatus. All hodoscopes were 1/2 inch thick plastic scintillator. Widths, lengths, and z-positions are listed in table 4.

TABLE 4

HODOSCOPE POSITIONS AND COUNTER SIZES

Bank	z	Nr. ctrs.	Width	Height	Counter Width	Counter Length
AX	-3.20	36	1.84	1.02	.102	.51
AY	-3.20	20	1.84	1.02	.102	.92
BX	-2.16	38	1.94	1.12	.102	.56
BY	-2.16	22	1.94	1.12	.102	.97
CX	9.13	28	1.42	0.64	.051	0.64
CY	9.14	48	1.42	0.64	.027	0.75
DX	16.88	44	2.24	1.10	.051	1.10
DY	16.89	48	2.24	1.10	.046	1.12
E	21.25	80	3.37	1.77	wide: .102 narrow: .051	0.88
F	22.85	80	3.37	1.77	wide: .102 narrow: .051	0.88

All dimensions are in meters.

The arrangement of counters is illustrated in figures 17 - 19. The C- and D-bank scintillators were wrapped in aluminized Mylar and packed tightly together in a light-tight container; E- and F-bank scintillators were overlapped 1/4 inch.

Each counter bank had a rectangular hole located at the point where muons with momenta close to the central momentum of the beam would pass through. The object of the hole was to reduce triggers from accidental coincidences of beam muons with single muons arising from other sources; the acceptance was affected slightly by the presence of the hole. Table 5 gives locations of the hole in each bank.

TABLE 5

BEAM HOLE POSITION

Bank	Hole Size	Hole Location
CX	Δx=.102	x_c=.055
	Δy=.054	y_c=-.007
DX	Δx=.102	x_c=.081
	Δy=.091	y_c=-.020
E	Δx=.142	x_c=.183
	Δy=.089	y_c=0.000
F	Δx=.147	x_c=.177
	Δy=.089	y_c=0.000

All dimensions are in meters.
Δx and Δy and the width and height of the hole,
and (x_c, y_c) gives the location of the center.

Counters were plateaued by using minimum ionizing muons while running parasitically with an upstream experiment. Phototube voltages were set through

a pair of CAMAC-controlled high voltage supplies, LeCroy 1440's.

The veto banks had movable 'jaws' that could be remotely controlled to close down on the (3 inch) beam pipe or open wide. The vetos were always used in the closed position. The A and B banks were offset relative to one another by 1/2 counter width, and the more downstream bank (B) had one extra counter (in both x and y) to allow this.

2.9 The Trigger

The trigger was designed to select events with two or more penetrating tracks originating at the target. The CY, DY, E, and F banks were used to count the number of tracks, while the CY and DY alone enforced the requirement that the tracks point back to the target; the E and F banks were behind steel walls and thus provided the muon identification. In this run of the experiment, the CX and DX banks played only a limited role. Upstream of the target the A and B banks provided a veto against events involving a muon from the halo. The trigger was implemented in two stages, known as level I and level II.

2.9.1 Level I

In the first stage of the trigger, the tracks were counted in CY, DY, and E; because of its timing the F bank did not participate in the trigger at this stage. The level I trigger was defined by

$$LEVEL\ I = CTRIG \cdot DTRIG \cdot ETRIG \cdot \overline{VETO}.$$

To obtain the quantity CTRIG, the left and right counters of the CY bank were ORed together to produce 24 full-row signals which were then tested for adjacencies and summed. If the result of the sum was ≥ 3, or the sum was exactly 2 and there was no adjacency, CTRIG was positive. The CY counters entering in this calculation were required to be in coincidence with an overlapping CX counter. DTRIG was defined in the same way, using the DY bank. ETRIG was also defined in the same way, but had no coincidence requirement.

The veto was defined by forming coincidences between AX and BX, and AY and BY hits in the following way. First, as with the CY and DY banks described above, left and right, and up and down halves were ORed to produce full length counters. Matches were then made between the banks by allowing a given hit in

A to match with either of two hits in B. Logically, the veto was defined:

$$VETO = \sum_i AX_i \cdot (BX_i + BX_{i+1}) + \sum_i AY_i \cdot (BY_i + BY_{i+1}).$$

Finally, the Level I was also required to be in coincidence with the RF signal from the Main Ring, to improve the timing for the drift chambers, and the total number of CY hits was required to be less than 10. A positive output from Level I caused the MWPC hits to be gated into their latches, the drift chamber clocks to start, and a gate to be sent to the latches that saved the hodoscope hits.

2.9.2 Level II

The second part of the trigger consisted of matching CY and DY hits to check whether the tracks pointed back to the target. For this the y-counters were used because the x-view involved the bending in the magnet. Level II was simply defined by

$$LEVEL\ II = (CYM \geq 2) \cdot (DYM \geq 2)$$

where CYM counted the number of instances in which a CY counter could be matched with a DY counter to point back to the target, and DYM counted the number of cases in which a DY counter could be matched with a CY counter to point back to the target. The CY and DY banks were designed so that a straight line passing through the target and the middle of counter CY_i would pass between counters DY_i and DY_{i+1}; the CY match therefore involved one CY counter and the OR of two DY counters. Similarly, the DY match allowed two CY counters to satisfy one DY counter. In order to allow for multiple scattering in the dump, the CY and DY counters were first lumped together in adjacent pairs to form "fat" counters; thus, in fact, there were 12 *fat* CY counters to be matched with 12 *fat* DY counters. The net effect of Level II was to reduce the trigger rate by a factor of 2.

To form the final trigger, the Level II was ANDed with Level I and FTRIG. A positive signal at this point initiated the MWPC and Drift Chamber readout processes, and sent an interrupt to the online computer to begin the event processing. This was called Level III, but is not to be confused with the Level III trigger in the 1984 run (which involved a mass calculation).

2.10 Data Acquisition

The online computer was a PDP 11/45 with bipolar memory and extra bulk memory storage. The bulk storage allowed the computer to keep incoming data in memory until the end of the beam spill, at which point it was written to tape.

Each event on tape included all hodoscope, MWPC, and drift chamber hits, as well as a set of bits indicating the precise state of the trigger logic. Approximately 300-400 events were logged per spill, at normal intensity, and 300,000 events were written per tape.

Between spills the computer decoded events in memory to produce event displays and histograms of any item in the event record. Histograms could be easily created, accumulated, and displayed, allowing one to monitor hodoscope hits, chamber illuminations, logic bits, and scalar sums continuously during the running.

Independently of the computer, many fast logic outputs were scaled and displayed on visual scalars that allowed one to observe singles rates and coincidence rates in counter banks, beam monitors, and various combinations of trigger elements.

The dead time in this experiment was typically around 50%, the bulk of the dead time coming from event processing. The veto contributed 3-5% to this quantity.

CHAPTER III

ANALYSIS OF THE DATA

Using the hardware described in the preceding chapter, experiment 615 ran for approximately three weeks with the dimuon trigger, writing a total of about 60 raw data tapes. The analysis methods used to extract useful physics information from the data are described in this chapter: §3.1 deals with the track reconstruction software, §3.2 with cuts and event selection criteria, and §3.3 with the Monte Carlo and its use in the analysis; §§3.4-3.11 cover various systematic aspects of the experiment and the handling of the data.

3.1 Event Reconstruction

Three distinct stages of analysis were used to process the data and bring it from its raw form on the primary tapes to its final form. Each stage of the analysis was carried out by a different program, and each stage wrote its results to a new set of tapes. The labor was divided among the stages as follows. Stage 1 decoded the primary tapes, and searched for track segments in the upstream and downstream portions of the spectrometer. Stage 2 selected events of mass ≥ 2 GeV/c^2, matched up- and downstream segments, and performed a global fit on each linked track. Stage 3 performed a slightly refined fit, and began making event- selection cuts. Each of the stages will now be described in more detail.

3.1.1 Stage 1: The search for track segments

In the track-finding algorithm two concepts have played a key role and should be defined at the outset. The first is that of the *road*. A road is simply a narrow swath through the detector within which the program searches for a track. Roads may be wide, having widths of many centimeters, or narrow,

having widths of a few millimeters, and may be defined in either the x-z plane or the y-z plane. Their use will be described shortly. The second concept is that of the *fit-and-toss loop*. This is an iterative fit procedure in which one begins with a set of hits, fits them for a track, finds the particular hit contributing the most to χ^2, tosses it out of the set, computes the fit again, finds the new hit contributing the most to χ^2, tosses it out, and so forth. The loop terminates if either the number of hits remaining drops below some minimum (usually 5), or if the hit contributing the most to χ^2 is not contributing more than some maximum (usually 2.5^2 or 3.0^2).

The track search began in the downstream portion of the spectrometer where the density of hits was generally lower and the intrinsic resolution of the detectors higher. Using hits in the DX, E, and F hodoscope banks, the program defined a wide road ($\pm$ 7.5cm) in the x-z plane of the drift chambers. The road did not require that there be hits in all three hodoscope banks; any two would suffice. Within this road, the program considered in turn every pair of x-hits in the drift chambers, formed by selecting a hit from the downstream group of chambers, and another from the upstream group. Taking these hits as end points, the program defined a narrow road to be the strip lying within $\pm$2mm of the line joining these points. If there were more than 5 hits in this narrow road, they were considered candidates for a track. When all possible narrow roads within the wide road had been considered, the list of candidate tracks was ordered so that the candidates with the greatest number of hits were first in the list. Though up to 20 candidates would be considered, there was usually only one (60% of the time) or two (30% of the time). Each candidate was put through a fit-and-toss loop. The first one to exit the loop successfully was considered a track and was written to tape.

The entire search in the drift chambers was conducted using only hits from x-chambers, and the resulting fit was a line in the x-z plane. Because there were only 4 planes of U and V hits, almost any set of UV hits could appear to give an acceptable track in the y-z plane. The search for these tracks was therefore delayed until the next stage of the analysis, when more information was available to constrain the possibilities.

Once a track was found in the drift chambers, a search for its upstream mate was begun in the MWPC's. Two methods were available to be used in this

search, a *fast method* and a *slow method,* which differed in how they set up their roads. Both methods, however, exploited the fact that the track had to meet the drift chamber track in the middle of the analysis magnet, and thus the downstream end of the x-road was constrained. This meeting point was known as the *match point.* The methods also exploited the (empirical) fact that track slopes in x were tightly correlated with track position in x. Thus from the knowledge of the match point, one could predict the most likely position of the track at some point in the MWPC's upstream.

The fast method defined wide x-roads first by using this most likely x-position in the C-bank, and drawing a line between it and the match point. If this failed to turn up a track, subsequent x-roads were defined by using CX hits instead of the most likely x-position. In either case, the roads were $\pm$5cm about the line. A wide y-road was defined by considering, in turn, all combinations of CY and DY hodoscope hits, all projections from the target to CY hits, and all projections from the target to DY hits. (Note that here, as in all cases where hodoscopes are involved in track finding, no one hodoscope bank is ever required for the search to be successful. The hodoscopes were useful to speed the search but care was taken in the software design to ensure that missing hodoscope hits would not impair the track finding efficiency.) With the two roads defined, a *tube* could be defined by their intersection, and all hits in this tube were put through a fit-and-toss loop.

The slow method was used whenever the hit densities were high, or when the fast method failed to produce a track. In this method, narrow tubes were defined by using the MWPC hits themselves. The upstream end of the tube was defined by picking an X and a U hit, or an X and a V hit, or a U and a V hit in the first MWPC module, and selecting a similar pair in the third MWPC module. The line drawn between these two points as required to pass within 2 cm of the match point in x, and point to within 6 cm of the target in y. All hits lying within 4mm of this line were then put through a fit-and-toss loop.

Any track successfully emerging from the fit-and-toss loop was written to tape provided it had at least 5 hits and pointed to within 4 cm of the match point in x and 99 cm of the target in y. A more stringent assessment of the track quality was made to determine whether the MWPC track searching should continue or terminate. If the track had 8 or more hits, or pointed to within 1cm of

the match point in x and 5 cm of the target in y, the search would be terminated provided the χ^2 probability of the fit was greater than 1%. Otherwise the search continued until an improved track satisfying these criteria was found or all possible roads had been exhausted. Once the MWPC search was concluded, the finding in the drift chambers picked up where it had left off. The drift chamber search continued until all possible roads had been considered. At this point all found tracks were already on tape, and the next event was read in for processing.

In developing the reconstruction software it was found that the execution time was dominated by a small number of events that required inordinately long processing times. These events seldom yielded interesting mu-pair events, and the program speed was significantly increased by incorporating time and event-length cuts that removed them. Time was spent most liberally in the routine doing the *slow method* of search in the MWPCs, and therefore elapsed time was checked in this routine. If it exceeded 150 ms, the search was terminated immediately and the next event begun. By analyzing a sample of these eliminated events, this cut was estimated to result in a 0.8% loss of real mu-pair events. And additional cut was used to exclude from all processing events that contained too many chamber hits. The limit was set at 200 MWPC hits or 200 drift chamber hits; also, if *both* had 100 or more hits, the cut was imposed. This eliminated events dominated by hadronic spray, as well as events with readout problems which generated long strings of false MWPC hits. The cut was similarly estimated to result in a 1.3% loss of real mu-pair events.

The full effect of these cuts, as well as the effect of the reconstruction algorithm itself and the event selection cuts to be described below, was studied by superimposing Monte Carlo events on actual events from the data tapes. This study, and its conclusions will be discussed in detail in §3.7.

The secondary tape written by this program contained essentially all the information found in the primary event record (though much reorganized) except that hits lying farther than 5cm in x, or 10cm in y from any track were not included in the hit list. Thus each track written to secondary tape carried along with it a generous tube of hits so that the second stage of analysis could improve the track finding without being limited. Since the drift chamber tracks did not include y information, all U and V drift chamber hits passing through a vertical column of $\pm$5cm in width about the track were also written out.

3.1.2 Stage 2: Global fits

The second level of track reconstruction read secondary tapes and reanalyzed events using the data in the secondary event record. The class of events analyzed was restricted to those having a pair of tracks with invariant mass ≥ 2 GeV/c^2, the mass calculation being performed with the track segments found by the first stage of analysis.

This secondary search began by finding tracks in the MWPCs, generating endpoints and roads (of ± 3 mm) in a manner similar to the ***slow method*** described in the preceding section.[41] A higher speed was achieved by imposing a series of gradually relaxing constraints. Initially only 9-hit tracks were sought; if none turned up, 8-hit tracks were sought, and so on, until 5 hits were tried. Up to 20 tracks could be found, and accepted tracks were required to strike at least 2 out of 3 of the CX, CY, and DY hodoscope banks, and point to the target within a reasonable window. Downstream, in the drift chambers, the search proceeded in a manner much like that described for the drift chamber search in the preceding section but the road used was ± 1.5 mm. Two out of three of DX, E, and F hodoscope hits were required. The U and V planes were also searched, and a full x and y projection of the track reconstructed.

The up- and downstream tracks were the fitted as a single track to improve the track parameters and extract the momentum. This global fit included corrections for the fringe fields and slight y-bending of the analysis magnet. More importantly, the global fit was part of a fit-and-toss loop. This meant that the final set of hits, both upstream and downstream, were judged by their effect on the χ^2 of the fully linked 3-dimensional track. The fit-and-toss loop also included a search for alternate hits, so that better hits could be substituted for poorer ones if they existed.

The output of this program was a tertiary tape which included all the information of the secondary tape, and added the results of the fits performed at this level.

3.1.3 Stage 3: Cuts

A third level was employed to refine the results generated by the second level analysis and to begin to impose cuts to extract a clean high mass sample. Cuts were imposed both on information supplied by the stage 2 analysis, and also

on information resulting from the additional analysis done here. This analysis includes a more refined global fit procedure in which the tracks are carried through the analysis magnet using the measured magnetic field maps, and a fit to the pair vertex that includes the effect of scattering in the dump, the finite size of the beam, and the uncertainties of the fitted track vectors.

The cuts imposed initially were as follows.

-- There must be exactly two tracks in the event.

-- The two tracks must be *in-time*.

-- The two tracks must lie within the spectrometer fiducial volume.

-- The pair must satisfy the Level I trigger.

Requiring there be exactly one pair in the event simplifies the task of establishing a correspondence between Monte Carlo and data. The requirement that the tracks be in time is based on a fit to the drift chamber tracks that includes an extra parameter allowing the track to be offset in time relative to when the drift chamber trigger gate is defined. Since the resolution of the drift chambers is about 250μm, and the drift velocity is about 20ns/mm, the effective temporal resolution of the chambers is about 5ns. For a fitted track, many chambers were involved, and a resolution of about 2.4ns was achieved. This is sufficient to eliminate tracks from neighboring buckets. The spectrometer fiducial volume is defined by the transverse dimensions of the analysis magnet ($\pm$ 36 inches in x, $\pm$ 18 inches in y), which was the principal limiting aperture in the apparatus. The event was rejected if a track passed through the coil or the iron of the analysis magnet.

Events passing these preliminary cuts were subjected to a global fit that used field maps of the analysis magnet, yielding final track vectors in the spectrometer. The desired quantities, of course, are the track vectors at the production point in the target, and for this an energy loss correction and a vertex fit were employed. A detailed description of these procedures will be found elsewhere, [42] but a brief summary is in order here.

Energy loss was corrected by using an empirical formula to increase the measured momentum by an amount Δp. Monte Carlo studies determined a

parametrization for Δp that was unbiassed over the range of momentum encountered. Since energy is lost by several mechanisms (ionization, bremstrahlung, pair production, and nuclear collisions), this empirical technique proved the simplest.

The vertex fit minimized a χ^2 based on multiple scattering errors, chamber measurement errors, and beam size. The fit yielded two slopes, θ_1 and θ_2, of the two tracks involved, and a position x of the common vertex. The method may be summarized as follows.

In the absence of any bending, scattering, or measurement error, the true track position (x_{T_1}) and slope (θ_{T_1}) of track #1 measured downstream of the selection magnet may be related to the position (x) and slope (θ_1) at the target by

$$\begin{pmatrix} \theta_1 \\ 0 \\ x \end{pmatrix} = R_1 \begin{pmatrix} \theta_{T_1} \\ 0 \\ x_{T_1} \end{pmatrix} \quad \text{where} \quad R_1 = \begin{pmatrix} 1 & 0 & 0 \\ 0 & 0 & 0 \\ -z & 0 & 1 \end{pmatrix}.$$

The reason for the 3-dimensional notation will become clear in a moment. Including the errors due to the measurement of the track in the chambers ($\Delta\theta_c$,0,Δx_c) and multiple scattering ($\Delta\theta_s$,0,Δx_s), as well as the bending in the magnet, ($\Delta\theta(p)$,0,$\Delta x(p)$), one has

$$\begin{pmatrix} \theta_1 \\ 0 \\ x \end{pmatrix} = R_1 \begin{pmatrix} \theta_m - \Delta\theta_c - \Delta\theta_s - \Delta\theta(p) \\ 0 \\ x_m - \Delta x_c - \Delta x_s - \Delta x(p) \end{pmatrix}$$

where the subscript m refers measured quantities. Analogous expressions may be written for track #2, where the slope parameters now occupy the second slot. Thus, for instance,

$$\begin{pmatrix} 0 \\ \theta_2 \\ x \end{pmatrix} = R_2 \begin{pmatrix} 0 \\ \theta_{T_2} \\ x_{T_2} \end{pmatrix} \quad \text{where} \quad R_2 = \begin{pmatrix} 0 & 0 & 0 \\ 0 & 1 & 0 \\ 0 & -z & 1 \end{pmatrix}.$$

The covariance matrix associated with (θ_1,0,x) is derived from the covariance matrices associated with the measurement error (V_c) and multiple scattering (V_s) in the standard way:[43]

$$V_1 = R_1 V_{c_1} R_1^T + R_1 V_{s_1} R_1^T.$$

A similar expression holds for V_2, corresponding to the second track. The source of V_c and V_s will be discussed below.

The expected value of the vector $v_1 = (\theta_1, 0, x)$ is just $\bar{v}_1 = (\theta_{m_1} - \Delta\theta(p_1),\ 0,\ x_{m_1} - \Delta x(p_1))$, and similarly for v_2. Defining χ^2 by

$$\chi^2 = (v_1 - \bar{v}_1) V_1^{-1} (v_1 - \bar{v}_1)^T + (v_2 - \bar{v}_2) V_2^{-1} (v_2 - \bar{v}_2)^T,$$

one finds χ^2 minimized by quantities θ^*_1, θ^*_2, and x^*, as computed from the quantity $v^* \equiv (\theta^*_1, \theta^*_2, x^*)$ where

$$v^* = V(V_1^{-1}\bar{v}_1 + V_2^{-1}\bar{v}_2),$$

and

$$V = (V_1^{-1} + V_2^{-1})^{-1}.$$

In practice the vertex v is further constrained to be centered about the beam center by including in χ^2 a third term, $(v_3 - \bar{v}_B) V_3^{-1} (v_3 - \bar{v}_B)$, where $v_3 = (0,0,x)$, $\bar{v}_B = (0,0,0)$, and $V_3 = \begin{pmatrix} 0 & 0 & 0 \\ 0 & 0 & 0 \\ 0 & 0 & \sigma_B^2 \end{pmatrix}$. This also modifies the expression for V: $V = (V_1^{-2} + V_2^{-1} + V_3^{-1})^{-1}$.

The covariance matrix of the measurement error, V_c is taken from the global fit, while the covariance matrix of scattering must be calculated in the following way. The beam dump consists of a sequence of scatterers (absorbers) of varying physical lengths and radiation lengths (X_0). The covariance matrix for scattering by a single medium of length Δz is given by[44]

$$V = \begin{pmatrix} \sigma_\theta^2 & 0 & \rho\sigma_x\sigma_\theta \\ 0 & 0 & 0 \\ \rho\sigma_x\sigma_\theta & 0 & \sigma_x^2 \end{pmatrix}$$

where $\sigma_x^2 = \sigma_0^2(\Delta z)^3/6$, $\sigma_\theta^2 = \sigma_0^2(\Delta z)/2$, $\rho = \sqrt{3/4}$, and $\sigma_0^2 = (.021)^2/X_0 p^2$ for a singly charged particle of momentum p (GeV/c). For n consecutive media, the scattering matrix after the nth medium may be defined by a recursive relation:

$$V_n = R(\Delta z_n) V_{n-1} R^T(\Delta z_n) + V$$

where $R = \begin{pmatrix} 1 & 0 & 0 \\ 0 & 0 & 0 \\ \Delta z & 0 & 1 \end{pmatrix}$ is the transport matrix. This recursion was used to calcu-

late V_{θ_1}, and a similar one used for V_{θ_2}.

The vertex fit is applied in both the x– and the y–view, allowing one to extract the full set of track vectors at the interaction point, and the χ^2 associated with the fits. The χ^2 probabilities for the x and y vertex fits are used in the selection of events. The track vectors obtained by this method are then Lorentz transformed into the beam-target center of mass to compute x_F, and into the mu-pair rest frame to compute the angles θ^* and ϕ^*.

After the global track fits and the two vertex fits, the following cuts are imposed on the sample.

-- All 12 hodoscopes pointed to by the tracks must be on.

-- The full trigger logic must be satisfied by these hodoscopes.

-- The tracks must be of opposite sign.

-- The pair invariant mass must be $\geq$ 2 GeV/c^2.

-- The χ^2 probabilities for both the x and the y vertex fits must be $\geq$ 2%.

At this point the event was written to quaternary tape for preservation as part of the final high mass sample.

3.2 Event Selection

To obtain the final sample of high mass events for this analysis, the events surviving the cuts described in the last section are subjected to another series of cuts, listed in the table below. The quaternary tape written by stage 3 has about 112K events on it, but these are predominantly J/ψ's. The mass cut is therefore the most striking of the cuts, as it pares the sample to about 3K. In the table below, the numbers of events affected by each of the cuts is indicated. The first three cuts mainly select the kinematic region of interest although requiring $x_F \leq 1.0$ also cuts some events with very large x_F which arise from accidental pairings of beam muons with muons from secondary π-decay.

The halo cut is designed to remove those events in which a μ^- from the beam has paired with a μ^+ from the decay of a secondary π^+. These events have a distinct kinematic signature, as one may see in figure 20 and 21. In figure 20 on sees a scatter plot of track slope (θ_x) versus track momentum. The

TABLE 6

EVENT SELECTION CUTS

Cut	Nr. Events Left	Nr. Events Cut
$4 < M < 8.5$ GeV/c^2	3060	~109K
$0.0 < x_F < 1.0$	2808	252
$0.18 < x_1 < 1.0$	2707	101
Halo Cut	1409	1298
$p^{\pm} > 10$ GeV/c	1360	49
Fiducial	1322	38

enhancement at low $|\theta_x|$ and high $|p^-|$, and the corresponding enhancement at high θ_x and low p^+ signal the presence of such events. In figure 21 one sees a comparison of p^+ and p^- spectra, and again, the presence of these events is manifested as an enhancement of events with low p^+ or high p^-.

The halo cut exploits the salient characteristics of these events, the low angle of the μ^- and the high ratio p^-/p^+. In figure 22 is shown a scatter plot of events with $(p_T^-)^2$ on the vertical axis, and $|p^-/p^+|$ on the horizontal axis. The separation of events is clear. The cut discards events with

$$(p_T^-)^2 \leq 0.32|p^-/p^+| - 0.40$$

as illustrated in the figure. The effect of the cut is seen in figure 23 and 24, which show the θ-p plot and the $p^{\pm}$ spectra after the cut. The enhancements present in figures 20 and 21 are now gone.

Cutting on $p^{\pm} \leq 10$ GeV/c removes those events where catastrophic energy loss has occurred. Below p=10 GeV/c the Monte Carlo no longer reproduces the data well; one finds in this region that the data outweigh the Monte Carlo by about a factor of 2. These events, if not cut, end up at low x and high $\cos\theta^*$.

The fiducial cut requires that all tracks be at least 5mm away from the edge of any counter bank, including the inner edge near the beam hole.

3.3 The Monte Carlo

A Monte Carlo program was written to simulate this experiment for use in calculating the acceptance of the detector, as well as understanding and evaluating its performance. A description of the program and the uses to which it was put now follows.

The generation of events involves choosing the x, y, and z of the interaction, the momenta of the interacting π^- and N, and the 6 variables characterizing the muon pair. The coordinates x and y are generated using the known profile of the beam, and z is generated using the exponential absorption in the target and dump. The beam is allowed to continue into the dump, and some events are generated there. The π^- momenta are drawn from the momentum spectrum of the beam, shown in figure 45; the source of this distribution will be discussed in a later section. The nucleon momentum is generated using a Fermi gas model with power-law tails.[45]

The muon pair itself is characterized by 6 variables, which, for the purpose of generating events are chosen to be x_1, x_2, P_T, $\cos\theta^*$, ϕ^*, and Φ_{LAB}. The hadronic variables x_1 and x_2 are generated directly from the shapes of the pion and nucleon structure functions; this will be discussed in some detail in the next chapter. P_T is generated according to a parametrization

$$\frac{1}{P_T}\frac{d\sigma}{dP_T} = \left(1+\frac{P_T^2}{b^2}\right)^{-6}$$

where the variable b is extracted from the data and takes on the values 2.63, 2.51, 2.50, and 2.17 in the x_F intervals 0.0-0.25, 0.25-0.50, 0.50-0.75, and 0.75-1.00 respectively. $\cos\theta^*$ is generated according to $1+\alpha\cos^2\theta^*$ where α is given by

$$\alpha(x_1,M) = \frac{(1-x_1)^2 - \frac{4}{9}\frac{<k_T^2>}{M^2}}{(1-x_1)^2 + \frac{4}{9}\frac{<k_T^2>}{M^2}}. \qquad 3.1$$

The value of $<k_T^2>$ is taken from the data. This parametrization is consistent with E444 data and will be seen in chapter 5 to be consistent with the data

analyzed here. The two angular variables ϕ^* and Φ_{LAB} are generated with flat distributions.

Once generated, the six kinematic variables of the mu-pair are converted to two track momenta $\mathbf{p}^+$ and $\mathbf{p}^-$, which are then propagated through the apparatus. In the target and dump the tracks are propagated piece-wise, with multiple Coulomb scattering and energy loss being applied in each segment. The piece-wise application of energy loss is important in the dump because of the magnetic field. Transport through the field uses the results of the fits to the field shape and includes the fringe fields. Energy loss is computed taking into account losses from ionization, bremstrahlung, pair production, and nuclear collisions. The tracks are not propagated through the analysis magnet, but the final momentum is appropriately smeared to reflect the natural momentum resolution of the spectrometer. The result of this transport is a set of new track vectors, $\mathbf{p}_\ell^+$ and $\mathbf{p}_\ell^-$, representing the muon tracks as they appear in the spectrometer, and embodying the effects noted above. From this point on, the Monte Carlo event is handled just as the real events are.

Using the vectors $\mathbf{p}_\ell^\pm$, the vertex fit is performed to generate the reconstructed versions of the original $\mathbf{p}^\pm$, and these in turn are used to compute the reconstructed values of M, x_F, P_T, $\cos\theta^*$, ϕ^*, and Φ_{LAB}. It should be noted that x_F, $\cos\theta^*$, and ϕ^* all depend on the beam and target momenta, which in the Monte Carlo and in real life are drawn from distributions. In analyzing the data, one does not have the benefit of knowing the true momenta, but only the averages, namely $<p_\pi> = 263$ GeV/c and $<p_N> = 0$. Therefore in the Monte Carlo, too, these reconstructed values are based on fixing $<p_\pi> = 263$ GeV/c and $<p_N> = 0$. Thus smearing due to beam spread and Fermi motion are properly represented.

As with the data, a cut is made on the χ^2 probability of the vertex fit, requiring the probabilities for the fits in both the x-view and the y-view to be greater than 2%. This has the effect of removing events produced in the dump; after this cut, only 1% of the sample is due to events not produced in the target. After passing this cut, all tracks are required to lie within the fiducial volume of the detector, and must reach the final hodoscope bank without ranging out. Hodoscopes struck by the tracks are required to satisfy all levels of the trigger logic. Using mean chamber efficiencies, the numbers of MWPC and drift

chamber hits are generated and required to be each ≥ 5. The event is not put through the full event reconstruction software as this would be extremely time consuming. The effects of the reconstruction have instead been reviewed in a separate study and will be discussed in a later section. Hodoscope efficiencies are dealt with in later stages of the analysis, as it is useful to study results both with and without hodoscope efficiencies included. The cuts listed in §3.2 are also applied to all Monte Carlo events.

All events surviving these cuts are considered to be accepted events and may be compared with the data. Figure 25 shows the comparison of data and Monte Carlo in the x and y profiles of the detector illumination, at the C bank (after the selection magnet) and at the D bank (after the analysis magnet). Agreement between data and Monte Carlo in these plots is not strongly dependent on the physics of the generation scheme, but tests more directly the accuracy of the transport, multiple scattering, and energy loss software of the program. Figures 26 - 28 show comparisons of distributions in all kinematic variables, including distributions of $\cos\theta^*$ in bins of x_1. One sees in figure 28 that the data are in good qualitative agreement with the Monte Carlo which incorporates an x-dependent $\cos\theta^*$ ditribution. In all these plots the Monte Carlo has been normalized to have 1322 events overall.

3.4 Detector Acceptance

Overall, the acceptance of the detector is 4.6% for mu-pairs of masses between 4.0 and 8.5 GeV, and $x_F \geq 0$. This includes measured chamber and hodoscope efficiencies in addition to the geometrical acceptance determined by the layout of the detector and the kinematics of mu-pair production, and the logical acceptance imposed by the trigger and event selection cuts made in the analysis.

The acceptance of the spectrometer is studied by comparing the number of events surviving to the number of events generated. For acceptance in a particular variable, the surviving events are binned according to the reconstructed value of that variable, while the generated events are binned according to the generated value. The bin-by-bin ratio of these two gives the acceptance. Specifically, using $\cos\theta^*$ as an example, and subscripts R and G to indicate reconstructed and generated values,

$$\text{Acceptance}(\cos\theta^*) = \frac{dN_R/d(\cos\theta^*)_R}{dN_G/d(\cos\theta^*)_G}.$$

The careful attention paid to the distinction between reconstructed and generated values is necessary to correct for the effect of smearing. Although the events appearing in a given bin may not have been generated in that bin, the acceptance as defined here provides a number that allows one to compute from the observed bin population the true bin population.

Figures 29 - 33 illustrate the acceptance for this experiment. Figure 29 shows M and P_T acceptances and indicates the relatively weak dependence of the acceptance on these variables. By contrast, figure 30 shows the strong forward peaking of the x_F and x_1 acceptances, a characteristic feature due to the action of the selection magnet and the fact that the detector is live in the central region. (The selection magnet also plays a role in the mass acceptance, but this is apparent only at masses below about 2 GeV.) The angular acceptances shown in figure 31 are smooth and have little effect on this analysis. Figure 32 shows the $\cos\theta^*$ acceptance in four helicity frames. In all frames the dependence of the acceptance on $\cos\theta^*$ is quite marked. This may be traced to the fact that an event with a large value of $|\cos\theta^*|$ corresponds to the case where, in the mu-pair center of mass frame, one muon is nearly forward and the other nearly backward. In the lab frame the backward muon is soft and travelling at a large angle. Such events are lost primarily because the relatively narrow y-aperture of the analysis magnet intercepts the soft muon. The acceptance is slightly asymetric in part because the hole in the trigger banks is asymetrically located, and in part because the halo cut employed in this analysis is intrinsically asymetric. For the Collins-Soper frame, figure 33 shows the acceptance in $\cos\theta^*$ for four bins of x_1.

3.5 Hodoscope Efficiencies

Hodoscope efficiencies, if they are anything other than 100%, introduce a bias into the trigger that can in turn alter the acceptance profiles in kinematic variables of interest. For extracting distributions in $\cos\theta^*$, in particular, an accurate knowledge of acceptance is important as the raw distributions are dominated by the acceptance, making the acceptance corrections large.

In the test run, from which this data sample was taken, a number of counters proved to be inefficient. The effects of the inefficiencies do not show up clearly on raw displays of hodoscope illuminations and thus the problems were not uncovered during the run. Illuminations of hodoscope hits associated with

reconstructed tracks show trouble in about 10-15 of the 332 trigger counters, the most serious cases of inefficiency occuring in the D bank. This is illustrated in figure 34. Light horizontal and vertical bands, in comparison with darker neighboring bands, indicate the presence of inefficient DY and DX counters.

Because hodoscopes are part of the trigger, measuring the efficiencies is not entirely trivial, as events with hodoscope failures do not trigger the apparatus, and do not appear on tape. It proved possible to circumvent this situation by culling from the data all events with three tracks. Since the trigger required only two tracks, the third track is, in some sense, independent of the trigger. In reality, the trigger knows nothing of tracks, but only of the totality of hodoscope hits, and the possibility was thus opened for using events with only two tracks but extra hodoscope hits. This was necessary because the total 3-track sample was quite small. Special care was taken to ensure that the use of extra hits did not bias the result. The measurements with the pure 3-track sample proved to agree quite well with the measurements from the combined sample in the regions where the 3-track events were plentiful enough to make the comparison statistically significant.

The study of hodoscope efficiencies involved careful fitting of all tracks concerned, and precise measurements of hodoscope positions. Each hodoscope in the experiment was assigned its own alignment constants, measured to be accurate to the resolution of the tracks themselves. Tracks were required to pass stringent "quality-control" cuts involving minimum numbers of hits, and fit χ^2's. Most importantly, when the efficiency of a given hodoscope was under scrutiny, all other hodoscopes struck by the track were required to be on. The efficiencies were then measured at 7-8 points along the counter (depending on which bank was being measured) and the resulting efficiency pattern fit to a low-order polynomial to give a smooth fit to the efficiency over the length of the counter. This process was carried out for every trigger counter in the experiment and the results of the fits tabulated in convenient form for use in the Monte Carlo. Figure 35 illustrates the efficiency in a row of the DY bank; both the measured efficiencies and the values used in the Monte Carlo are shown. The Monte Carlo therefore knew the efficiency at every point of every counter, with a typical precision of a few percent. With these efficiencies in use, the Monte Carlo's ability to reproduce the hodoscope illuminations was significantly improved. Figures 36 and 37 show the illumination plots of the DX and DY banks when the hodoscope

efficiencies are in the Monte Carlo.

The effect of the inefficiencies was most pronounced for events with negative $\cos\theta^*$. This was because the lowest efficiencies were encountered principally near the center of the apparatus, just west of the midline. This region is populated by stiff negative tracks. Figure 38 shows the ratio of $\cos\theta^*$ acceptance calculated with inefficient hodoscopes to that calculated assuming fully efficient hodoscopes. There is an overall loss of efficiency and a distinct bias against $\cos\theta^*<0$. Figure 39 shows the same thing in four bins of x_1; the same basic pattern is present at all values of x_1, perhaps slightly more pronounced at high x_1.

The sensitivity of the acceptance to the measured efficiencies was studied by adjusting the efficiency measurements up and down 10%, an amount generally larger than the error in the measurements. Deviations from the acceptance ratios shown in figures 38 and 39 were slight and well within errors.

3.6 Chamber Efficiencies

Chamber efficiencies may also affect acceptances, but the effect is less direct as it must be filtered through the event reconstruction algorithms which are designed to handle a certain amount of chamber inefficiency.

Efficiencies were measured by projecting tracks into chambers and asking for a hit within $\pm$4mm. Tracks chosen for this had to have hits in all *other* planes, and had to have all associated hodoscope hits on. In the MWPC's, efficiencies thus measured were recorded for each 8-wire group, ie., for each pre-amp. In the drift chambers, efficiencies were recorded wire by wire. Typical results are shown in figures 40 and 41, for the MWPCs and drift chambers, respectively.

Non-wire-related efficiencies were also studied. These involved efficiencies around support wires and other support structures in the chambers, and efficiencies near the beam region. No evidence for loss of efficiency was found in the beam region. In the MWPC's there were some missing wires and missing pre-amps (deliberately removed for various reasons), and in the drift chambers there were electronic problems in the readout (giving rise to a distinctive pattern of inefficiency) and support structures that contributed to the efficiency losses.

3.7 Reconstruction Efficiency

The efficiency of the reconstruction programs has been studied, principally by Monte Carlo, but also by visual scanning of approximately 200 events. The two methods are in very good agreement. Each yields essentially the same figure for the reconstruction efficiency, and, more important, both agree on the predominant causes for reconstruction failures. The Monte Carlo study is more precise and more thorough, and hence will be discussed here.

The Monte Carlo was used to generate 10K events within the spectrometer acceptance. Chamber hits were assigned in accordance with the chamber efficiencies discussed above, and extra (background) hits are put in to simulate natural conditions. These extra hits are of two varieties, *correlated* and *uncorrelated*. Correlated hits are those hits which lie near particle trajectories and are due to δ-rays produced by the track; uncorrelated hits are everything else -- stale hits from previous buckets, debris from hadronic punch-through, dark current in the chambers, and so forth. To reproduce these backgrounds, real events were reconstructed, and all track-associated hits removed. The remaining hits were then superimposed on Monte Carlo events, simulating the uncorrelated background, and those hits occuring within 1cm of a track were superimposed about the Monte Carlo tracks, simulating the correlated background. The uncorrelated backgrounds depended on beam intensity, and therefore a random sample of all events in the data sample was prepared in order to generate a representative set of background hits.

The events were passed through the 3 levels of reconstruction, including all the cuts in the third level, and any event surviving was considered to be a properly reconstructed event. Comparison of actual track vectors before and after reconstruction showed that this criterion of proper reconstruction did in fact pick out correctly reconstructed events. The mean reconstruction efficiency was found to be $93\pm1\%$. Of the events in the lost 7%, roughly one-third were lost because of the confusion caused by the presence of extra hits, and about two-thirds were lost because of chamber inefficiencies. The extra hits were more troublesome in the MWPCs where the spatial resolution is poorer, while the inefficiencies were more troublesome in the drift chambers where the efficiencies were generally lower, and the the layout of the chambers conspired to make misreconstruction more likely when hits were absent.

The reconstruction efficiency was also examined as a function of the kinematic variables of interest, and found to be flat in all cases. Figure 42 shows the reconstruction efficiency plotted against M, x_F, P_T, $\cos\theta^*$, ϕ^*, and Φ_{LAB}. The efficiency in $\cos\theta^*$ is also examined for four bins of x_F and found to be flat in all. This is illustrated in figure 43. Thus, apart from an overall normalization factor, the reconstruction algorithms have not affected the acceptances.

3.8 Beam Momentum

Accurate knowledge of the beam momentum (p_π) is important for the correct calculation of x_F and x_1, since, to first order at least,

$$x_F = \frac{p_z^+ + p_z^-}{p_\pi} \qquad 3.2$$

Apparatus for measuring the beam momentum directly was not in place during the test run, but a measurement could be made indirectly by measuring the momentum of decay muons that are produced in the beam and pass through the spectrometer.

These beam muons may be thought of as having two components. Pions and kaons decaying very far upstream (between the target the the momentum slit) will give rise to muons, some of which will fall within the momentum and angle bite of the beam. These will be transported along with the hadron beam and arrive at the experimental target with a momentum spectrum centered about the central momentum of the beam. Though useful for measuring the beam momentum, the spectrometer has --by design-- no acceptance for these. They pass through the beam hole in the trigger banks. Decays occuring in the final straight section of the beamline --after the last quadrupole triplet-- are not momentum selected, and give rise to a broad spectrum of muons. The lower edge of this spectrum is sharply defined by the kinematics, and occurs at

$$p_\mu = p_\pi \frac{m_\mu^2}{m_\pi^2}.$$

The apparatus has excellent acceptance for these tracks, and they may be used to determine p_π. The edge defined by this equation is softened and shifted by the contribution from kaons in the beam, the intrinsic spread of p_π, and the energy loss in the absorber.

The Monte Carlo program HALO[46] has been used to generate the spectrum of muons at the experimental target. These muons are transported through the apparatus by this experiment's Monte Carlo, and their momentum spectrum in the spectrometer, after acceptance cuts, is compared to the data in figure 44. The low edge of the peak is due to the kinematic cut-off, and therefore contains the desired information, while the upper fall-off is due simply to acceptance cuts. The data are drawn from a run in which the trigger was set to accept single tracks, and consist predominantly of muons from the beam. The agreement has been achieved by adjusting the central beam momentum in HALO. As a result of this adjustment, the beam momentum is estimated to be

$$<p_\pi> = 263 \text{ GeV/c}.$$

The uncertainty may be inferred from figure 44 to be about the width of one histogram bin, hence, $\sim$4 GeV/c. With this beam tune HALO also predicts the beam momentum spectrum, as shown in figure 45.

3.0 Resolution and Smearing of Kinematic Variables

Although the mean pion momentum, and momentum spectrum, are known from these measurements, the actual energy of the interacting pion is not known on an event-by-event basis, and this gives rise to a smearing of the measured x_F values. Since $\sigma_{p_\pi} \approx 3\% p_\pi$, one expects from equation 3.2 that $\sigma_{x_F} \approx 3\% x_F$. Additional smearing arises from the measurement error on the muon momenta themselves, however, and the two effects taken together result in

$$\sigma_{x_F} \approx .03 x_F \sqrt{1+0.4x_F^2}.$$

Thus even at high x_F the resolution is still dominated by the beam spread.

At low x_F there is another contribution to σ_{x_F} coming from Fermi motion of the nucleon in the target. The fact that Fermi motion does not contribute at high x_F may be seen by computing $x_F = 2P_L^*/\sqrt{s}$. When Fermi motion is present, the transformation from the lab to the beam-target center of mass is affected, altering both $\sqrt{s}$ and P_L^*. At high x_F, however, the effect cancels. Expressing x_F directly in terms of the pion, nucleon, and mu-pair energies and momenta, one has

$$x_F = \frac{E_{\mu^+\mu^-}}{E_\pi} \frac{(\beta_{\mu^+\mu^-} - \beta)}{(E_N - p_N)/(E_\pi + E_N)}.$$

In this equation all quantities are expressed in the lab frame. $\beta_{\mu^+\mu^-}$ is the velocity of the mu-pair, and β is the velocity of the center of mass itself. A mu-pair with x_F=0 is stationary in the center of mass, and so of course has $\beta_{\mu^+\mu^-} = \beta$. But for $x_F > 0$, one has $\beta < \beta_{\mu^+\mu^-} < 1$, and in the high-$x_F$ limit, $\beta_{\mu^+\mu^-} \rightarrow 1$. Since, however,

$$1-\beta = (E_N-p_N)/(E_\pi+E_N),$$

one sees that x_F becomes completely independent of the Fermi momentum p_N in this limit. (Intuitively this result if obvious when one considers that $x_F \approx x_1-x_2$. Since a high x_F, $x_F \approx x_1 \approx 1$, the smearing of the nucleon variable, x_2, has little effect on x_F in this region.) At lower x_F, however, this convenient cancellation does not take place, and the Fermi momentum affects x_F and therefore smears the measurement of x_F. The net result is that σ_{x_F} varies from about .015 at $x_F \sim 0$ to about .035 at $x_F \sim 1$.

Figure 46 shows a Monte Carlo calculation of σ_{x_1} (x_1 is closely related to x_F, but is of more interest to the structure function measurements). The Monte Carlo includes, as always, beam momentum spread, momentum resolution of the analysis magnet, and Fermi motion. The values of σ_{x_1} shown in the figure follow closely the expectations discussed above. Also shown is the shift in the the reconstructed x_1 values as a result of smearing on a falling spectrum. This shift depends on the shape of the pion structure function, and will become an issue in the next chapter.

In $\cos\theta^*$ -- the other variable of central interest in this study -- the problems are not so difficult. Indeed, the resolution in $\cos\theta^*$ is quite good, varying between .02 and .04, and the smearing is completely negligible. This is illustrated in figure 47. The figure shows $\sigma_{\cos\theta^*}$ and $\Delta_{\cos\theta^*}$ both as a function of $\cos\theta^*$ itself, and as a function of x_1.

3.10 Background Subtraction

Single muons which happen to coincide in time with one another can trigger the apparatus and contribute to a background of accidental mu-pairs which must be removed. The background is small for masses greater than 4 GeV, but is concentrated at $\cos\theta^* \approx \pm 1$ where the signal is also small.

A rough estimate of the magnitude of the background can be made by considering $\mu^+\mu^+$ pairs. Random accidentals should have approximately equal numbers of like sign and opposite sign pairs. Above M = 4GeV, 6 $\mu^+\mu^+$ pairs were observed, suggesting a background of 12 $\mu^+\mu^-$ pairs. A more refined estimate was made by randomly combining pairs of single muons from a run taken with a singles trigger (the same run as used in the beam momentum measurement discussed above). Since the tracks on this tape reflect all the sources of single muons in their actual proportions, the random pairings should properly represent the accidental background. The pseudo-events created by these random pairings were processed exactly as the normal data were, and yielded a total of 11 events after cuts. The normalization, however, is arbitrary and must be established separately.

Normalization of the 11 pseudo-events is achieved in the following way. When the halo cut is *not* applied, the raw $\cos\theta^*$ distributions are dominated in the region $\cos\theta^* \rightarrow -1$ by contributions from events including a beam muon. This is illustrated in figure 48a. The same feature naturally appears in the pseudo-events when the halo cut is not applied; this is shown in figure 48b. A reasonable estimate of the background normalization is therefore made by scaling the pseudo-events so the populations of the lowest bins of these plots match. This yields a normalization factor of 1.19, and therefore an estimated background of 13.1 events, in good agreement with the 12 events estimated from the like-sign events. Distributions of these 13.1 events are shown in figure 49.

3.11 Normalization

Although the shapes of the structure functions and angular distributions are independent of the absolute normalization of the data, the measurement of the K-factor requires knowledge of the true cross-section. Given the observation of N mu-pairs, the cross-section per nucleon may be inferred from

$$\sigma = \frac{N/\epsilon}{N_\pi f N_0 \rho \lambda (1-e^{-L/\lambda})} \qquad 3.3$$

where ϵ is the acceptance of the detector (including reconstruction efficiencies), N_π is the total number of pions striking the target, f is the live-time correction, N_0 is Avogadro's number, and ρ, λ, and L are the density, absorption length, and physical length of the target. Equation 3.3 assumes an A-dependence of A^1,

consistent with recent measurements of mu-pair production.[47] In practice, the quantity $\rho\lambda(1-e^{-L/\lambda})$ is replaced by $\sum_i \rho_i\lambda_i(1-e^{-L/\lambda_i})$ to sum over the different components of the tungsten alloy target.

The live-time correction factor represents the fraction of time that the apparatus was able to accept a trigger. The trigger was disabled when the online computer was reading in data and when a veto occurred; the bulk of the dead-time was due to the computer. The live-time fraction, f, was monitored continuously, and stayed in the range .45-.55 except during high intensity runs when it dropped to .20.

The number of pions, N_π, incident on the target was measured by use of an ionization chamber placed in the beam just upstream of the target. The chamber measured total charge released by ionization when the beam passed through, and was calibrated by activating a copper foil placed over the chamber and subsequently measuring the decays of ^{24}Na produced. The ionization measurement was checked for run-to-run stability by comparing with counts from the most downstream set of hodoscope banks. A 3% correction factor was also applied to account for back scatter from the target.

CHAPTER IV

THE PION STRUCTURE FUNCTION

In this chapter the pion structure function will be extracted from the data and fitted to several proposed parametrizations. The nucleon structure function, which appears in the cross section along with the pion structure function will also be studied. The chapter is organized in the following way: §4.1 discusses the form of the cross section and illustrates its relationship to the structure functions; §4.2 discusses ways of parametrizing the pion structure function; §4.3 and §4.4 review results of other measurements of pion and nucleon structure functions; §4.5 discusses methods of analysis, and §4.6 presents results; §4.7 covers systematic errors, and §4.8 makes some general remarks and observations.

4.1 Structure functions and the Lepton Pair Cross section

As noted in chapter I, the parton model relates the lepton pair cross section to the structure functions of the interacting hadrons. For $\pi^- N \rightarrow \mu^+\mu^- X$ equation 1.8 may be written

$$\frac{d^2\sigma}{dx_1 dx_2} = \frac{4\pi\alpha^2}{3s}\frac{1}{3x_1^2x_2^2}\sum_i e_i^2\Big[\, x_1 q_i^{\pi}(x_1)x_2\overline{q}_i^{N}(x_2) + x_1\overline{q}_i^{\pi}(x_1)x_2 q_i^{N}(x_2)\Big] \qquad 4.1$$

The sum is over all (light) quark and anti-quark flavors, including both valence and sea distributions. If the sum is expanded so all the individual quark distributions are displayed (subscripts V and S stand for valence and sea),

$$\frac{d^2\sigma}{dx_1 dx_2} = \frac{4\pi\alpha^2}{9sx_1^2x_2^2}\left[\left(\frac{2}{3}\right)^2 x_1\overline{u}_V^{\pi}(x_1)x_2 u_V^{N}(x_2) + \left(\frac{1}{3}\right)^2 x_1 d_V^{\pi}(x_1)x_2\overline{d}_S^{N}(x_2) + \cdots\right]$$

it may then be collapsed and reorganized such that all pion valence terms are

collected in one group, and all pion sea terms are collected in another group. Calling these $F^{\pi}(x_1)$ and $S^{\pi}(x_1)$, respectively, one has

$$\frac{d^2\sigma}{dx_1 dx_2} = \frac{4\pi\alpha^2}{9sx_1^2x_2^2}\left[F^{\pi}(x_1)G(x_2) + S^{\pi}(x_1)H(x_2)\right]. \qquad 4.2$$

Invariance of the strong interactions under isospin rotations and charge conjugation ensures that $\bar{u}_V^{\pi}(x_1) = d_V^{\pi}(x_1)$, and thus

$$F^{\pi}(x_1) = x_1\bar{u}_V^{\pi}(x_1) = x_1 d_V^{\pi}(x_1).$$

The pion sea structure function is taken to be SU(3) symmetric:

$$S^{\pi}(x_1) = x_1 u_S^{\pi}(x_1) = x_1\bar{u}_S^{\pi}(x_1) = x_1 d_S^{\pi}(x_1) = x_1\bar{d}_S^{\pi}(x_1) = x_1 s_S^{\pi}(x_1) = x_1\bar{s}_S^{\pi}(x_1).$$

The nucleon structure functions $G(x_2)$ and $H(x_2)$ are linear combinations of the individual quark distributions given by

$$G(x_2) = \frac{1}{9}\left[4\frac{Z}{A}x_2 u_p(x_2) + 4(1-\frac{Z}{A})x_2 d_p(x_2) + 5x_2\lambda_p(x_2)\right] \qquad 4.3a$$

and

$$H(x_2) = \frac{1}{9}\left[(1+3\frac{Z}{A})x_2 u_p(x_2) + (4-3\frac{Z}{A})x_2 d_p(x_2) + 11x_2\lambda_p(x_2)\right] \qquad 4.3b$$

where the sea distribution, $\lambda_p(x_2)$, is given by

$$x_2\lambda_p(x_2) = x_2 u_S^p(x_2) = x_2\bar{u}_S^p(x_2) = x_2 d_S^p(x_2) = x_2\bar{d}_S^p(x_2) = 2x_2 s_S^p(x_2) = 2x_2\bar{s}_S^p(x_2),$$

and isospin invariance has been used to express neutron quark distributions in terms of proton quark distributions. The normalization of $s_S^p(x_2)$ is supported by deep inelastic scattering data[48]. One will recognize the structure function $H(x_2)$ as the familiar F_2 of deep inelastic scattering theory, but $G(x_2)$ is characteristic only of lepton pair production.

As it stands, equation 4.2 is complete, but will not reproduce the data. The K-factor, discussed in §1.6, must be introduced on the right hand side to account for the discrepancy.

4.2 Parametrizations (and Nomenclature)

The pion valence quark distribution is parametrized by

$$x_1 \bar{u}_V^{\pi}(x_1) = \frac{1}{B(\alpha,\beta+1)} x_1^{\alpha}(1-x_1)^{\beta} \qquad 4.4$$

where Euler's beta function, defined by

$$B(x,y) = \frac{\Gamma(x)\Gamma(y)}{\Gamma(x+y)},$$

normalizes to one $\bar{u}$ valence quark, $\int_0^1 \bar{u}_V^{\pi}(x_1)dx_1 = 1$. This experiment studies only the region $x_1 \geq 0.2$, and thus the pion sea makes little contribution to the cross section. For the purpose of analysis the pion sea will be taken from reference 50.

Interest in the behaviour of the pion structure function at large x_1 was noted in chapter 1 and linked to a suggested form:

$$F^{\pi}(x_1) \sim x_1\left[(1-x_1)^2 + \frac{2}{9}\frac{<k_T^2>}{M^2} \right]. \qquad 4.5$$

For the purpose of experimental study this may be parametrized

$$F^{\pi}(x_1) = Ax_1^{\alpha}\left[(1-x_1)^{\beta} + \gamma \right] \qquad 4.6$$

leaving the parameters α, β, and γ to be determined by best fits to the data, A being fixed by the normalization condition. The shape of the structure function at low x_1 is determined by α, while at high x_1 it is fixed by β and γ. The normalization, A, is closely linked to α because the normalization integral mentioned earlier is dominated by contributions at low x_1. Because there is no data below x_1=.2, it is useful in practice simply to fix the value of α. As noted in chapter I, there are theoretical reasons for expecting $F^{\pi}(x_1) \sim \sqrt{x_1}$ at low x_1, so α=1/2 is a natural choice. The prediction of the higher twist model, equation 4.5, however, represents the case α=1. Although this model is only conceived to hold at "high x_1" –x_1>.5, say– the lack of data at low x_1 and the high mean value of x_1 for this experiment make this case a reasonable possibility. The data will therefore be fit to four different trial forms of $F^{\pi}(x_1)$, which represent the range of theoretical predictions:

1. $A\sqrt{x_1}(1-x_1)^\beta$
2. $A\sqrt{x_1}\left[(1-x_1)^\beta + \gamma\right]$
3. $Ax_1\left[(1-x_1)^\beta + \gamma\right]$
4. $Ax_1\left[(1-x_1)^2 + \gamma\right]$

The last form is essentially that of the higher twist model. Because of the statistical limitations of this sample, however, the parameter γ will be treated as a constant. The higher twist model makes predictions for the x_1, M^2, and P_T^2 dependence of γ, but detailed studies of γ's dependence on these variables, if any, will be left for a higher statistics data sample. An estimate of the parameter $<k_T^2>$ may be made by setting $\gamma = \frac{2}{9}\frac{<k_T^2>}{M^2}$ and fixing M^2 at the mean square mass of these data, $<M^2> = 26.6$ GeV ^{2}.

More recent work on the higher twist model was noted in chapter I and associated with a form

$$F^\pi(x_1) = x_1\left[(1-x_1)^2 + \frac{1}{2}\frac{x_1^2\lambda^2}{M^2}\right] \qquad 4.7$$

and a value of λ^2 can be estimated. The data prove to be insensitive to the x_1^2 factor, however, and in practice it turns out that $\lambda^2 \approx \frac{4}{9}<k_T^2>$.

4.3 Pion Structure Function: Results from other Lepton Pair Experiments

Several groups have used lepton pair production to extract the pion structure function, and have fitted results to the form of equation 4.4; in most cases a K-factor has also been extracted, or can be estimated from the published information. A summary of these results is given in table 7. All experiments included in the table study the reaction $\pi^- N \rightarrow \mu^+\mu^- X$; the various pion energies used, E_π, are indicated in GeV.

TABLE 7

RECENT FITS TO THE PION STRUCTURE FUNCTION

Exp't	E_π	K	α	β	# evts	Ref.
E444	225	(1)	1/2	1.27 ± .06	2000	49
NA3	150	2.49 ± .37	.41 ±.05	.92 ± .04	16000	50
"	200	2.3 ± .5	.45 ±.12	1.17±.09	7000	50
"	280	2.22±.33	.41±.05	1.01±.08	12000	50
NA10	194	2.51±.09	.39±.02	1.11±.03	110000	51
Omega*	40	2.45±.42	.44±.12	.98±.15	3600	52
Goliath	150,175	~ 2.8	1/2	1.57±.18	500	53

In this table (as in all others to come) quantities which are constrained in the fitting are indicated without errors. A fit to the form given in equation 4.5 has also been performed[54] by the E444 collaboration, with the result that $<k_T^2> = 1.1 \pm 0.3$.

It is apparent from the table that there is relatively little agreement on the value of β: one sees values of 0.9, 1.0, 1.1, 1.2, 1.3, and 1.6. β, of course, characterizes the shape of the structure function at high x_1, and this range of values emphasizes our ignorance of the structure function out there. K and α seem to show more agreement. One should bear in mind, however, that K and α tend to be highly correlated, and it is not clear that one can take values of K or α from this table and expect them to be meaningful in isolation from one another. β and α are also correlated, though not so strongly as K and α, and this, too, must affect one's interpretation of the table.

* The structure function parameters α and β in the Omega experiment are based on a fit to the data below the J/ψ, $2<M<2.7$. The K-factor is based on a comparison of $d\sigma/dM$ of the entire sample with the Drell-Yan prediction calculated using the pion structure function of NA3 (200 GeV) and the CDHS nucleon structure functions.

Except as noted for Omega, these experiments all cover approximately the same range of mass ($\sim$4 to $\sim$8 GeV). Goliath and Omega explicitly impose a cut requiring $x_F \leq .8$, while in NA10 the acceptance effectively vanishes beyond $x_F \sim .8$. NA10's acceptance in rapidity, y, imposes a correlation between x_1 and M such that at the lowest mass range considered, M=4.5, the data is limited to the region $x_1 \leq .7$. A subtler, but important point is that NA3, NA10, and Omega all use the *same* nucleon structure function (based on the 1979 CDHS results) as input to extract $F^{\pi}(x_1)$. Goliath uses the parametrization of Buras and Gaemers[55], which is based on SLAC e-p and FNAL μ-p data, while E444 extracts the shapes of both $F^{\pi}(x_1)$ and $G(x_2)$ without recourse to either of these.

4.4 Nucleon Structure Functions: Results from Deep Inelastic Scattering Experiments

The scattering of leptons from nuclear targets[56] has provided measurements of the quark distributions in nucleons over certain ranges of x and Q^2 (corresponding to x_2 and M^2 of this work), and may be used to provide estimates of the structure function $G(x_2)$. Two neutrino experiments, CDHS[57] at CERN, and CCFRR[58] at FNAL are considered here. A comparison of $G(x_2)$ derived from each of these is shown in figure 50, indicating good agreement in shape, but some discrepancy in overall normalization. In this work, the version of $G(x_2)$ used is CCFRR's.

The CCFRR nucleon structure functions are parametrized at $Q_0^2 = 10$ GeV^2 by

$$2xF_1(x,Q^2) = a(1+ex)(1-x)^f Z(x,Q^2)$$

$$xF_3(x,Q^2) = a(1+c_d' \ (1-x))x^b(1-x)^c Z(x,Q^2)$$

where $Z(x,Q^2) = 1+(g-h\sqrt{x})log_{10}Q^2/Q_0^2$ determines the rescaling with Q^2. From the parametrization of $xF_3(x,Q^2)$ one can read off the valence distributions:

$$xu^V(x,Q^2) = ax^b(1-x)^c Z(x,Q^2)$$

$$xd^V(x,Q^2) = ac_d' \ x^b(1-x)^{c+1} Z(x,Q^2).$$

The sea is given by

$$5x\lambda(x,Q^2) = 2xF_1(x,Q^2) - xF_3(x,Q^2).$$

With the parameters a, b, c, d, e, f, g, and h fitted under the R=0 assumption, the function $G(x_2)$ can be computed [59].

4.5 Methods of Analysis: General Remarks

The specific techniques used to extract $F^\pi(x_1)$ from the data will be discussed along with the results in §4.6. Some more general aspects of the analysis will be dealt with here.

To begin with, the basic cross section, equation 4.2, is simplified to eliminate the need to extract the pion sea distribution, $S^\pi(x_1)$. (Such an extraction can not be done unambiguously with this data sample.) Defining a "correction function,"

$$Q(x_1,x_2) = \frac{F^\pi(x_1)G(x_2) + S^\pi(x_1)H(x_2)}{F^\pi(x_1)G(x_2)}$$

equation 4.2 may be rewritten to yield

$$\frac{d^2\sigma}{dx_1 dx_2} = \frac{4\pi\alpha^2}{9sx_1^2x_2^2}F^\pi(x_1)G(x_2)Q(x_1,x_2) \qquad 4.11$$

In this analysis, Q will be evaluated using results from the NA3 experiment. At x_1=0.2, $Q \approx 1.3$, but it falls rapidly as x_1 increases; above x_1=.5, $Q \equiv 1.0$ and thus it plays little role in determining the high-x_1 behaviour of $F^\pi(x_1)$. Introducing the total luminosity L_0, the reconstruction efficiency R, the detector efficiency (acceptance) ϵ, and the K-factor, K, the number of events per unit area of x_1–x_2 space may be written

$$\frac{d^2N}{dx_1 dx_2} = \left[L_0 R \frac{4\pi\alpha^2}{9s}\frac{\epsilon(x_1,x_2)Q(x_1,x_2)}{x_1^2x_2^2}\right]KF^\pi(x_1)G(x_2) \qquad 4.12a$$

The quantity in brackets may be regarded as a "weight function," $W(x_1,x_2)$ so that

$$\frac{d^2N}{dx_1 dx_2} = W(x_1,x_2)KF^\pi(x_1)G(x_2) \qquad 4.12b$$

relates the raw data to the structure functions directly. With Monte Carlo to measure acceptances, $W(x_1,x_2)$ may be determined.

The data are binned as illustrated in figure 51, with 16 equal bins in x_1 and 10 graduated bins in x_2. Other binnings have been tried to ensure that the results do not depend on the choice of binning. For future reference, the columns in x_1 will be labelled with an index i, i=1,...,16, and the rows in x_2 will be labelled with an index j, j=1,...10. Because of the relationships $x_1 x_2 s = M^2$, and $x_1 - x_2 = x_F$, curves of constant mass appear as hyperbolae in x_1-x_2 space, and curves of constant x_F appear as straight lines. Thus the kinematic cuts $4.0 \leq M \leq 8.5$ GeV^2 and $x_F \geq 0.0$ appear as shown in the figure.

A Monte Carlo is used to compute the acceptances ϵ_{ij} of the bins, as discussed in §3.4. Enough events are generated so that the statistical error on ϵ_{ij} is much smaller than the error on the events in this bin. Typically, $\sigma_{\epsilon_{ij}}/\epsilon_{ij} \sim .03$–$.04$. A more important systematic uncertainty in ϵ_{ij} arises, however, because of our fundamental ignorance of the pion structure function at high x_1.

This uncertainty hinges on the fact that one does not know which of the forms of $F^{\pi}(x_1)$ to use in generating the Monte Carlo events. The data of table 7 offer little help, given the spread of β values, and, as will be seen later, the χ^2 for the four trial fits shown above are not sufficiently different to select one of them unambiguously. On the other hand, the calculated acceptance at high x_1 *does* depend on which is used. This dependence stems from the fact that some fraction of the events at high x_1 are there by virtue of having been "smeared up" from lower x_1. The size of this smeared component depends in part on the spread of the beam momentum, as discussed in §3.9, and in part on the shape of the structure function. The acceptance, which is the ratio of events accepted in some bin to events generated in that bin, is sensitive to the smearing, and thus to the choice of structure function. If the Monte Carlo uses a structure function with a large value of γ, the acceptance at high x_1 is lower than if a small value of γ is used. The fitted structure function is in turn affected by this change in acceptance, in such a way that a large (small) value of γ in the Monte Carlo means that a large (small) value of γ will be favored in the fit. One might hope that a study of events smeared beyond x_1=1 would clarify the issue of smearing, but in fact there are only 2 data events in this region, and most reasonable structure functions predict something close to this.

For the present it will suffice to note that the solution to the problem has been to exclude events in the highest x_1 bin ($.95 \leq x_1 \leq 1.0$) from all structure

function analysis. Quantitatively, this placement of the cut may be justified as follows. The Monte Carlo was run 3 times with 3 different structure functions used to generate the events:

Version A uses $F^{\pi}(x_1) = \sqrt{x_1}(1-x_1)^{1.40}$

Version B uses $F^{\pi}(x_1) = x_1[(1-x_1)^{1.80} + .0050]$

Version C uses $F^{\pi}(x_1) = x_1[(1-x_1)^2 + .0085]$.

The specific parameter values used here are results of fits to the data, as will be seen in the sections that follow. Acceptance is compared in the 16 bins of x_1 for each of the versions. In the first 14 bins ($x_1 \leq .90$) the acceptances agree well within errors. In the 15th bin ($.90 \leq x_1 \leq .95$) the acceptance of version A is 13% higher than version B, while version C is 13% lower. In the 16th bin ($.95 \leq x_1 \leq 1.0$) these same figures become 45% and 30%, respectively. Clearly both bins are sensitive to the smearing, but it is out of the question to eliminate both as the measurement of $F^{\pi}(x_1)$ at high x_1 would be seriously compromised. The solution has been to exclude bin 16 and compute acceptances with version B. The residual 13% systematic uncertainty in the acceptance of the 15th bin is then translated into a systematic error on the fit parameters. (Systematic errors will be discussed in §4.7.)

4.6 The Pion Structure Function: Results

The extraction of $F^{\pi}(x_1)$ from equation 4.12 may be done by means of a weighted projection onto the x_1-axis. If a specific choice is made for $G(x_2)$, one may integrate equation 4.12 over x_2 in the following manner:

$$\frac{dN}{dx_1} = \left[L_0 R \frac{4\pi\alpha^2}{9sx_1^2} \int \frac{\epsilon(x_1,x_2)\,G(x_2)\,Q(x_1,x_2)}{x_2^2}\,dx_2 \right] KF^{\pi}(x_1).$$

This leads to

$$N_i = W_i K F_i,$$

where the bin weights, W_i, are given by

$$W_i = L_0 R \frac{4\pi\alpha^2}{9s} \int\int_{\Delta x_i} \frac{\epsilon(x_1,x_2)\,G(x_2)\,Q(x_1,x_2)}{x_1^2 x_2^2}\,dx_1\,dx_2,$$

and the F_i are $F^\pi(x_1)$ evaluated at the mean bin value. Initially $G(x_2)$ is taken to be that derived from the CCFRR data.

In the table that follows, the projected values are fitted to the four trial forms of $F^\pi(x_1)$. In each case the K-factor is included in the fit so that the shape parameter β will not be distorted by being forced also to handle the normalization, although K is probably not meaningful, given the remarks made earlier, except for cases 1 and 2. Errors quoted in table 8 are statistical only, and it should be noted that a 15% overall systematic uncertainty in the normalization applies to K.

TABLE 8

FITS TO PION STRUCTURE FUNCTION USING CCFRR VERSION OF $G(x_2)$

Fit	K	α	β	γ	χ^2/d.o.f.	χ^2 C.L.
1	2.1±.1	1/2	1.41±.06	~	9.0/13	77%
2	2.1±.1	1/2	1.31±.11	-.0106±.0117	8.0/12	78%
3	~	1	1.78±.11	.0040±.0039	11.2/12	51%
4	~	1	2	.0085±.0020	15.0/13	31%

The confidence levels of the fits range from 30% to 80% and are thus quite acceptable. Because several other experiments have measured values of α around 0.40, (see table 7), it is interesting to see the effect of constraining α=0.40. This yields K=2.5±0.1 and β=1.34±0.06, with χ^2/d.o.f = 10.1/12. The small background of accidental pairs, discussed in §3.10, has not been subtracted from the data in these fits; such a subtraction does not affect the fits significantly, though the χ^2 of the last two forms is decreased by ~2 units.

Fit #4 uses a form of $F^\pi(x_1)$ like that proposed by Berger and Brodsky. If one interprets $\gamma=\frac{2}{9}\frac{<k_T^2>}{M^2}$ where M^2=26.6 GeV^2 is taken to be the mean

square mass of this sample as before, then $<k_T^2> = 1.01 \pm .24$ GeV.^{2} Fitting to $x_1\left[(1-x_1)^2 + x_1^2\gamma\right]$ yields $\gamma = .0095 \pm .0023$, which is not significantly different from the value quoted in table 8. Translated into λ^2, it means $\lambda^2 = .50 \pm .12$ GeV^2. It should also be noted that restricting the fit to the "high-x_1" region, $x_1 \geq .5$ as required by the model, does not significantly change either the fitted parameters or the χ^2 confidence level.

These results are not model-independent, however. Behind them lie two assumptions: (1) that $G(x_2)$ as determined from deep inelastic neutrino scattering is the correct form for use in massive lepton pair production; and (2) that the cross section factorizes into a form $F^\pi(x_1)G(x_2)$. Both of these assumptions may be tested.

In a sense, the factorization hypothesis has already passed a test in that the projected F_i values fit to a smooth functional form with good χ^2. A more direct test may be made, however, by using $F^\pi(x_1)$ and $G(x_2)$ to form the quantity

$$\chi^2 = \sum_{i,j}\left(\frac{N_{ij} - W_{ij}KF_iG_j}{\sigma_{ij}}\right)^2,$$

where the weights W_{ij} are given by

$$W_{ij} = L_0 R \frac{4\pi\alpha^2}{9s}\epsilon_{ij}\int\int_{\Delta x_i \Delta x_j}\frac{Q(x_1,x_2)}{x_1^2 x_2^2}dx_2 dx_1,$$

and the F_i and G_j are $F^\pi(x_1)$ and $G(x_2)$ evaluated at the mean center of each bin. For the fits above, this yields a χ^2 of 102.0 for 89 degrees of freedom, corresponding to a confidence level of 16%. The data are thus reasonably well represented by this set of structure functions.

The question remains whether the particular $G(x_2)$ used here is appropriate. If the projection technique is "turned on its side," $F^\pi(x_1)$ may be used to project out $G(x_2)$. When this is done using $F^\pi(x_1)$ from fit #1, the resulting values of G_j seem to fall rather more steeply than the $G(x_2)$ used above. These G_j may be parametrized by $(1-x_2)^\delta$, and this new form for $G(x_2)$ used to extract a new form for $F^\pi(x_1)$. This in turn may then be used to extract a new $G(x_2)$, and so on, iteratively. The process converges rapidly. The results for $G(x_2)$ are shown in figure 52. In figure 53 the same data are plotted with the standard (deep inelastic scattering) version of $G(x_2)$; one sees immediately the data favor a more steeply

falling function than that provided by the deep inelastic scattering results. The final result for $G(x_2)$ using this method is

$$G(x_2) \sim (1-x_2)^{3.19\pm.49}.$$

This result is in good agreement with E444[60] although the analysis techniques are different.

Unfortunately, however, the *ad hoc* nature of the $(1-x_2)^\delta$ parametrization leaves the normalization of this $G(x_2)$ in doubt, and thus the K-factor undetermined. One solution is to suppose that above some value of x_2 the $(1-x_2)^\delta$ parametrization must "tie on" to the $G(x_2)$ of deep inelastic scattering. This allows one to extract a K-factor, but the point at which the tie-on is made is arbitrary, and the K-factor depends (mildly) on that point. In figures 52 and 53, the tie-on point was set at x_2=0.2, yielding a K-factor of 1.9±0.1. The data are scaled by 1/K in this figure.

Another possibility is to use a (somewhat) less arbitrary parametrization. Combining the CCFRR results for the u and d valence quark distributions in the nucleon with the sea quark distribution measured by CFS[61] generates a form of $G(x_2)$ that is almost indistinguishable from $(1-x_2)^{3.19}$. Using this hybrid form gives a value of K=1.8±.1.

The nucleon structure function as measured here is in good agreement with that measured in other lepton pair experiments. Figure 54 shows data from this experiment along with data from E444 and NA3; all three experiments are seen to be in good agreement with one another. The three sets of data have been separately normalized to give a least-squares match to the CCFRR version of $G(x_2)$ over the range $.10 \leq x_2 \leq .35$.

Results on $F^\pi(x_1)$ are shown in the table below. Plots of the data with fit #1 and with fit #4 superimposed are shown in figures 55 and 56.

TABLE 9

FITS TO $F^{\pi}(x_1)$ AFTER PROJECTION WITH $G(x_2)$=.74(1−x_2)$^{3.19}$

Fit	α	β	γ	χ^2/d.o.f.	χ^2 C.L.
1	1/2	1.53±.07	∼	8.6/13	80%
2	1/2	1.52±.11	−.0004±.0069	8.6/12	73%
3	1	1.98±.12	.0052±.0025	13.8/12	32%
4	1	2	.0056±.0019	13.8/13	39%

The modified version of the nucleon structure function, $G(x_2)$, now climbs higher at low x_2, causing the pion structure function to fall lower at high x_1. This is apparent in the table above. As was done above, values of $<k_T^2>$ and of λ^2 may be estimated, yielding results

$$<k_T^2> = .67 \pm .23 \text{ GeV}^2$$

and

$$\lambda^2 = .32 \pm .11 \text{ GeV}^2.$$

The same results are obtained if the fit is restricted to the "high- x_1" region, $x_1 \geq .5$. The factorization χ^2 is now 103.8 for 89 degrees of freedom. Though $G(x_2)$ is now different, $F^{\pi}(x_1)$ has accommodated, and the quality of the overall fit to the data is about the same. Values of $F^{\pi}(x_1)$ and $G(x_2)$ are given in table 10.

TABLE 10

VALUES USED IN FITS TO $F^{\pi}(x_1)$ AND $G(x_2)$

x_1	$F^{\pi}(x_1)$	x_2	$G(x_2)$
.214	.213±.070	.041	.818±.086
.259	.351±.050	.052	.628±.034
.309	.279±.036	.069	.613±.029
.360	.243±.029	.092	.503±.032
.410	.267±.027	.122	.452±.033
.462	.200±.024	.157	.397±.035
.514	.205±.020	.196	.416±.041
.565	.177±.017	.242	.322±.057
.616	.155±.014	.291	.458±.102
.667	.117±.011		
.717	.111±.010		
.768	.078±.0079		
.819	.064±.0063		
.870	.034±.0046		
.919	.017±.0029		

The value of $<k_T^2>$, if interpreted literally in the context of the higher-twist model, should be closely related to the mean square momentum of the mu-pairs themselves, because in this model there is no source of transverse momentum beyond the intrinsic transverse momentum of the annihilating quarks. Figure 57 illustrates the mean square transverse momentum of the mu-pairs as a function of x_1. One sees that at low x_1 the typical value is $<p_T^2> \approx 1.6$ GeV^2, but at high x_1 this has fallen to about 0.8 GeV^2, close to the fitted value of $<k_T^2>$. This fall-off is not attributable to a compression of phase space, however, because x was defined (see §1.2) to take P_T into account. One concludes that the mechanisms[20]

which give rise to large values of $<p_T^2>$ are not as important at high x_1 as at lower values of x_1. It appears from figure 57 that at high x_1, $<p_T^2>$ is consistent with the mu-pair transverse momentum coming entirely from the intrinsic transverse momentum of the annihilating quarks.

An attempt has also been made to look at the behaviour of $F^\pi(x_1)$ in 2 broad mass ranges with this data sample. The small size of the sample, unfortunately, makes a more detailed investigation impossible, and limits even the conclusions from this crude study. The regions are indicated below.

Low Mass	$4 \leq M \leq 6$	$<M^2>=25.9\text{GeV}^2$
High Mass	$5 \leq M \leq 8.5$	$<M^2>=36.6\text{GeV}^2$

Fits to $F^\pi(x_1)$ in these mass regions are compared below; the change in γ from the low mass region to the high mass region is consistent with $1/M^2$ dependence, but cannot be regarded as statiscally significant.

TABLE 11

COMPARISON OF $F^\pi(x_1)$ AT HIGH AND LOW MASS

		Low Mass			High Mass		
Fit	α	β	γ	χ^2/d.o.f.	β	γ	χ^2/d.o.f.
1	1/2	1.48±.06	~	10.5/13	1.57±.09	~	15.1/12
2	1/2	1.53±.12	.0038±.0073	10.2/12	1.64±.19	.0037±.0084	15.0/11
3	1	2.00±.12	.0073±.0026	14.0/12	2.07±.07	.0060±.0022	19.0/11
4	1	2	.0074±.0020	14.0/13	2	.0050±.0026	19.1/12

4.7 Systematic Considerations

The chief systematic uncertainties in $F^{\pi}(x_1)$ arise from the uncertainty of the mean beam energy, $<P_{\pi}>$, and the uncertainty in the acceptance at high x_1 due to the problem discussed in §4.5. This section reviews how these uncertainties affect the fit parameters.

It will be recalled from chapter III that $<P_{\pi}>$ was measured indirectly, by studying the momentum spectrum of single muons generated by the decay of beam pions; the result of the measurement was $<P_{\pi}>=263\pm4$ GeV/c. Since, to a good approximation,

$$x_F = \frac{p_{\mu^+} + p_{\mu^-}}{p_{\pi}},$$

all values of x_F must therefore be regarded as systematically uncertain at the level of $\sim$ 2%. This uncertainty feeds through into the structure function determination and affects both the overall shape and the high- x_1 character of the fit.

The table below summarizes the systematic uncertainties in the variables K, β, and γ arising from the beam energy and acceptance uncertainties noted earlier. The errors in the first row correspond to varying the beam energy by $\pm2\%$. K is affected because of its correlation with β and γ.

TABLE 12

SYSTEMATIC ERRORS IN $F^{\pi}(x_1)$

Source	ΔK	$\Delta\beta$	$\Delta\gamma$
Beam energy	$\pm$.10	+.07	-.0025
		-.10	+.0045
Acceptance	$\pm$0.0	+.03	-.0020
		-.02	+.0015

A 15% uncertainty in the luminosity, L_0, also leads to an uncertainty in K of

$\pm.3$. Uncertainty in the correct choice of $G(x_2)$ and normalization of the nonstandard choices suggests an additional uncertainty in K of $^{+0.0}_{-0.2}$. Note also that the choice of α=.40 increased K by .4.

A study was also made to check for any systematic errors introduced by the method of iterated projections. For this purpose, Monte Carlo was used to generate 100 fake data sets of 1300 events each, using simple forms $F^{\pi}(x_1) \sim (1-x_1)^2$ and $G(x_2) \sim (1-x_2)^3$. Each data set was processed by the same software used to analyze the data, with the same number (3) of iterations. The mean power fitted to the pion structure function was 2.012 ± 0.009; and the mean power fitted to the nucleon structure function was 2.95 ± 0.05. (The errors are errors on the *mean*.) Clearly there is no sign of systematic bias here.

4.8 Concluding Remarks on Structure Functions

In this chapter, the structure functions $F^{\pi}(x_1)$ and $G(x_2)$ have been extracted from a data sample of $\sim$1320 muon pair events and fitted to various functional forms. A few comments may suffice to summarize the situation.

$F^{\pi}(x_1)$ tends to be steeper are high x_1 that most previous measurements, but the χ^2 confidence levels of the fits are good. The scale breaking term in $F^{\pi}(x_1)$ has been measured in one other experiment, and agrees within errors with the value found here.[63] The higher twist model is consistent with observations made in this chapter, but the form of $F^{\pi}(x_1)$ predicted by this model is by no means the only one consistent with the data, and in fact has generally shown the highest χ^2 of the forms considered.

The nucleon structure function observed here rises above the deep inelastic scattering (DIS) results for $x_2 \leq 0.1$. It is worth noting that in the range of Q^2 considered here DIS experiments do not go as low in x_2 as lepton pair experiments; indeed, approximately 50% of the events in this sample lie outside the range of, for instance, the CCFRR data. Other differences include the fact that the DIS experiments used here for comparison employed iron targets, while this experiment used tungsten. Most previous lepton pair experiments have used the DIS forms as fixed input, and in fact have used the *very same* form; this analysis suggests that such a course is risky. It is true that $F^{\pi}(x_1)$ can accomodate different forms of $G(x_2)$ and still give an acceptable χ^2 for the comparison to the

data, but *internal consistency* of the analysis has forced the use of the non-standard form of $G(x_2)$. The example of the hybrid form of $G(x_2)$ indicates that the disagreement with DIS measurements can be pushed entirely into the sea distribution $x_2\lambda(x_2)$.

The K-factor is consistent with a value in the range 1.8 to 2.5. This is entirely due to systematic questions concerning α, $G(x_2)$, and the total luminosity, L_0; the statistical error on K is the least troublesome aspect. Any plan to study K's functional dependence on the hadronic variables of the problem must first overcome these systematic problems.

The high statistics sample produced by this experiment and currently being analyzed should be able to resolve more clearly the true shape of $F^{\pi}(x_1)$ and $G(x_2)$, and study the functional dependence of the scale breaking term, γ.

CHAPTER V

THE LEPTON PAIR ANGULAR DISTRIBUTION

This chapter views the lepton pair data from a new angle. In chapter IV the leptonic degrees of freedom (θ^* and ϕ^*) were integrated over and the analysis focussed on the hadronic variables x_1 and x_2. In this chapter the leptonic variables will be studied explicitly, and correlations between θ^* and x_1, and θ^* and P_T will be investigated. The fact that one can exploit these angular degrees of freedom contributes both to the power of the lepton pair experiment as a tool for studying hadronic phenomena, and to the difficulty of its analysis. Large numbers of events are required if one wishes to study a process differentially in many variables.

5.1 The Cross Section in θ^* and ϕ^*

The leptonic degrees of freedom are emphasized when the cross section is expressed in terms of the helicity structure functions. In chapter I this was written (equation 1.3):

$$\frac{d\sigma}{d^4q d\Omega^*} = \frac{1}{32\pi^4}\left(\frac{\alpha}{Ms}\right)^2\left[W_T(1+\cos^2\theta^*) + W_L\sin^2\theta^* + W_\Delta\sin 2\theta^*\cos\phi^* + W_{\Delta\Delta}\sin^2\theta^*\cos 2\phi^*\right]$$

The helicity structure functions W_T, W_L, W_Δ, and $W_{\Delta\Delta}$ may be functions of the hadronic variables M, x_F, and P_T, but have no hidden dependence on θ^* or ϕ^*. Defining the angular distribution by

$$\frac{dN}{d\Omega^*} = \left(\frac{d\sigma}{d^4q}\right)^{-1}\frac{d\sigma}{d^4q d\Omega^*},$$

and using

$$\frac{d\sigma}{d^4q} = \frac{1}{12\pi^3}\left(\frac{\alpha}{M_\delta}\right)^2 (2W_T + W_L), \qquad 5.1$$

which may be obtained from equation 1.3 by integration, one has

$$\frac{dN}{d\Omega^*} = \frac{3}{8\pi}\frac{1}{(A+2)}\left[1+\cos^2\theta^* + A\sin^2\theta^* + B\sin 2\theta^*\cos\phi^* + C\sin^2\theta^*\cos 2\phi^*\right] \qquad 5.2$$

where $A = W_L/W_T$, $B = W_\Delta/W_T$, and $C = W_{\Delta\Delta}/W_T$. One often encounters variables other than A, B, and C in the literature.[63] The angles θ^* and ϕ^* are referred to some set of axes determined by one's choice of helicity frame; the Collins-Soper, S-channel, T-channel, and U-channel helicity frames were defined in chapter I.

When integrated over ϕ^* the angular distribution becomes

$$\frac{dN}{d(\cos\theta^*)} = \frac{3}{4(A+2)}\left(1+\alpha\cos^2\theta^*\right) \qquad 5.3$$

where

$$\alpha = \frac{1-A}{1+A} = \frac{W_T - W_L}{W_T + W_L}. \qquad 5.4$$

Because of the small size of the data sample, the analysis of this chapter will focus on the $\cos\theta^*$ distributions, with the principal aim being to measure α and study its dependence on x_1 and P_T.

5.2 Measurements of α vs. x_1: Results of Other Experiments

Many experiments have published measurements of α based on global data samples[2] but only a handful have studied α differentially in x_1. These include E444,[64] NA3,[65] NA10,[66] and OMEGA.[67] Their results are summarized in table 13 and plotted in figure 58; all measurements quoted are made in the T-channel helicity frame. A glance at the figure reveals immediately the state of our current knowledge.

TABLE 13

SUMMARY OF MEASUREMENTS OF α AT VARIOUS x_1 VALUES

x_1*	E444	NA3		NA10		OMEGA†
		$P_T<1$	$P_T>1$	$P_T<1$	$P_T>1$	
.30	1.40±.50	−.17±.65	.75±.27			
.50	.88±.28	.73±.19	.46±.19			
.70	.57±.28	.81±.23	.75±.23			
.90	−.16±.32	1.85±.54	.81±.40			
.30				.44±.12	.49±.08	
.41				.71±.61	.61±.11	
.56				.24±.16	.65±.22	
.66				−.39±.37	.53±.37	
.23						.56±.49
.36						.92±.30
.53						.12±.29
.75						.12±.40

* The x_1 value indicated is the bin center. In the case of the OMEGA data, x_1 is estimated from the published values of x_F and M.

† OMEGA data are from a lower mass range, M=2-2.7 GeV; the other experiments explore the range M>4 GeV.

5.3 Results on $\cos\theta^*$ Distributions

For the study of $\cos\theta^*$ distributions, the data are binned in 15 bins of $\cos\theta^*$ and acceptance corrected bin by bin. Bins with less than .2% acceptance are not used. The background study discussed in chapter III indicated that one expects

in this sample approximately 13 background events, mostly concentrated at $|\cos\theta^*|>.7$. The artificial background events generated by that study are subtracted bin by bin from the raw data before acceptance correction. The effect of the background subtraction on the measurement of α is in all cases less than the statistical error on α.

Figure 59 shows $\cos\theta^*$ distributions in the four helicity frames, based on the global data sample. The solid lines are fits to $1+\alpha\cos^2\theta^*$, and the values of α obtained from these fits are indicated in table 14.

TABLE 14

GLOBAL FITS TO $1+\alpha\cos^2\theta^*$

Frame	α	χ^2/d.o.f.
Collins-Soper	.82±.26	19.6/10
S-Channel	.17±.19	13.3/11
T-Channel	.82±.20	14.8/12
U-Channel	.35±.22	17.0/11

In these results it is apparent that the Collins-Soper and T-channel frames show the greatest degree of spin-alignment.

The $\cos\theta^*$ distributions may also be studied in 4 x_1 bins, x_1=.2–.4, x_1=.4–.6, x_1=.6–.8, and x_1=.8–1.0. These distributions, together with the fits, are shown in figure 60 for the Collins-Soper frame, and figure 61 for the T-channel. There is evidence in these figures that the angular distribution is changing as a function of x_1. The table below summarizes the results of the fits.

The χ^2 values for these fits are all quite acceptable. Taken together, the χ^2 values are 51.9 for 48 degrees of freedom in the T-channel, and 44.0 for 45 degrees of freedom in the Collins-Soper frame. The data are thus well fit by a variable α that falls with increasing x_1. This effect was first observed in E444, and is consistent with the higher twist model. Figures 62 and 63 show the α plotted against x_1 for Collins-Soper and T-channel respectively. The prediction of

TABLE 15

FITS TO $1+\alpha\cos^2\theta^*$ IN COLLINS-SOPER AND T-CHANNEL

x_1	Collins-Soper		T-Channel	
	α	χ^2/d.o.f.	α	χ^2/d.o.f.
.2-.4	1.72±.74	15.1/10	1.79±.63	17.9/12
.4-.6	.95±.44	8.4/11	1.18±.46	3.8/11
.6-.8	.55±.39	8.3/12	.35±.31	14.9/12
.8-1.	-.13±.49	12.2/12	-.26±.37	15.3/13

the Berger-Brodsky model is superimposed. In calculating this curve, the values $M^2 = 26.6$ GeV^2 and $\lambda^2 = .32$ GeV^2 are used, the latter value having been estimated from the structure function fits in the last chapter.

The data show the same qualitative trend with x_1 as the theoretical prediction, but the error bars are large. How significant is the effect? To make a quantitative test of the sensitivity of the data to variation in α, a fit was made constraining α to be the same in all x_1 bins.* In the Collins-Soper frame this yielded $\alpha = .71\pm.24$, with a χ^2 of 49.3 for 48 degrees of freedom (χ^2 C.L. = 42%); in the T-channel, the results were $\alpha = .68\pm.20$, and $\chi^2 = 61.9$ for 51 degrees of freedom (χ^2 C.L. = 14%). These are still acceptable fits to the data. On the other hand, forcing $\alpha = 1$ for all four bins of x_1, in conformity with the parton model expectation, yields a χ^2 of 59.1 for 49 degrees of freedom (χ^2 C.L. = 14%) in the Collins-Soper frame, and 74.5 for 52 degrees of freedom (χ^2 C.L. = 2%) in the T-channel.

These measurements of α can be related to the structure function measurements of the last chapter, and good agreement is found. It will be recalled from

* This is not the same as fitting the data globally, since a separate normalization for each x_1 region is allowed. In the global fit, the high x_1 data are outnumbered by the low x_1 data, so the fitted α merely reflects the α characteristic of the dominant (lower) x_1 region.

chapter I (or equation 5.1) that the pion structure function measured in chapter IV is related to the helicity structure functions by

$$F^{\pi}(x_1) \sim W_T(x_1) + \frac{1}{2} W_L(x_1) \qquad 5.5$$

where the W_T and W_L are integrated over all remaining variables. The higher twist model in particular specifies that the scale breaking parameter, γ, measured in the structure function fits of the last chapter, should be simply $\frac{1}{2} W_L$. Since the angular distribution parameter A, defined in equation 5.2, is related to W_L by $A = W_L / W_T$, the relationship

$$\frac{1}{2} W_T A \approx \gamma \qquad 5.6$$

should hold. Using $W_T = (1-x_1)^2$, and, $A = (1-\alpha)/(1+\alpha)$, one therefore expects

$$\frac{1}{2}(1-x_1)^2 \frac{1-\alpha}{1+\alpha} \approx \gamma$$

at high x_1. Taking the values of α from the highest-x_1 bin, one finds the angular distribution measurements lead to the following estimates:

$$\gamma \approx .0085 \pm .0068 \qquad \text{(T-channel)}$$
$$\gamma \approx .0065 \pm .0065 \qquad \text{(Collins-Soper).}$$

These figures are to be compared with the result

$$\gamma = .0056 \pm .0019$$

found in the pion structure function analysis; the agreement is quite good.

Systematic errors on α are estimated from the uncertainties of the background subtraction, the hodoscope efficiency correction, and from the statistics of the Monte Carlo acceptance calculation to be

$$\Delta\alpha_{syst} < 0.3.$$

It is important to note that neither the background subtraction nor the hodoscope efficiency correction has *created* the variation of α with x_1. If neither of these procedures is used in the analysis, α is increased by 0.2 in the critical bin, $x_1 = .8 \rightarrow 1.0$. This is still well within the statistical error of $\sim$0.4, and does not

significantly alter the conclusion. Moreover, the angular distribution of muon pairs resulting from J/ψ decay has been studied in this experiment, using the same method of background subtraction and the same hodoscope efficiency correction, but α in this case is not observed to vary at all with x_1. With approximately 75K J/ψ's in the sample, the statistics of this measurement is quite good. The variation seen here is therefore not likely to result from systematic problems.

Another potential source of distortion is the variation of α with P_T; it is known that QCD corrections to the classical Drell-Yan model lead to a dependence of the angular distribution on P_T. The result of Collins' calculation of this effect was discussed in chapter I. In terms of the the $\cos\theta^*$ distribution, the prediction for α is

$$\alpha = \frac{1-\frac{1}{2}\frac{P_T^2}{M^2}}{1+\frac{3}{2}\frac{P_T^2}{M^2}}.$$

In figure 64 the $\cos\theta^*$ distribution is plotted in 3 bins of P_T/M in the Collins-Soper frame. Figure 65 shows the same for the T-channel. In both cases, fits to $1+\alpha\cos^2\theta^*$ are superimposed, and the fitted values of α are given in table 16.

TABLE 16

VALUES OF α IN 3 REGIONS OF P_T/M

	α	
P_T/M	Collins-Soper	T-channel
.0-.17	1.18±.52	1.23±.54
.17-.30	.86±.42	.71±.40
.30-.80	.57±.59	.74±.51

Figure 66 shows the values of α plotted against P_T/M with the above prediction superimposed. The agreement with the prediction is good, but the errors are

large, and it is not clear that one is even testing a QCD prediction at these values of P_T/M. It was noted in chapter I that the parton model with intrinsic parton transverse momentum included predicts a dependence of α on P_T; at low P_T/M, the parton model and this QCD model both predict $\alpha \approx 1-2(P_T/M)^2$.

In any case, the effect of P_T on α is clearly quite small in the region of P_T considered, and thus cannot be responsible for the fall of α with increasing x_1. This is particularly true given that the mean P_T has been observed (figure 57) to fall with x_1. From the values of $<p_T^2>$ taken from figure 57, one may deduce that α would be $\geq .96$ if the gluon bremstrahlung mechanism were the only one altering the angular distribution.

5.4 Conclusions

The variation of α with x_1 previously seen in E444 is observed again in these data. The effect is consistent with the Berger-Brodsky model prediction for $\alpha(x_1)$. A constant value of α also provides a satisfactory fit to the data, but at a somewhat lower confidence level. The relationship between α and the scale breaking piece of the pion structure function is predicted by the higher twist model and confirmed here quite strikingly. Dependence of α on P_T is observed, and seen to be in good agreement with the QCD prediction. The dependence is small and becomes significant only at large P_T; this means the leading twist and higher twist effects are cleanly separated in this experiment.

CHAPTER VI

CONCLUSIONS

This dissertation has reported on the analysis of a sample of high- mass muon pairs. The experimental apparatus was designed to give good acceptance at high-x and this study focussed specifically on the characteristics of the mu-pair production in this kinematic region. Both pion and nucleon structure functions have been extracted, along with the associated K-factor, and the mu-pair angular distribution has been studied both globally and in bins of $x_1$and P_T/M. In addition, results were obtained for $<p_T^2>$ vs. x_1.

The material presented here has proven to be consistent with predictions of the higher-twist model. This pion structure function can be fit quite acceptably by the form involving a small constant term, though it fits as well -- or better -- to more traditional forms. The $\cos\theta^*$ distributions, on the other hand, are fit well by the model prediction, and poorly by the standard Drell-Yan prediction. Many diverse and seemingly unrelated features of the data are neatly tied together when viewed in the context of the higher-twist model. Both the angular distribution coefficient α and the mean transverse momentum of the mu-pairs, $<p_T^2>$, can be quantitatively related to the longitudinal piece, γ, of the pion structure function.

The model itself, despite the name, "higher-twist," has its origin in simple, phenomenologically appealing concepts, and the single gluon exchange embodied in the model presents a plausible way of generating the high-x tail of the pion wave function. Indeed, one expects the high-x component to be produced largely by some single hard process: a conspiracy of soft processes seems unlikely. The model thus appears to rest on a natural basis, and it is not at all surprising that the general predictions of Berger and Brodsky's QCD calculation are anticipated

by the phenomenological arguments of Farrar and Jackson, and even, to a lesser extent, argued heuristically from considerations of the manner in which one expects the classical Drell-Yan picture to break down.

Still, it should be borne in mind that the data sample analyzed here is quite small, and the analysis limited, therefore, in scope. The apparent consistency of the data with the predictions reflects only agreement with the most general aspects of the model and the detailed predictions of the model have, of necessity, gone unexamined. Simplifications in this analysis have included regarding the longitudinal structure function as a constant, and treating only the projected $\cos\theta^*$ distributions. Even with this relatively conservative approach, the statistical errors on quantities of interest remain significant.

The nucleon structure function at low-x has presented some interesting features whose significance remains to be understood. The agreement with other muon-pair experiments on this issue strengthens the observation.

The results presented in this dissertation make a small contribution to our understanding of hadronic structure. By use of the muon pair production process, the experiment has been able to study some aspects of hadronic structure not available to the more traditional deep inelastic scattering experiments, and to test our understanding of the strong interactions in novel ways. The technique remains a powerful one that will doubtless see future application.

REFERENCES

1. For general introductions to QCD, see F.E. Close, *An Introduction to Quarks and Partons*, Academic Press, New York (1979); C. Quigg, *Gauge Theories of the Strong, Weak, and Electromagnetic Interactions*, Benjamin/Cummings, Reading Massachusetts, (1983); J.D. Bjorken, "Elements of Quantum Chromodynamics," Proc. of the Summer Institute on Particle Physics, Stanford University, (1979).
2. For some general reviews of this subject, see I.R. Kenyon, Rep. Prog. Phys., **45**, 1261, (1982); E.L. Berger, in Proc. of the Drell-Yan Workshop, Fermilab, (1983); E.L. Berger, in Proc. of the APS/DPF Conf., Maryland, (1982) (AIP Conf. Proc. #98, Subseries #29); R. Stroynowski, Phys. Rep., **71**, 1, (1981); C.S. Lam and W.-K. Tung, in Proc. of the Quangzhou Conf. on Theo. Part. Phys., Guangzhou, PRC, (1980); W.-K. Tung, in Lectures of the 1981 Summer School in Part. Phys., Hefei, Anhui, China (to be published by Science Press, Beijing); J.E. Pilcher, Proc. of the Int. Lepton-Photon Symp., Fermilab, (1979); J. LeFrancois, in Proc. of the XXth Int. Conf. on HEP, Madison, (1980).
3. J.H. Christenson, *et al.*, Phys. Rev. Lett. **25**, 1523, (1970)
4. S.D. Drell and T.M. Yan, Ann. Phys. **66**, 578, (1971); Phys. Rev. Lett. **25**, 316, (1970)
5. C.S. Lam and W.-K. Tung, Phys. Rev. **D18**, 2447, (1978); see also R.J. Oakes, Nuovo Cim. **44A**, 440, (1965).
6. C.S. Lam and W.-K. Tung, Phys. Rev. **D21**, 2712, (1980) C.S. Lam and W.-K. Tung, Phys. Lett. **80B**, 228, (1979)
7. P.W. Johnson and W.-K. Tung, Phys. Rev. Lett. **45**, 1382, (1980)
8. These relationships may be brought out more clearly if a different set of angles are used. See W.-K. Tung, Zeit. Phys. **C13**, 355, (1982)

9. For a general description of parton model principles, see R.P. Feynman, *Photon-Hadron Interactions*, W.A. Benjamin, Inc., Reading, Massachusetts, (1972). The application of the model to lepton pair production is given in reference 4; reference 5 expresses parton model results in terms of the language used here.

10. J.C. Collins and D.E. Soper, Phys. Rev. **D16**, 2219, (1977); see also E.L. Berger, *et al.*, Phys. Rev. **D17**, 858, (1978), and reference 5.

11. See the review by I.R. Kenyon in reference 2 for data on global measurements of α. A weighted average of these measurements (Kenyon's table 6) yields $\alpha = 0.97 \pm 0.8$.

12. S.D. Drell and T.-M. Yan, Phys. Rev. Lett. **24**, 181, (1970); G.B. West, Phys. Rev. Lett. **24**, 1206, (1970); see also Feynman, reference 9, or Close, reference 1.

13. S.J. Brodksy and G.R. Farrar, Phys. Rev. Lett. **31**, 1153, (1973); V.A. Matveev, *et al.*, Lett. al Nuovo Cim. **7**, 719, (1973)

14. Z.F. Ezawa, Nuovo Cim. **23A**, 271, (1974)

15. G. Alteralli, *et al.*, Nucl. Phys. **B69**, 531, (1974); G. Farrar, Nucl. Phys. **B77**, 429, (1974)

16. G.R. Farrar and D.R. Jackson, Phys. Rev. Lett. **35**, 1416, (1975); see also G. Farrar in Proc. of the Rencontre de Moriond, (1975), vol 1, p369. Credit must also be given to Ezawa, reference 14.

17. A.I. Vainshtein and V.I. Zacharov, Phys. Lett. **72B**, 368, (1978)

18. H.D. Politzer, Nucl. Phys. **B129**, 301, (1977); C.T. Sachrajda, Phys. Lett., **73B**, 185, (1978); R.K. Ellis, *et al.*, Nucl. Phys. **B152**, 285, (1979)

19. G. Alterelli, *et al.*, Nucl. Phys. **B157**, 461, (1979); J. Kubar-Andre and F. Paige, Phys Rev. **D19**, 221, (1979); B. Humpert and W.L. Van Neervan, Phys. Lett. **89B**, 69, (1979); K. Harada and T. Muta, Phys. Rev. **D22**, 663, (1980)

20. R.K. Ellis, *et al.*, Phys. Lett. **104B**, 45, (1981); Nucl. Phys. **B211**, 106, (1981); C.Y. Lo and J.D. Sullivan, Phys. Lett., **86B**, 327, (1979); F. Halzen and D.M. Scott, Phys. Rev. **D18**, 3378, (1978); Phys. Rev. Lett., **40**, 1117, (1978); Phys. Rev. **D19**, 216, (1979)

21. K. Kajantie, *et al.*, Phys. Lett. **74B**, 384, (1978); Nucl. Phys. **B144**, 422, (1978); T. Grandou, *et al.*, Phys. Lett. **101B**, 267, (1981); R.L. Thews, Phys. Rev. Lett. **43**, 987, (1979); J. Cleymans and M. Kuroda, Nucl. Phys. **B155**, 480, (1979); Phys. Lett. **80B**, 385, (1979); Phys. Lett. **105B**, 68, (1981); see also next reference.

22. J.C. Collins, Phys. Rev. Lett. **42**, 291, (1979)

23. E.L. Berger and S.J. Brodsky, Phys. Rev. Lett. **42**, 940, (1979); E.L. Berger, Zeit. Phys. **C4**, 289, (1980)

24. S.J. Brodsky, E.L. Berger, and G.P. Lepage, in Proc. of the Drell-Yan Workshop, Fermilab, (1983).

25. S. Matsuda, Phys. Lett. **119B**, 207, (1982)

26. D.L. Preston, Los Alamos preprint, LA-UR-83-298

27. A. Mueller, in Proc. of the Drell-Yan Workshop, Fermilab (1983)

28. See Berger, reference 23, and also E.L. Berger, Phys. Lett. **89B**, 241, (1980)

29. M. Haguenauer, *et al.*, Phys. Lett. **100B**, 185, (1981)

30. L.F. Abbott and R.M. Barnett, Ann. of Phys. **125**, 276, (1980); L.F. Abbott *et al.*, Phys. Rev. **D22**, 582, (1980); L.F. Abbott *et al.*, Phys. Lett. **88B**, 157, (1979)

31. See first two items, previous reference.

32. K.J. Anderson, *et al.*, Phys. Rev. Lett. **42**, 944, (1979); G.E. Hogan, *et al.*, Phys. Rev. Lett. **42**, 948, (1979); C.B. Newman, *et al.*, Phys. Rev. Lett. **42**, 951, (1979); K.J. Anderson, *et al.*, Phys. Rev. Lett. **43**,1219, (1979);

33. S. Palestini, *Forward Production of High Mass Muon Pairs in Pion-Nucleon Interactions*, thesis, unpublished, Princeton University (1984)

34. C. Adolphsen,thesis, in preparation; University of Chicago (1985).

35. K.J. Anderson *et al.*, Phys. Rev. Lett.,**37**, 799, (1976)

36. See N. Giokaris, *Measurement of the Angular and Atomic Weight Dependences of High Transverse Momentum Hadron Production in π^--N Collisions*, thesis, unpublished, University of Chicago, (1981), and references therein.

37. Halo. A Computer Program to Calculate Muon Halo. CERN 74-17.

38. Atherton *et al.*, CERN 80-07.

39. See reference 34 for more information on this point.

40. G. Gollin *et al.*, IEEE Trans. in Nucl. Sci., **NS-26**, 59, (1979)

41. For more details on the secondary search, see S. Palestini, reference 33.

42. Details will be found in reference 34.

43. Frodesen, Skjeggestad, and Tofte, *Probability and Statistics in Particle Physics*, Columbia University Press, New York (1979).

44. B. Rossi, *High Energy Particles*, Prentice-Hall, New York (1952).

45. See reference 34.

46. HALO. A Computer Program to Calculate Muon Halo. CERN 74-17.

47 M. L. Swartz *et al.*, Phys. Rev. Lett., **53**, 32, (1984). See also M. L. Swartz, *The Atomic Mass Dependence of Massive Muon Pair Production in 225 GeV/c π^--Nucleon Interactions*, thesis, unpublished, University of Chicago (1984).

48. See, for instance, Abramowicz *et al.*, Zeit. Phys. **C17**, 283, (1983)

49. C. B. Newman *et al.*, reference 32; see also C. B. Newman, *Measurement of High Mass Muon Pairs Produced in Hadronic Collisions and a Determination of the Pion Structure Function;* thesis, unpublished, University of Chicago (1979), and G. E. Hogan, *Production of High Mass Muon Pairs by 225 GeV/c Hadron Beams and a Determination of the Pion Structure Function* thesis, unpublished, Princeton University (1979).

50. J. Badier *et al.*, Zeit. Phys. **C18**, 281, (1983); S. Weisz, *Production de Dimuons de Hautes Masses Dans L'experience NA3;* thesis, unpublished, Orsay (1981). For a description of the NA3 apparatus, see J. Badier *et al.*, Nucl. Instr. and Methods **175**, 319, (1980).

51. J. Varela, Proc. of the 1983 Rencontre de Moriond, La Plagne, France. For a description of the NA10 apparatus, see L. Anderson *et al.*, Nucl. Instr. and Methods **223**, 26, (1984).

52. M. J. Corden *et al.*, Phys. Lett. **96B**, 417, (1980). For a description of the Omega apparatus, see M. J. Corden *et al.*, Phys. Lett. **96B**, 411, (1980).

53. R. Barate *et al.*, Phys. Rev. Lett. **43**, 1541, (1979). For a description of the Goliath apparatus, see M. A. Abolins *et al.*, Phys. Lett. **82B**, 145, (1979).

54. K. J. Anderson *et al.*, fourth item, reference 32.

55. A. J. Buras, K. J. F. Gaemers, Nucl. Phys. **B132**, 249, (1978).

56. For good reviews of deep inelastic scattering experiments, see F. Eisele, Proc. of the XXI International Conf. on High Energy Physics, Paris (1982), and also, F. Dydak, 1983 International Lepton-Photon Symposium, Cornell University Ithaca, New York

57. J. G. H. deGroot *et al.*, Phys. Lett. **82B**, 456, (1979) J. G. H. deGroot *et al.*, Zeit. Phys. **C1**, 143, (1979) For more recent CDHS results, see reference 48. The parametrization of the 1979 CDHS results is taken from reference 50, while the parametrization of the 1983 CDHS results is taken from Eichten *et al.*, Rev. Mod. Phys. **56**, 579, (1984).

58. D. B. MacFarlane *et al.*, to be published in Zeit. Phys. See also, M. V. Purohit, *Nucleon Structure Functions from ν_μ–Fe Interactions and a Study of the Valence Quark Distribution,* thesis, unpublished, California Institute of Technology (1983) [Nevis preprint R#1298], and D. B. MacFarlane, *Nucleon Structure from Neutrino Interactions in an Iron Target with a Study of the Singlet Quark Distribution,* thesis, unpublished, California Institute of Technology (1983) [Nevis preprint R#1297].

59. The parametrization is discussed in Purohit's thesis (reference 58), appendix F. The parameter values used in this analysis are a=2.3691, b=.5348, c=2.5473, d=1.6489, e=.7607, f=2.5761, g=.3324, h=.9512. These were obtained from F. S. Merritt and P. G. Reutens of the CCFRR collaboration. A fit to the data (contained in Purohit's thesis, appendix G) confirmed the values and supplied a covariance matrix needed to compute the error in $G(x_2)$.

60. See Hogan's thesis, reference 49. Unpublished data of C. B. Newman of the E444 collaboration show $G(x_2) \sim (1-x_2)^{3.18\pm.59}$.

61. D. M. Kaplan *et al.*, Phys. Rev. Lett. **40**, 435, (1978). It is not immediately clear that this measurement of the sea should fit our data better than the CDHS or CCFRR results. The CFS data are confined to $.2 \leq x_2 \leq .5$, while the critical discrepancy seen here occurs at $x_2 \leq .1$.

62. See S. Palestini, reference 33.

In this case, $\lambda = (1-A)/(1+A)$, $\mu = B/(1+A)$, and $\nu/2 = C/(1+A)$. One also sees

$$\frac{dN}{d\Omega} = \frac{3}{16\pi}\left[1+\cos^2\theta + \left(\frac{1}{2}-\frac{3}{2}\cos^2\theta\right)A_0 + 2\cos\theta\sin\theta\cos\phi A_1 + \frac{1}{2}\sin^2\theta\cos 2\phi A_2\right];$$

in this case, $A_0=A/(1+A/2)$, $A_1=B/(1+A/2)$, and $A_2=2C/(1+A/2)$.

64. K.J. Anderson *et al.*, fourth item, reference 32.

65. J. Badier *et al.*, Zeit. Phys. **C11**, 195, (1981)

66. B. Betev *et al.*, in Proc. of the XXII Conf. on HEP, Leipzig, (1984)

67. M.J. Corden *et al.*, Phys. Lett. **96B**, 417, (1980)

Figure 1 -- Parton model picture of the deep inelastic scattering process. A lepton of momentum k interacts with a parton in the hadron through the exchange of a virtual boson of momentum q. P indicates the initial momentum of the hadron.

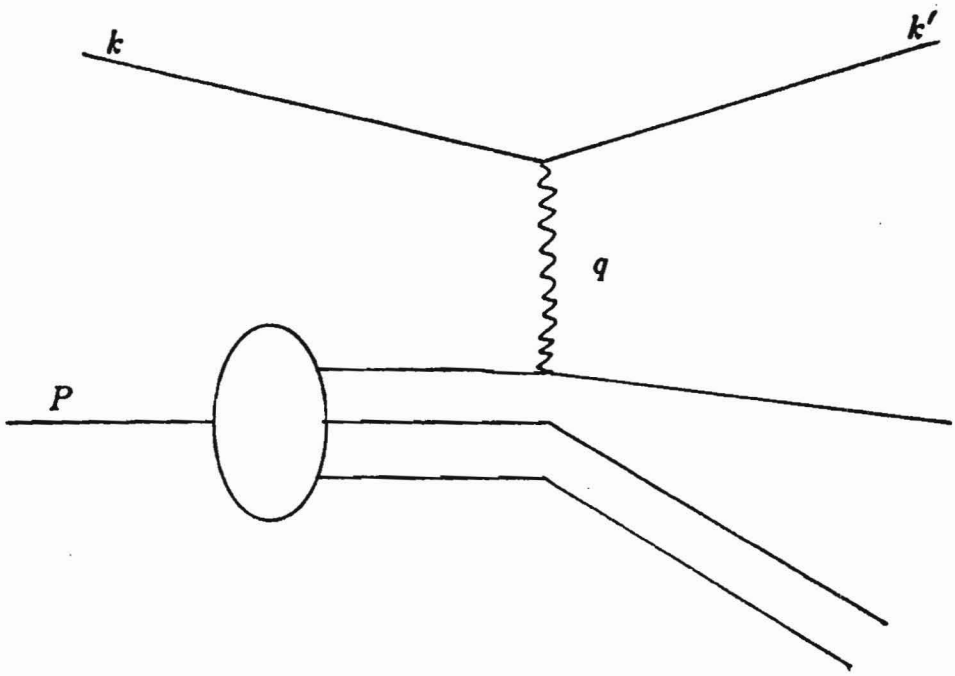
k
k'
q
P

Figure 2 -- Parton model picture of lepton pair production. Hadrons h_1 and h_2 collide and partons q and $\overline{q}$ annihilate to produce a virtual photon of momentum Q which subsequently decays into leptons l^+ and l^-.

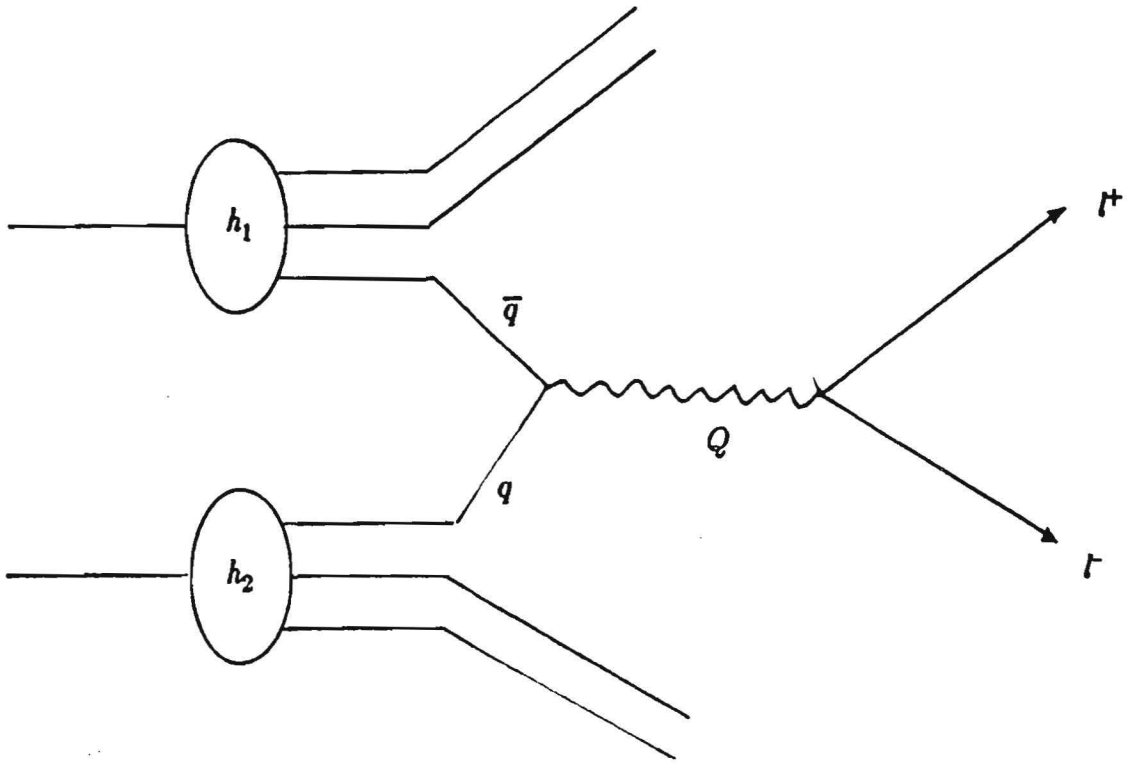
h_1
$\bar{q}$
Q
q
h_2
l^+
l^-

Figure 3 -- Definition of reference axes in the γ^* rest frame. See §1.3 for details.

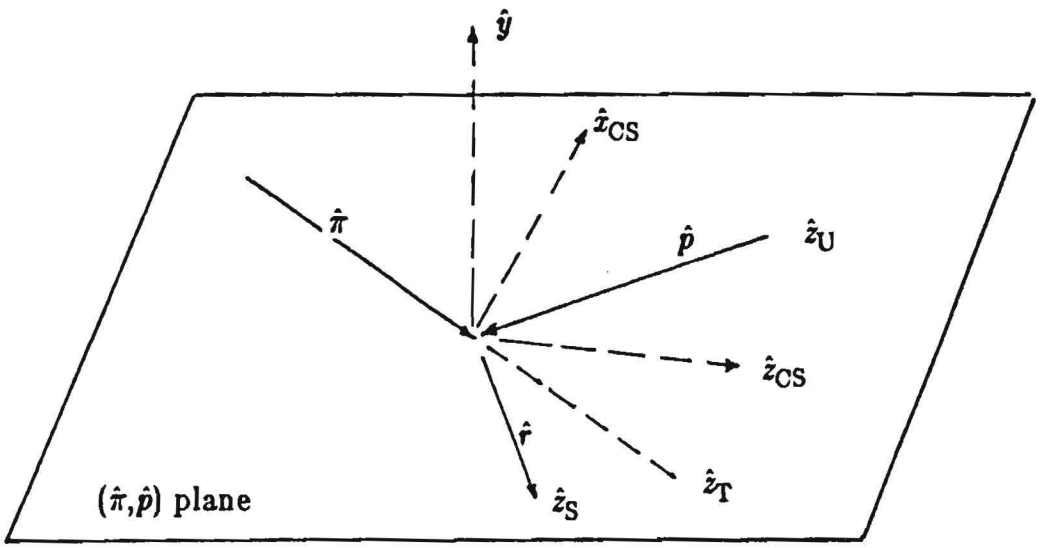
$\hat{y}$
$\hat{x}_{CS}$
$\hat{\pi}$
$\hat{p}$
$\hat{z}_U$
$\hat{z}_{CS}$
$\hat{r}$
$\hat{z}_T$
$\hat{z}_S$
$(\hat{\pi},\hat{p})$ plane

Figure 4 -- General illustration of the lepton pair production process, $h_1 h_2 \rightarrow l^+ l^- X$. The open circle represents the unknown hadronic processes the experiment seeks to decipher.

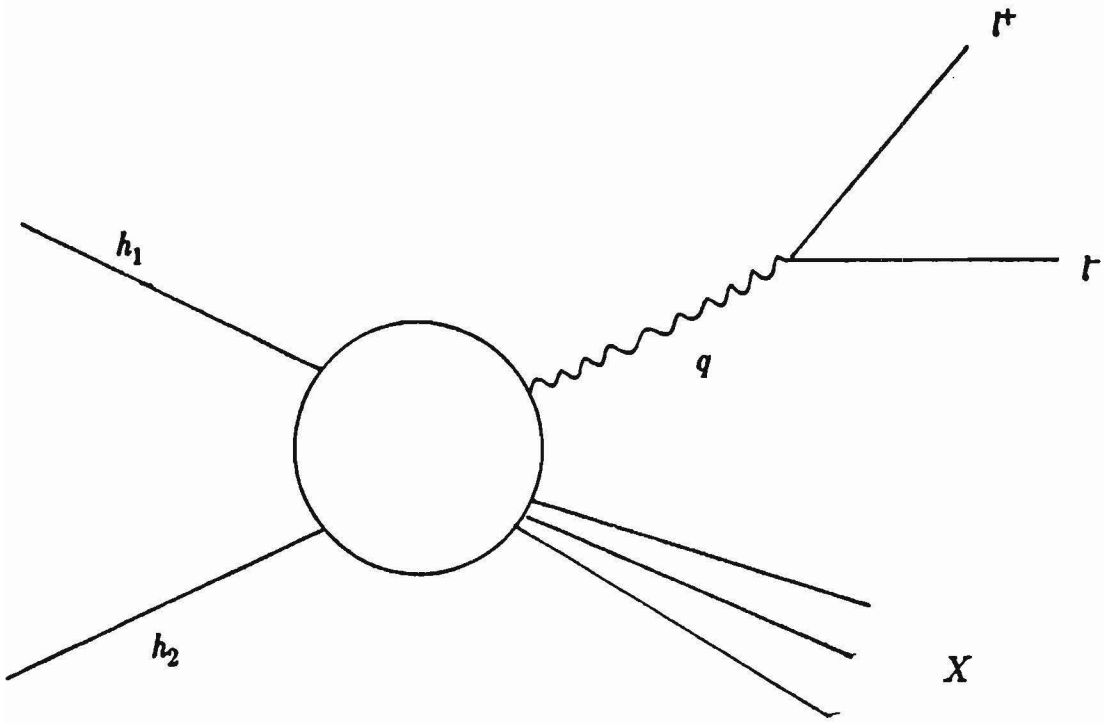
l^+
h_1
l^-
q
h_2
X

Figure 5 -- Illustration of the process used by Farrar and Jackson to generate the high-x component of the pion wave function. The diagram shows the hypothetical case of deep inelastic scattering off a pion.

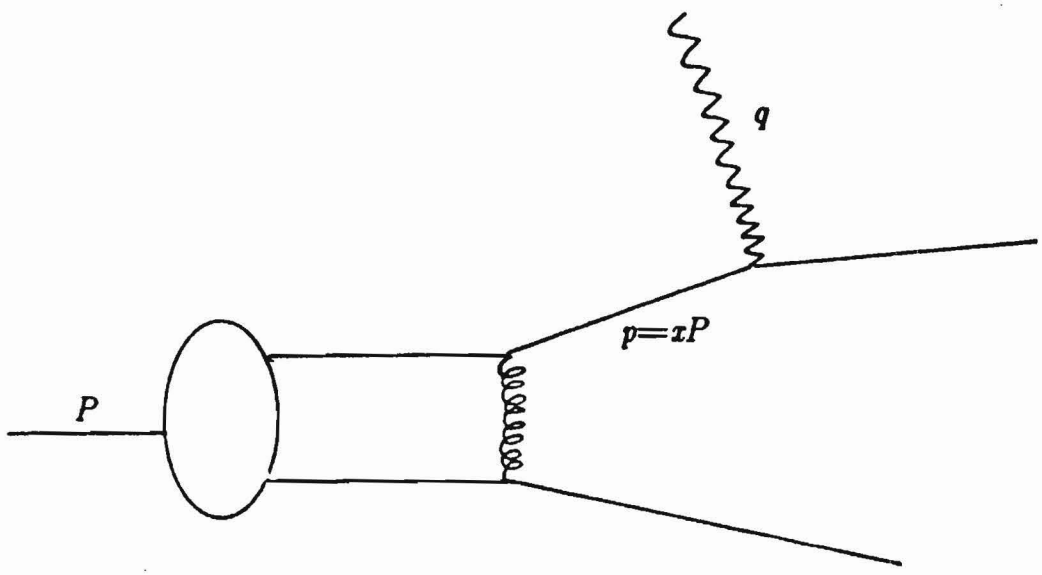
q
p=xP
P

Figure 6 – Illustration of the lowest order QCD correction to lepton pair production; (a) and (b) are "annihilation" channels, and (c) and (d) are "Compton" channels.

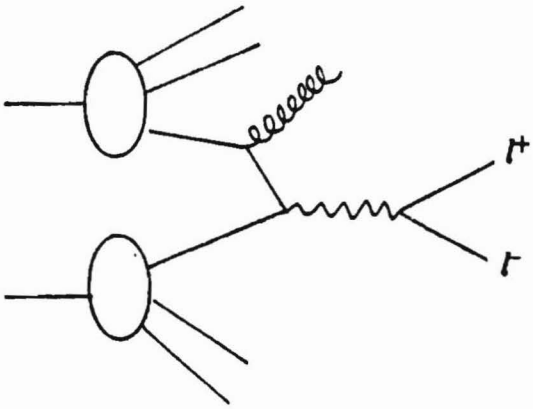

(a)

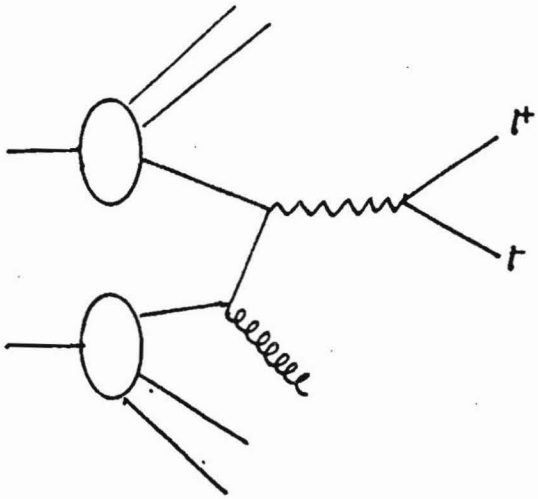

(b)

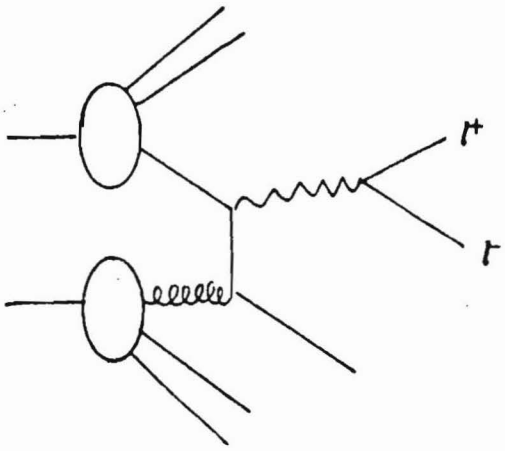

(c)

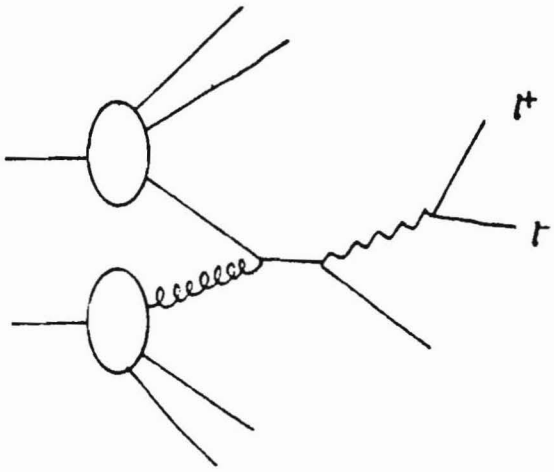

(d)

Figure 7 -- Diagrams used by Berger and Brodsky in their higher-twist model. The upper diagram is like that of the Farrar and Jackson model; the lower is required to maintain gauge invariance.

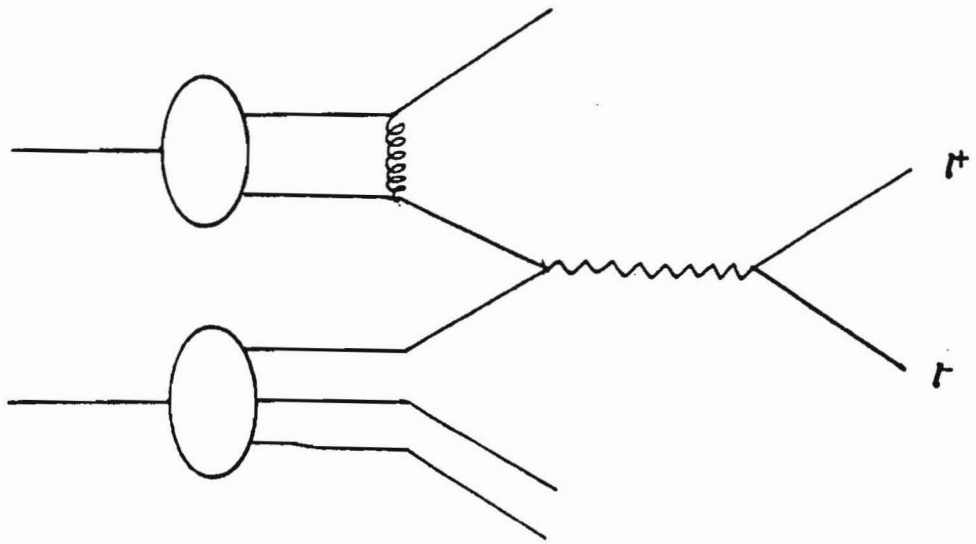
l^+
l^-

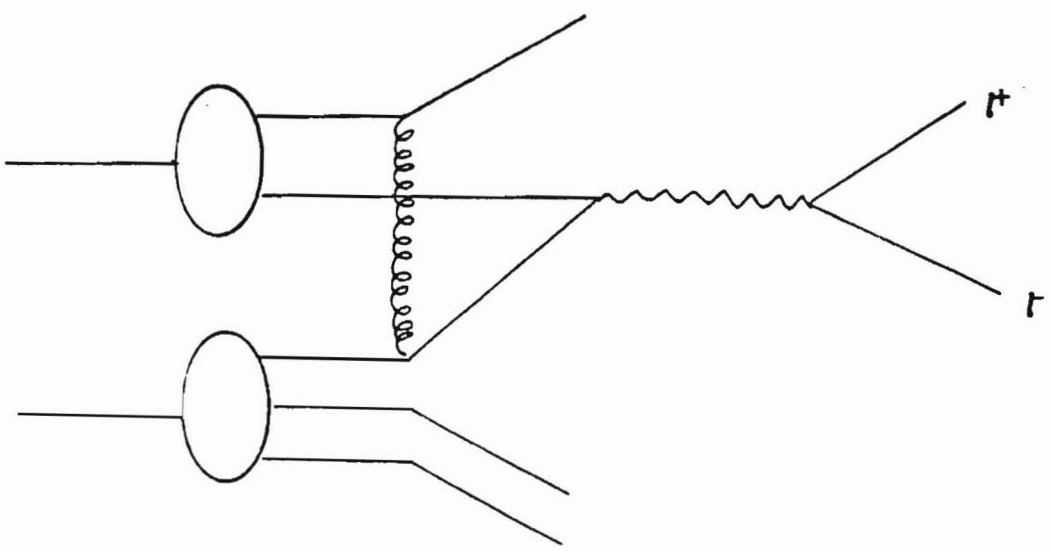
l^+
l^-

Figure 8 -- Plan and elevation views of the E615 experimental apparatus. A more detailed view of the spectrometer region is shown in figure 13.

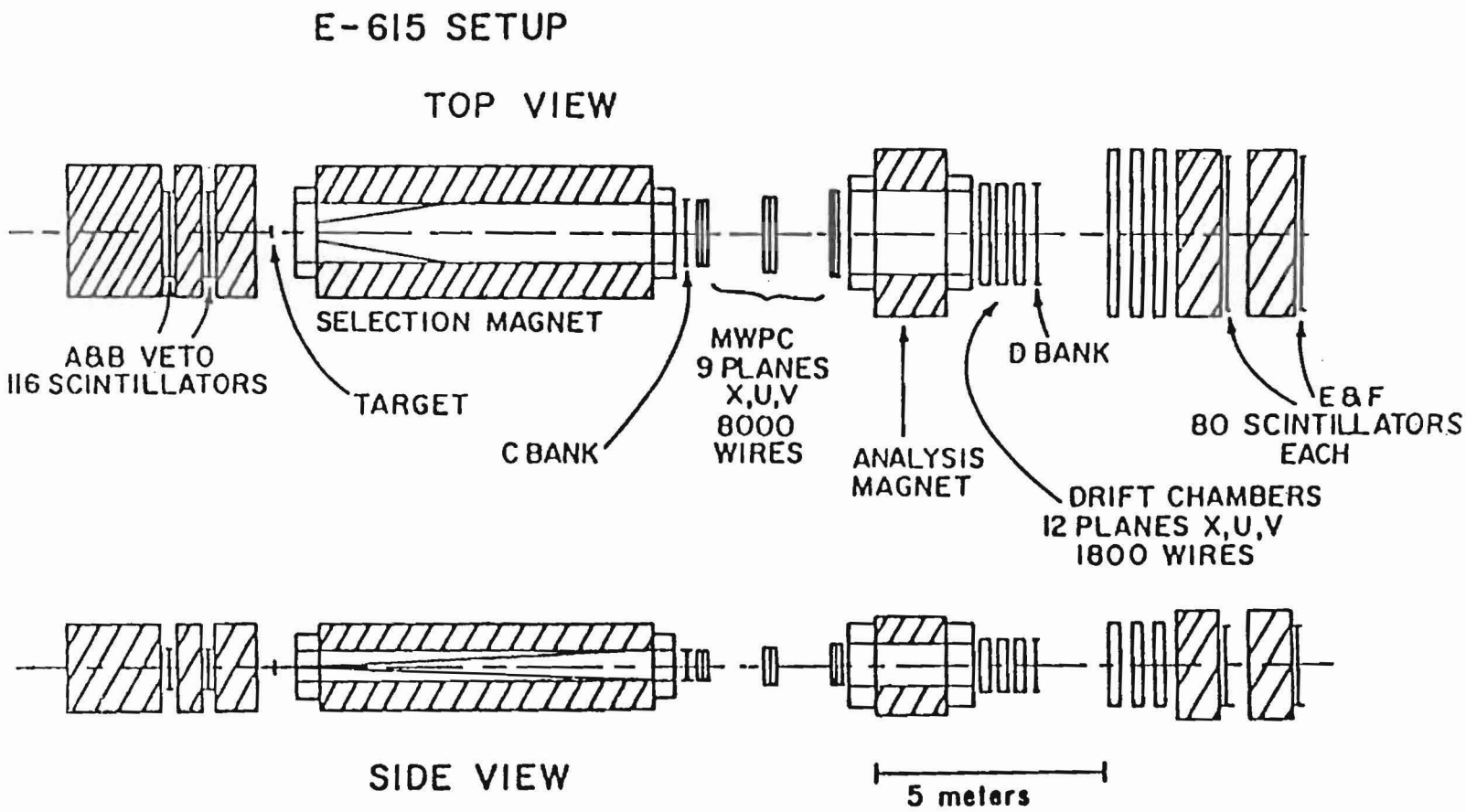
E-615 SETUP
TOP VIEW
A&B VETO
116 SCINTILLATORS
TARGET
SELECTION MAGNET
C BANK
MWPC
9 PLANES
X,U,V
8000
WIRES
ANALYSIS
MAGNET
D BANK
DRIFT CHAMBERS
12 PLANES X,U,V
1800 WIRES
E & F
80 SCINTILLATORS
EACH
SIDE VIEW
5 meters

Figure 9 -- Plan view of the selection magnet.

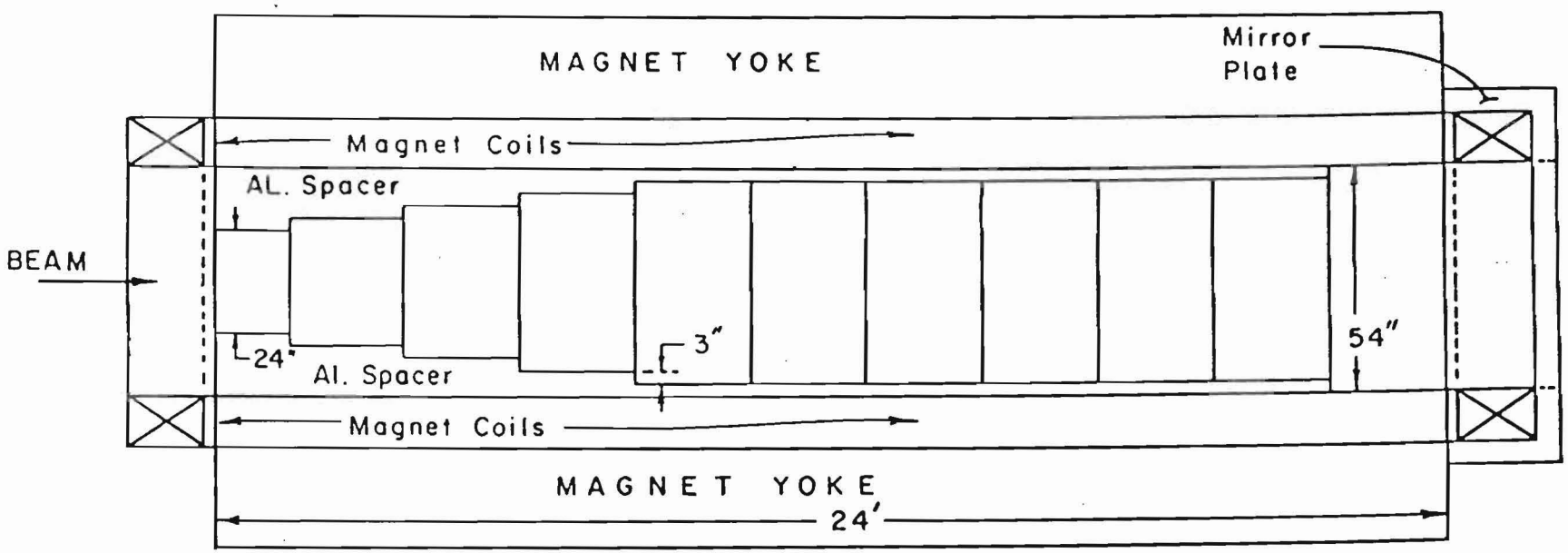
MAGNET YOKE
Mirror Plate
Magnet Coils
AL. Spacer
BEAM
24"
Al. Spacer
3"
54"
Magnet Coils
MAGNET YOKE
24'

Figure 10 -- Elevation view of the selection magnet, with the beryllium and carbon absorber labelled.

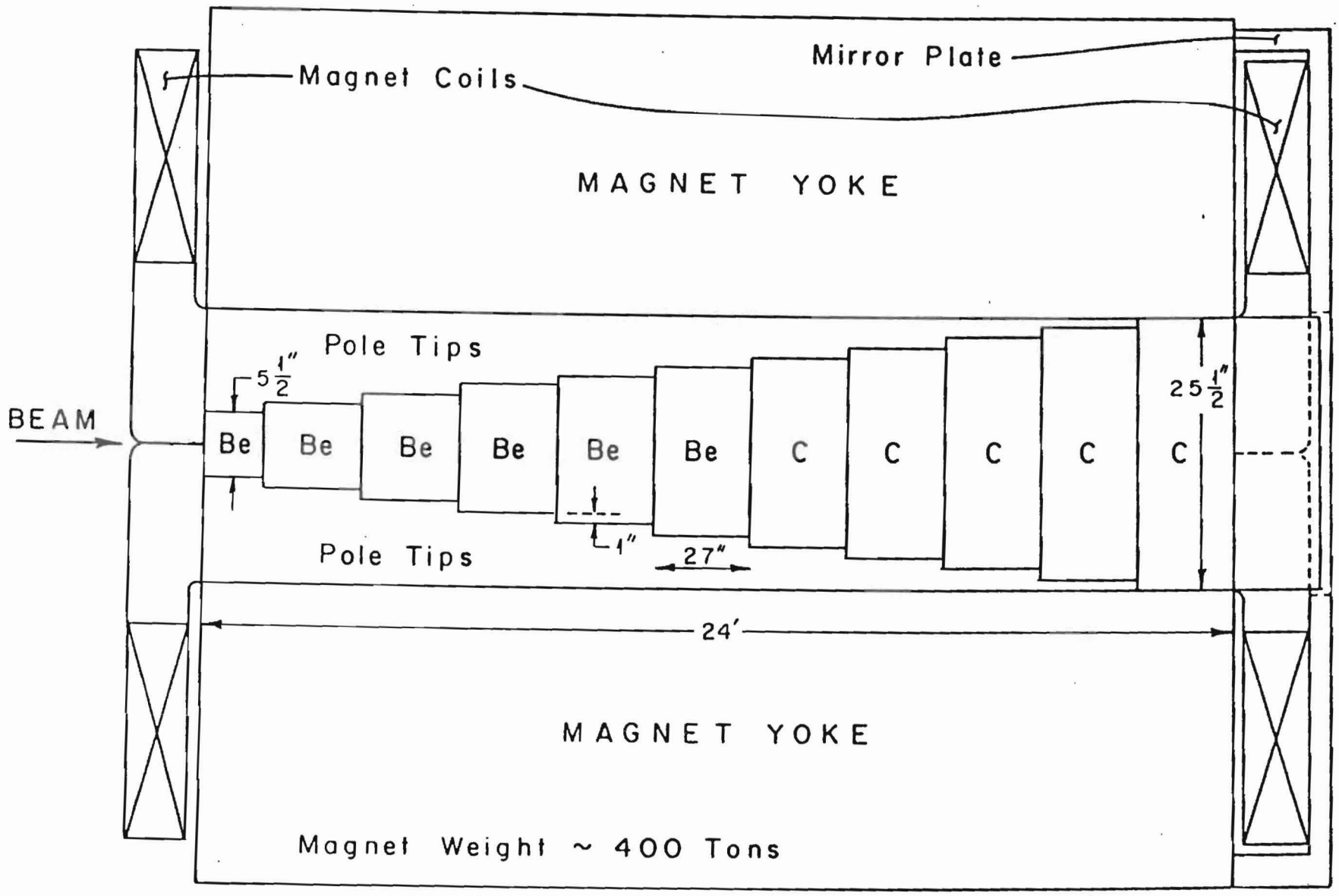
Mirror Plate
Magnet Coils
MAGNET YOKE
Pole Tips
5 1/2"
BEAM
Be
Be
Be
Be
Be
Be
C
C
C
C
C
25 1/2"
1"
27"
Pole Tips
24'
MAGNET YOKE
Magnet Weight ~ 400 Tons

Figure 11 -- Vertical field strength (B_y) in the selection magnet as a function of z along the central axis, x=0, y=0. B is in gauss, and z is in inches; z=0 at the upstream face of the magnet. Arrows indicate upstream and downstream edges of the magnet.

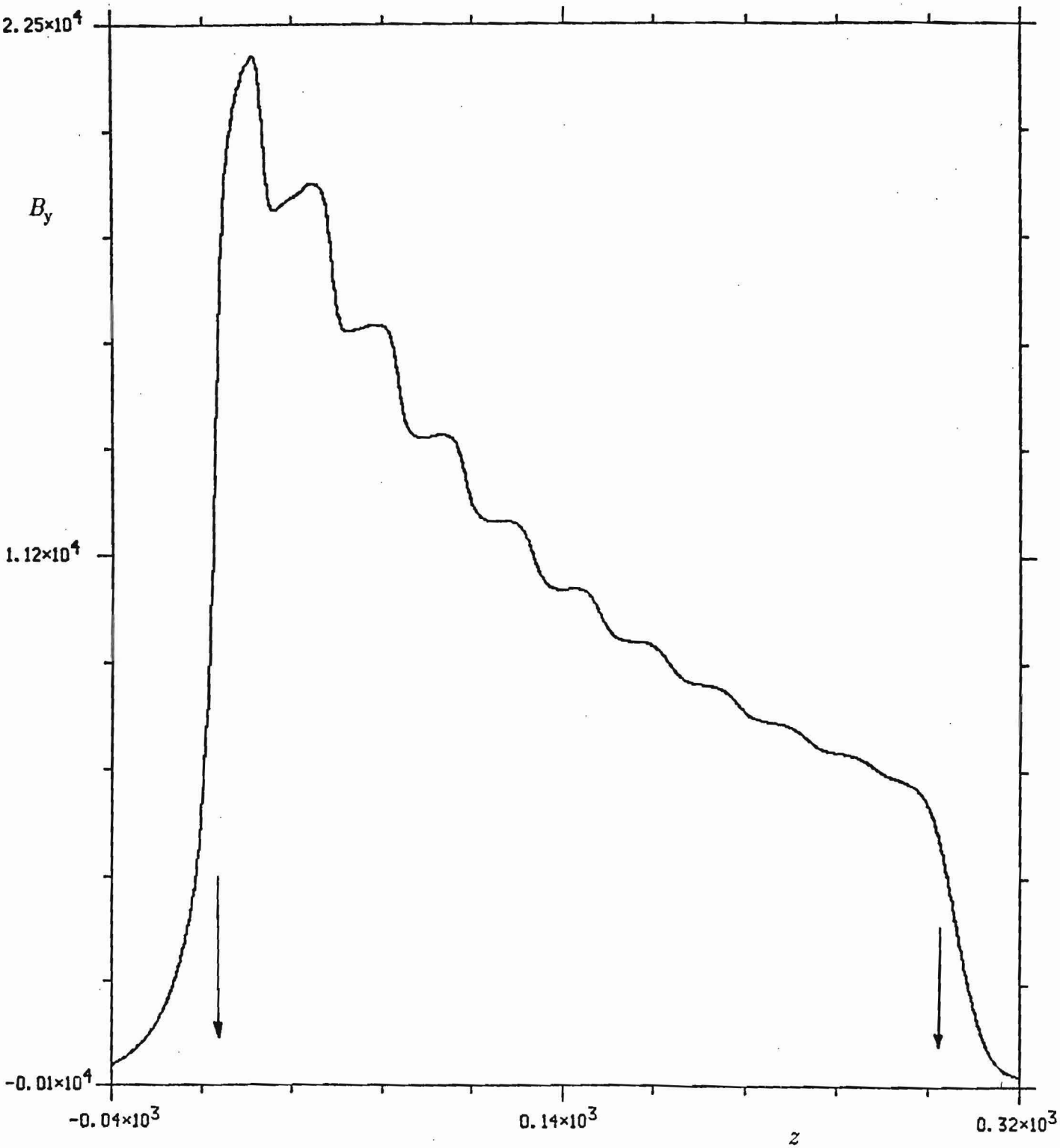
2.25×10^4
1.12×10^4
-0.01×10^4
B_y
-0.04×10^3
0.14×10^3
0.32×10^3
z

Figure 12 -- Vertical field strength (B_y) in the analysis magnet as a function of z. B is in kilogauss, z is in inches; z=0 at the center of the magnet. Arrows indicate center and edge of magnet.

× y=+0.0"
+ y=+4.0"
□ y=+9.5"
◇ y=+13.3"

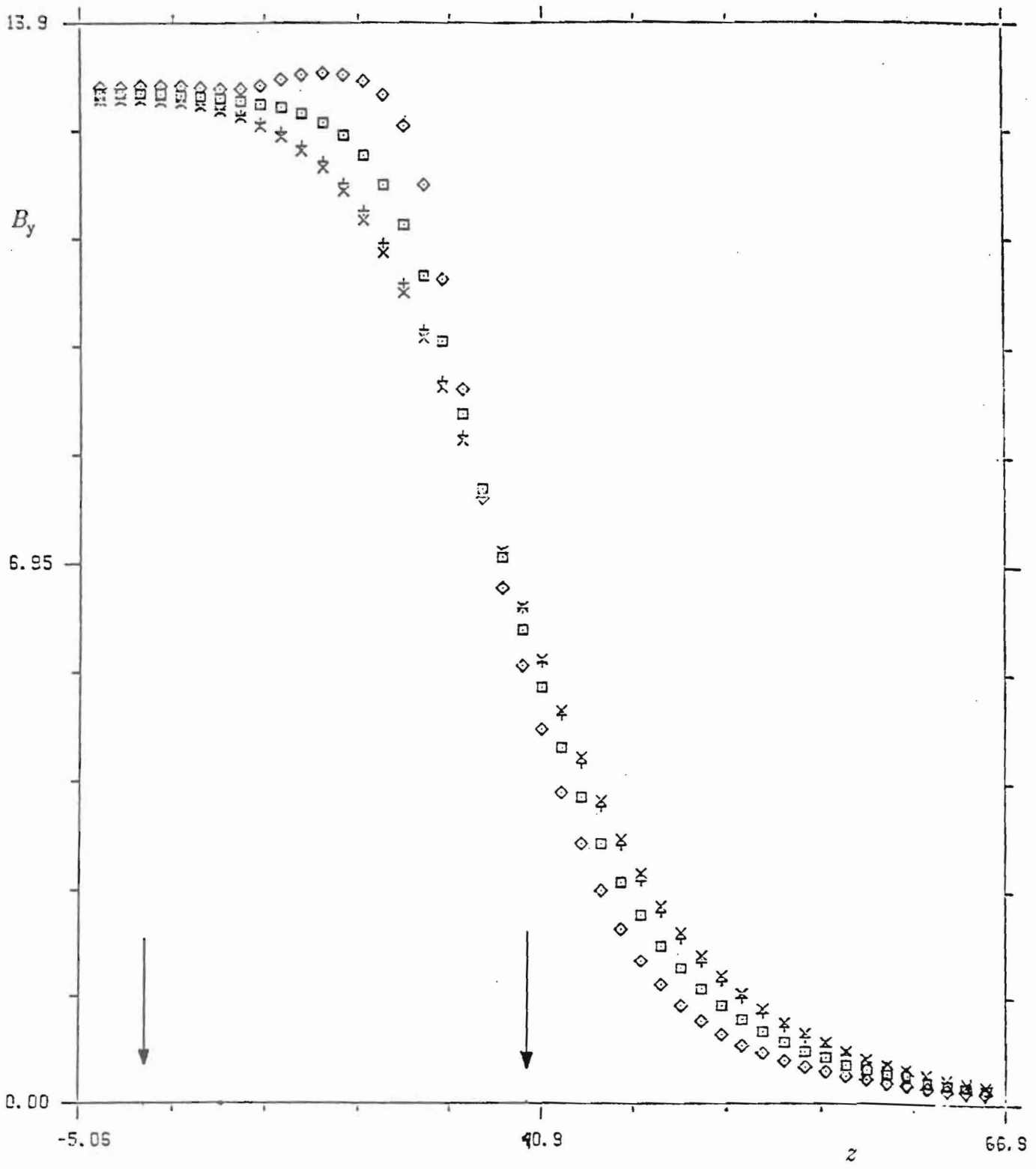
13.9
B_y
6.95
0.00
-5.06
40.9
66.9
z

Figure 13 -- Plan view of the spectrometer region indicating the layout of chambers and hodoscope planes. A typical event is superimposed.

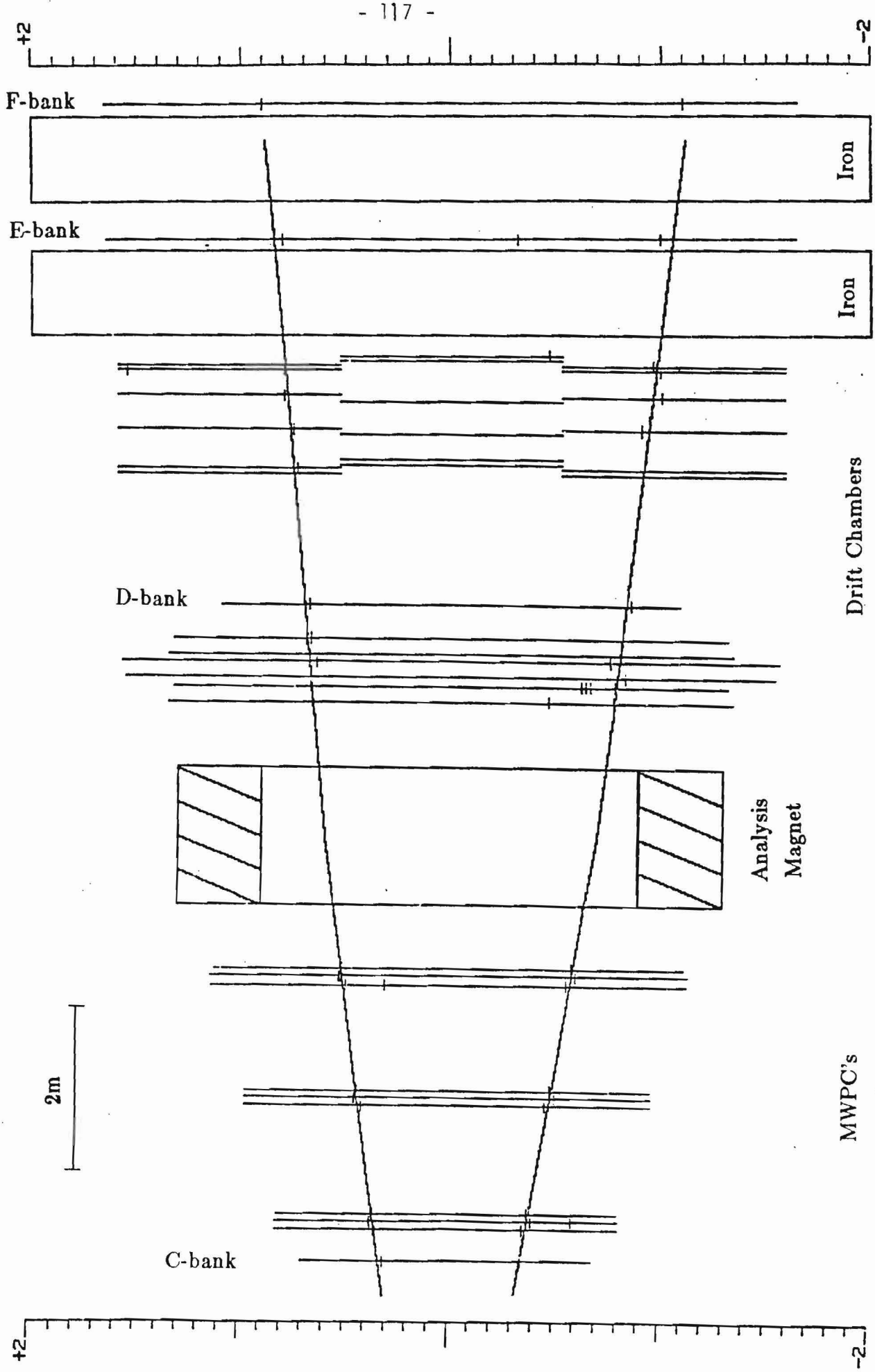
+2
-2
F-bank
Iron
E-bank
Iron
Drift Chambers
D-bank
Analysis
Magnet
MWPC's
2m
C-bank
+2
-2

Figure 14 -- Upper diagram shows layout of the high voltage MWPC cathode plane; lower diagram shows layout of MWPC anode wires. See text (§2.6.1) for details.

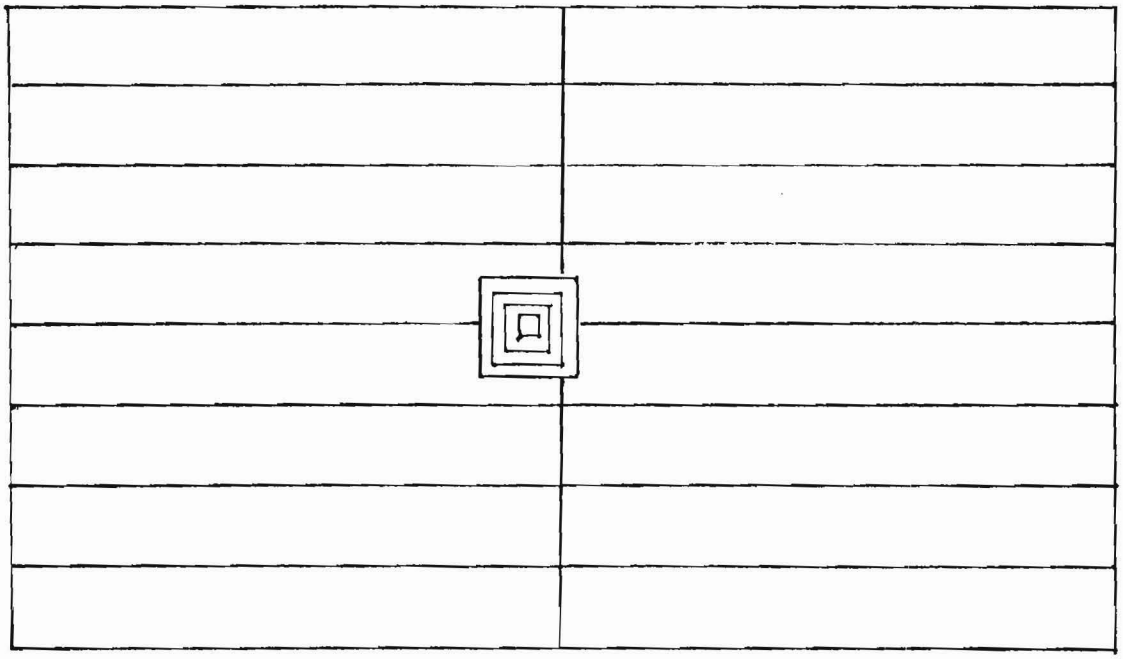

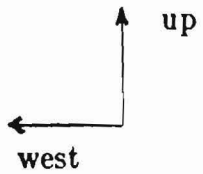
up
west

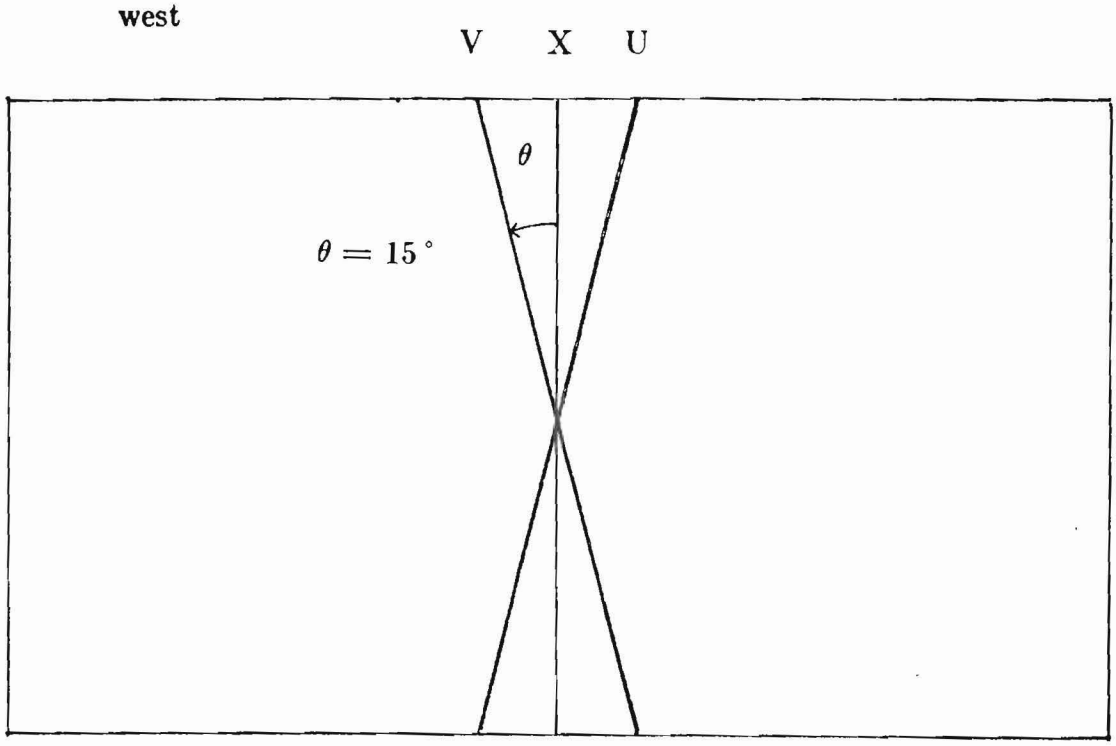
V
X
U
θ
θ = 15°

Figure 15 -- Organization of the MWPC readout electronics. See text (§2.6.2) for details.

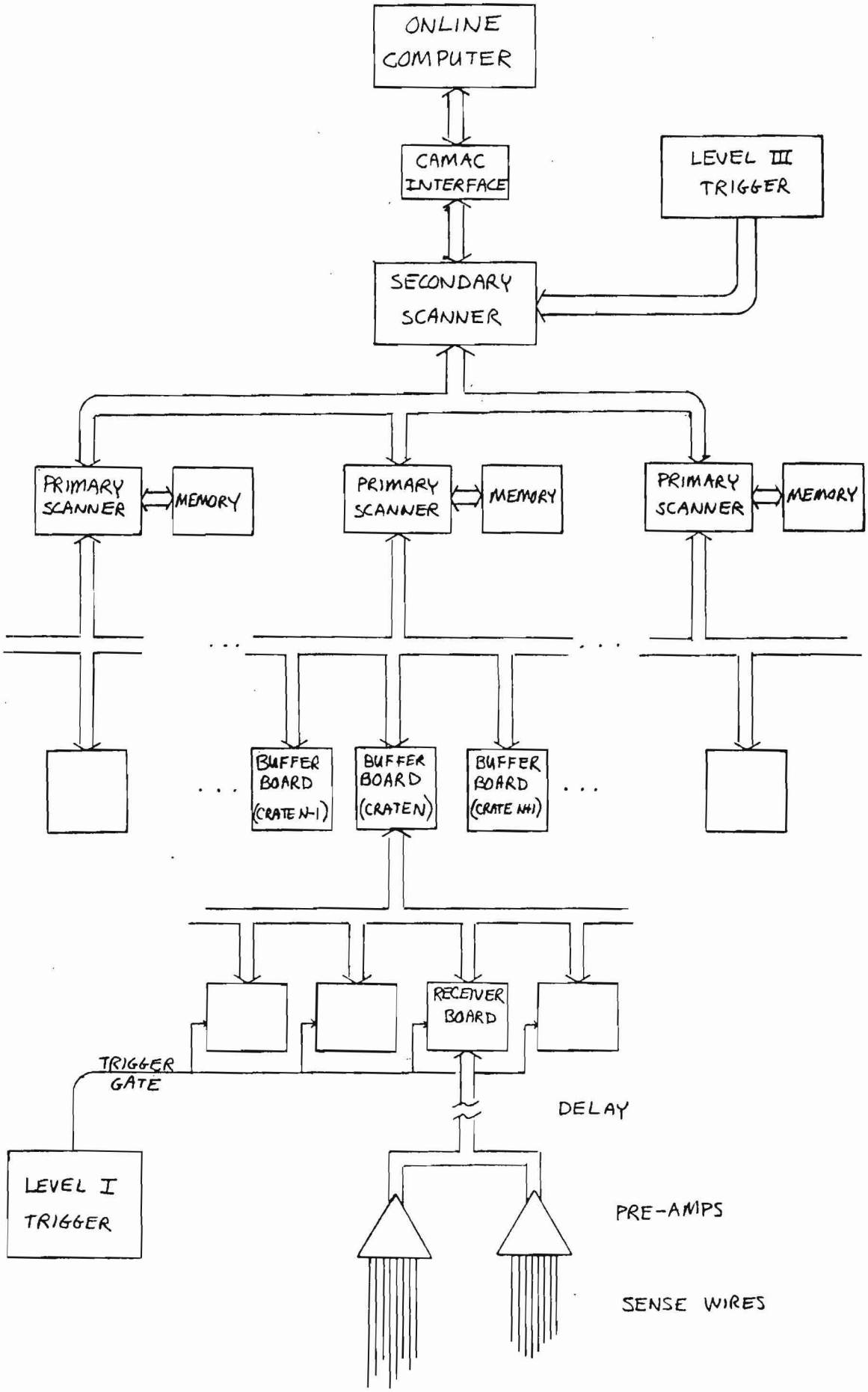
ONLINE COMPUTER
CAMAC INTERFACE
LEVEL III TRIGGER
SECONDARY SCANNER
PRIMARY SCANNER
MEMORY
PRIMARY SCANNER
MEMORY
PRIMARY SCANNER
MEMORY
BUFFER BOARD (CRATE N-1)
BUFFER BOARD (CRATE N)
BUFFER BOARD (CRATE N+1)
RECEIVER BOARD
TRIGGER GATE
DELAY
LEVEL I TRIGGER
PRE-AMPS
SENSE WIRES

Figure 16 -- Perspective drawing of hodoscope trigger planes with typical event superimposed. The CY, DY, E, and F banks are each required to have either 2 nonadjacent hits, or 3 or more. Details of the trigger are covered in §2.9.

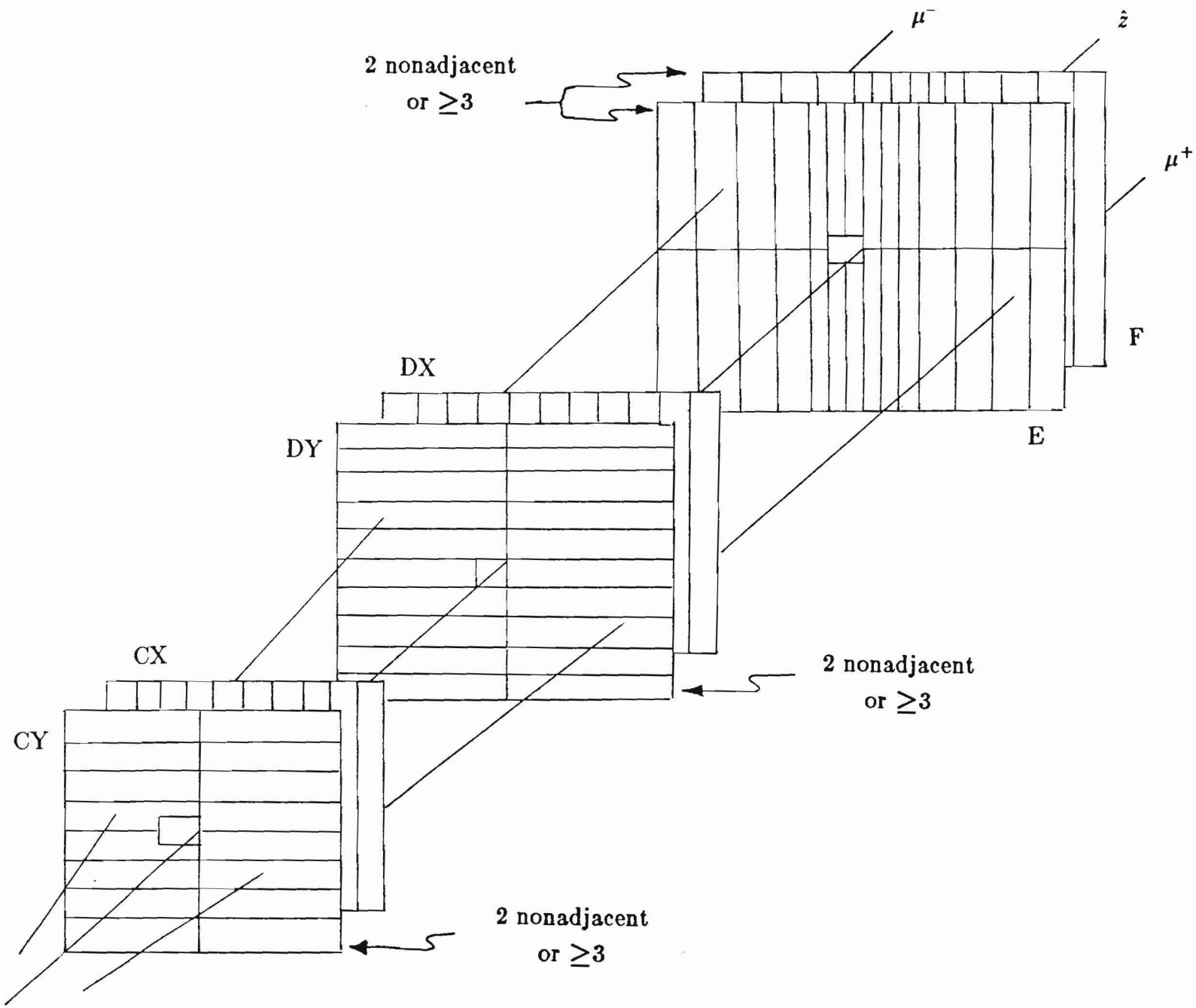
μ^-
$\hat{z}$
2 nonadjacent
or ≥ 3
μ^+
F
DX
DY
E
CX
2 nonadjacent
or ≥ 3
CY
2 nonadjacent
or ≥ 3

Figure 17 -- Diagram of the C hodoscope bank indicating the arrangement and sizes of counters. Upper drawing shows CX, lower shows CY. View is looking downstream.

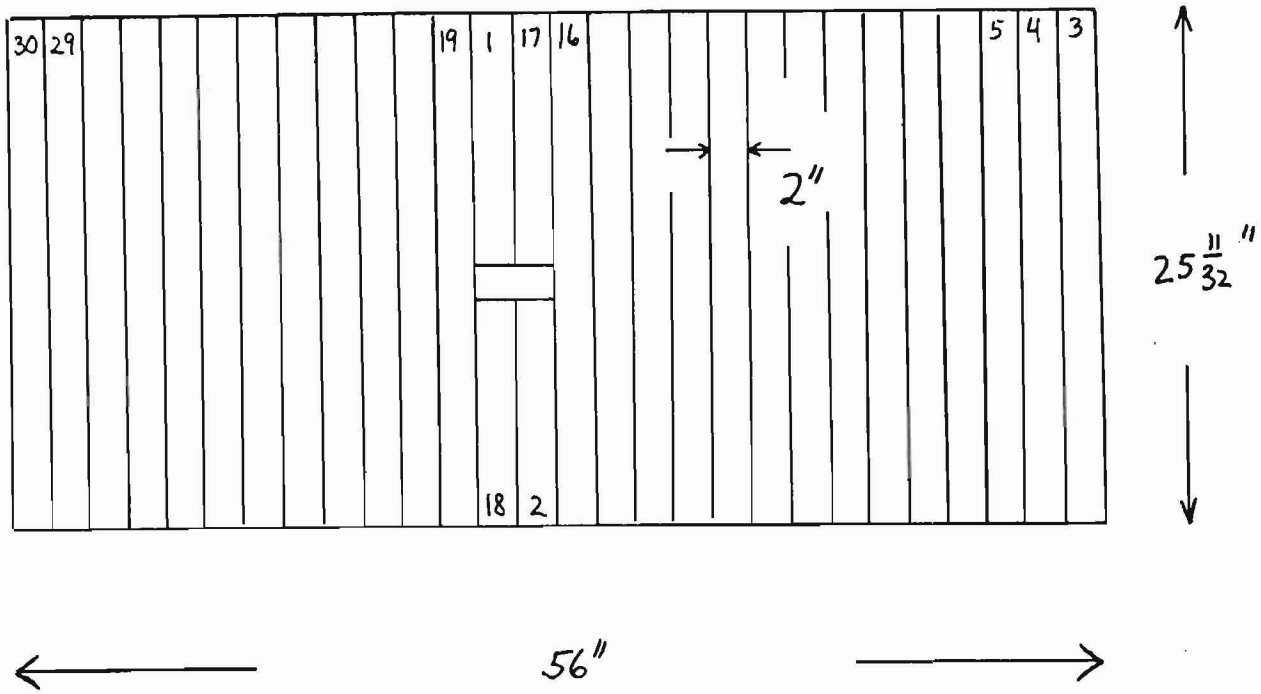
30
29
19
1
17
16
5
4
3
18
2
2"
25 11/32"
56"

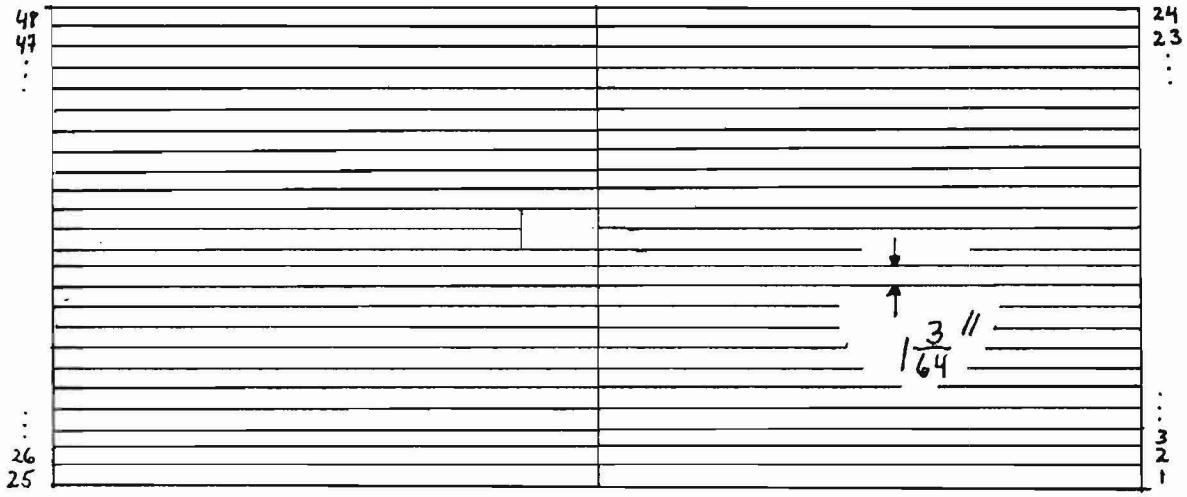
48
47
26
25
24
23
3
2
1
1 3/64"

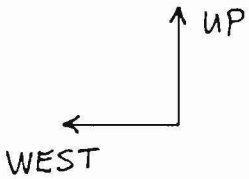
UP
WEST

Figure 18 -- Diagram of the D hodoscope bank indicating the arrangement and sizes of counters. Upper drawing shows DX, lower shows DY. View is looking downstream.

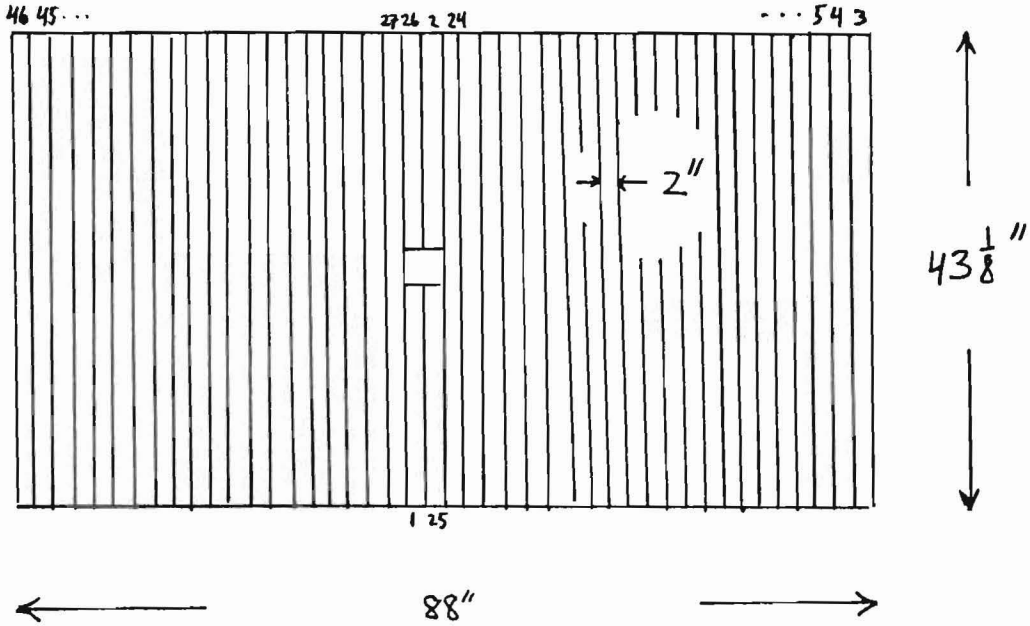
46 45 . . .
27 26 2 24
. . . 5 4 3
2"
43 1/8"
1 25
88"

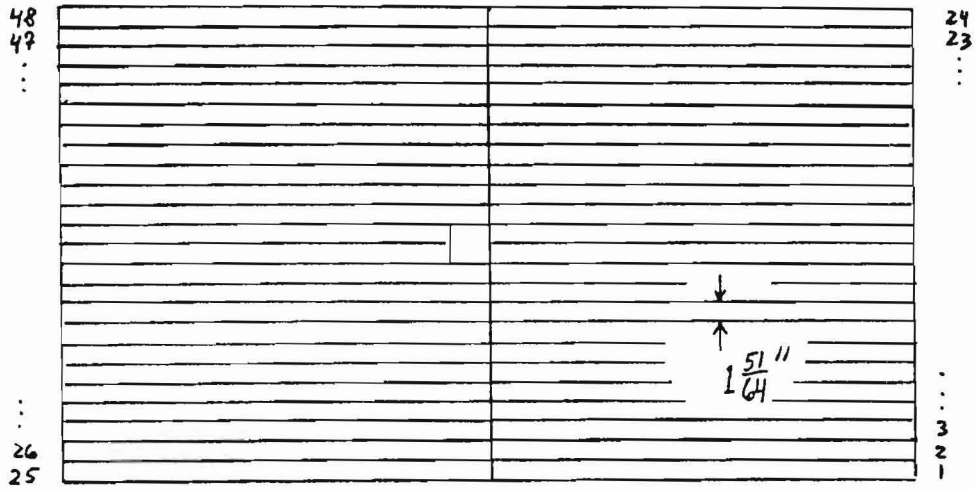
48
47
24
23
1 51/64"
26
25
3
2
1

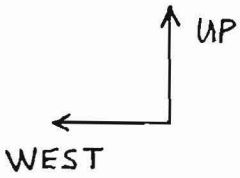
UP
WEST

Figure 19 -- Diagram of the E and F banks indicating the arrangement and sizes of counters. Note that the central region has narrower counters; this improves the acceptance for high-x events by reducing losses to the nonadjacency requirement. View is looking downstream.

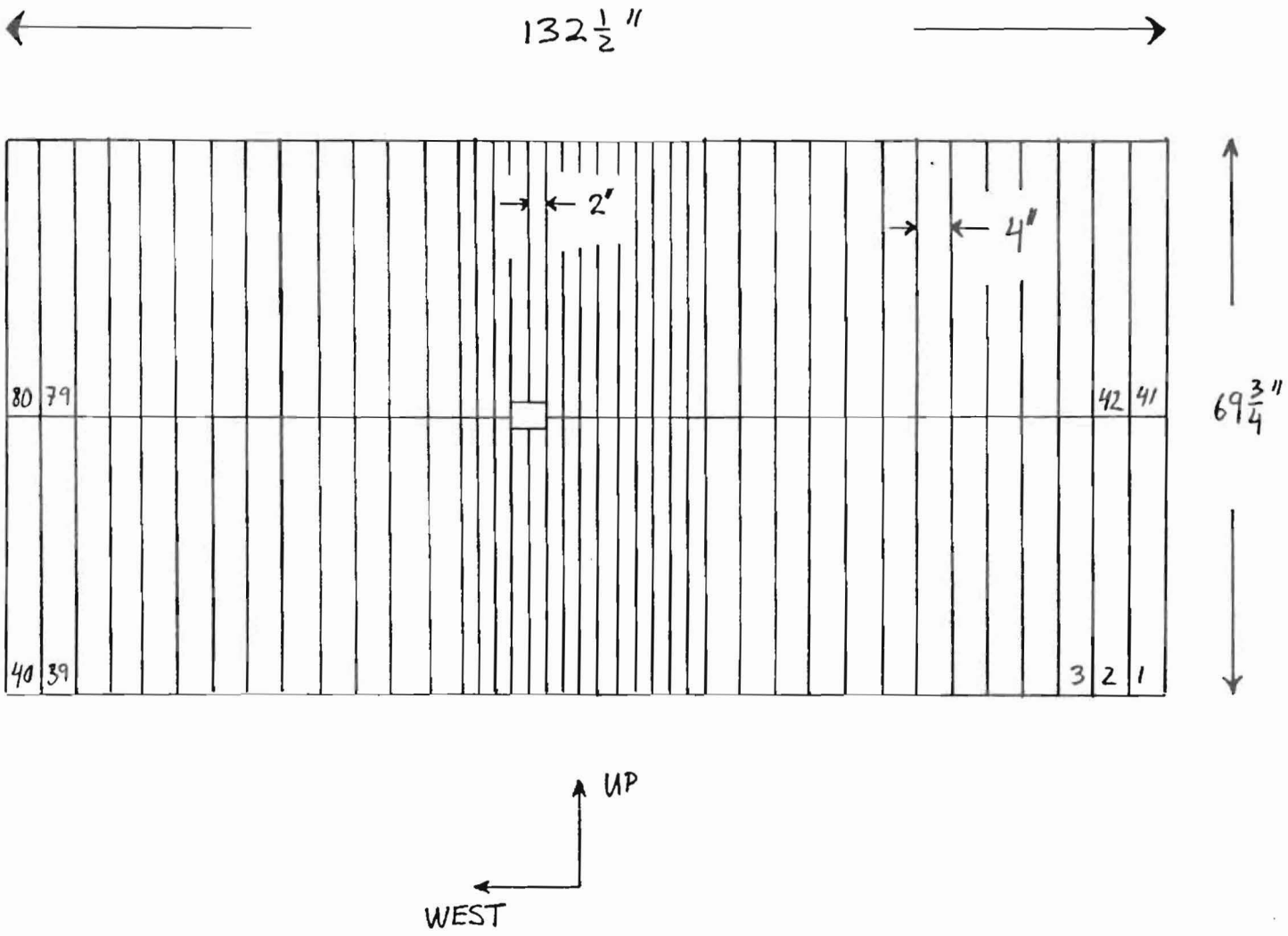
132 1/2"
2"
4"
69 3/4"
80
79
42
41
40
39
3
2
1
UP
WEST

Figure 20 -- Plot of θ_x vs. p at the target, before halo cut. Each dot represents one track (hence, two dots per event). The enhancement on the left is due to muons in the beam; the enhancement in the upper middle region is due to the decay of secondary π^+ and K^+.

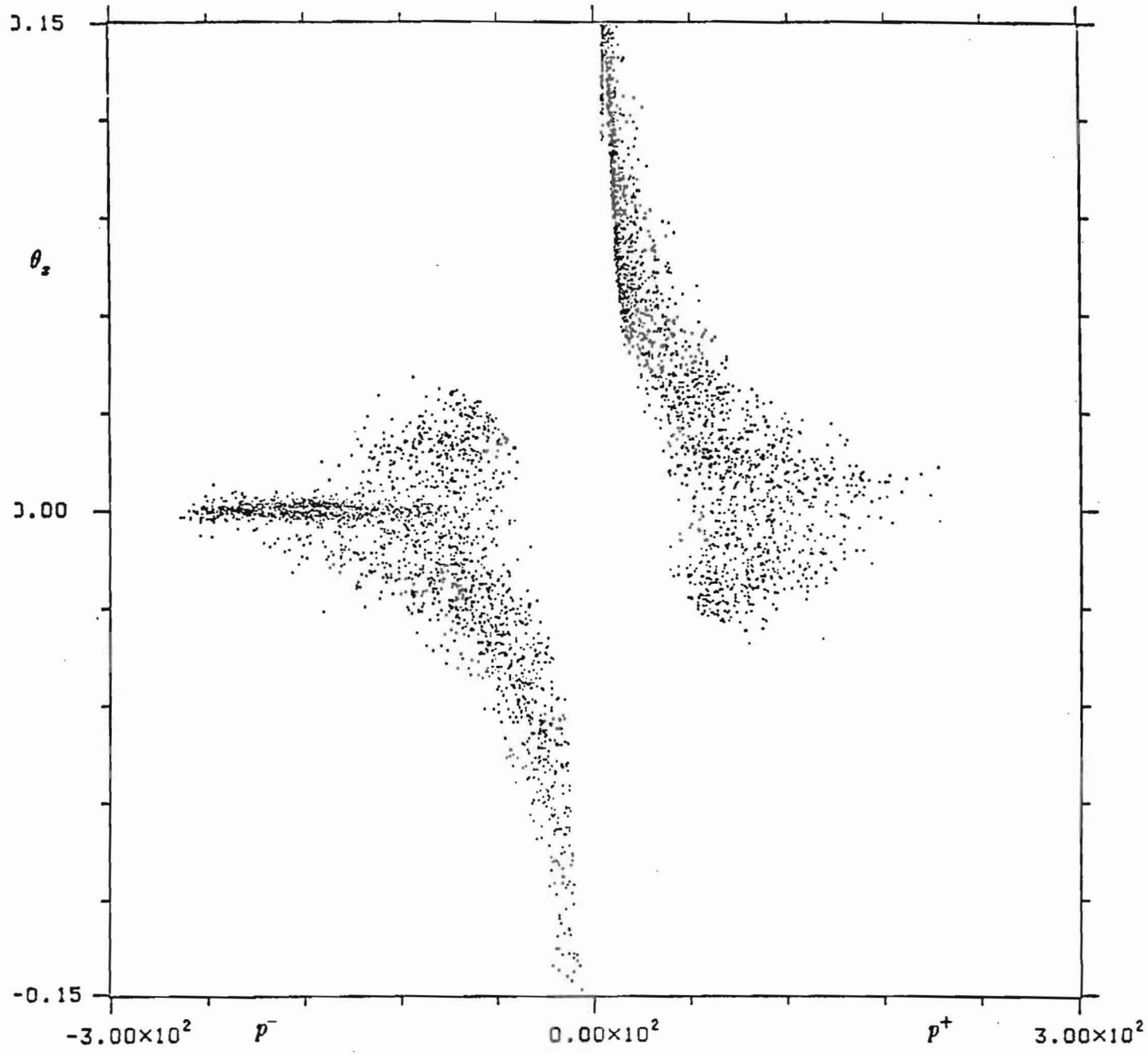
0.15
θ_z
0.00
-0.15
-3.00×10²
p^-
0.00×10²
p^+
3.00×10²

Figure 21 -- Comparison of momentum spectra for positive tracks (solid line) and negative tracks (crosses) before halo cut. The enhancement of soft positive and stiff negative tracks stands out very clearly.

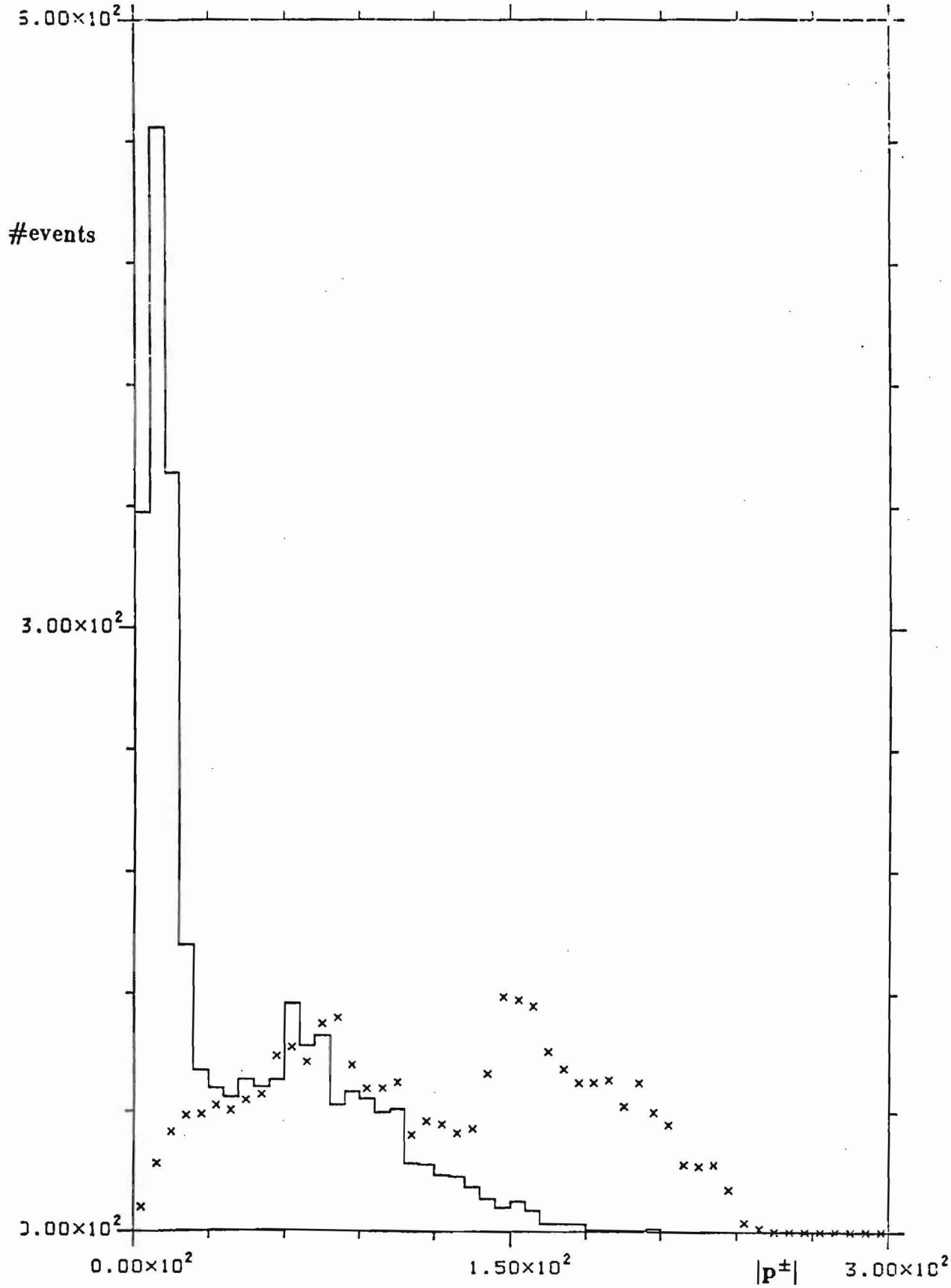
5.00×10²
#events
3.00×10²
0.00×10²
0.00×10²
1.50×10²
|p±|
3.00×10²

Figure 22 -- Illustration of the halo cut. See text (§3.2) for discussion.

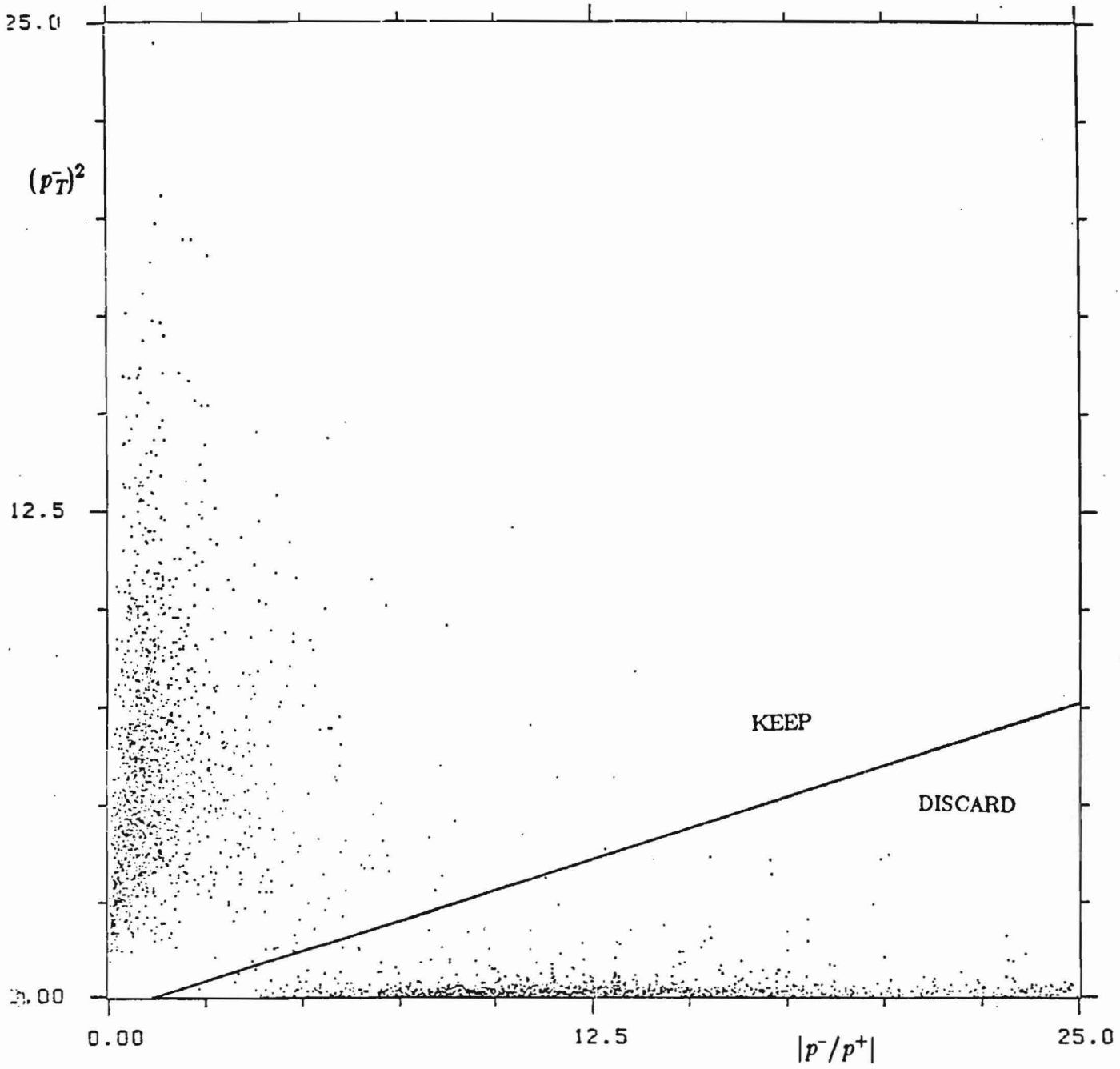
25.0
$(p_T^-)^2$
12.5
0.00
KEEP
DISCARD
0.00
12.5
25.0
$|p^-/p^+|$

Figure 23 -- Plot of θ_z vs. p after the halo cut.

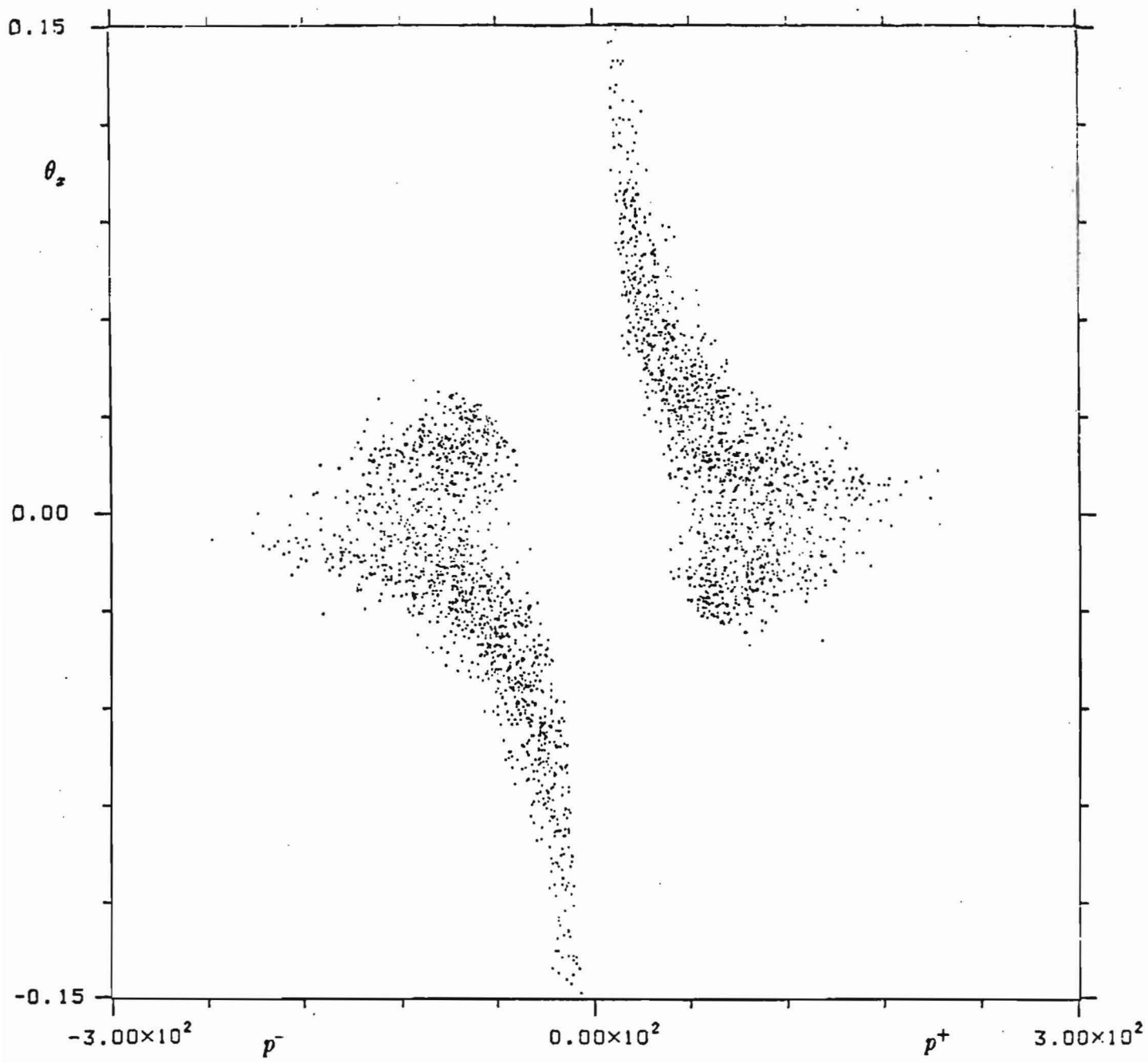
0.15
θ_x
0.00
-0.15
-3.00×10²
p^-
0.00×10²
p^+
3.00×10²

Figure 24 -- Comparison of momentum spectra after the halo cut.

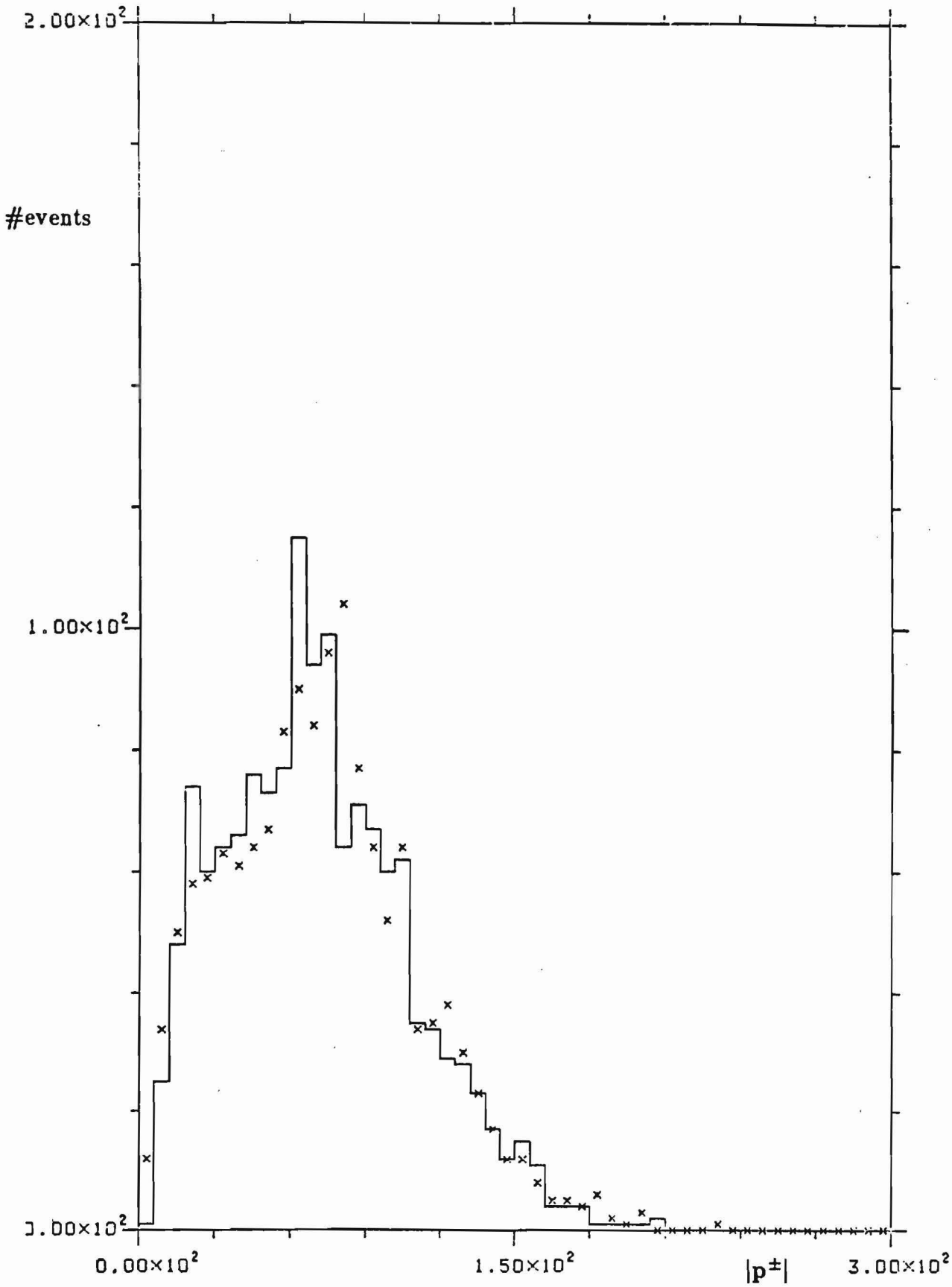
2.00×10²
#events
1.00×10²
0.00×10²
0.00×10²
1.50×10²
|p±|
3.00×10²

Figure 25 -- Comparison between Monte Carlo (solid line) and data (crosses) for x and y projections of the detector illumination.

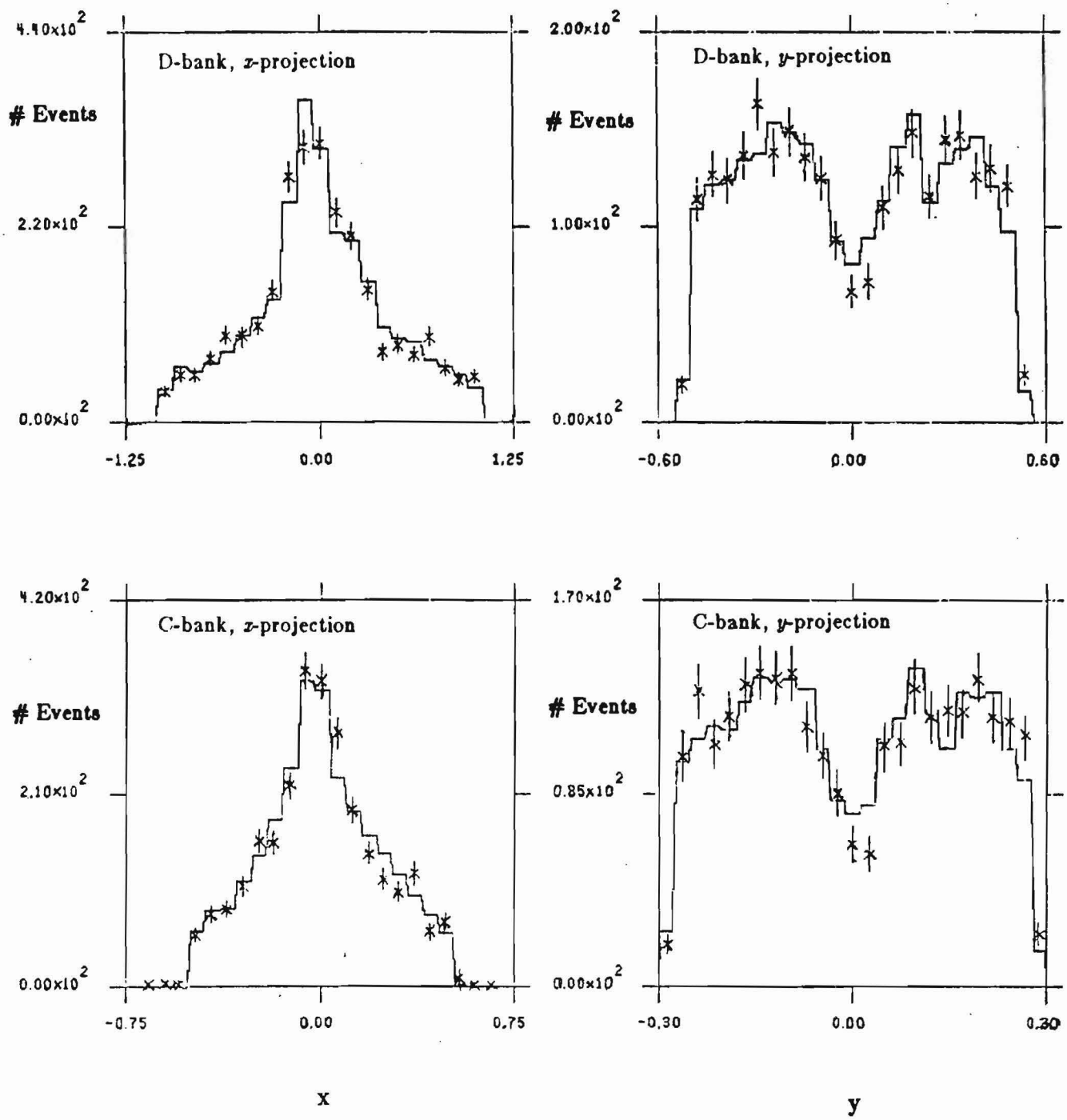
D-bank, x-projection
Events
4.40×10^2
2.20×10^2
0.00×10^2
-1.25
0.00
1.25
D-bank, y-projection
Events
2.00×10^2
1.00×10^2
0.00×10^2
-0.60
0.00
0.60
C-bank, x-projection
Events
4.20×10^2
2.10×10^2
0.00×10^2
-0.75
0.00
0.75
C-bank, y-projection
Events
1.70×10^2
0.85×10^2
0.00×10^2
-0.30
0.00
0.30
x
y

Figure 26 -- Comparison between Monte Carlo (solid line) and data (crosses) in six different kinematic variables.

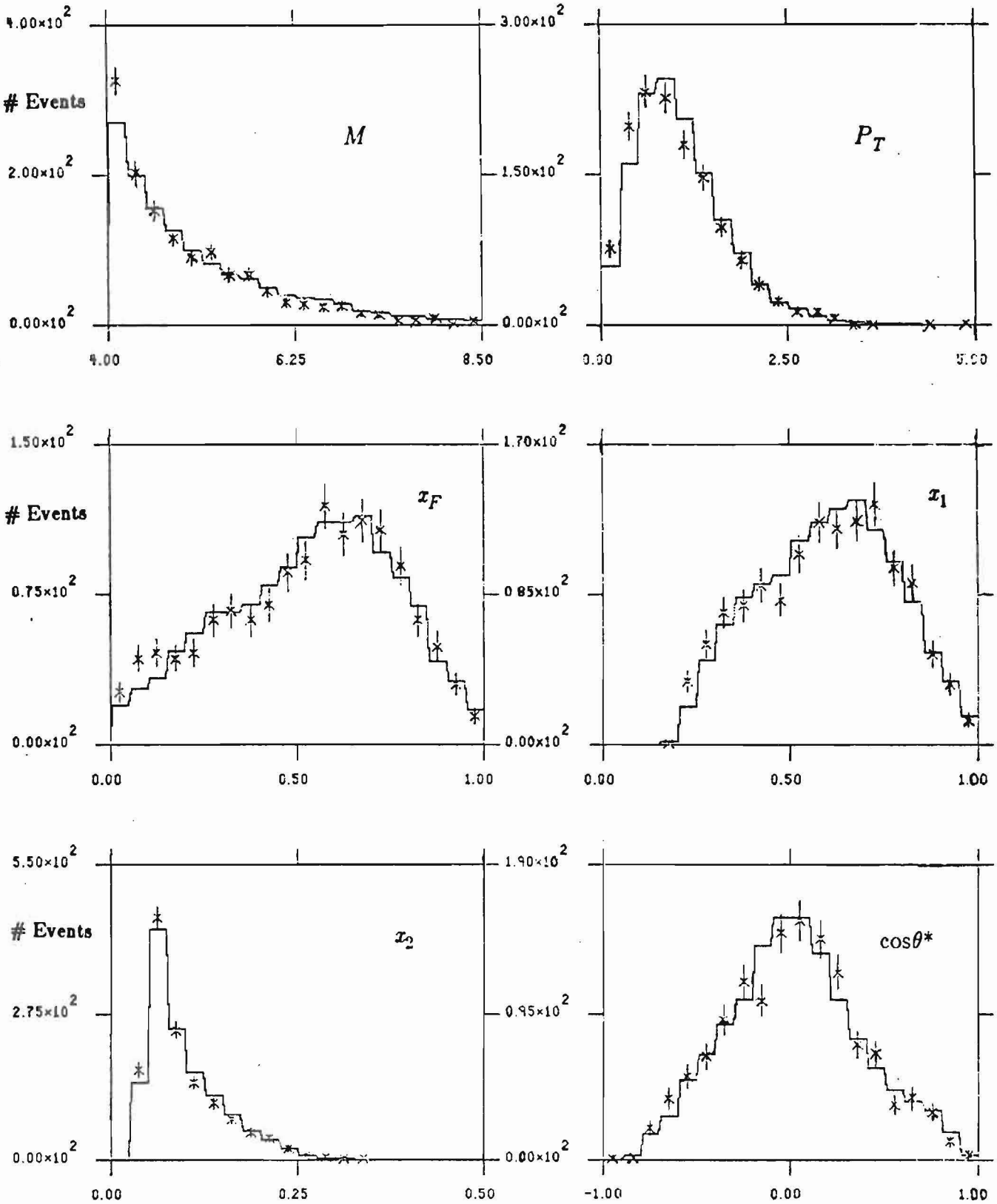
Events
M
P_T
x_F
x_1
x_2
$\cos\theta^*$
4.00×10^2
2.00×10^2
0.00×10^2
3.00×10^2
1.50×10^2
0.00×10^2
4.00
6.25
8.50
0.00
2.50
5.00
1.50×10^2
0.75×10^2
0.00×10^2
1.70×10^2
0.85×10^2
0.00×10^2
0.00
0.50
1.00
0.00
0.50
1.00
5.50×10^2
2.75×10^2
0.00×10^2
1.90×10^2
0.95×10^2
0.00×10^2
0.00
0.25
0.50
-1.00
0.00
1.00

Figure 27 -- Comparison between Monte Carlo (solid line) and data (crosses)

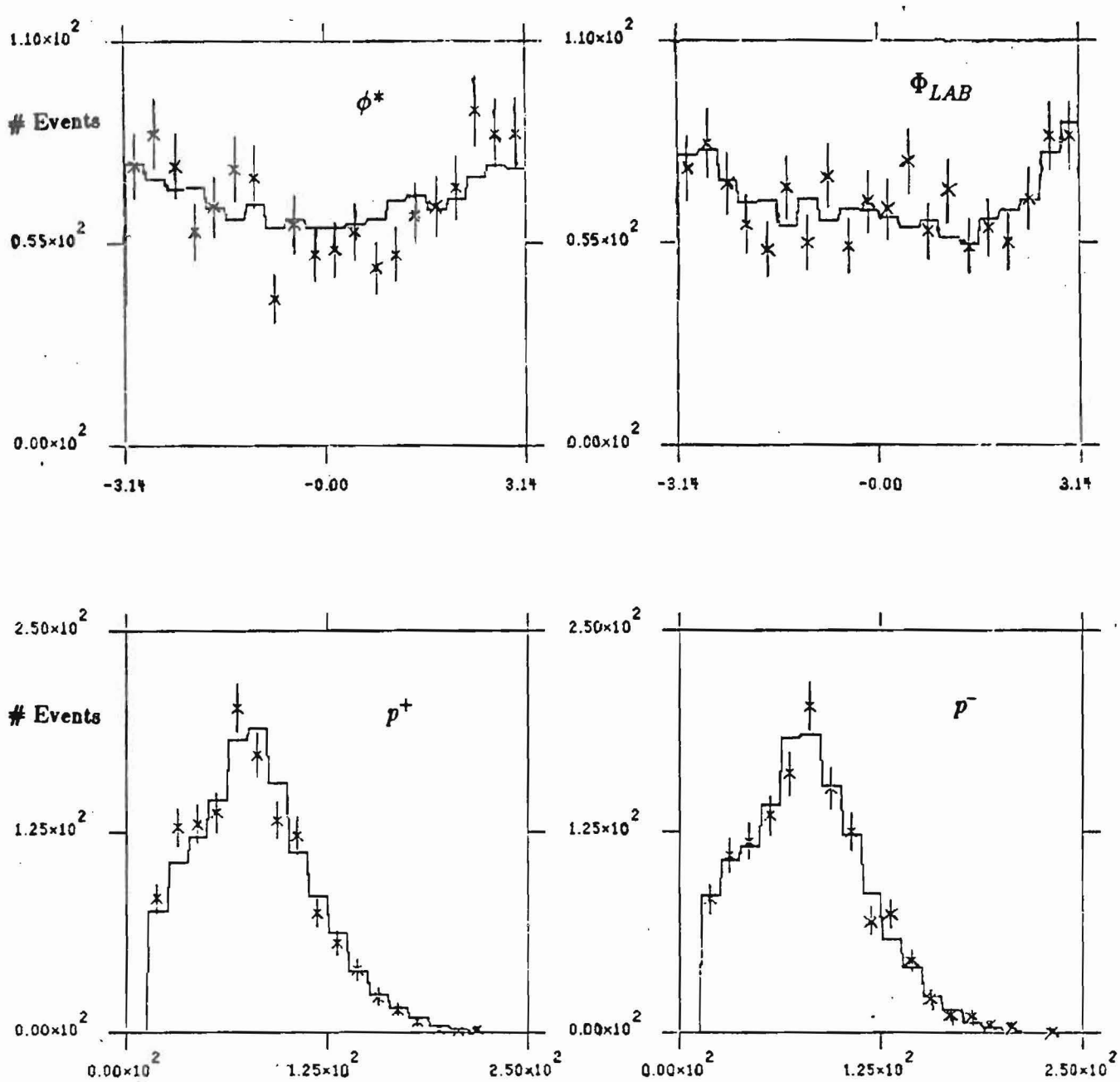
1.10×10^2
Events
0.55×10^2
0.00×10^2
-3.14
-0.00
3.14
φ*
Φ_LAB
2.50×10^2
1.25×10^2
0.00×10^2
p+
p-

Figure 28 -- Comparison between Monte Carlo (solid line) and data (crosses) for $\cos\theta^*$ in 4 bins of x_1.

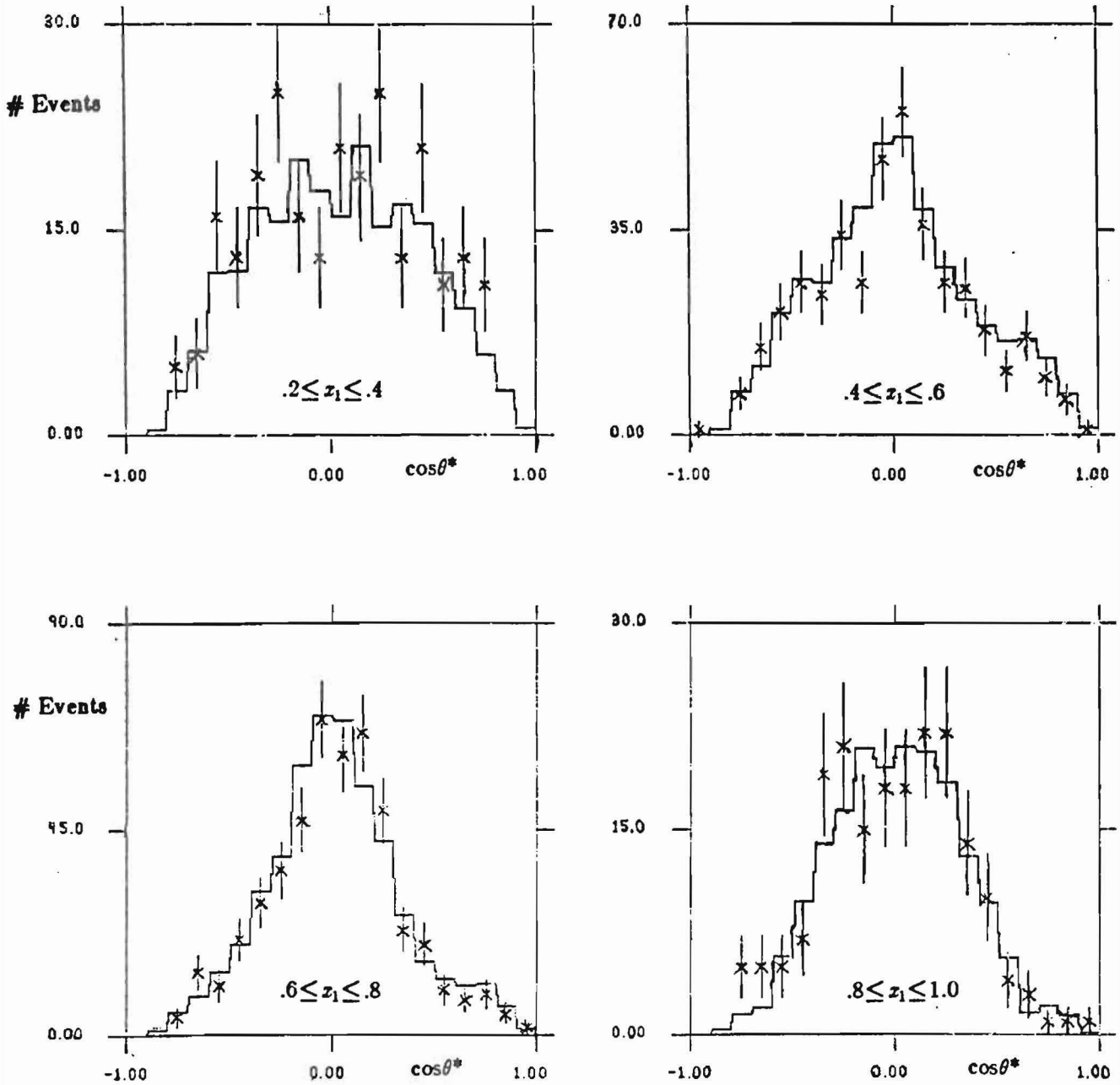
Events
30.0
15.0
0.00
-1.00
0.00
cosθ*
1.00
.2≤x₁≤.4
70.0
35.0
0.00
-1.00
0.00
cosθ*
1.00
.4≤x₁≤.6
Events
90.0
45.0
0.00
-1.00
0.00
cosθ*
1.00
.6≤x₁≤.8
30.0
15.0
0.00
-1.00
0.00
cosθ*
1.00
.8≤x₁≤1.0

Figure 29 -- Acceptance in Mass and P_T.

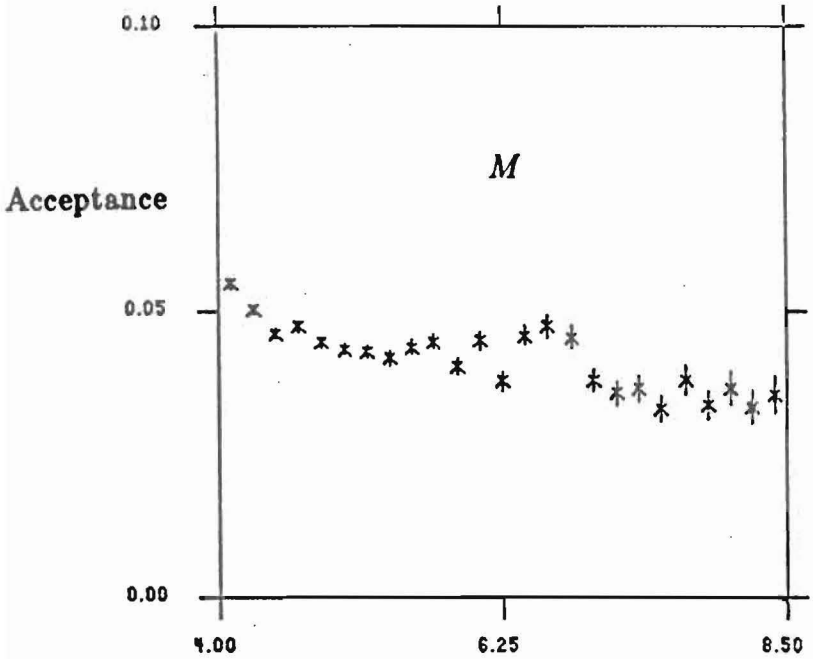
0.10
Acceptance
M
0.05
0.00
4.00
6.25
8.50

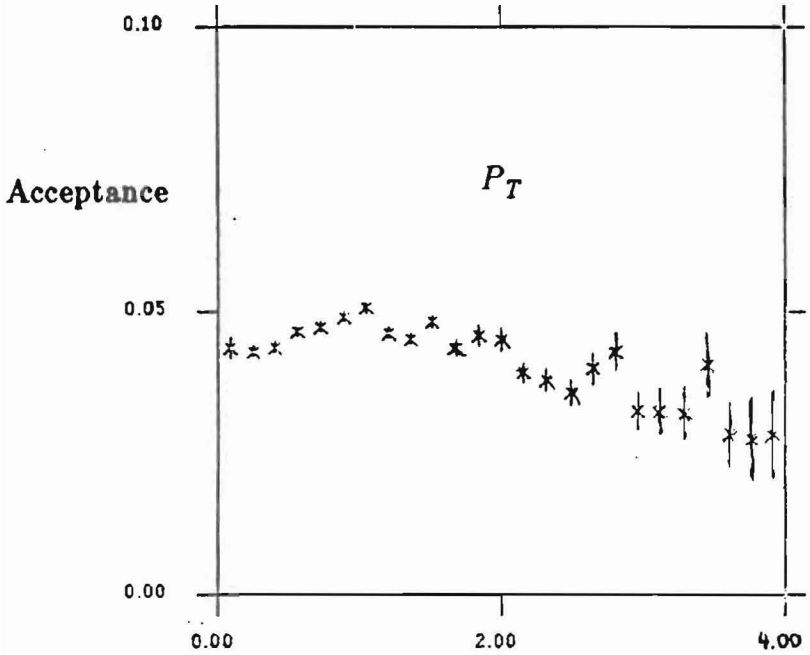
0.10
Acceptance
P_T
0.05
0.00
0.00
2.00
4.00

Figure 30 -- Acceptance in x_F and x_1.

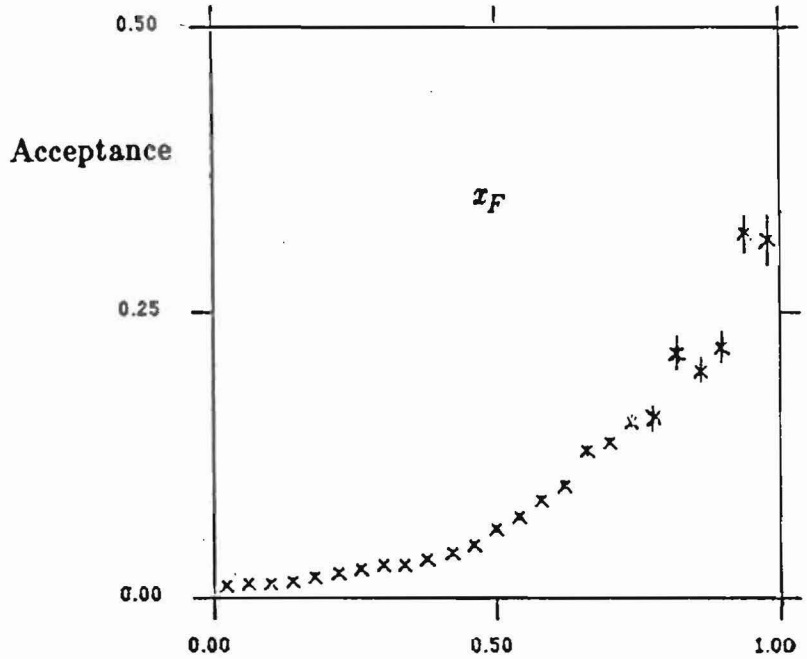
0.50
Acceptance
x_F
0.25
0.00
0.00
0.50
1.00

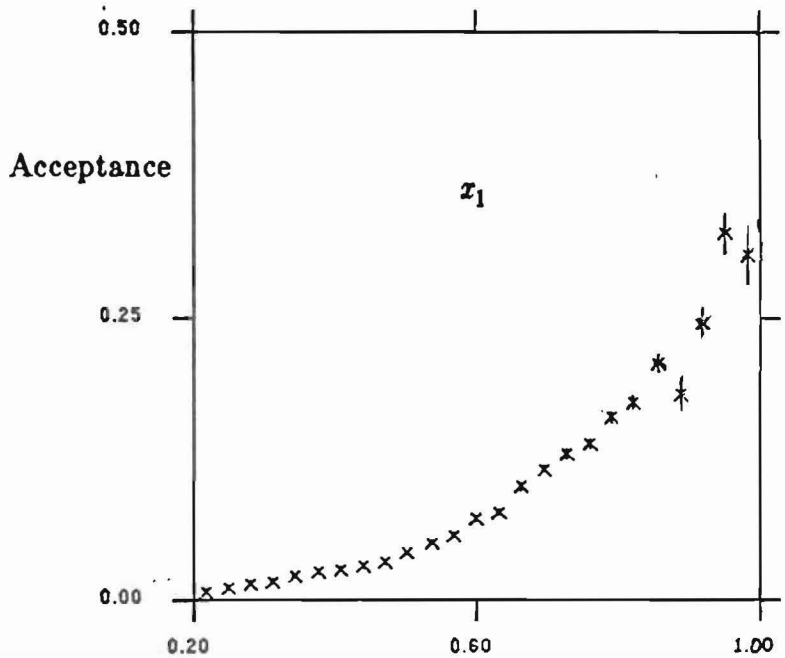
0.50
Acceptance
x_1
0.25
0.00
0.20
0.60
1.00

Figure 31 -- Acceptance in ϕ^* and Φ_{LAB}.

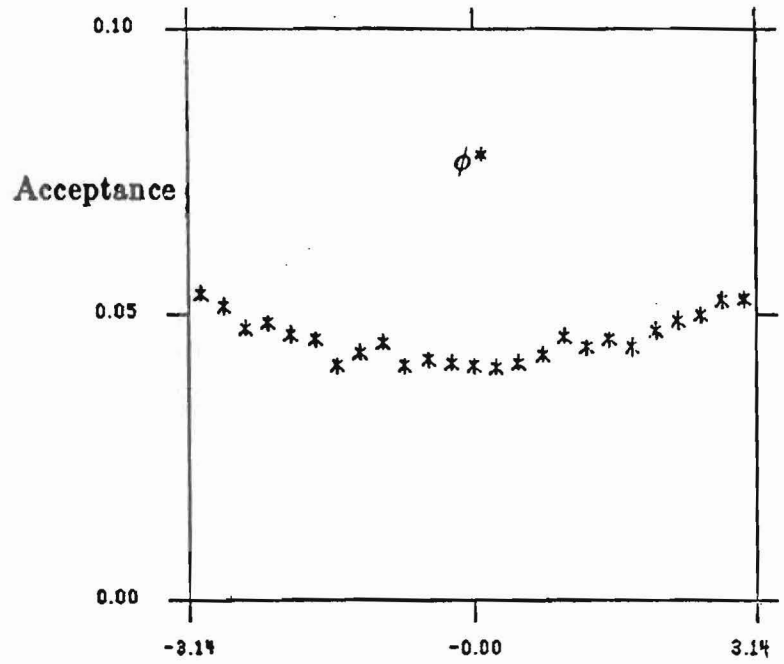
0.10
Acceptance
ϕ^*
0.05
0.00
-3.14
-0.00
3.14

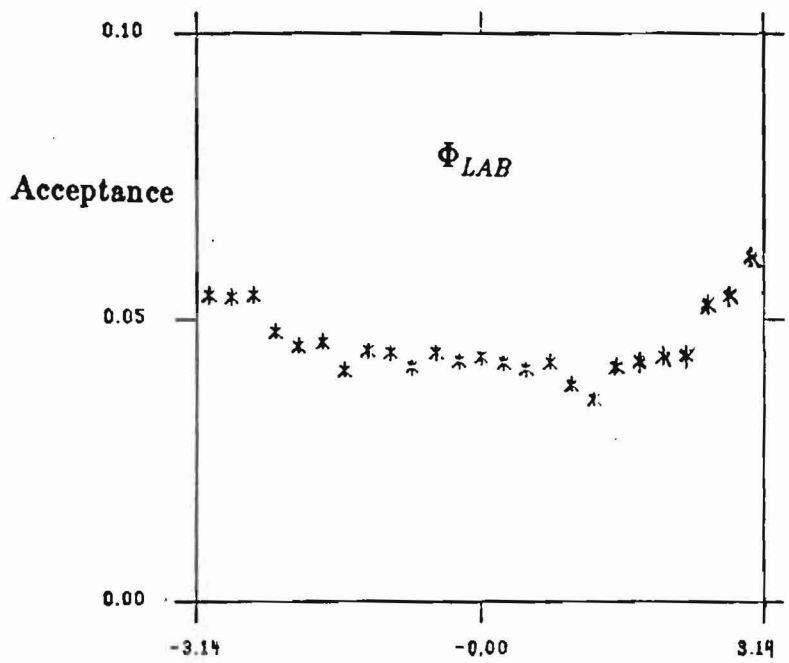
0.10
Acceptance
Φ_{LAB}
0.05
0.00
-3.14
-0.00
3.14

Figure 32 -- Acceptance in $\cos\theta^*$ in four helicity frames.

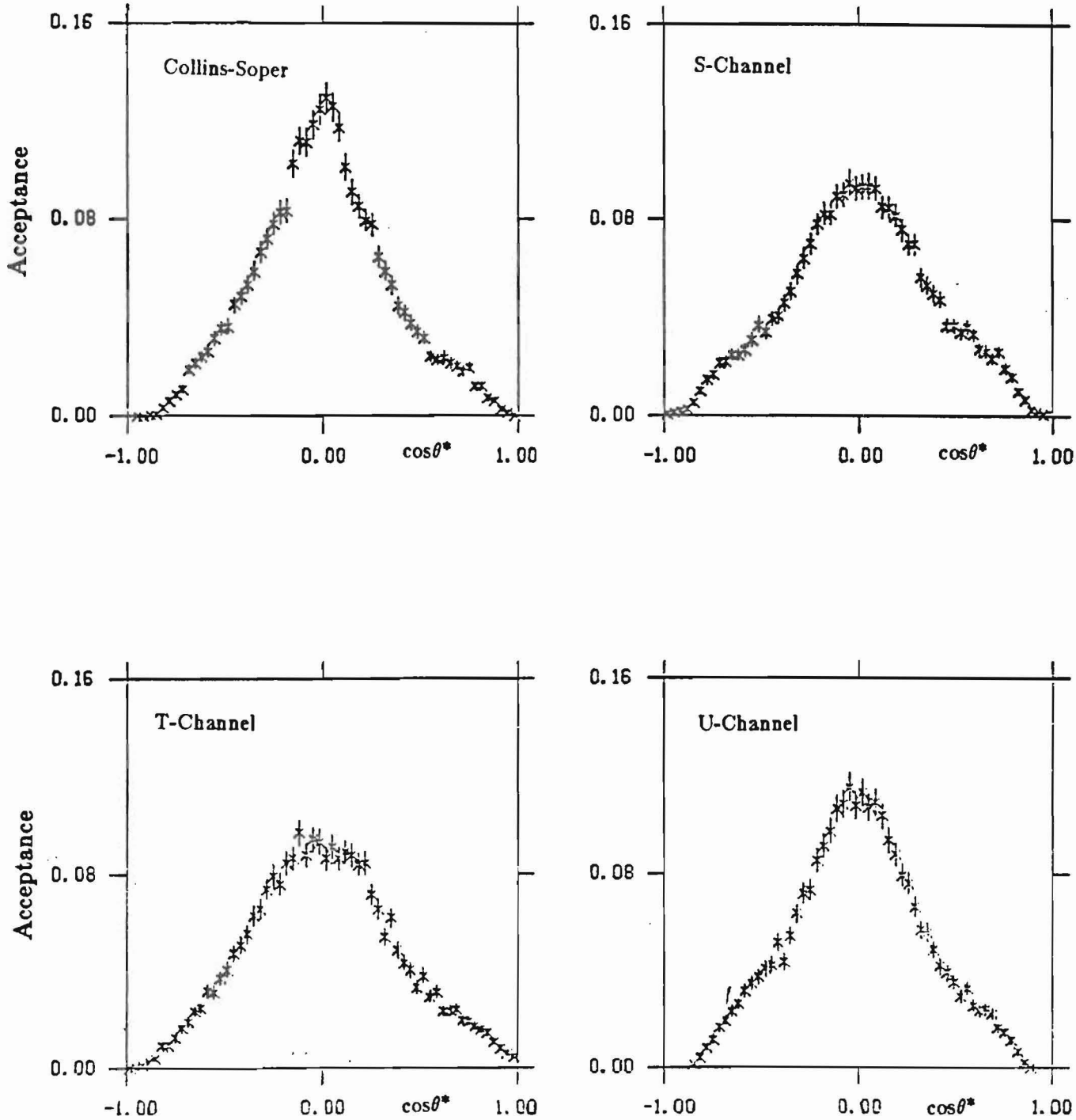
Collins-Soper
S-Channel
T-Channel
U-Channel
Acceptance
0.16
0.08
0.00
-1.00
0.00
cosθ*
1.00

Figure 33 -- Acceptance in $\cos\theta^*$ in four bins of x_1. (Collins-Soper frame)

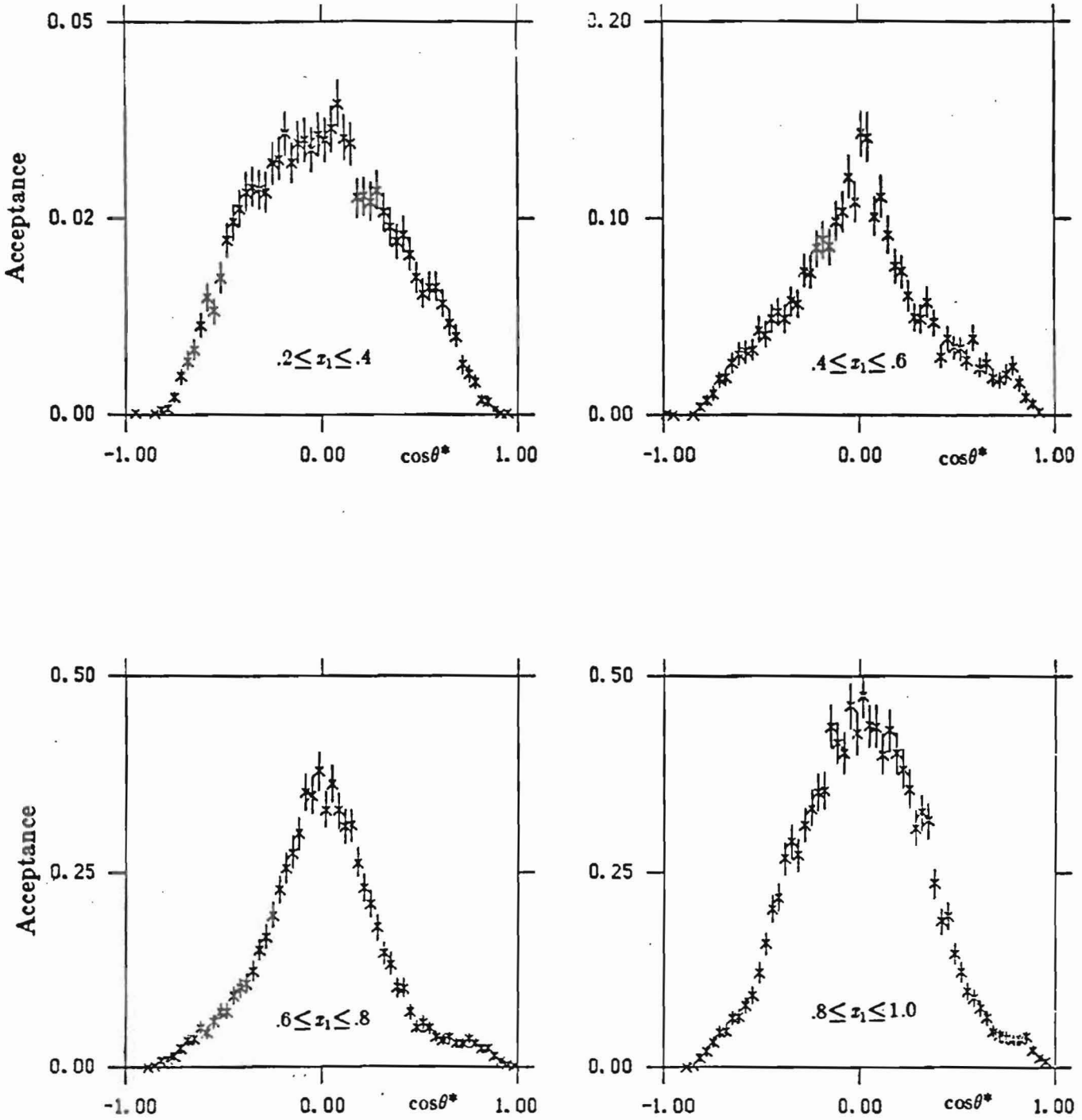
Acceptance
0.05
0.02
0.00
-1.00
0.00
cosθ*
1.00
.2≤x₁≤.4
0.20
0.10
0.00
-1.00
0.00
cosθ*
1.00
.4≤x₁≤.6
Acceptance
0.50
0.25
0.00
-1.00
0.00
cosθ*
1.00
.6≤x₁≤.8
0.50
0.25
0.00
-1.00
0.00
cosθ*
1.00
.8≤x₁≤1.0

Figure 34 -- Illumination plot at D-bank, illustrating hodoscope inefficiencies. Each entry represents one track, and each cell represents the overlap of a DX and DY counter. The view is looking upstream; the blank rectangle in the center is the beam hole. An inefficient counter is indicated by the arrow; the efficiency for that row is plotted in figure 35.

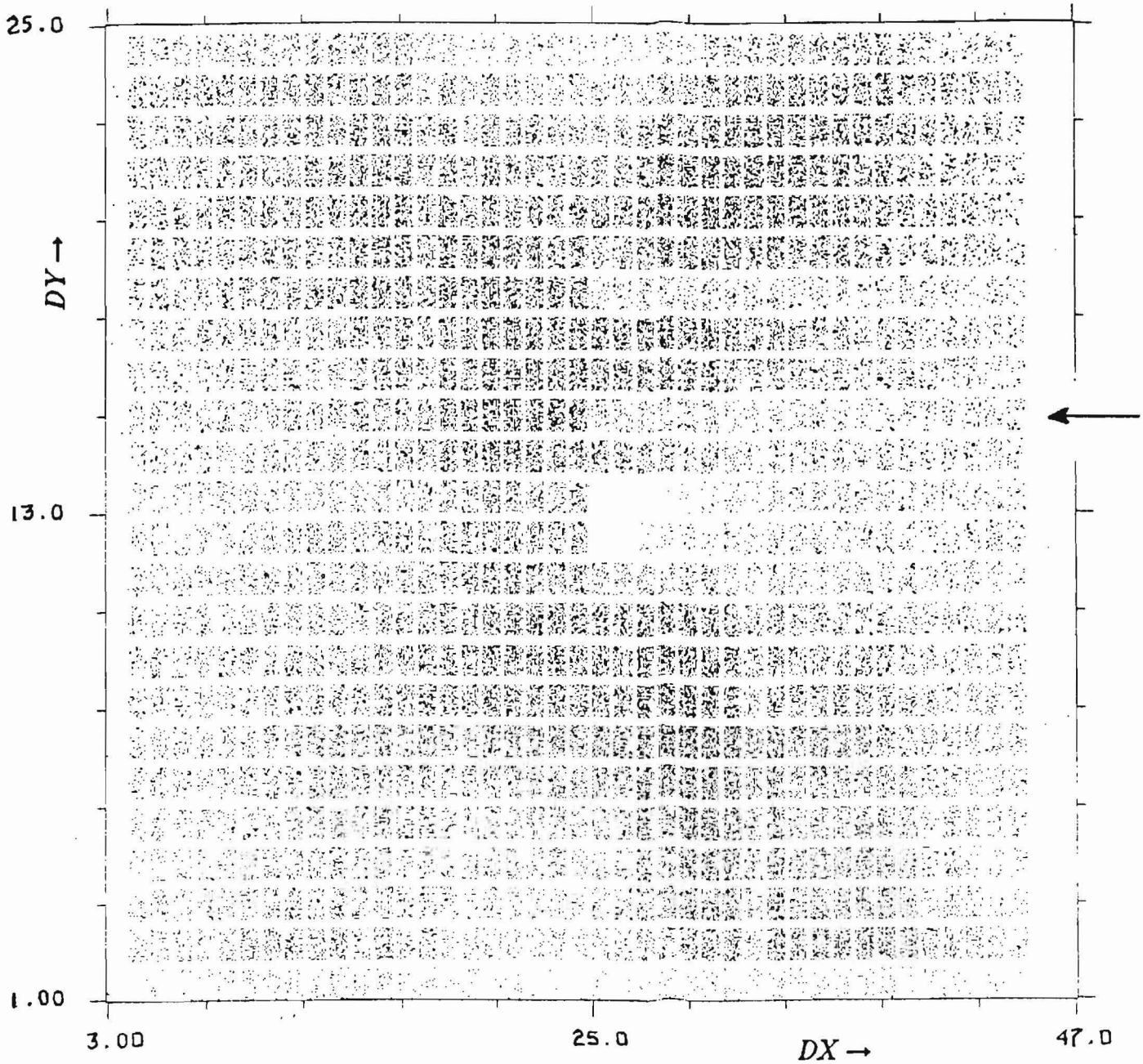
25.0
13.0
1.00
DY →
3.00
25.0
47.0
DX →

Figure 35 -- Efficiencies of hodoscopes DY15 and DY39 plotted against the number of the overlapping DX counters. Note that DY15 is fully efficient while DY39 shows poor efficiency. The position of these two counter is indicated by the arrow in figure 34.

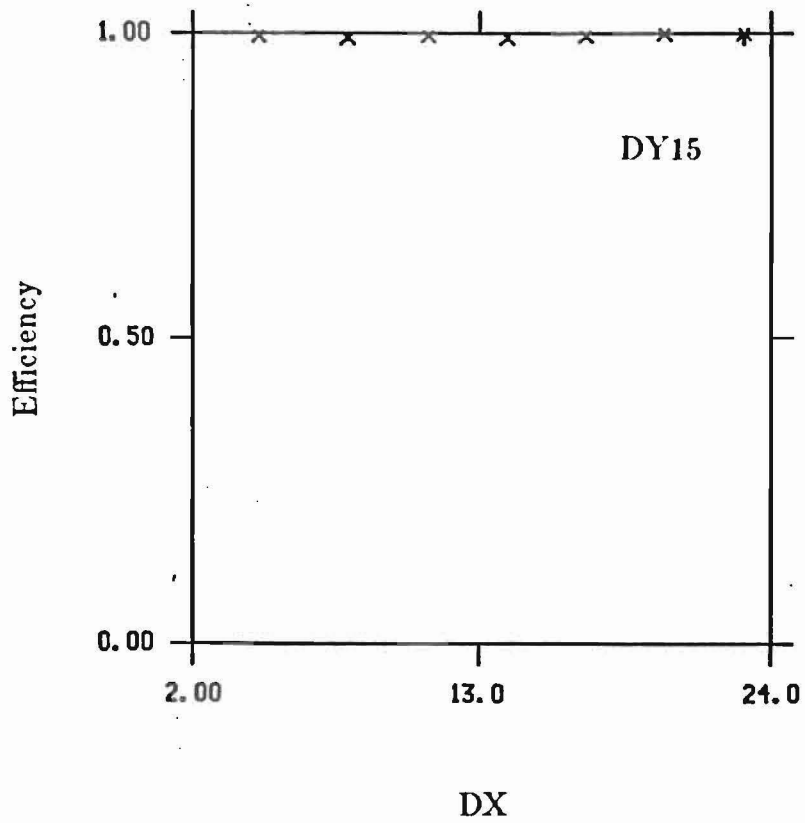
1.00
0.50
0.00
Efficiency
DY15
2.00
13.0
24.0
DX

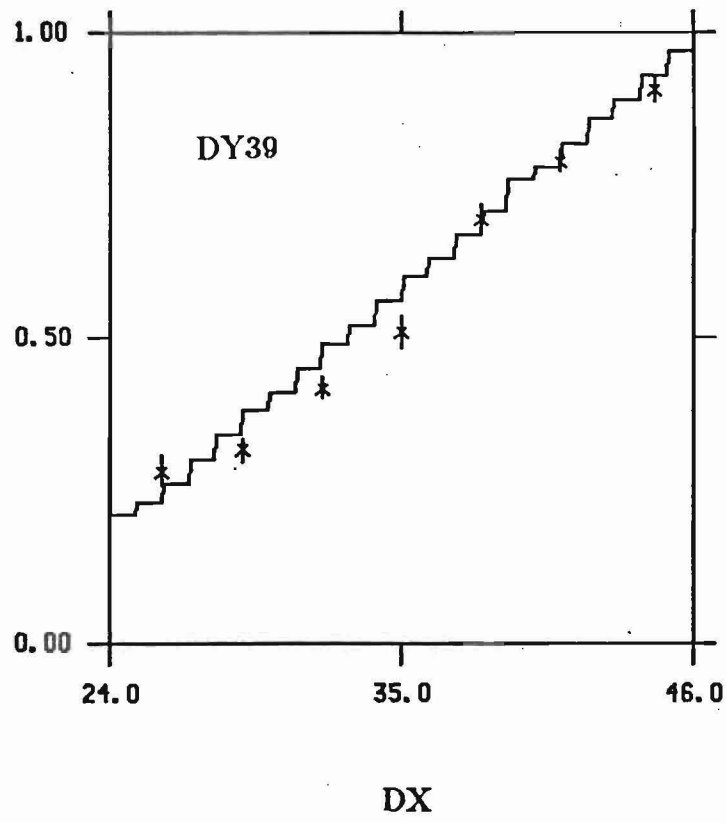
1.00
0.50
0.00
DY39
24.0
35.0
46.0
DX

Figure 36 -- Comparison of Monte Carlo (solid line) with data (crosses) at the DX-bank. Each bin represents one DX counter. The Monte Carlo has been corrected for hodoscope inefficiencies.

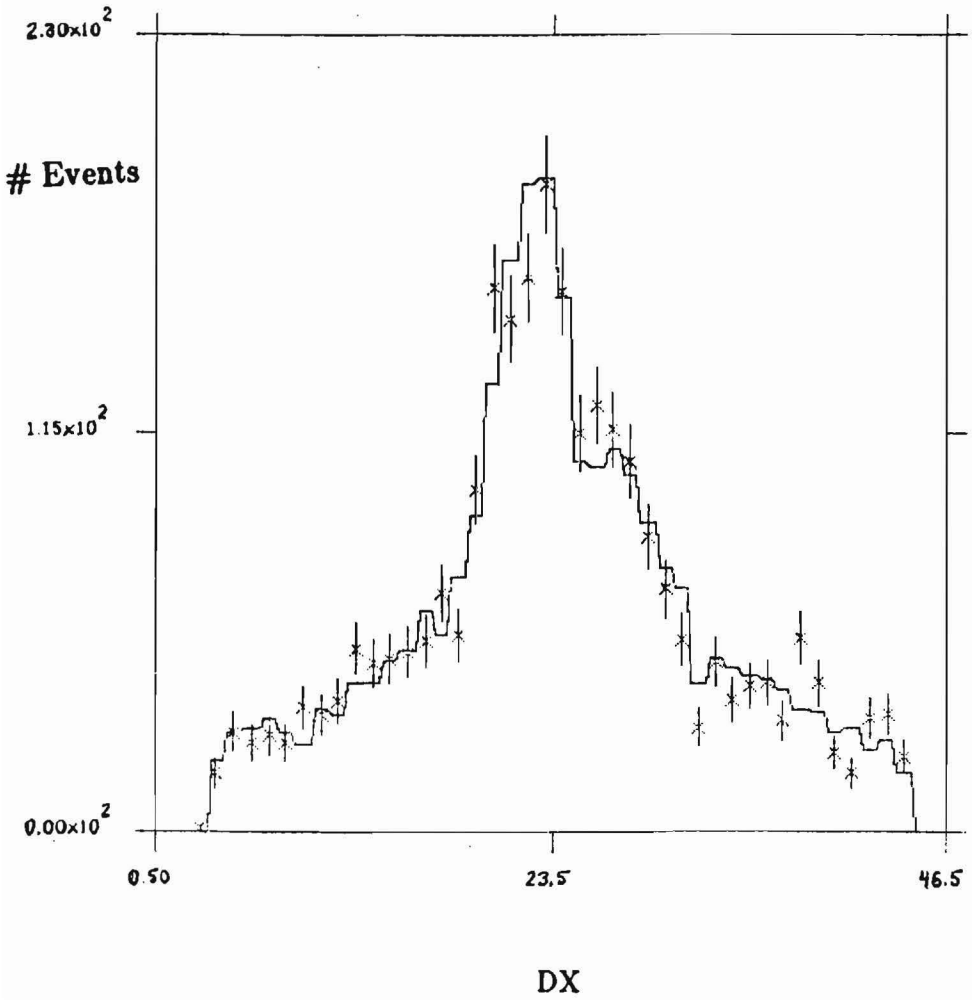
2.30x10^2
Events
1.15x10^2
0.00x10^2
0.50
23.5
46.5
DX

Figure 37 -- Comparison of Monte Carlo (solid line) with data (crosses) at the DY-bank. Each bin represents on DY counter. Upper plot is the east side of the bank (counters 1-24), lower plot is west side (counters 25-48). Monte Carlo has been corrected for hodoscope inefficiencies.

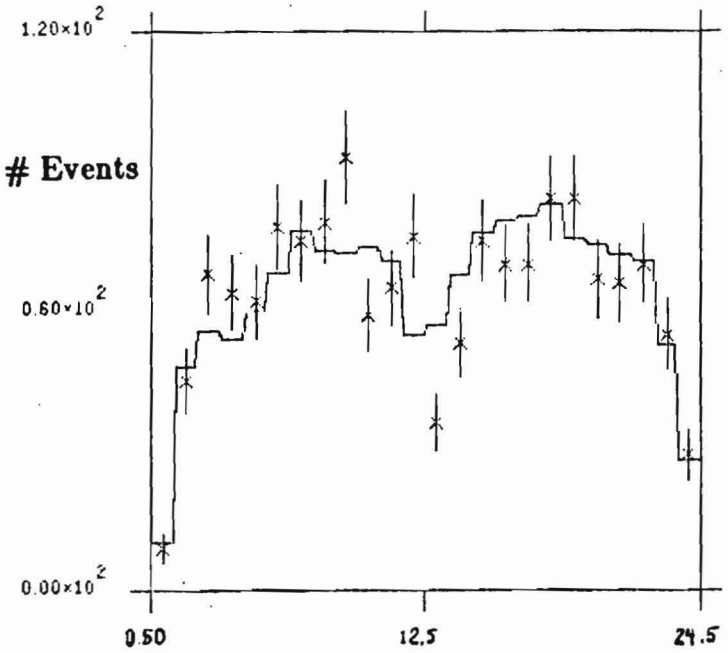
Events
1.20×10^2
0.60×10^2
0.00×10^2
0.50
12.5
24.5

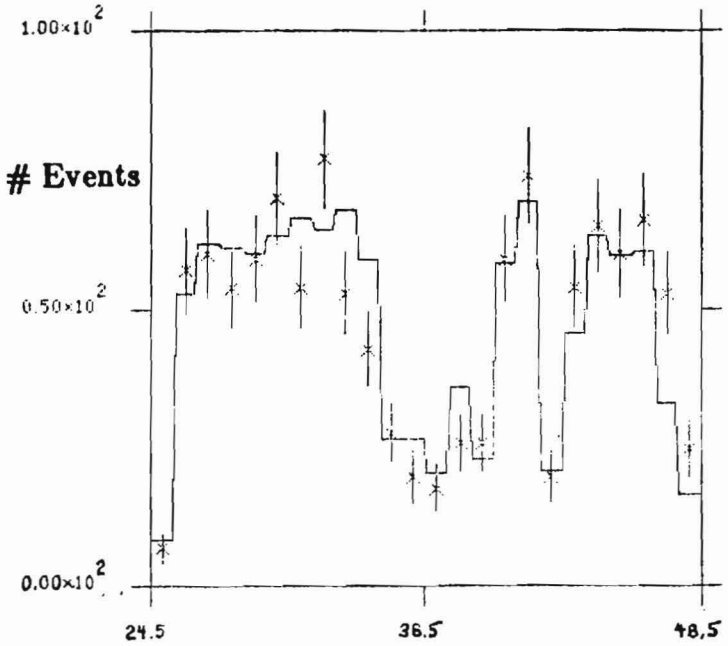
Events
1.00×10^2
0.50×10^2
0.00×10^2
24.5
36.5
48.5

DY

Figure 38 -- Ratio of acceptance in $\cos\theta^*$ after efficiency correction to acceptance in $\cos\theta^*$ before efficiency correction.

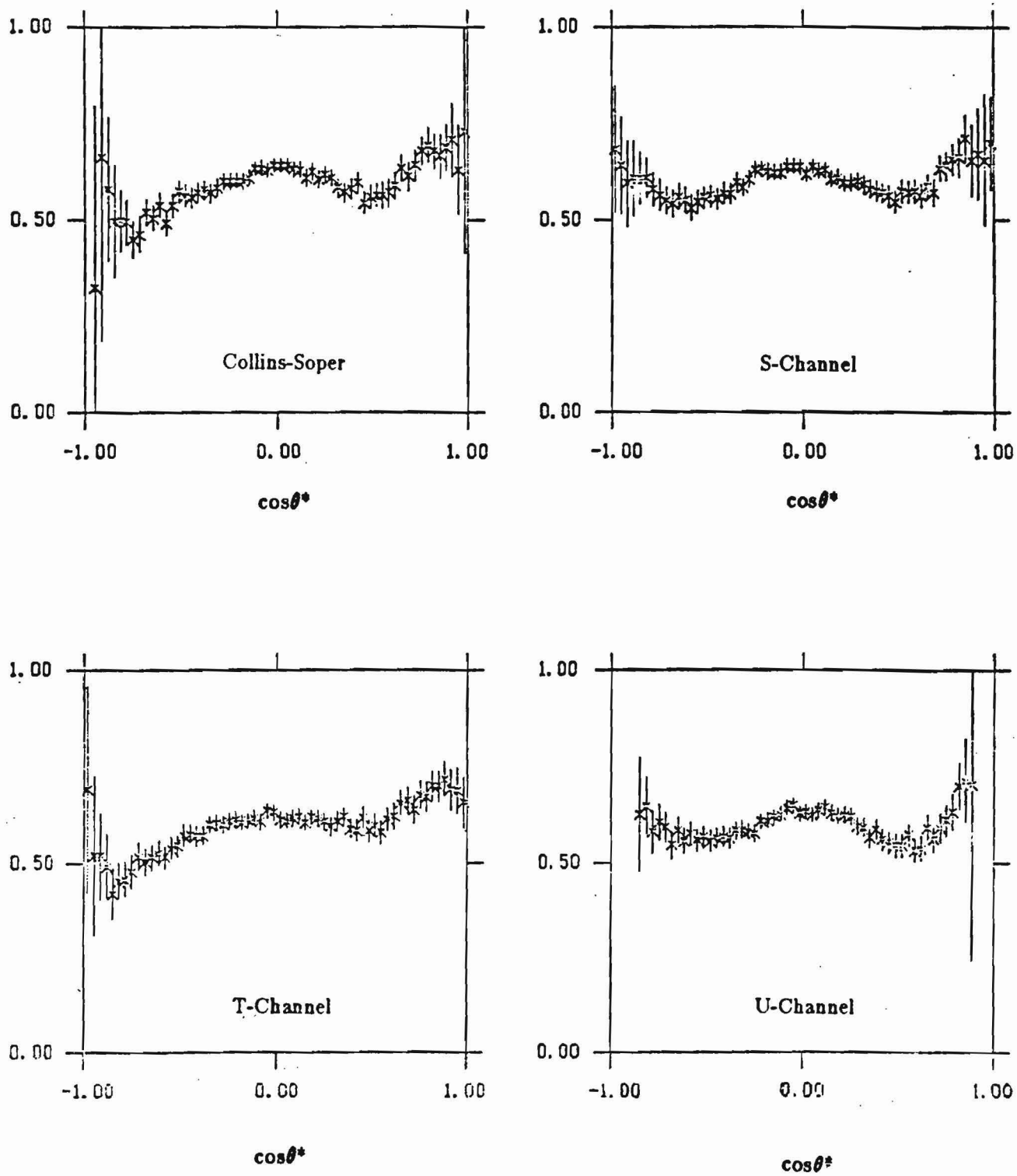
1.00
0.50
0.00
-1.00
0.00
1.00
cosθ*
Collins-Soper
S-Channel
T-Channel
U-Channel

Figure 39 -- Ratio of acceptance in $\cos\theta^*$ after efficiency correction to acceptance in $\cos\theta^*$ before efficiency correction in four bins of x_1. (Collins-Soper frame)

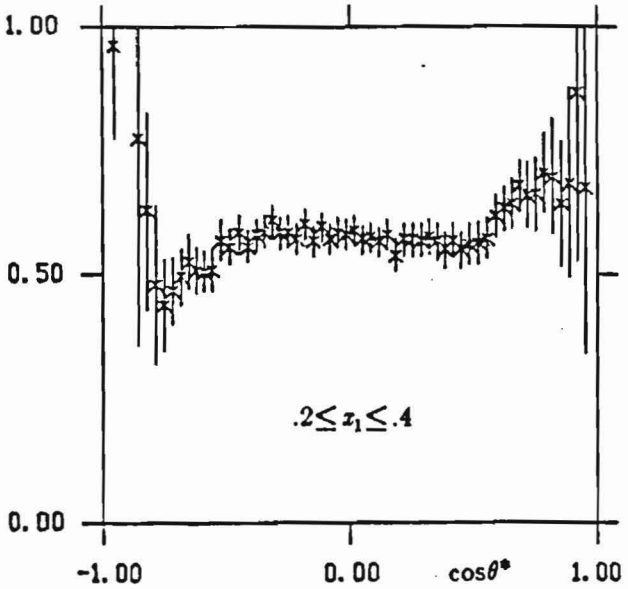
1.00
0.50
0.00
-1.00
0.00
cosθ*
1.00
.2≤x₁≤.4

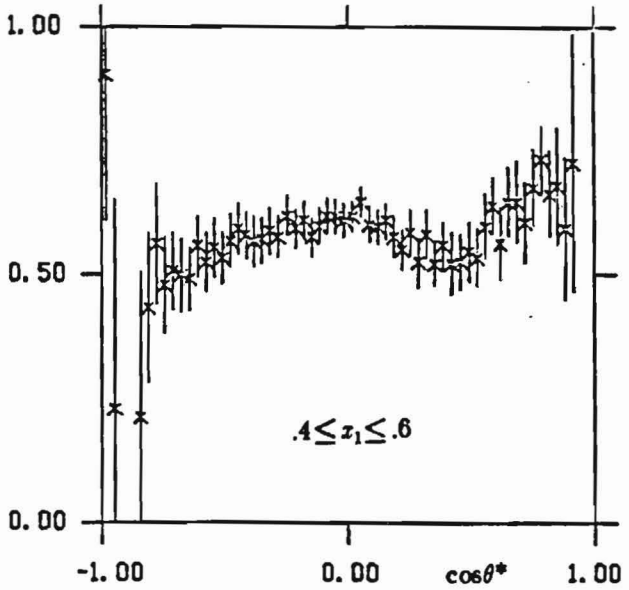
1.00
0.50
0.00
-1.00
0.00
cosθ*
1.00
.4≤x₁≤.6

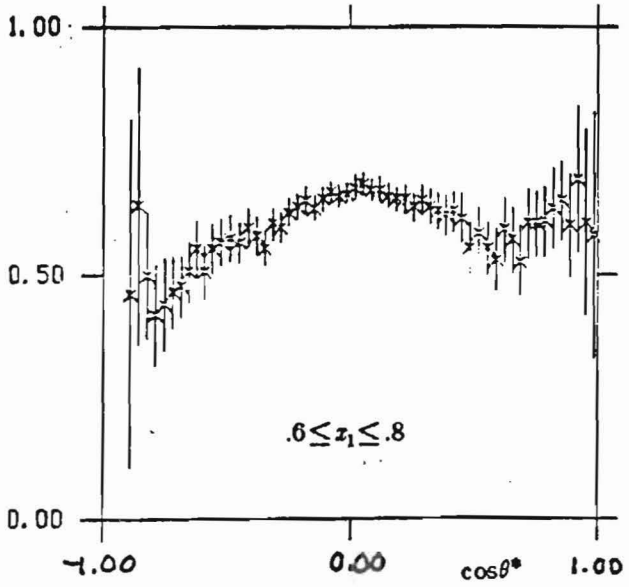
1.00
0.50
0.00
-1.00
0.00
cosθ*
1.00
.6≤x₁≤.8

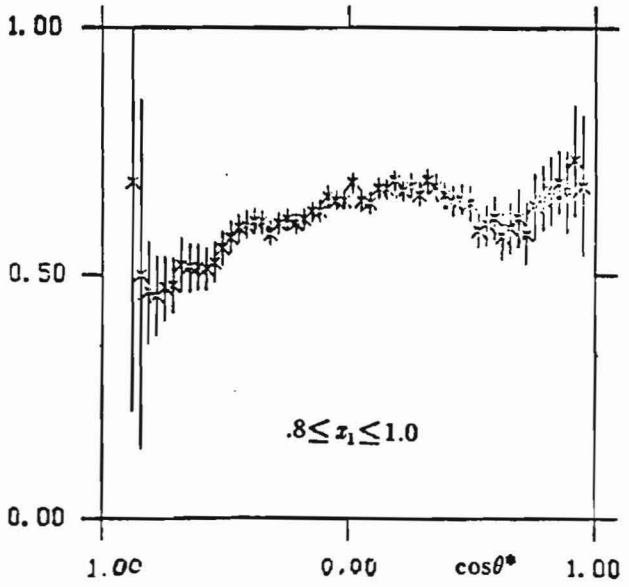
1.00
0.50
0.00
1.00
0.00
cosθ*
1.00
.8≤x₁≤1.0

Figure 40 -- Efficiency of MWPC plane #1, plotted against wire number. Each bin of the plot represents one pre-amp (8 sense wires). The plot illustrates both typical efficiencies and typical problems: the large gap was due to two pre-amp cards having been swapped; the next small dip is due to two missing wires; the next two dips are due to one missing wire or failing channel each. (The left-most gap is due to statistics at the edge.)

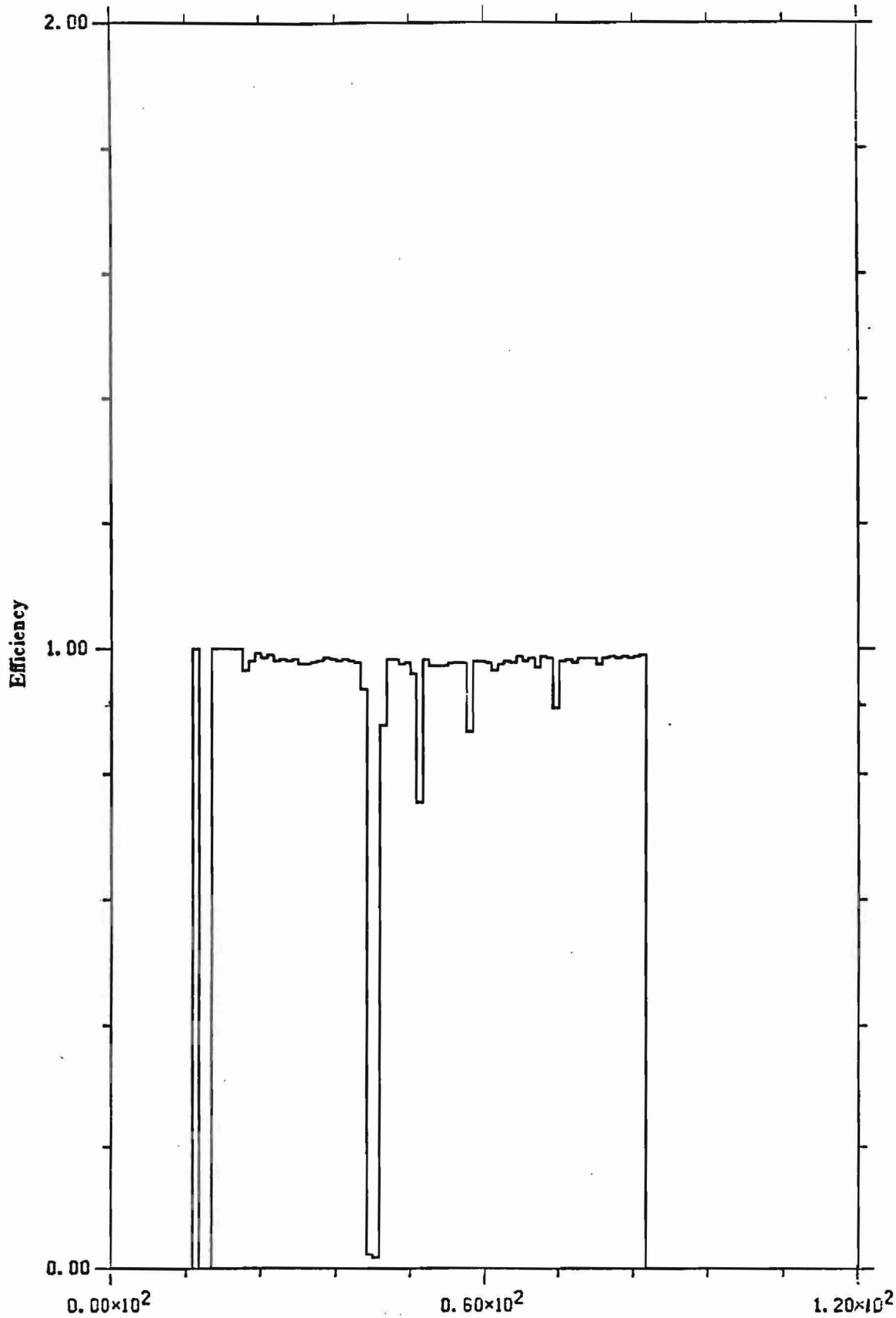
2.00
1.00
0.00
Efficiency
0.00×10^2
0.60×10^2
1.20×10^2

Figure 41 -- Efficiency of Drift Chamber plane #6, plotted against cell number. Each bin represents one cell. The 7-cell periodicity indicates trouble in a digitizer board.

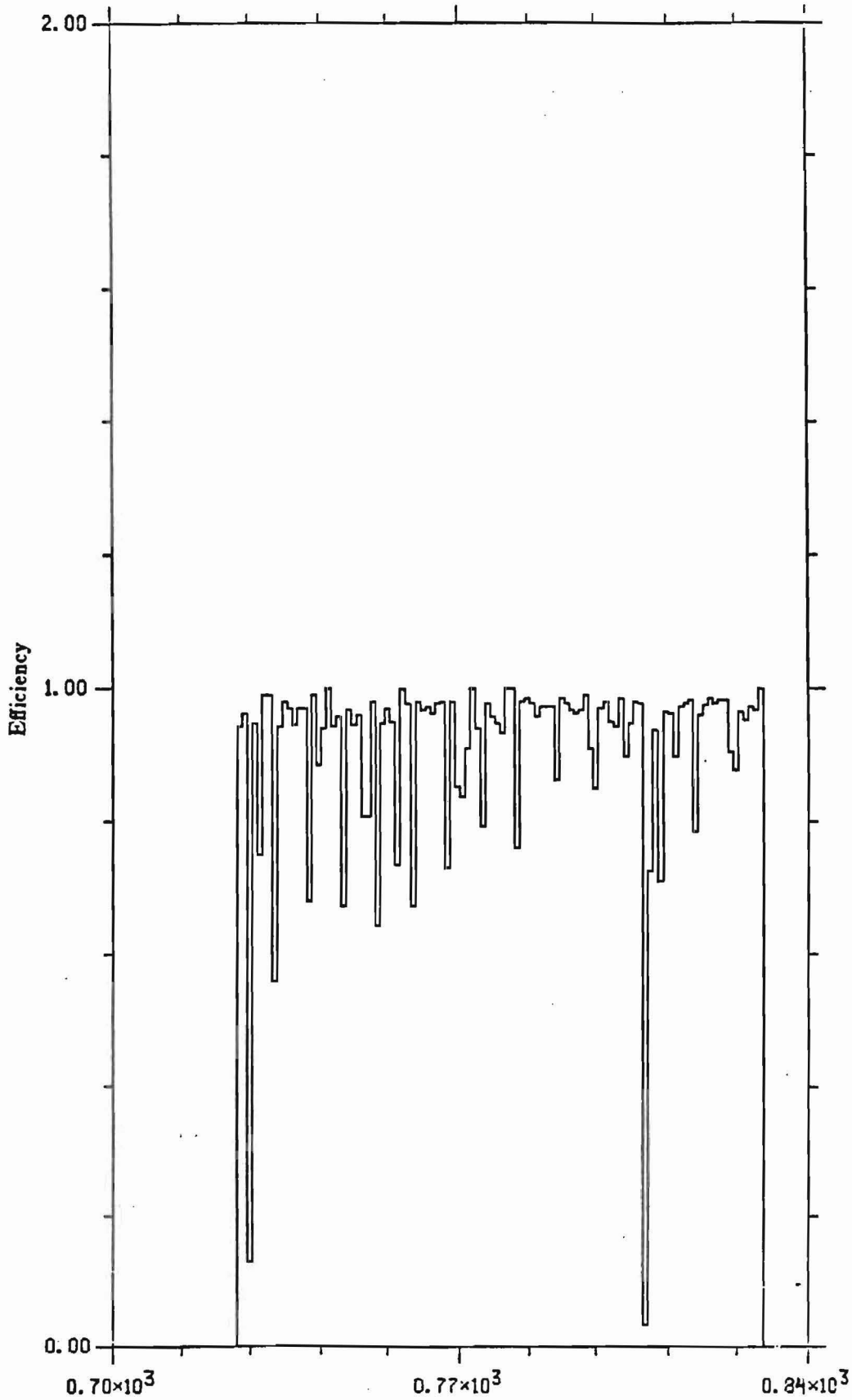
2.00
1.00
0.00
Efficiency
0.70×10^3
0.77×10^3
0.84×10^3

Figure 42 -- Reconstruction efficiency as a function of the kinematic variables.

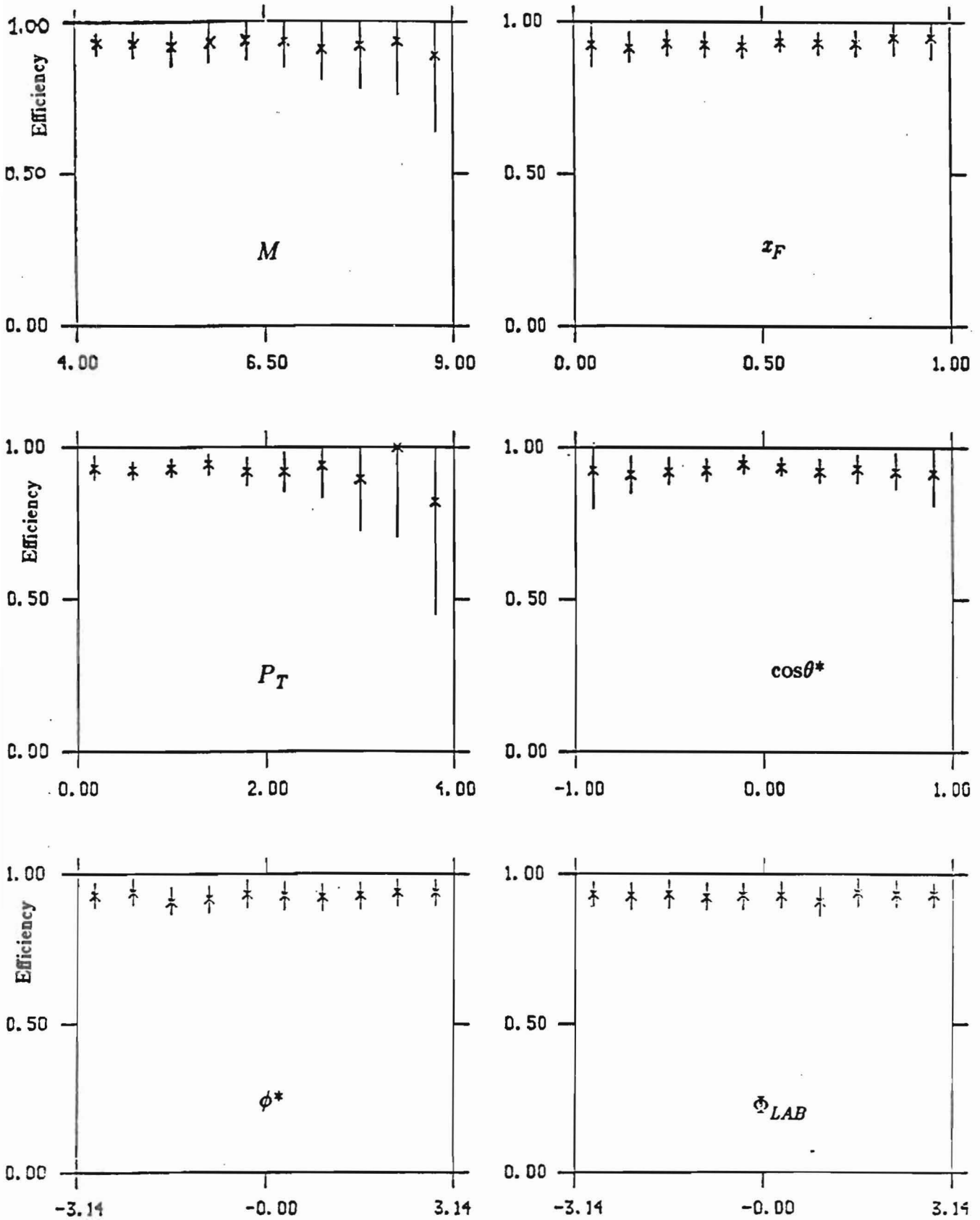
Efficiency
1.00
0.50
0.00
M
4.00
6.50
9.00
x_F
0.00
0.50
1.00
P_T
2.00
4.00
$\cos\theta^*$
-1.00
ϕ^*
-3.14
-0.00
3.14
Φ_{LAB}

Figure 43 -- Reconstruction efficiency as a function of $\cos\theta^*$ in four bins of x_1.

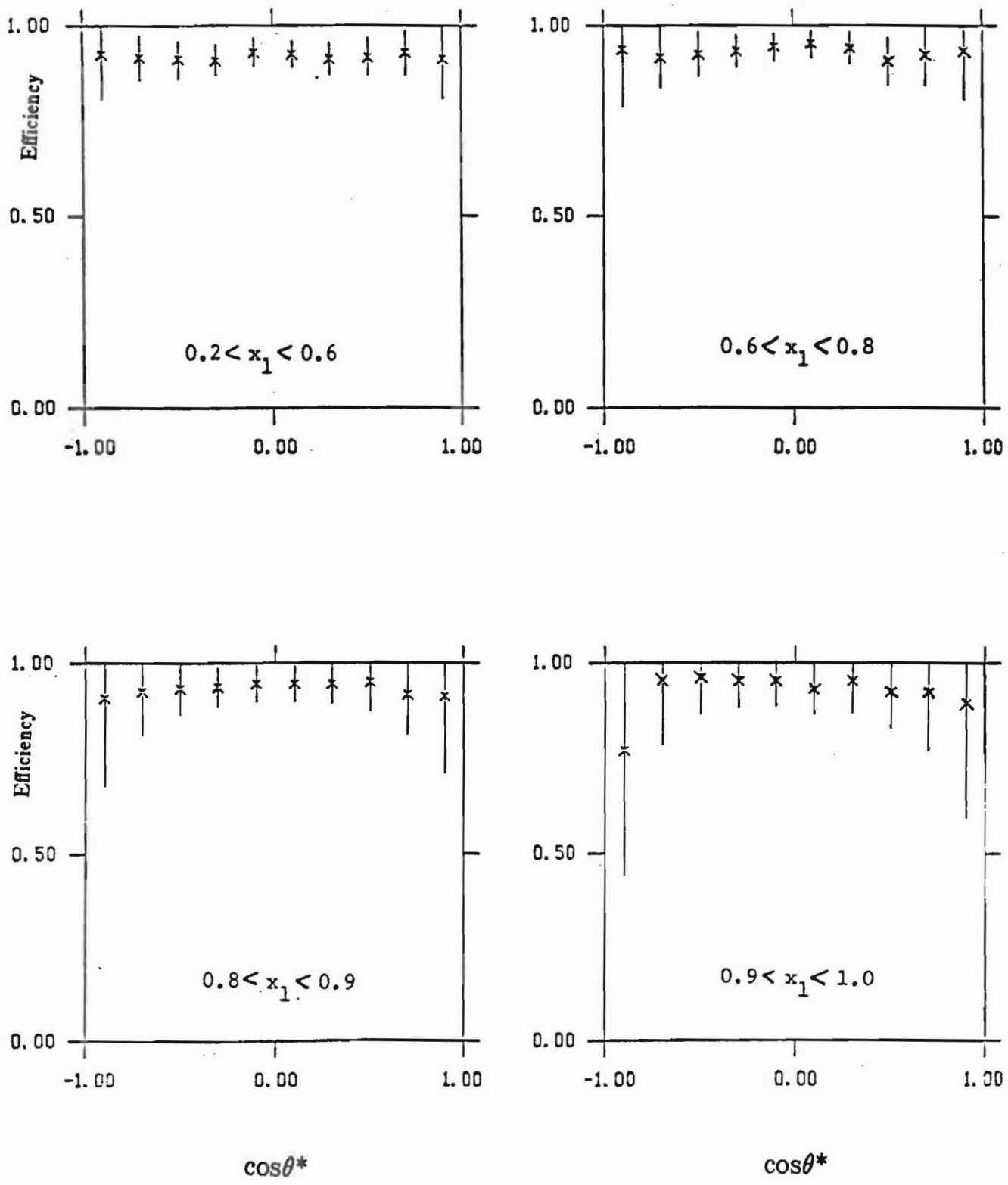
1.00
0.50
0.00
Efficiency
0.2< x1 < 0.6
0.6< x1 < 0.8
0.8< x1 < 0.9
0.9< x1 < 1.0
-1.00
0.00
1.00
cosθ*

Figure 44 -- Comparison of data (solid line) and Monte Carlo (crosses) for the momentum spectrum of beam muons in the spectrometer. The beam tune used in HALO for this comparison was $<p_\pi> = 263$ GeV/c.

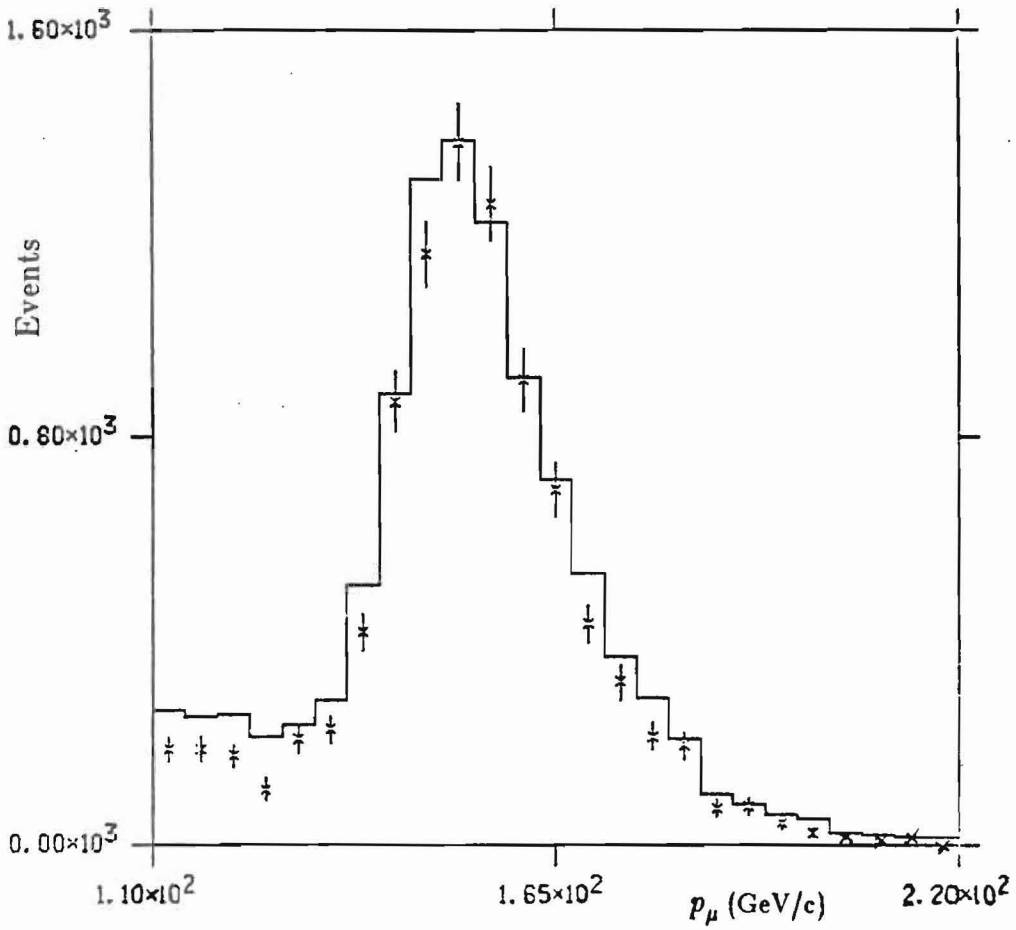
1.60×10^3
0.80×10^3
0.00×10^3
Events
1.10×10^2
1.65×10^2
2.20×10^2
p_μ (GeV/c)

Figure 45 -- Beam momentum spectrum predicted by HALO with $<p_\pi> = 263$ GeV/c.

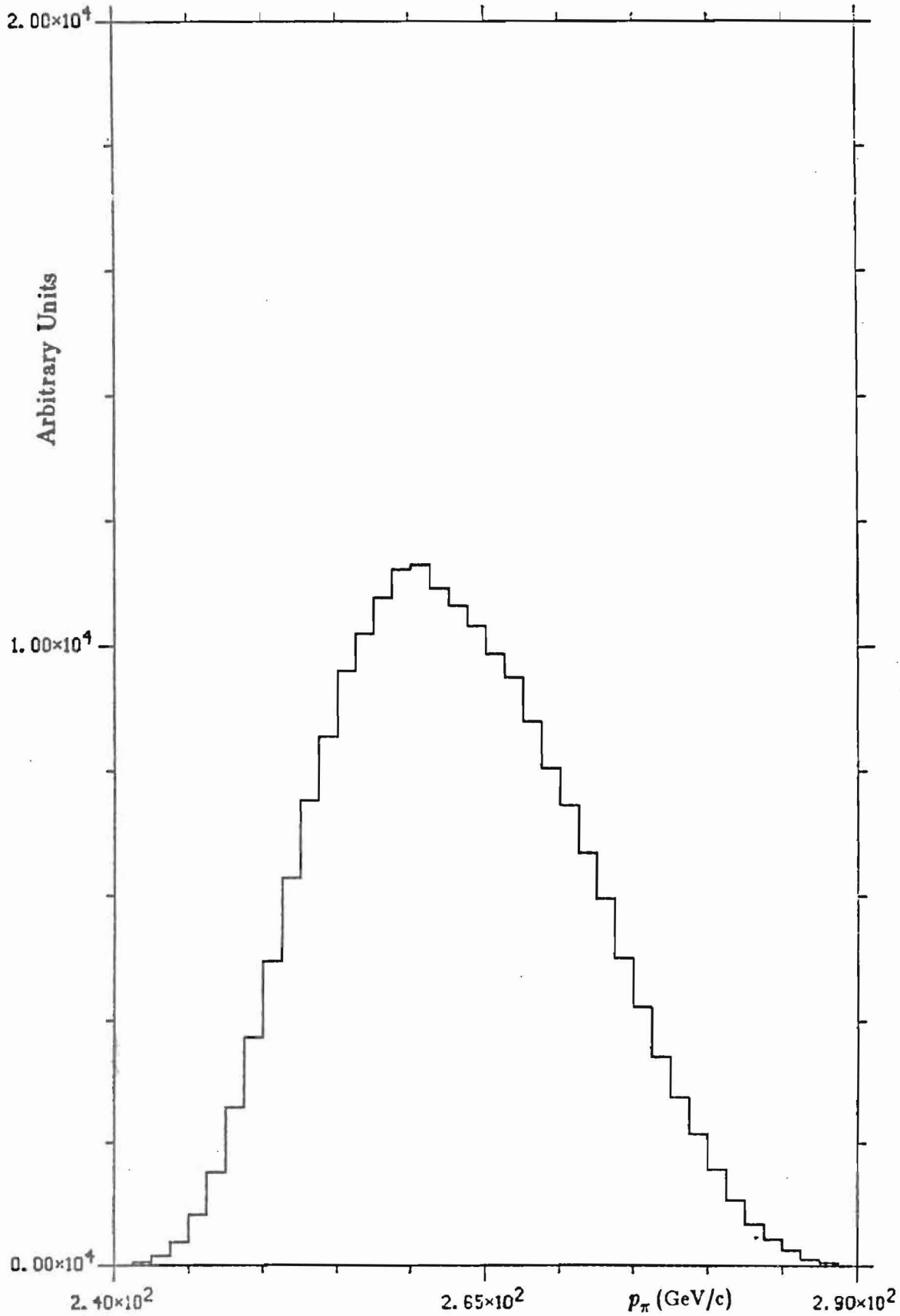
2.00×10⁴
1.00×10⁴
0.00×10⁴
Arbitrary Units
2.40×10²
2.65×10²
p_π (GeV/c)
2.90×10²

Figure 46 -- Resolution and smearing of x_1. Solid line indicates σ_{x_1}, dotted line indicates Δx_1, the shift between the reconstructed and generated values.

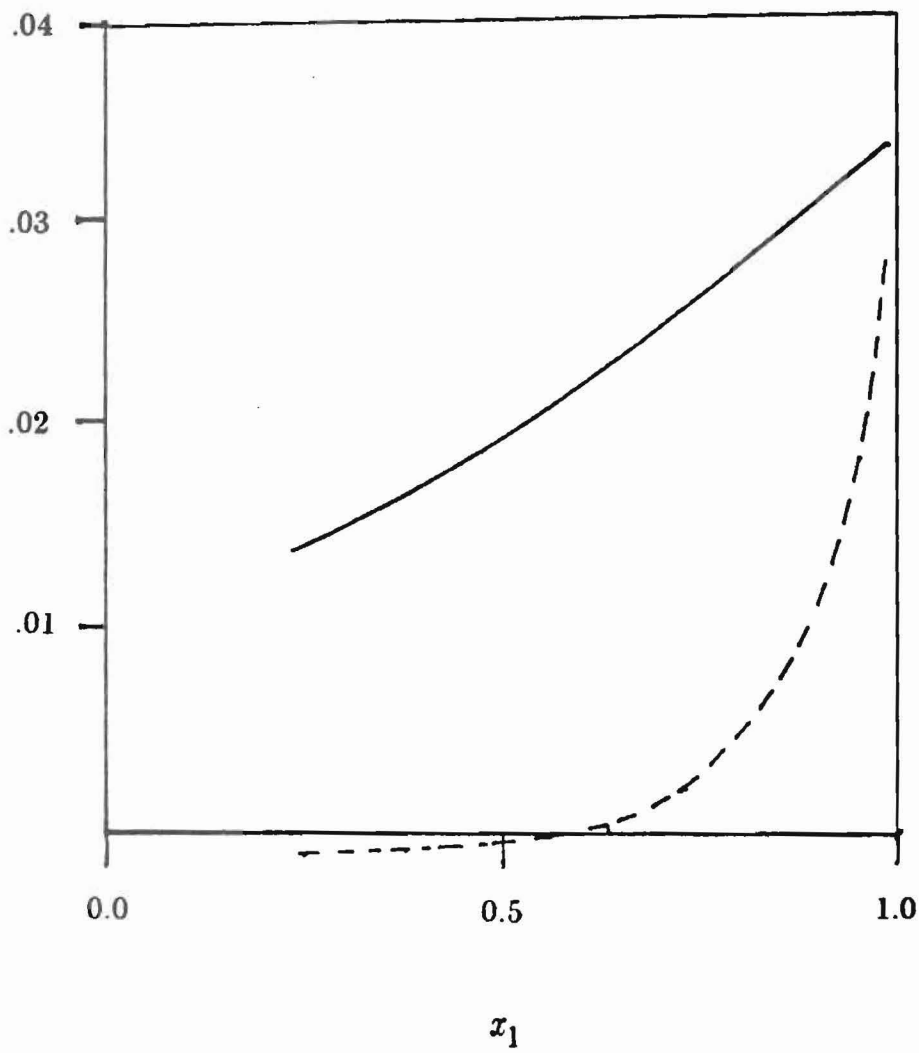
.04
.03
.02
.01
0.0
0.5
1.0
x_1

Figure 47 -- Resolution and smearing in $\cos\theta^*$. The upper plot shows $\sigma_{\cos\theta^*}$ (solid line) and $\Delta\cos\theta^*$ (dotted line) plotted against $\cos\theta^*$. The lower plot shows the same quantities plotted against x_1.

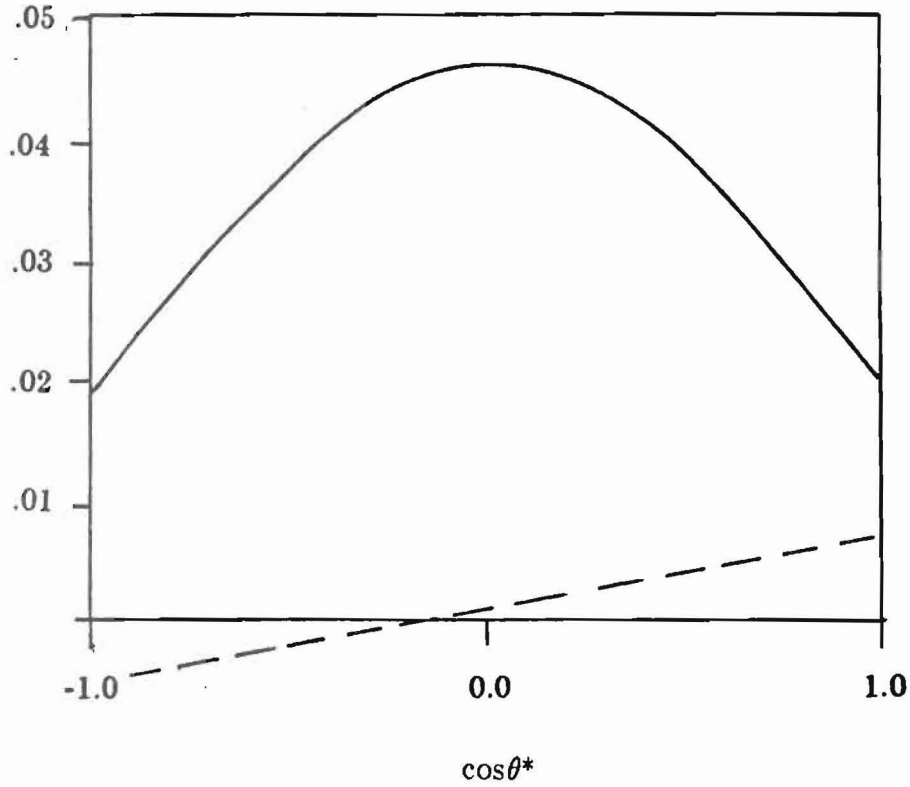
.05
.04
.03
.02
.01
-1.0
0.0
1.0
cosθ*

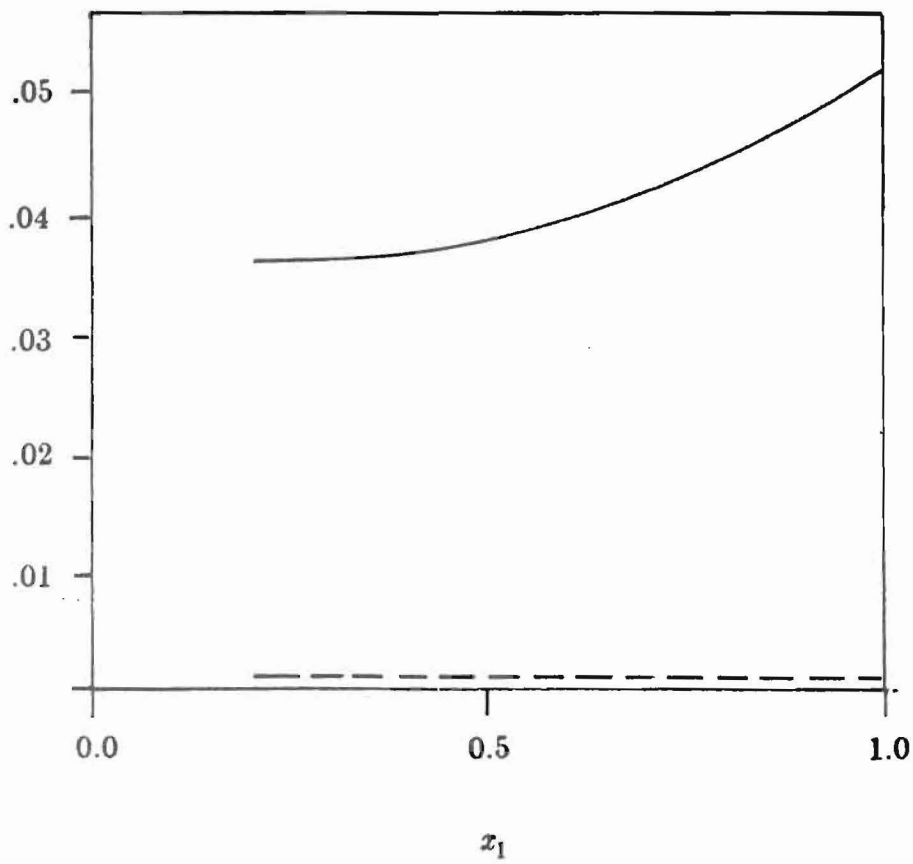
.05
.04
.03
.02
.01
0.0
0.5
1.0
x_1

Figure 48 -- Cosθ^* distributions for real events (upper plot) and for random combinations of single-muon tracks (lower plot). The background calculation is normalized by scaling the lower plot so the lowest bins of these plots match.

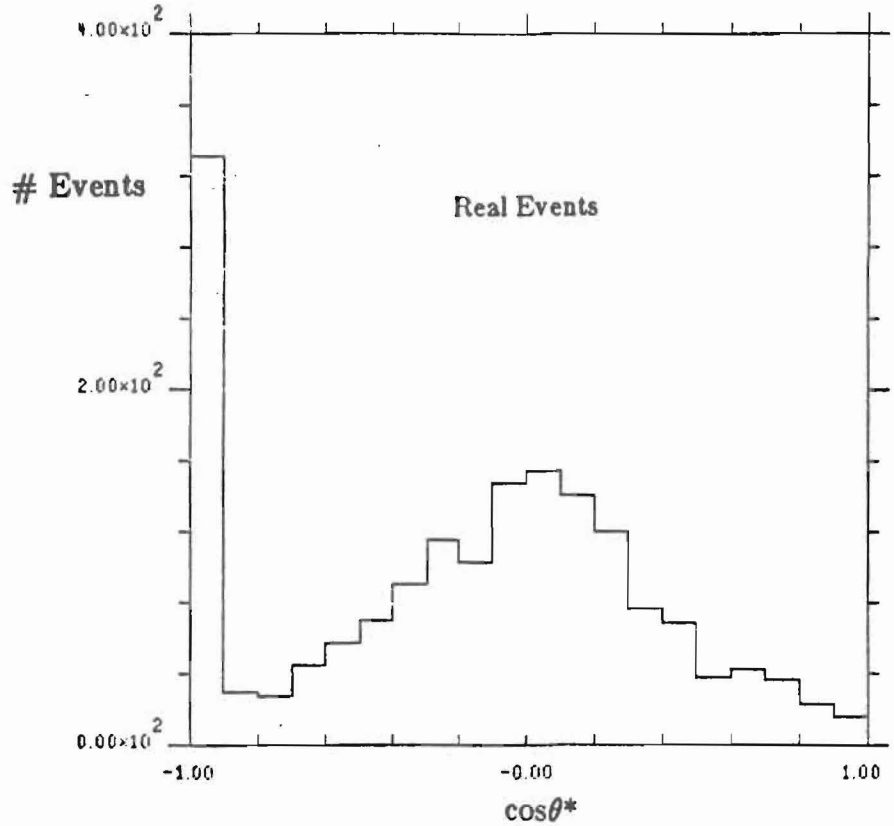
Events
Real Events
4.00×10^2
2.00×10^2
0.00×10^2
-1.00
-0.00
1.00
cosθ*

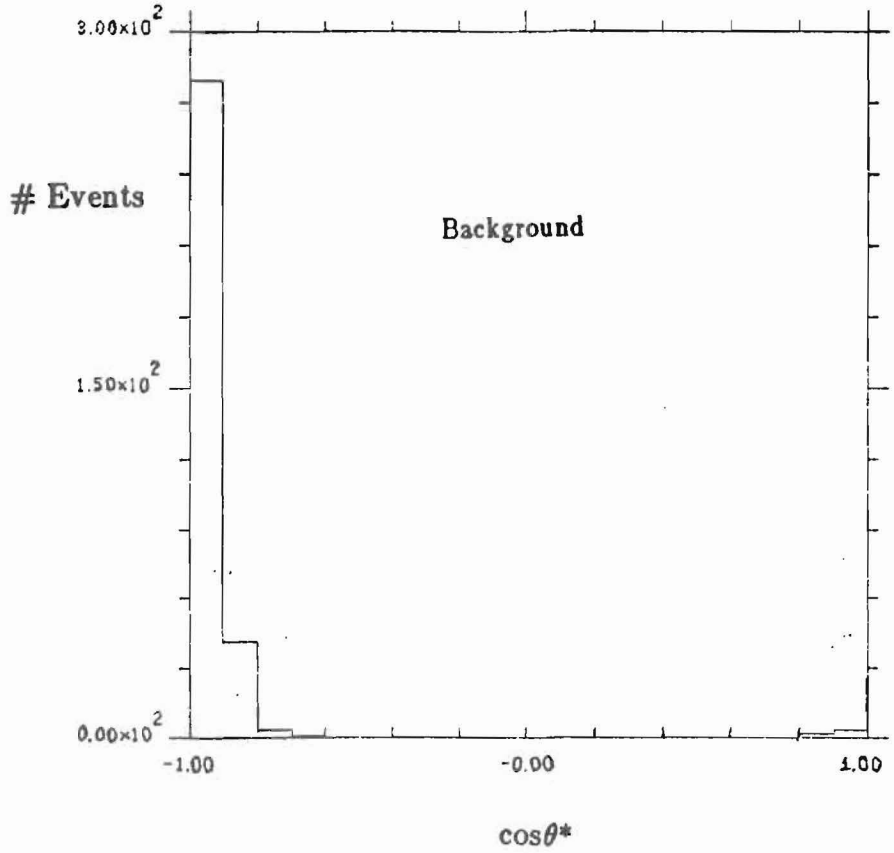
Events
Background
3.00×10^2
1.50×10^2
0.00×10^2
-1.00
-0.00
1.00
cosθ*

Figure 49 -- Distributions of the 13.1 background events in 6 kinematic variables.

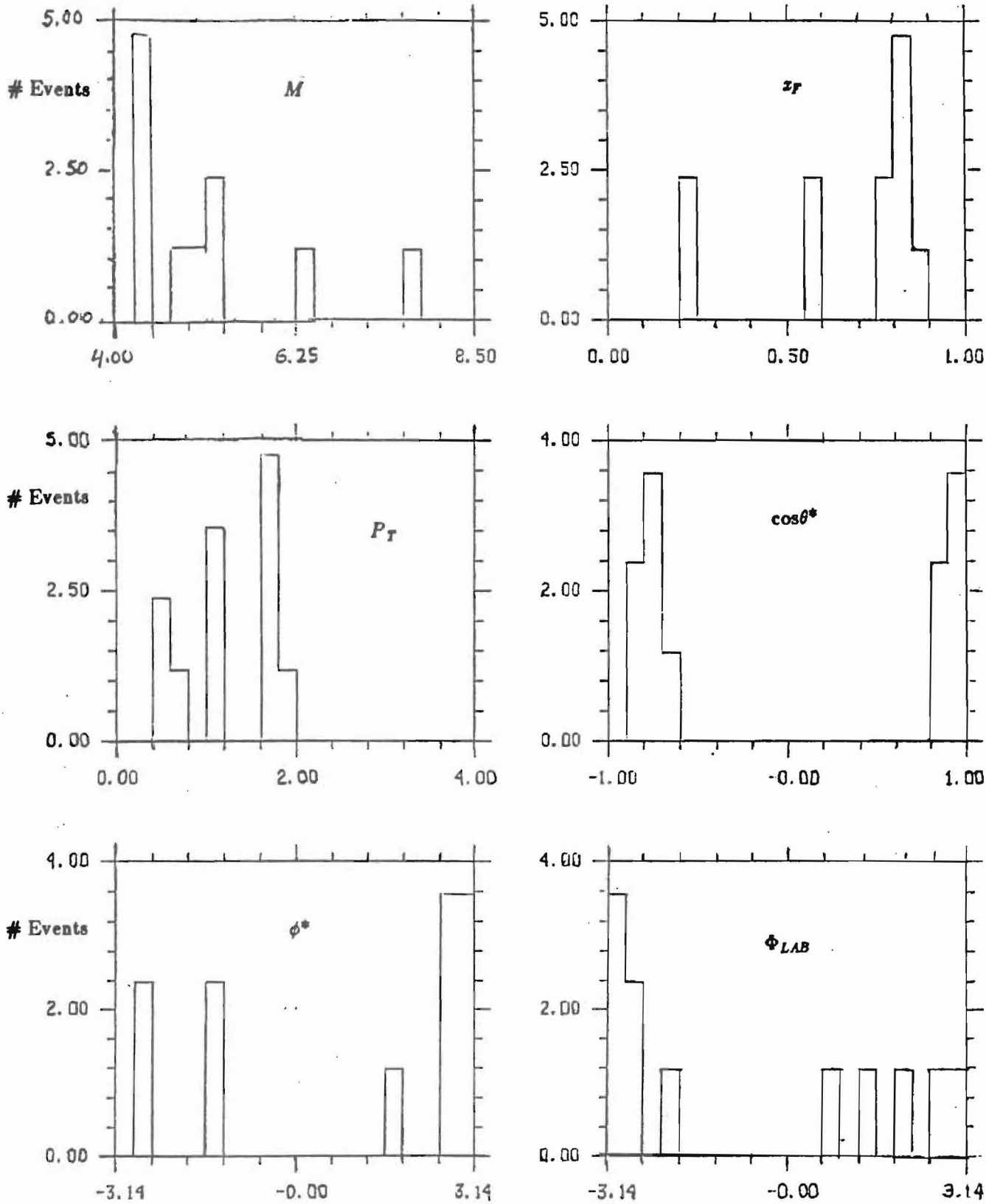
Events
M
5.00
2.50
0.00
4.00
6.25
8.50
x_F
5.00
2.50
0.00
0.00
0.50
1.00
Events
P_T
5.00
2.50
0.00
0.00
2.00
4.00
$\cos\theta^*$
4.00
2.00
0.00
-1.00
-0.00
1.00
Events
ϕ^*
4.00
2.00
0.00
-3.14
-0.00
3.14
Φ_{LAB}
4.00
2.00
0.00
-3.14
-0.00
3.14

Figure 50 -- Comparison of $G(x_2)$ determined by CDHS and CCFRR data. See reference 57 for sources.

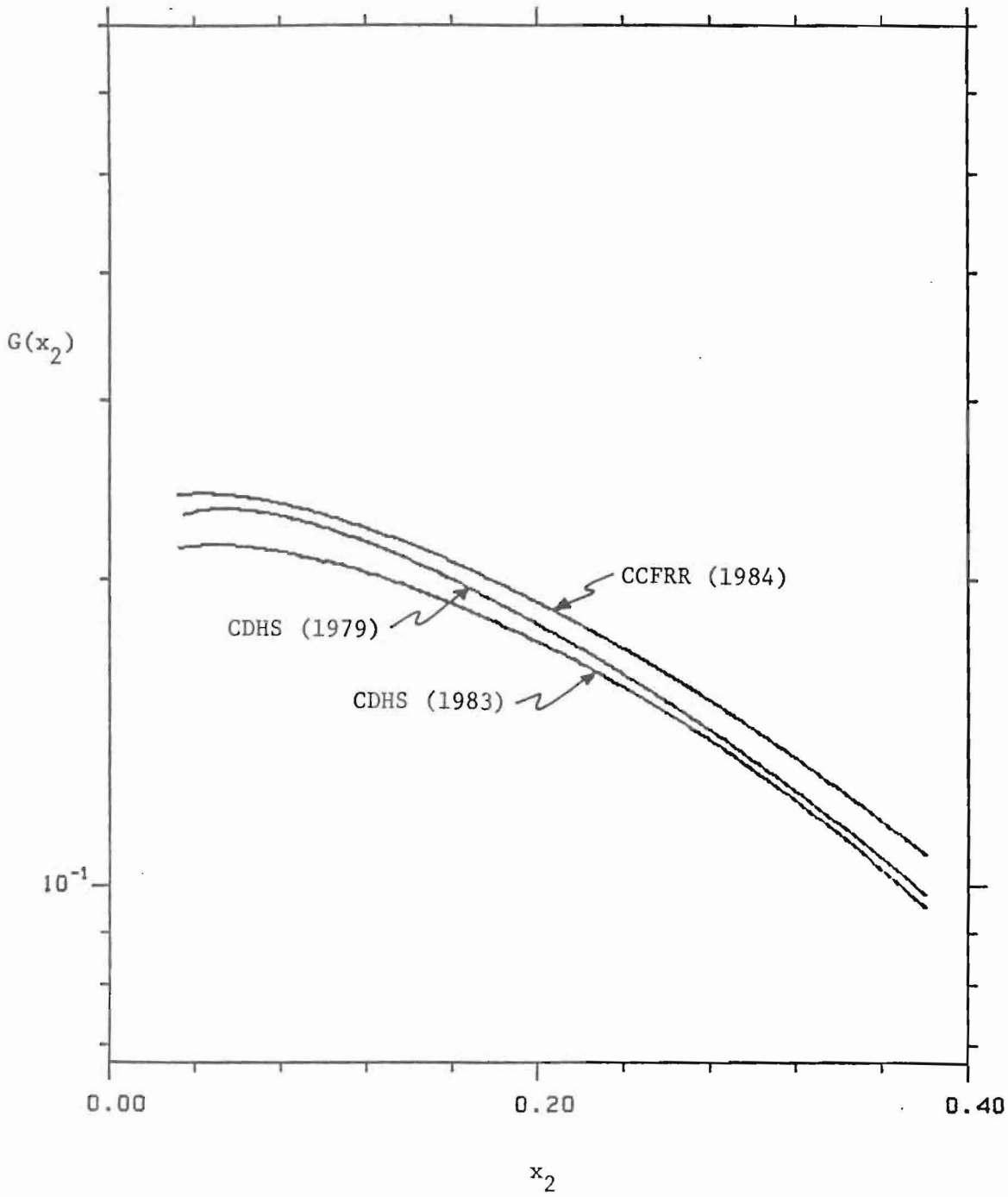
G(x2)
CCFRR (1984)
CDHS (1979)
CDHS (1983)
10-1
0.00
0.20
0.40
x2

Figure 51 -- Scatter plot of all events in x_1–x_2. Kinematic cuts, $4.0 \leq M \leq 8.5$ and $x_F \geq 0.0$, are shown, along with the binning used in this analysis.

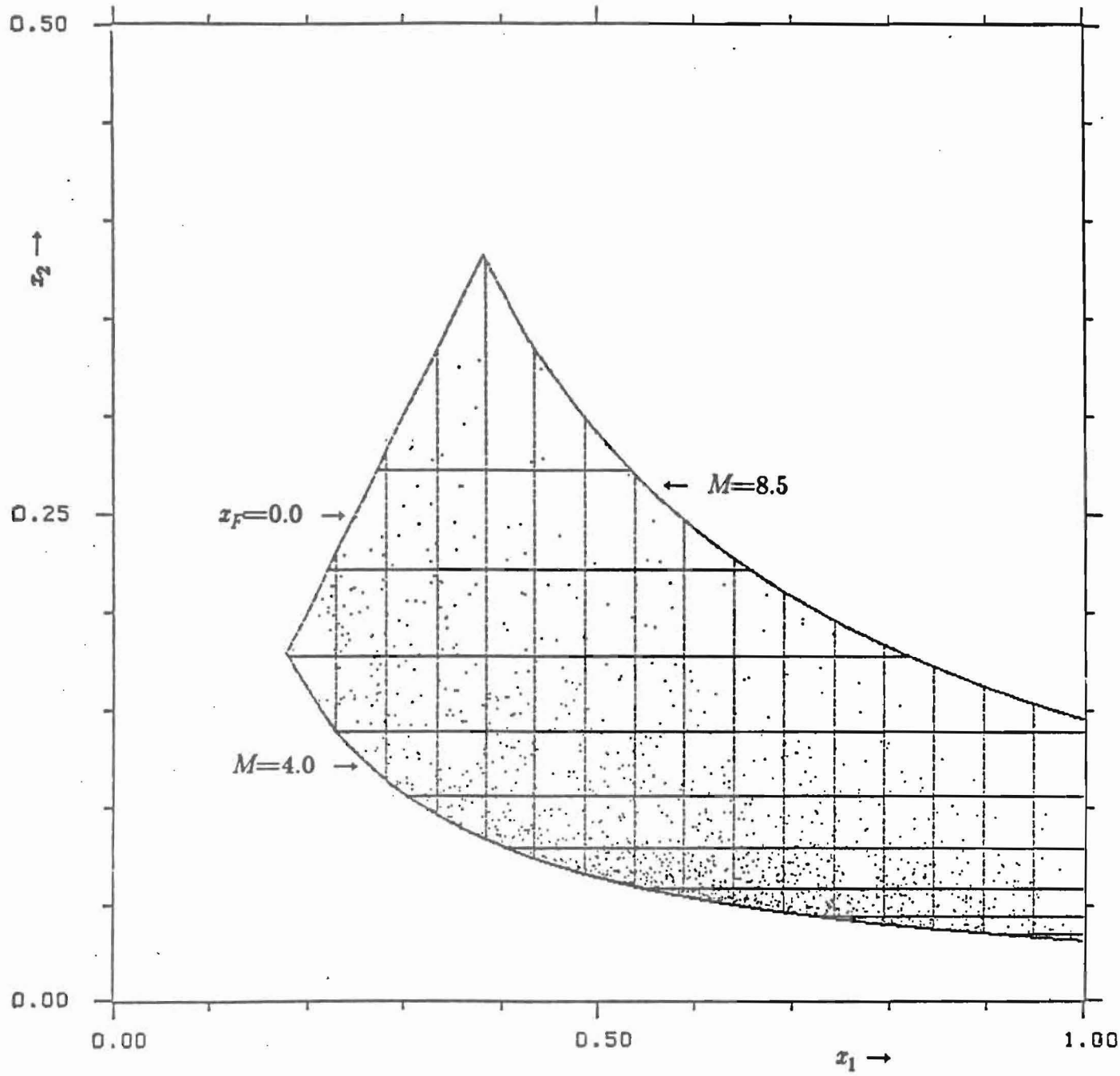
0.50
0.25
0.00
0.00
0.50
1.00
x_2 →
x_1 →
x_F=0.0 →
← M=8.5
M=4.0 →

Figure 52 -- $G(x_2)$ after iterated projections. The solid line is $G(x_2) = .39(1-x_2)^{3.19}$

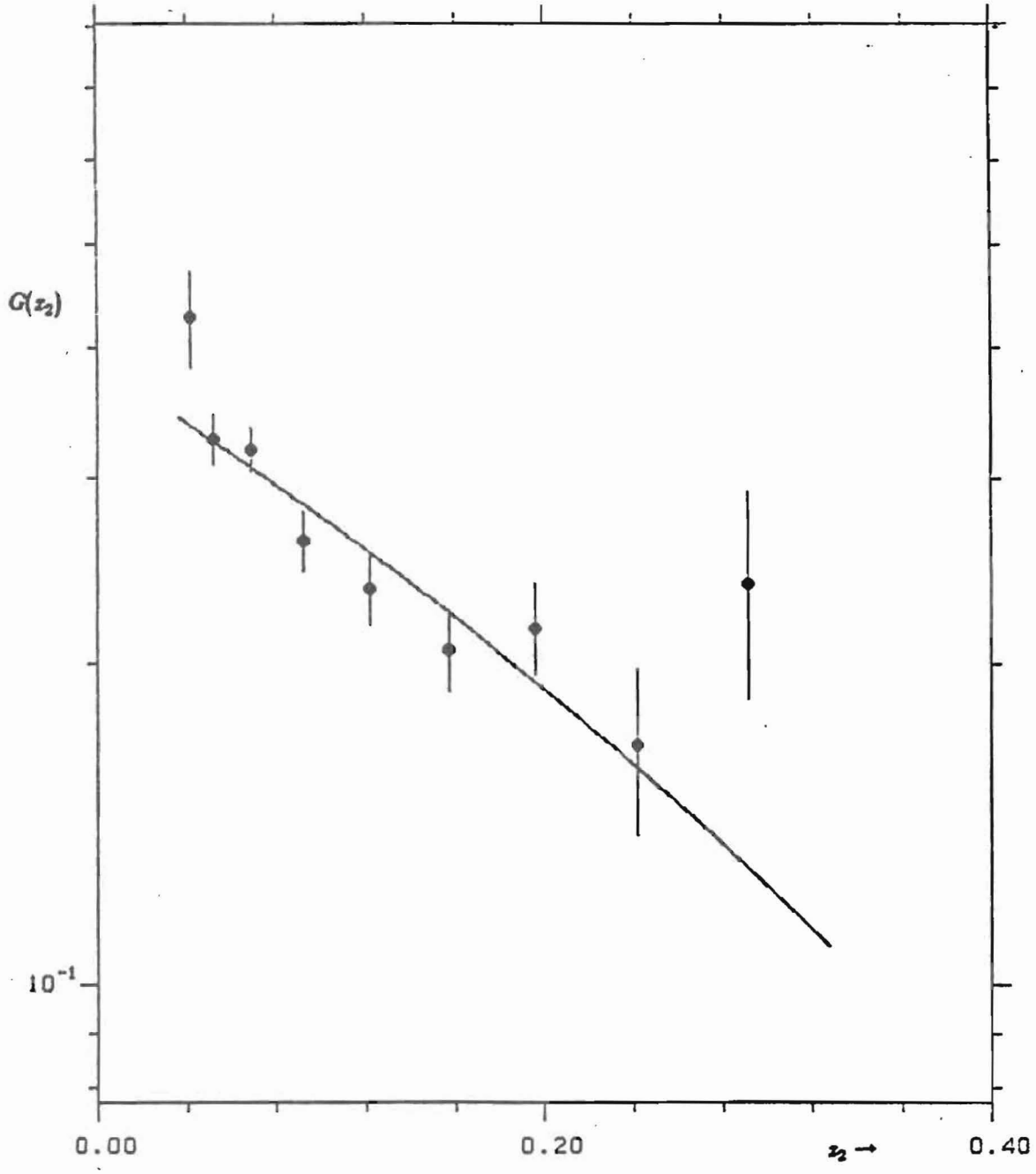
G(z₂)
10⁻¹
0.00
0.20
z₂ →
0.40

Figure 53 -- $G(x_2)$ after iterated projections. The solid line is $G(x_2)$ determined from CCFRR data; normalization of the data points is discussed in the text.

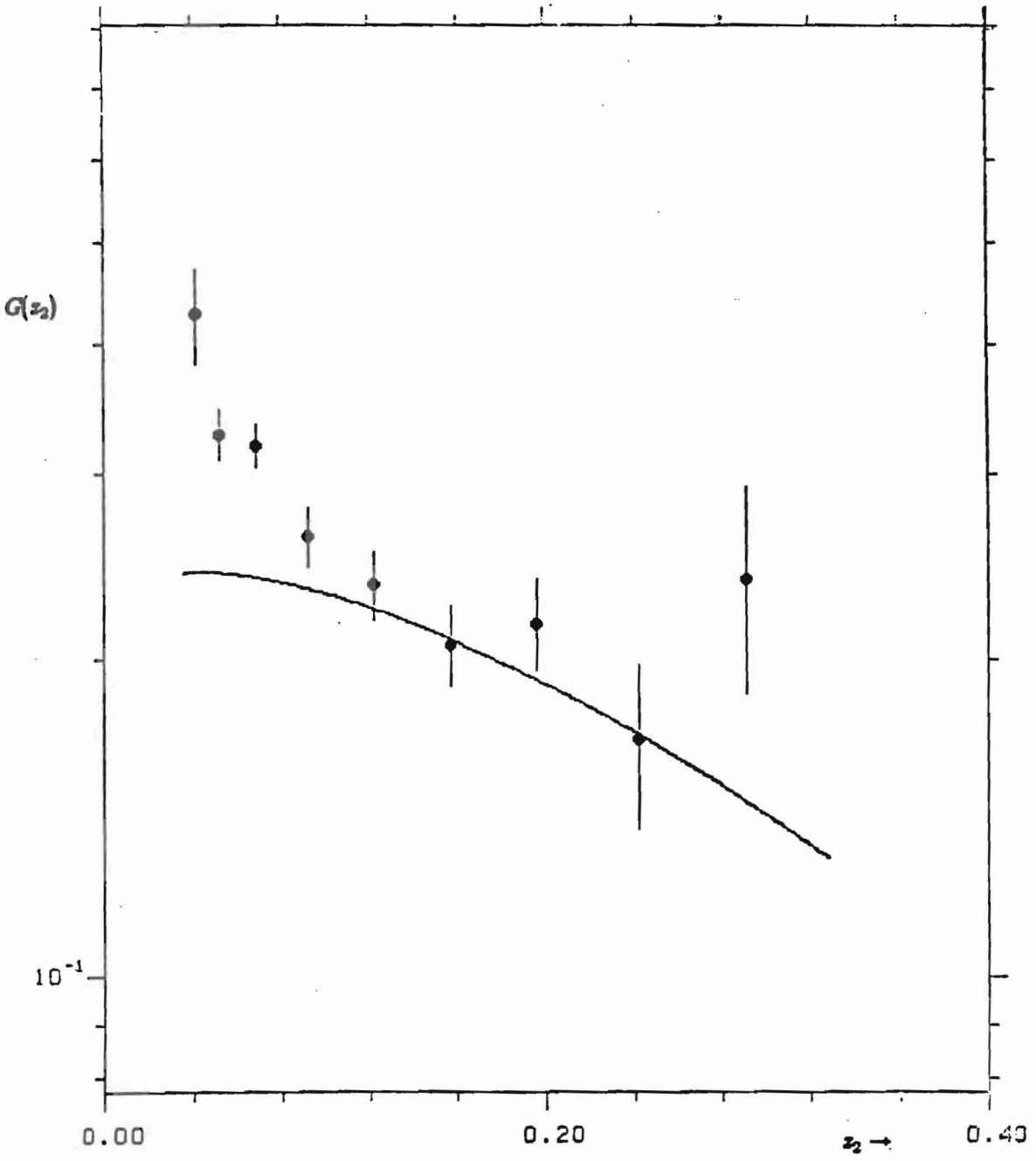
G(z₂)
10⁻¹
0.00
0.20
0.40
z₂ →

Figure 54 – Measurements of $G(x_2)$ by three mu-pair experiments. The solid curve is $G(x_2)$ computed from CCFRR results; normalization of the data is discussed in the text. The error bar to the left of the curve represents ± 1 standard deviation (statistical errors only) for the curve.

- This Experiment
- E444 (Reference 49)
- NA3 (Reference 50)

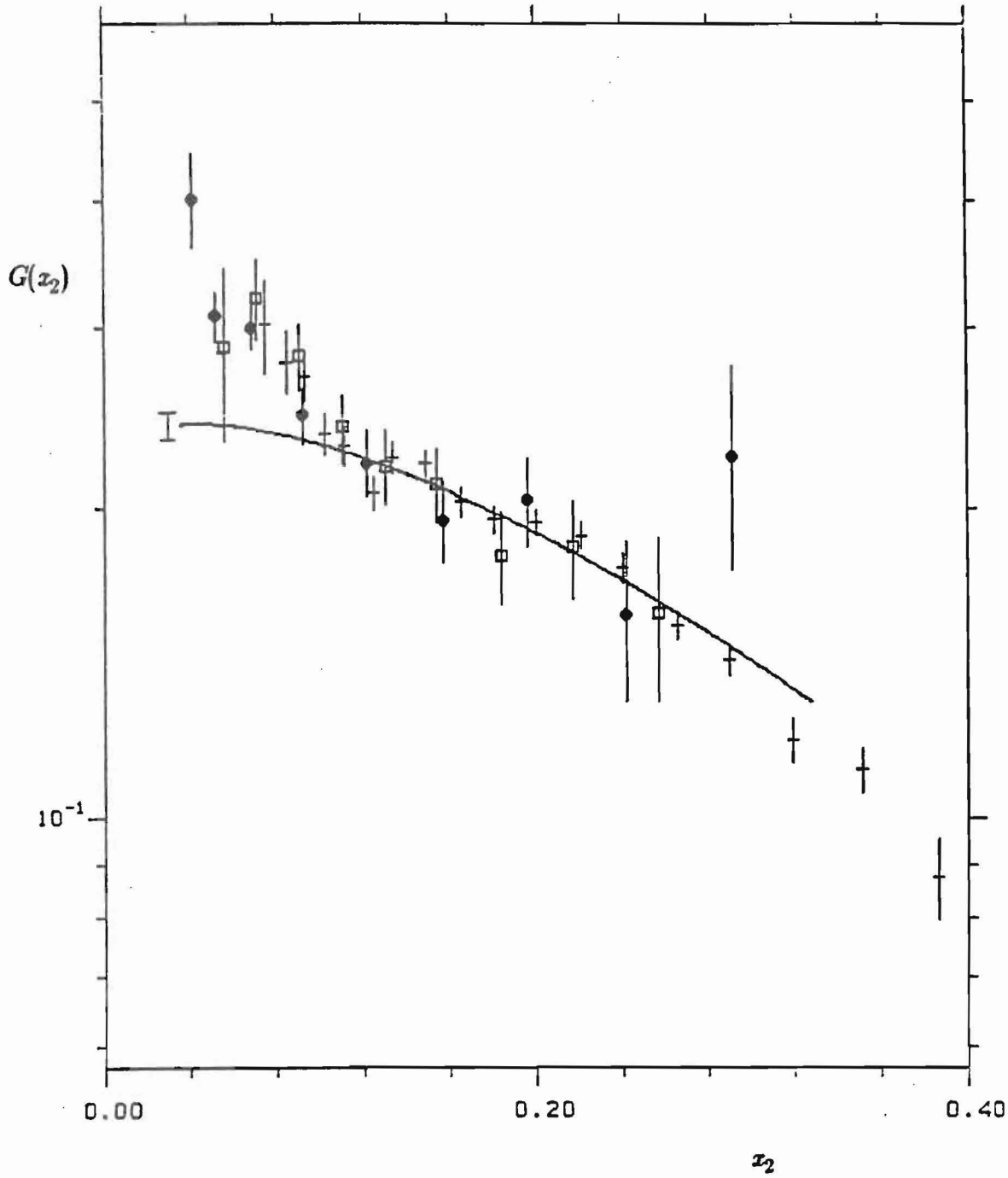
$G(x_2)$
10^{-1}
0.00
0.20
0.40
x_2

Figure 55 -- $F^{\pi}(x_1)$ after iterated projections. The solid line is $F^{\pi}(x_1) = .85\sqrt{x_1}(1-x_1)^{1.53}$.

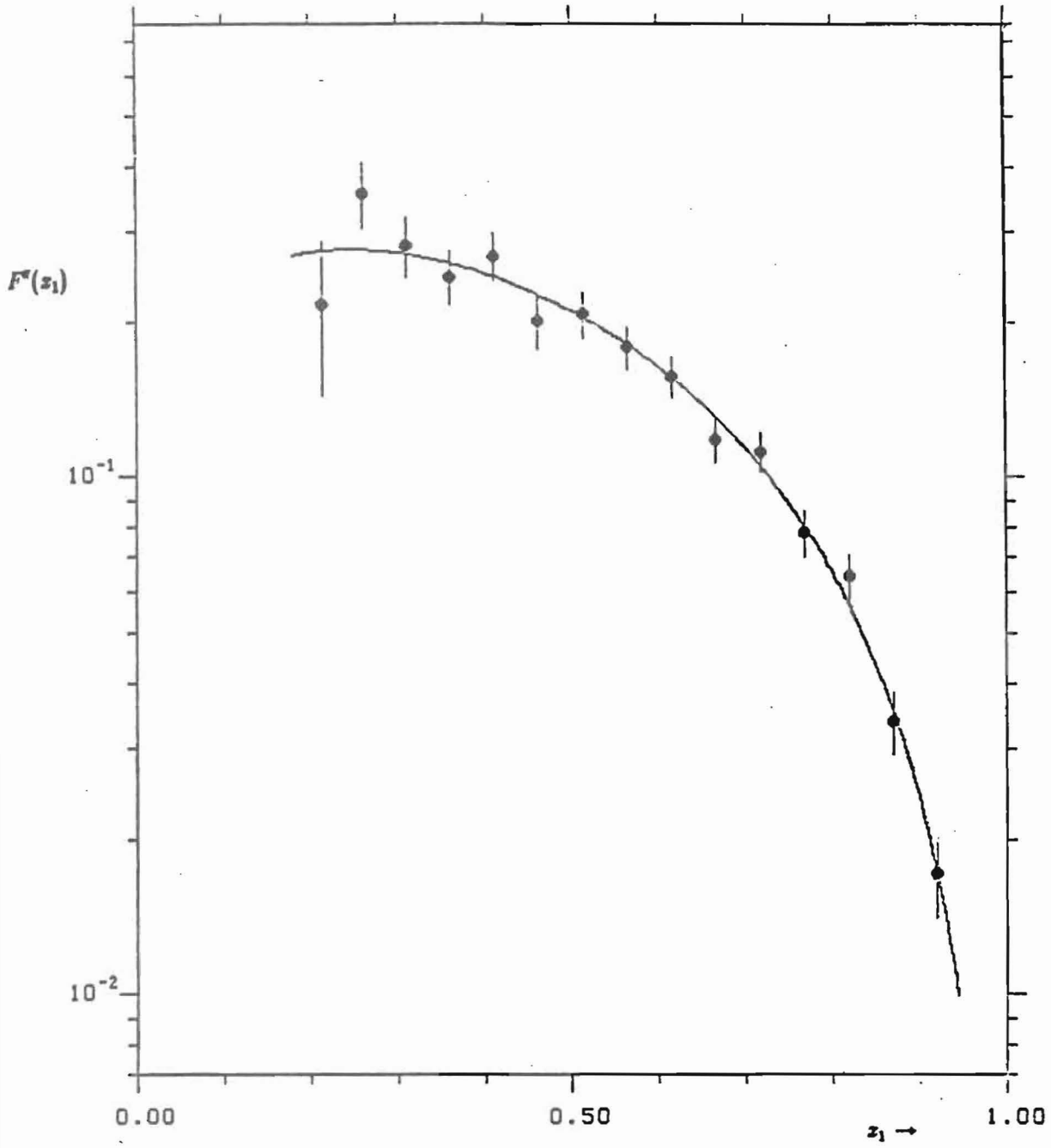
$F^{\pi}(z_1)$
10^{-1}
10^{-2}
0.00
0.50
1.00
$z_1 \rightarrow$

Figure 56 -- $F^{\infty}(x_1)$ after iterated projections. The solid line is $F^{\infty}(x_1) = 2.9x_1\left[(1-x_1)^2 + .0056\right]$

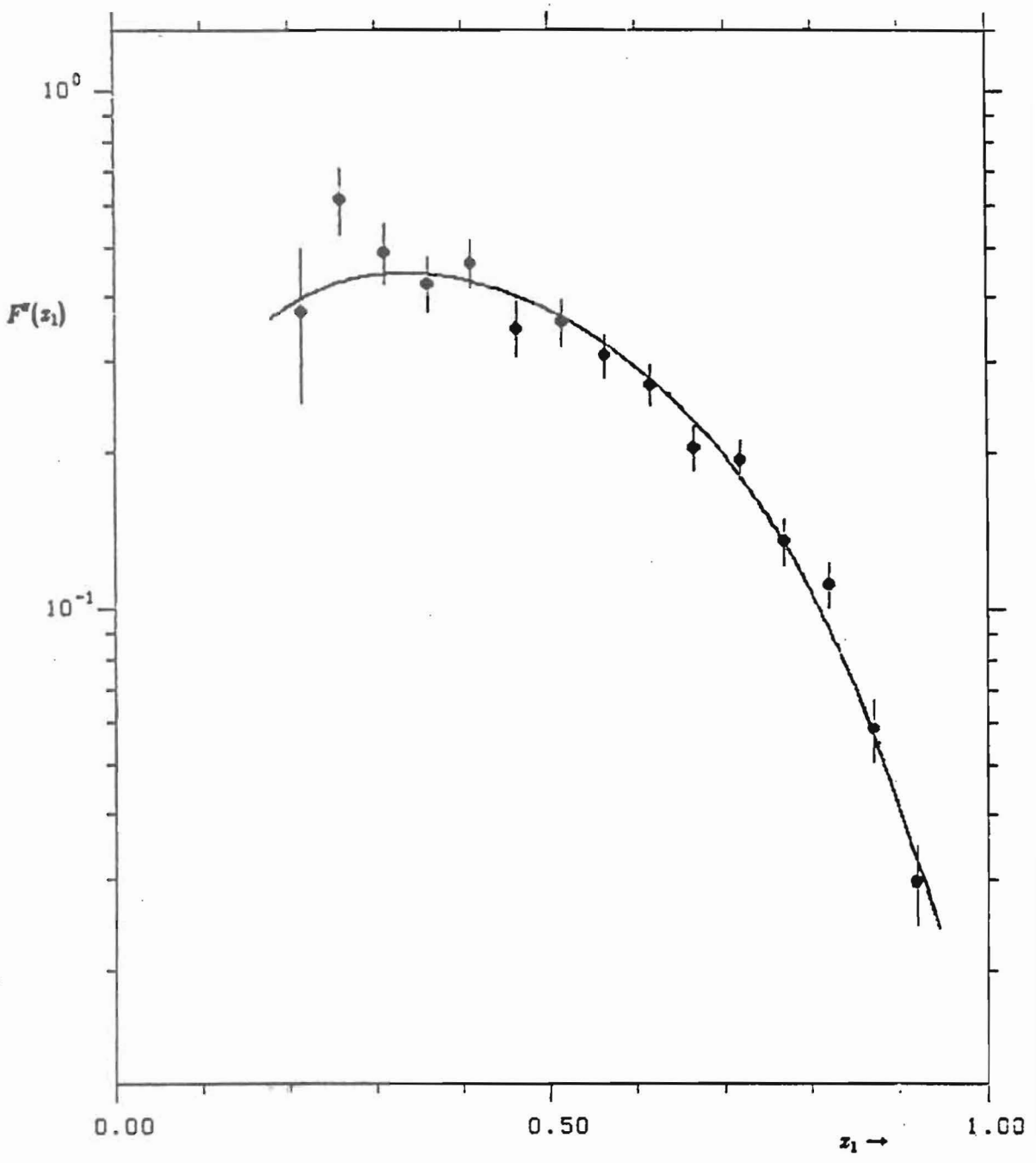
10^0
10^{-1}
$F^{\pi}(z_1)$
0.00
0.50
1.00
$z_1 \rightarrow$

Figure 57 – Plot of $<p_T^2>$ as a function of x_1.

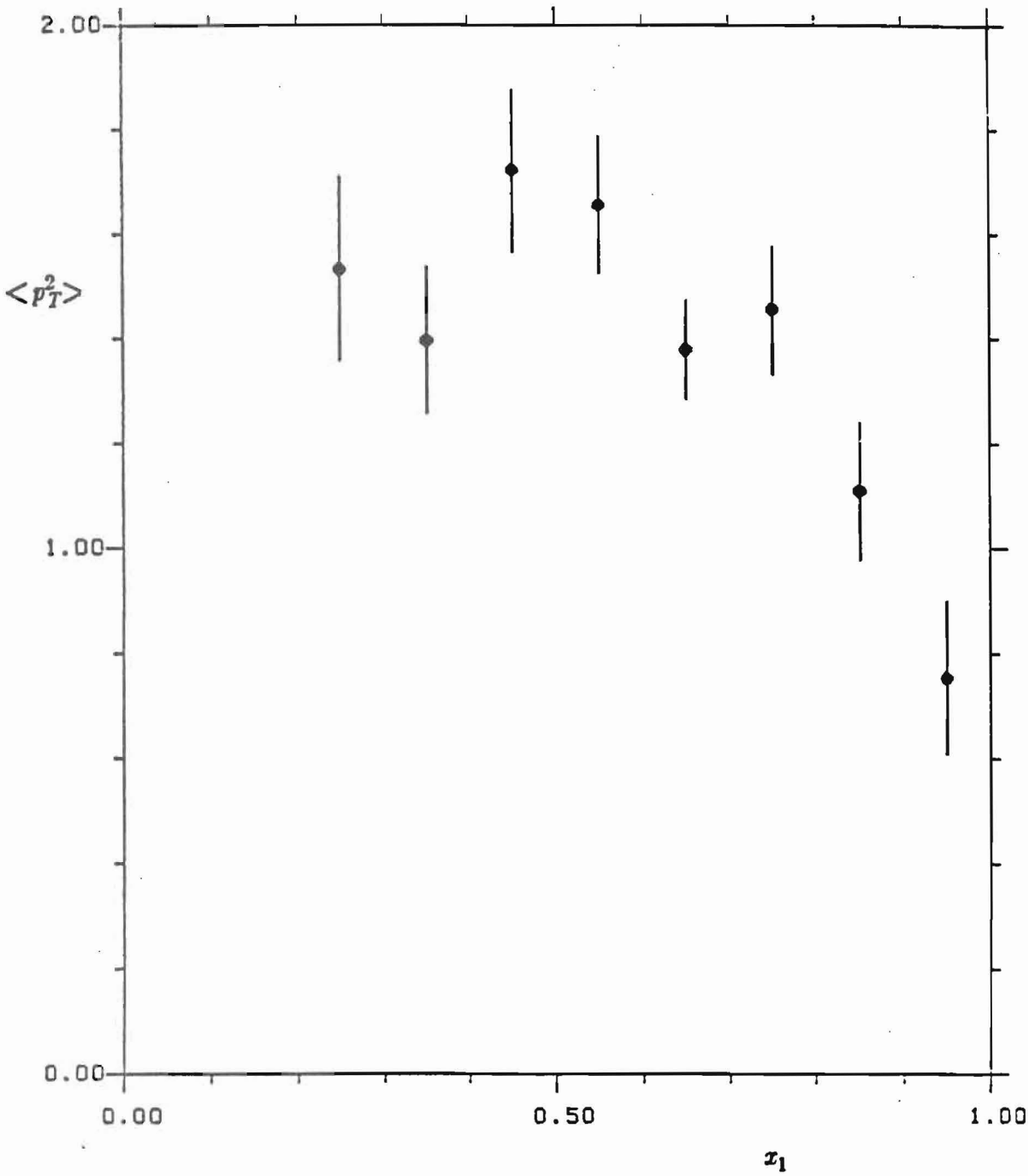
2.00
1.00
0.00
$<p_T^2>$
0.00
0.50
1.00
x_1

Figure 58 -- Existing measurements of α at various values of x_1
Dotted lines indicate $\alpha=\pm 1$.

NA3, $P_T<1$	NA3, $P_T>1$
NA10, $P_T<1$	NA10, $P_T>1$
E444	OMEGA (M=2-2.7)

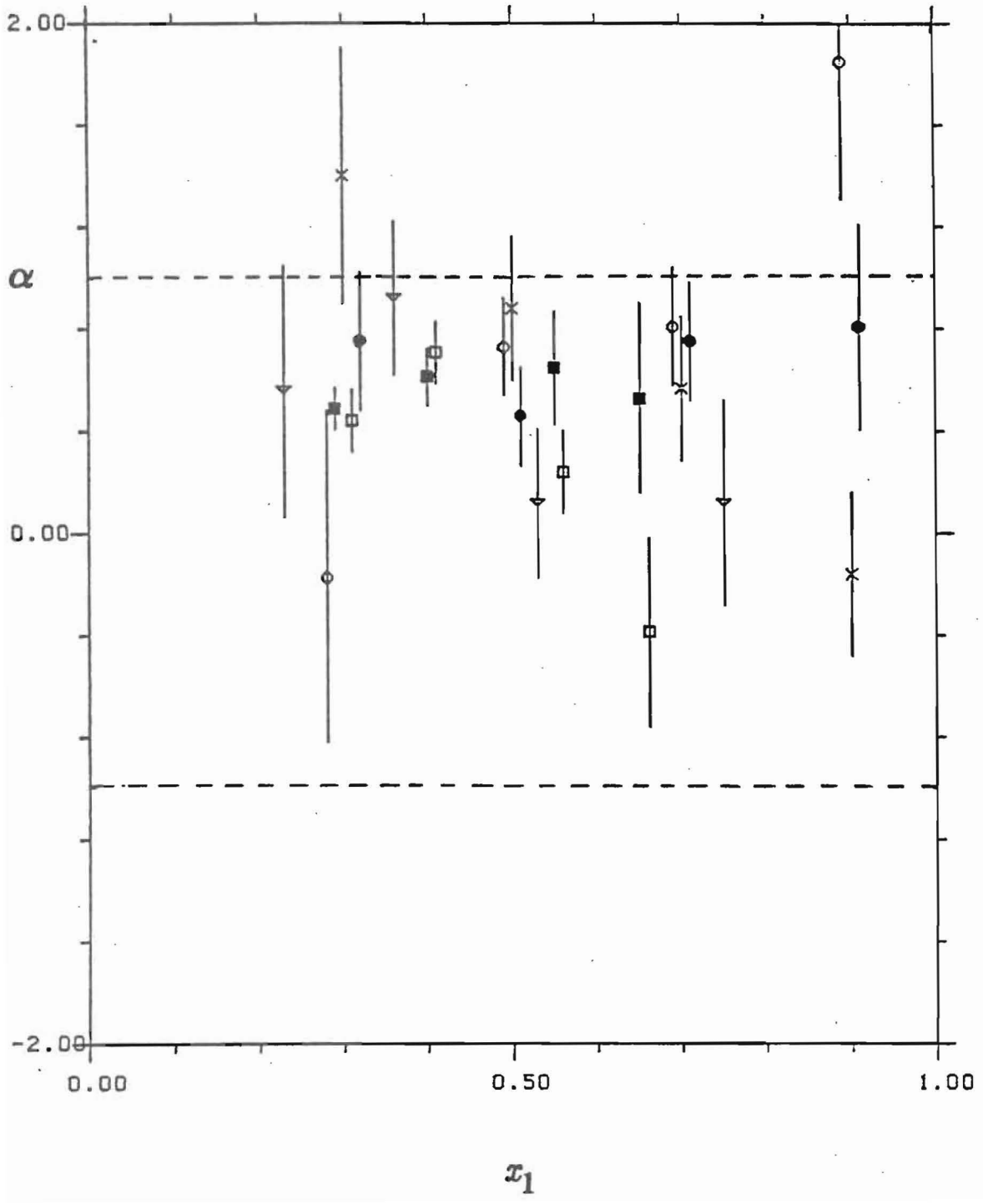
2.00
α
0.00
-2.00
0.00
0.50
1.00
x_1

Figure 59 -- Cosθ^* distributions in four helicity frames. The solid curves are fits to $1+\alpha\cos^2\theta^*$; values of α are contained in table 14.

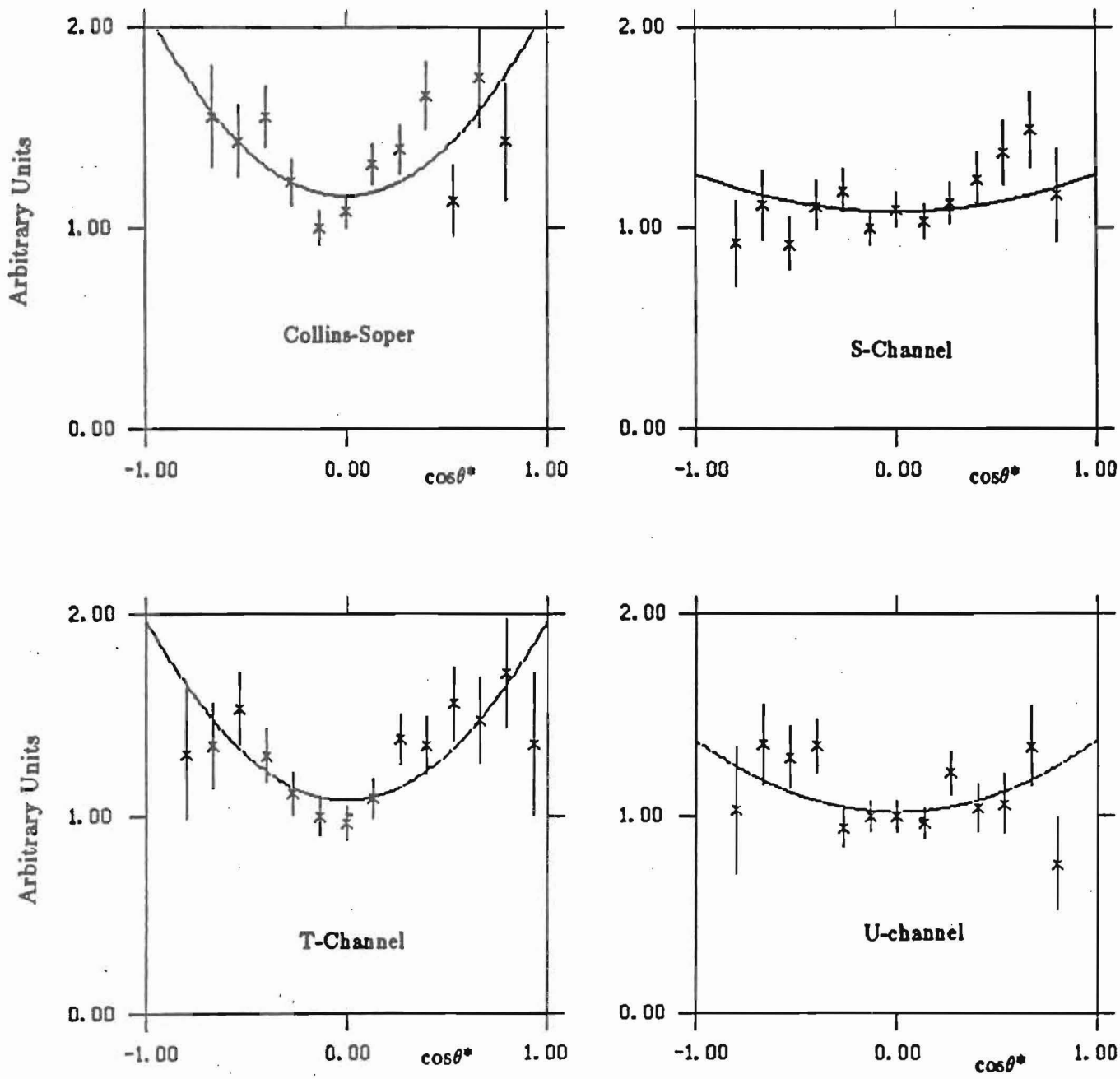
2.00
1.00
0.00
Arbitrary Units
Collins-Soper
-1.00
0.00
cosθ*
1.00
S-Channel
T-Channel
U-channel

Figure 60 -- Cosθ^* distributions in four regions of x_1. (Collins-Soper frame) The solid curves are fits to $1+\alpha\cos^2\theta^*$; values of α are contained in table 15.

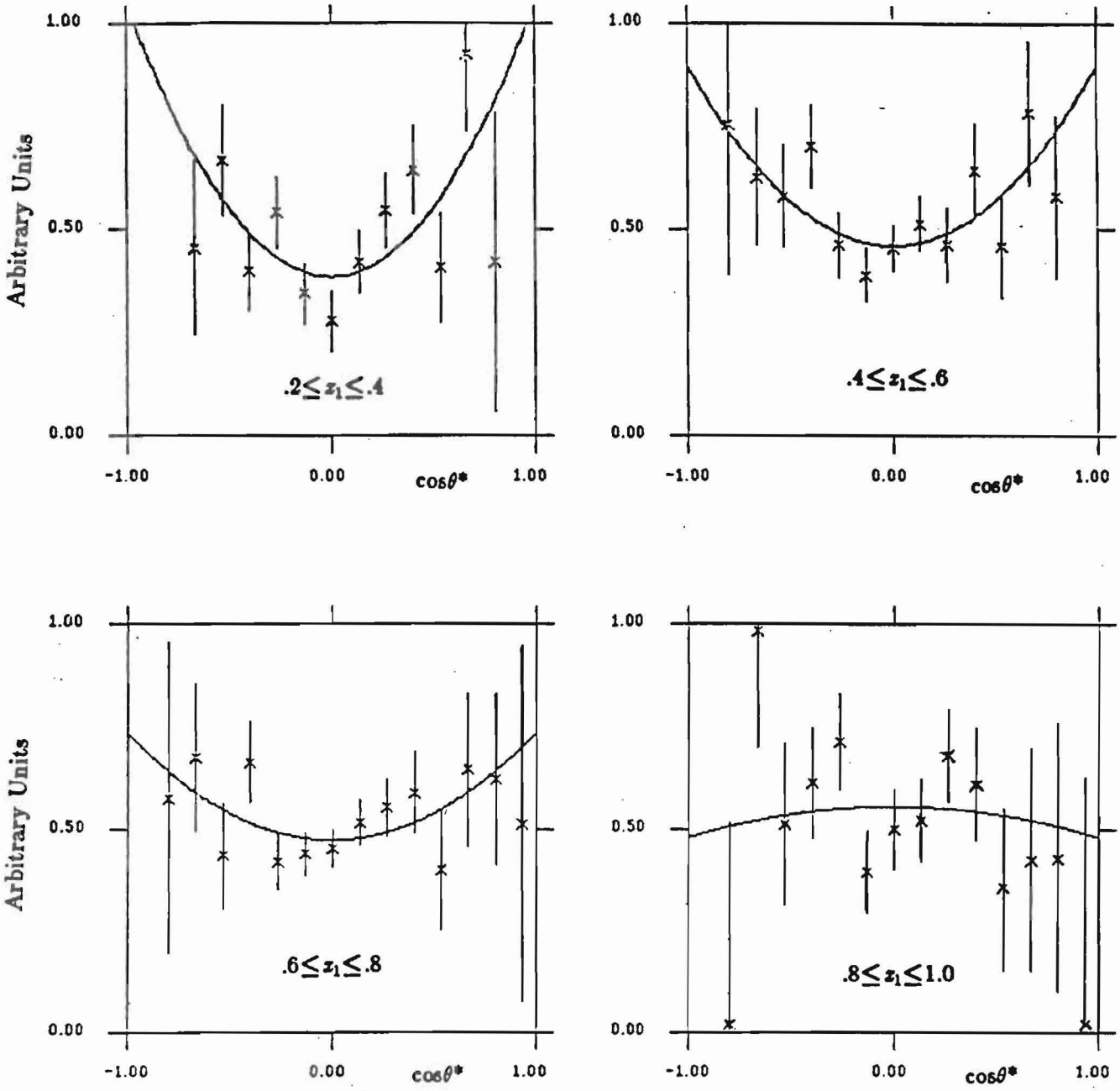
Arbitrary Units
1.00
0.50
0.00
-1.00
0.00
cosθ*
1.00
.2≤z_1≤.4
.4≤z_1≤.6
.6≤z_1≤.8
.8≤z_1≤1.0

Figure 61 -- Cosθ^* distributions in four regions of x_1. (T-Channel) The solid curves are fits to $1+\alpha\cos^2\theta^*$; values of α are contained in table 15.

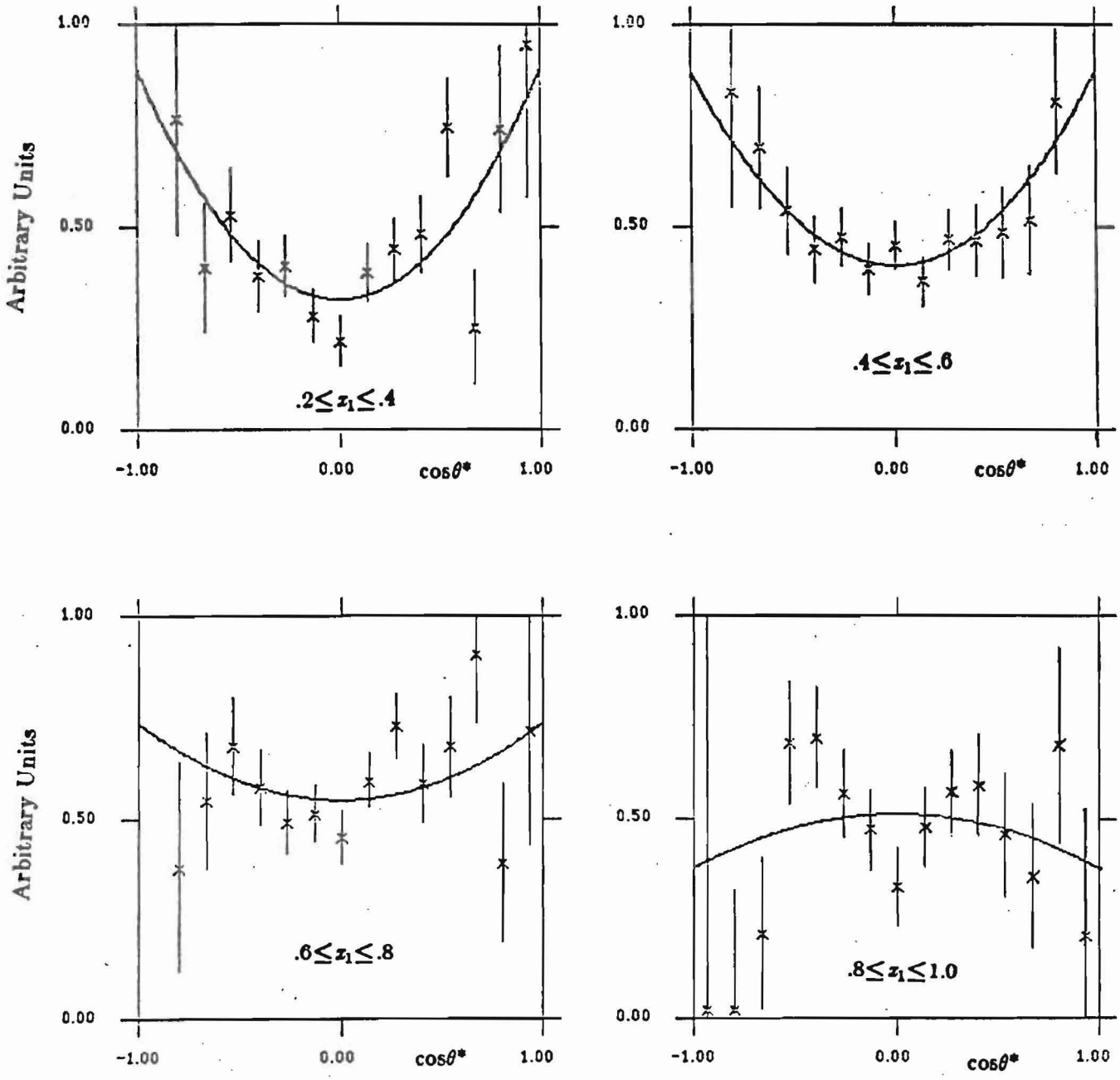
Arbitrary Units
1.00
0.50
0.00
-1.00
0.00
cosθ*
1.00
.2≤x1≤.4
.4≤x1≤.6
.6≤x1≤.8
.8≤x1≤1.0

Figure 62 -- Plot of α *versus* x_1. (Collins-Soper frame) The solid curve is described in the text.

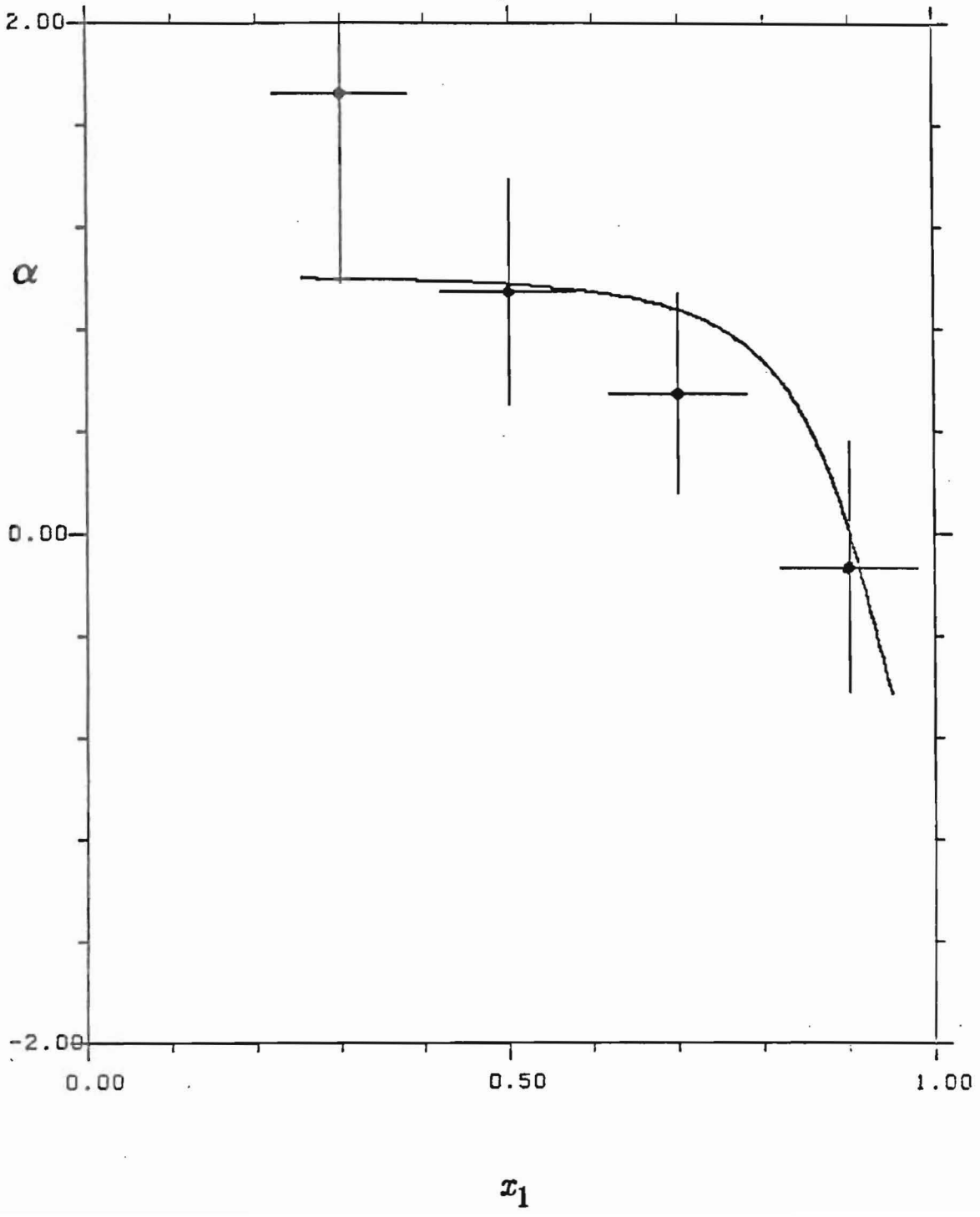
2.00
0.00
-2.00
α
0.00
0.50
1.00
x_1

Figure 63 -- Plot of α *versus* x_1. (T-Channel) The solid curve is described in the text.

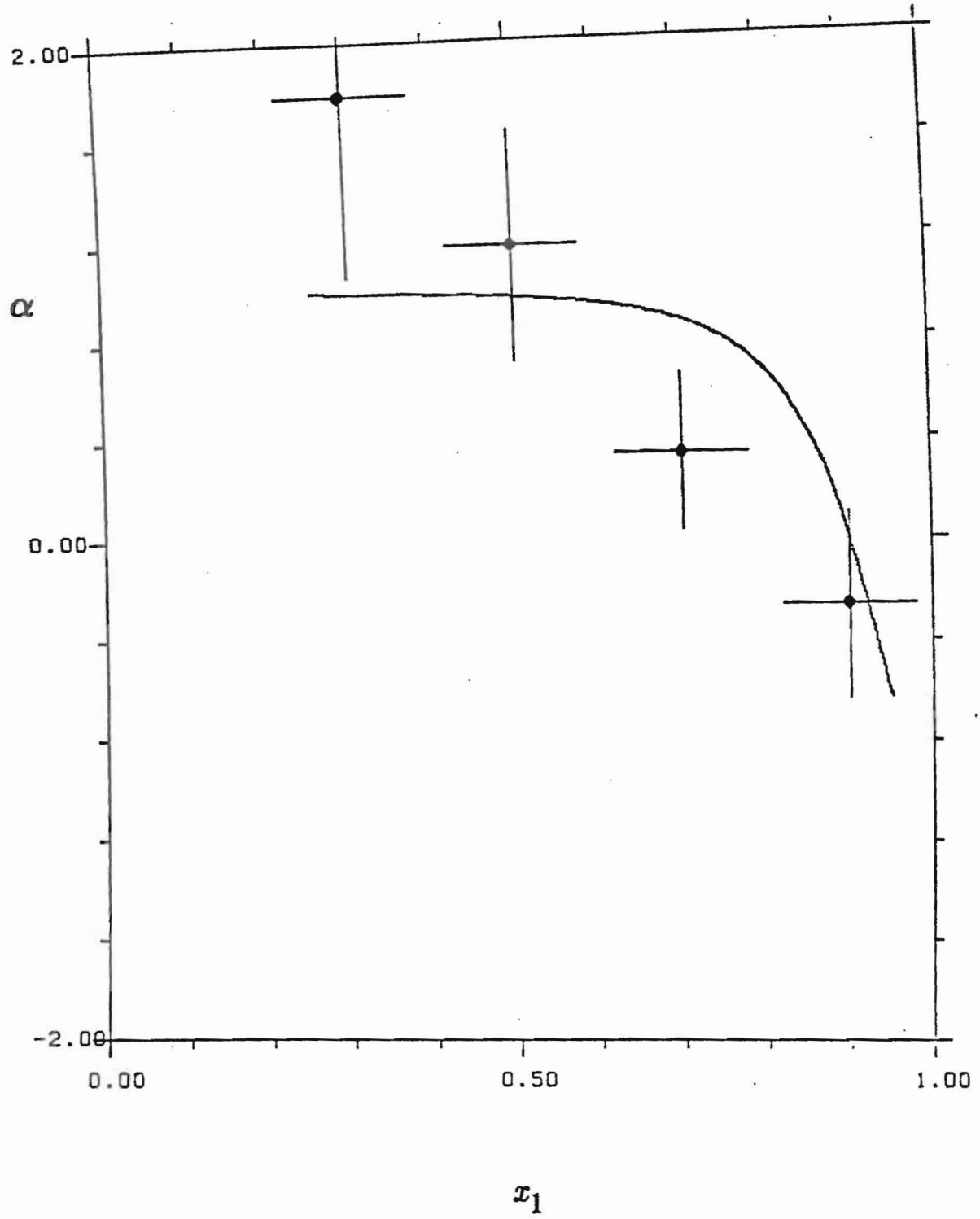
2.00
0.00
-2.00
α
0.00
0.50
1.00
x_1

Figure 64 -- Cosθ^* distributions in 3 regions of P_T/M. (Collins-Soper frame) The solid curves are fits to $1+\alpha\cos^2\theta^*$; values of α are contained in table 16.

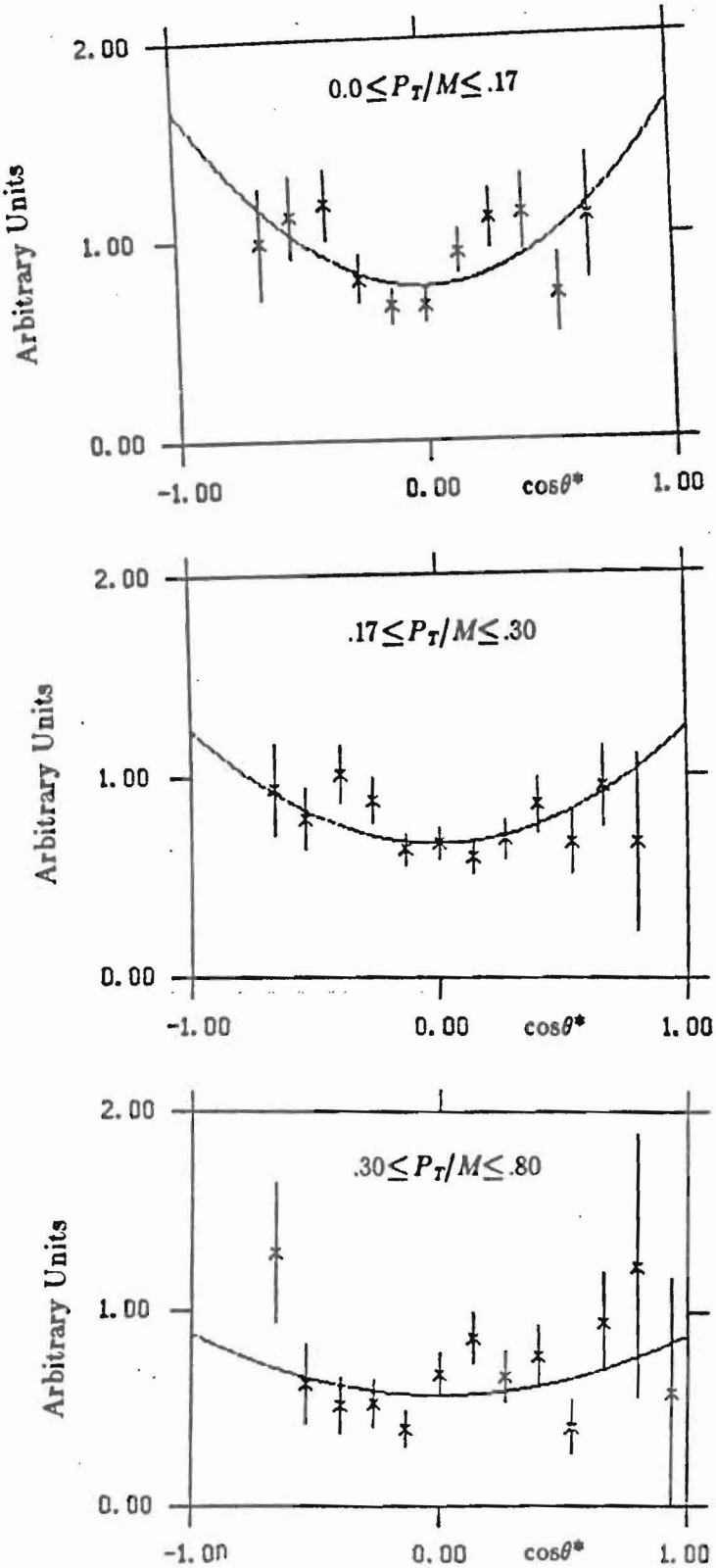
2.00
1.00
0.00
Arbitrary Units
$0.0 \leq P_T/M \leq .17$
-1.00
0.00
cosθ*
1.00
2.00
1.00
0.00
Arbitrary Units
$.17 \leq P_T/M \leq .30$
-1.00
0.00
cosθ*
1.00
2.00
1.00
0.00
Arbitrary Units
$.30 \leq P_T/M \leq .80$
-1.00
0.00
cosθ*
1.00

Figure 65 -- Cosθ^* distributions in 3 regions of P_T/M. (T-Channel) The solid curves are fits to $1+\alpha\cos^2\theta^*$; values of α are contained in table 16.

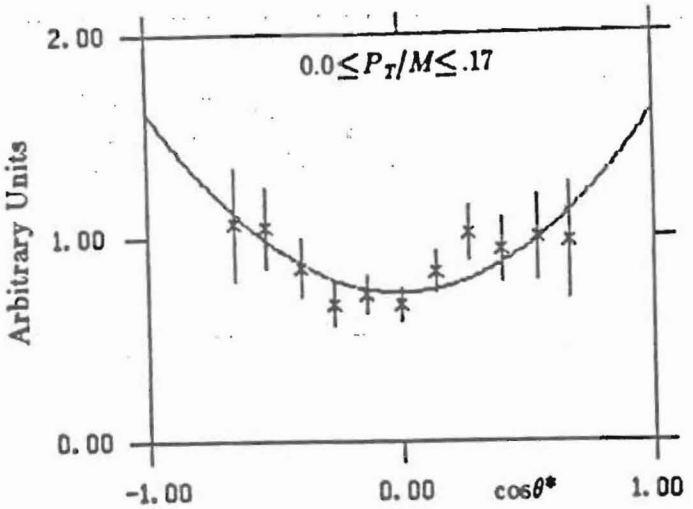
2.00
1.00
0.00
Arbitrary Units
$0.0 \leq P_T/M \leq .17$
-1.00
0.00
$\cos\theta^*$
1.00

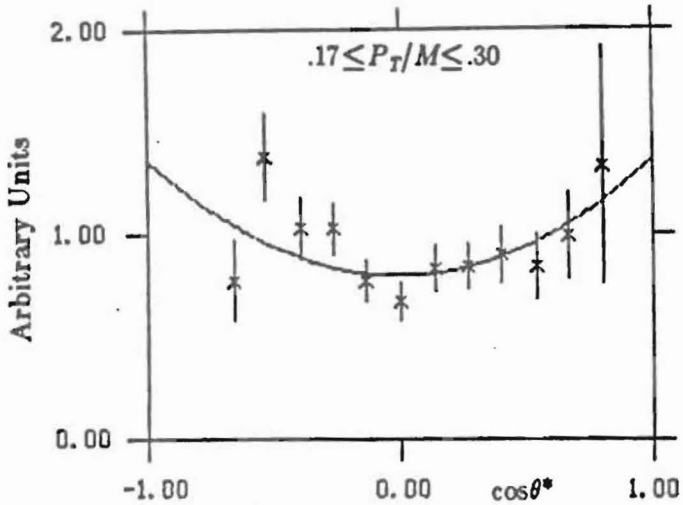
2.00
1.00
0.00
Arbitrary Units
$.17 \leq P_T/M \leq .30$
-1.00
0.00
$\cos\theta^*$
1.00

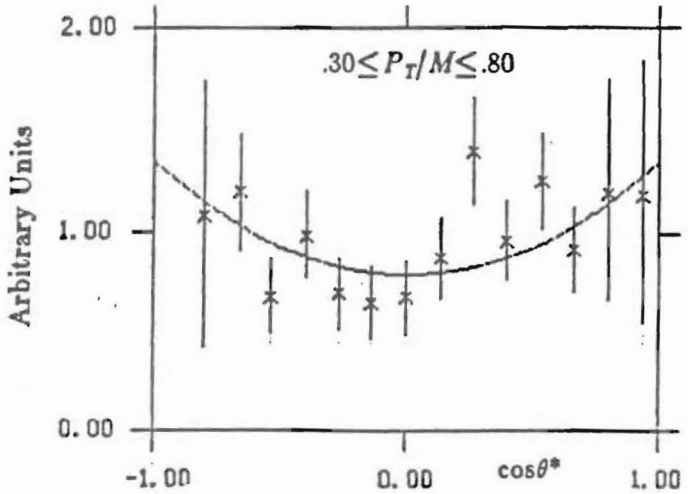
2.00
1.00
0.00
Arbitrary Units
$.30 \leq P_T/M \leq .80$
-1.00
0.00
$\cos\theta^*$
1.00

Figure 66 -- Plots of α *versus* P_T/M in Collins-Soper frame and T-Channel. The solid curves are described in the text.

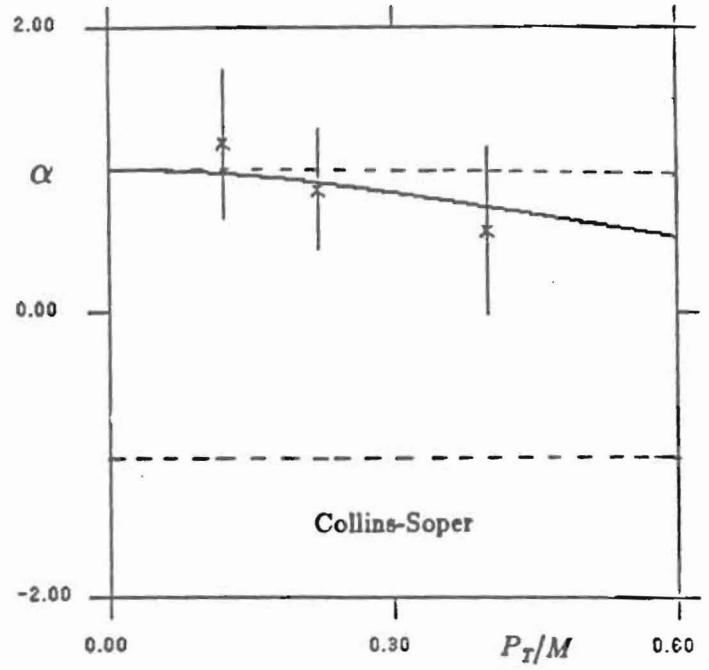
2.00
α
0.00
-2.00
Collins-Soper
0.00
0.30
P_T/M
0.60

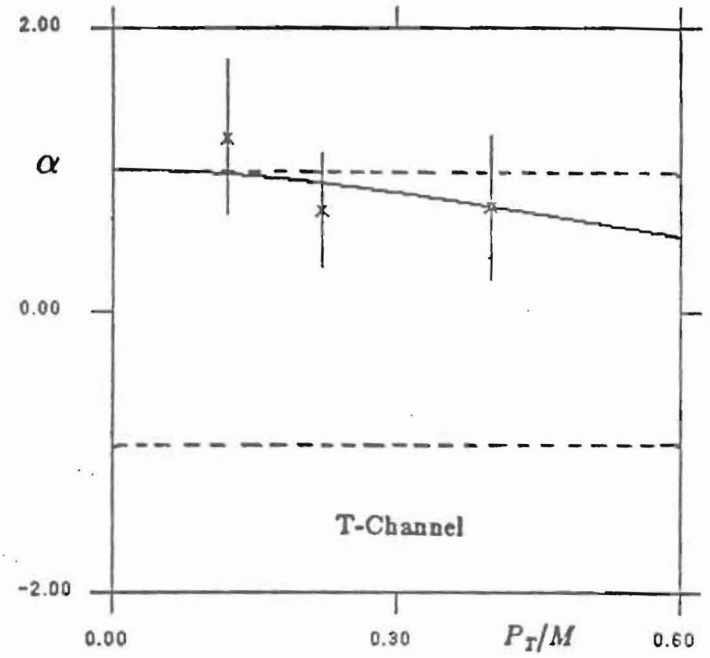
2.00
α
0.00
-2.00
T-Channel
0.00
0.30
P_T/M
0.60